Tréhu, A.M., Bohrmann, G., Rack, F.R., Torres, M.E., et al., 2003
Proceedings of the Ocean Drilling Program, Initial Reports Volume 204

4. SITE 1245[1]

Shipboard Scientific Party[2]

INTRODUCTION

Site 1245 (proposed Site HR3a) is located in 870 m of water on the western flank of Hydrate Ridge, ~3 km northwest of the southern summit (see Fig. **F1,** p. 51, in the "Leg 204 Summary" chapter). The three-dimensional (3-D) seismic data show that the bottom-simulating reflector (BSR) is at a depth of ~134 meters below seafloor (mbsf) at this site. As at all sites drilled during Leg 204, the temperature and pressure at the seafloor at Site 1245 are well within the gas hydrate stability zone (GHSZ), indicating that gas hydrates can exist within the entire stratigraphic section above the BSR if hydrate-forming gases are available in concentrations that exceed their in situ solubility. This site also samples seismic Horizon A. Horizon A can be mapped from the northern boundary of the seismic survey, where it clearly follows stratigraphic boundaries, to the summit, where Horizon A appears as a "bright spot" beneath the BSR. On its downdip edge, Horizon A appears to lap onto the boundary between coherent folded strata and the seismically incoherent facies interpreted to represent highly deformed sediments of the accretionary complex. Horizon A has been interpreted to be a "conduit" that transports fluids from the accretionary complex to the summit. Several unconformities, referred to as Horizons Y and Y′, overlie Horizon A and appear to represent discontinuities in sediment accumulation in a slope basin that was formed during the growth of an underlying accretionary anticline.

Primary objectives at Site 1245 were the following:

1. Determine the distribution, composition, and concentration of gas hydrate in the sediments on the western flank of Hydrate Ridge and contrast these parameters with those on the eastern flank of the ridge and in the adjacent slope basin, where the sub-

[1]Examples of how to reference the whole or part of this volume. [2]Shipboard Scientific Party addresses.

Ms 204IR-104

BSR fluid migration pathways inferred from seismic data are distinctly different.
2. Sample sediments and fluids from seismic Horizon A.
3. Sample the sedimentary section of the western flank of Hydrate Ridge below the BSR to provide constraints for interpreting variations in BSR strength across the western flank.
4. Be a reference site tying a north-south–trending transect that extends from Site 1245 to the summit (including Sites 1247–1250) with an east-west transect comprising Sites 1244–1246 and 1252.

Five holes were drilled at Site 1245 (Fig. F1). Hole 1245A was drilled to a depth of 380 mbsf (without coring) to obtain the initial logging-while-drilling (LWD) data for this site. Hole 1245B was cored to 473.7 mbsf using the advanced piston corer (APC) and extended core barrel (XCB). Holes 1245C and 1245D were cored to 201.7 and 24 mbsf, respectively, for extensive high-resolution geochemical and microbiological sampling. Hole 1245E was drilled to 473.7 mbsf and then cored to 540.3 mbsf using the rotary core barrel (RCB). Coring in Hole 1245E stopped short of the originally planned depth of 700 mbsf because the primary science objectives had been met and hole conditions were deteriorating. Eleven whole-round samples of sediment thought to contain gas hydrate were preserved in liquid nitrogen or in pressure vessels for post-cruise studies.

F1. Bathymetric map, Site 1245, p. 35.

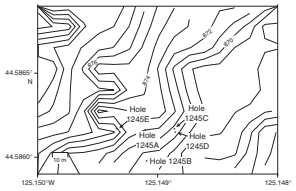

OPERATIONS

Five holes were drilled at this site (Table T1), under good weather conditions. Wind speed was 5–24 kt, gusting to 29 kt; seas were 4–9 ft; swell was 6–15 ft; and the prevailing sea-surface current was from the north at ~0.5–0.9 kt. Hole 1245A was drilled to a depth of 380 mbsf without coring on 18 July 2002 to obtain the initial LWD data for this site. We returned to this site from 6 to 13 August to core Holes 1245B–1245E (Table T1).

T1. Coring summary, p. 100.

The APC temperature (APCT) tool was run ten times and the Davis-Villinger Temperature Tool (DVTP) was run three times at this site. The pressure core sampler (PCS) was run six times, and five deployments were recovered core under pressure. Four deployments of HYACINTH were made at Site 1245, two each with the Hydrate Autoclave Coring Equipment (HYACE) Rotary Corer (HRC) and Fugro Pressure Corer (FPC). Technical and operational difficulties prevented these cores from being recovered under full pressure for further analysis (see **"Downhole Tools and Pressure Coring,"** p. 22). No in situ pressure measurements were made at this site.

Hole 1245A was drilled to obtain the initial LWD data for this site (see **"Downhole Logging,"** p. 26). Drilling proceeded at ~25 m/hr to total depth (TD) at 380 mbsf without difficulty, and real-time data were transmitted to the surface at a rate of 6 Hz. Given calm heave conditions, the real-time data record was changed to increase the depth resolution of formation evaluation logs with less emphasis on high-resolution weight-on-bit and torque measurements. Mud pump noise affected the data transmission to a lesser extent than at Site 1244. No sliding tests were conducted for the Nuclear Magnetic Resonance (NMR-MRP) tool. Total bit run was ~28 hr.

Hole 1245B was cored to 473.7 mbsf using the APC and XCB (Table T1). Special tool deployments (see Table T2, p. 72, in the "Leg 204 Sum-

mary" chapter) included five APCT tool and three DVTPP, three PCS from which two PCS cores were successfully recovered under pressure, and one HRC. The HYACINTH FPC (Core 204-1245B-18Y) recovered core; however, the flapper on the corer failed to close. Whirl-Paks and PFT were used for microbiology Cores 204-1245B-23X, 24X, 26X, 31X, 38X, 43X, and 49X. Hole 1245B was terminated at a total depth of 473.6 mbsf.

Hole 1245C was cored to 198.7 mbsf using the APC and XCB. Special tool deployments (see Table **T2,** p. 72, in the "Leg 204 Summary" chapter) included five APCT, three PCS, and three Drill String Acceleration (DSA) tool runs. Whirl-Paks and PFT were used for microbiology Cores 204-1245C-1H, 2H, 4H, 5H, 7H, 9H, 12H, 15X, 17X, 20X, 22X–26H, and 28X.

Hole 1245D was cored to 24.0 mbsf using the APC. These three cores were recovered for microbiological and chemical whole-round sampling. Whirl-Paks and PFT were used in all cores. No special tools were deployed in this hole.

Hole 1245E was drilled without coring with the RCB/center bit to 473.7 mbsf, followed with RCB coring to 540.3 mbsf. Hole conditions deteriorated and we were unable to clean up the hole below that point; therefore, we began to pull out for the prelogging wiper trip. At this point, the pipe became stuck and was not freed even after releasing the bit. After ~15 hr, preparations were made to sever the pipe; however, the pipe was successfully released and the hole was not abandoned. Logging in the upper 300 mbsf with the triple combination (triple combo) and Formation MicroScanner (FMS)-sonic wireline tool strings were successful (see **"Downhole Logging,"** p. 26).

The first helicopter rendezvous at this site occurred at 1308 hr on 13 August. Arriving passengers included Herbert Leyton, Schlumberger vertical seismic profile (VSP) engineer, and Roy Davis, Ocean Drilling Program (ODP)/Texas A&M University (TAMU) photographer. Departing passengers included Bill Gwilliam from the Department of Energy (DOE)/National Energy Technology Laboratory (NETL), Floris Tuynder, HYACINTH Fugro FPC engineer, and Dean Ferrell, ODP/TAMU senior electronic designer. Ben Bloys from Chevron-Texaco did not arrive because of weight limitations. A second trip of the helicopter brought Ben Bloys along with initial batch of VSP surface equipment. The remaining three-component VSP tools arrived on a third helicopter trip on 14 August. However, the plans for conventional, offset, and walkaway seismic lines were abandoned when the downhole seismometer would not clamp in Hole 1245E and the hole continued to collapse.

LITHOSTRATIGRAPHY

Site 1245 is located just west of the crest of southern Hydrate Ridge (see Figs. **F1,** p. 51, and **F5,** p. 55, both in the "Leg 204 Summary" chapter). Five holes (Holes 1245A–1245E) were drilled and four holes (Holes 1245B–1245E) were cored at Site 1245. Hole 1245B was cored to 471.7 mbsf, Hole 1245C was cored to 198.7 mbsf, Hole 1245D was cored to 24 mbsf, and Hole 1245E was cored from 473.7 to 540.30 mbsf (for 66.6 m). Recovery was generally good (Hole 1245B = 88.7%; Hole 1245C = 93.3%; Hole 1245D = 103.4%; and Hole 1245E = 27.7%).

We divide the sedimentary sequence recovered at Site 1245 into five lithostratigraphic units (Units I–V) (Figs. **F2, F3**) based on sedimentological criteria (e.g., variations in sedimentary structure, grain size, and

F2. Lithostratigraphic summary, p. 36.

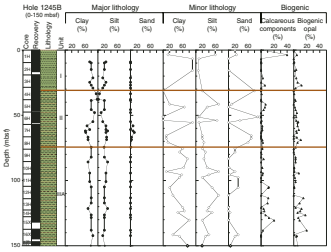

F3. Seismic reflection profile, p. 41.

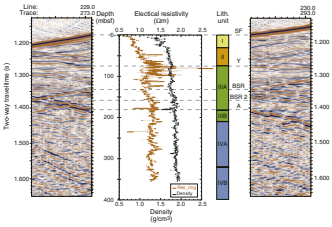

biogenic and lithologic components) and other parameters, such as calcium carbonate content (expressed as $CaCO_3$ weight percent), total organic carbon (TOC), and mineralogy from X-ray diffraction (XRD) (Figs. F2, F4). We also compare and correlate our results with the 3-D seismic data, downhole LWD data, and physical property measurements (magnetic susceptibility [MS] and gamma ray attenuation [GRA] density) to better define the entire stratigraphic sequence (Fig. F3). Based on the above criteria, we further divide lithostratigraphic Unit III into two subunits (Subunits IIIA and IIIB) and lithostratigraphic Unit IV into two subunits (Subunits IVA and IVB). Correlation of the lithostratigraphic units defined here with the other Leg 204 sites is summarized in Figure F10, p. 60, in the "Leg 204 Summary" chapter.

F4. Abundance of major, minor, and biogenic lithologies, p. 42.

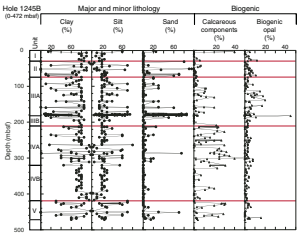

Lithostratigraphic Units

Lithostratigraphic Unit I

Intervals: Sections 204-1245B-1H-1 through 4H-2; 204-1245C-1H-1 through 4H-8; and 204-1245D-1H-1 through 3H-CC
Depths: Hole 1245B: 0.00–31.50 mbsf; Hole 1245C: 0.00–28.50 mbsf; and Hole 1245D: 0.00–24.00 mbsf
Age: late Pleistocene–Holocene

Good core recovery and correlation of lithostratigraphic Unit I in Holes 1245B and 1245C suggests that we recovered a complete record of lithostratigraphic Unit I at Site 1245. The majority of the sediments recovered in Hole 1245D were sampled for microbiology, but the sections we described do correlate with Holes 1245B and 1245C. Lithostratigraphic Unit I consists of dark greenish gray (5GY 4/1) nannofossil-bearing clay to silty clay with some foraminifer-bearing zones and a few thin (<1 cm) graded silt layers, which we interpret as turbidites. Coarser silt is present in the top 30 cm of Hole 1245C as a thick layer; however, it is homogenized with the surrounding clay as a result of coring-related disturbance and, thus, may be reworked. Authigenic carbonates are common, and both sulfide mineralization and bioturbation increase toward the base of lithostratigraphic Unit I.

The top of lithostratigraphic Unit I contains several clay zones with authigenic carbonate precipitation. Semiconsolidated to solid carbonate nodules were found in Hole 1245B in Sections 204-1245B-1H-4, 1H-5, and 2H-4 (Fig. F5), as well as in Hole 1245C in Section 204-1245C-1H-4. Sulfide mineralization increases toward the base of the unit and is observed as (1) an increase in the dark gray (N3) color of the sediment (e.g., intervals 204-1245B-3H-4 and 204-1245C-4H-3) and (2) an appearance of sulfide nodules (e.g., Sections 204-1245B-3H-6, 9–10 cm; 204-1245C-4H-3, 74 cm; and 204-1245C-4H-4, 121 cm).

The lithostratigraphic Unit I/II boundary is marked by a general downhole increase in the frequency of turbidites and the onset of coarser material (sand-size fraction) as well as by a slight increase in the relative abundance of siliceous microfauna (Figs. F2, F4).

F5. Carbonate nodule, p. 43.

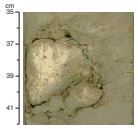

Lithostratigraphic Unit II

Intervals: Sections 204-1245B-4H-3 to 8H-7 and 204-1245C-4H-7 through 10H-7.
Depths: Hole 1245B: 31.50–76.00 mbsf and Hole 1245C: 28.50–77.00 mbsf

Age: middle Pleistocene

Lithostratigraphic Unit II consists of dark greenish gray (5GY 4/1) diatom-bearing clay and silty clay commonly interbedded with fine to very fine sand layers (Fig. F6). The sharp bases and graded nature of the sands suggest they were deposited by turbidity currents. The upper boundary of lithostratigraphic Unit II is defined by an increase in mean grain size (from clay to silty clay) as well as an increase in biogenic components (mainly siliceous). This boundary also correlates with an increase in the LWD resistivity and density (Fig. F3). The lower boundary of lithostratigraphic Unit II is defined by a decrease in grain size from sand to silt, accompanied by a slight decrease in biogenic opal (Figs. F2, F4). This decrease occurs at 76 mbsf in Hole 1245B and at 77 mbsf in Hole 1245C, which correlates well with the estimated depth of Horizon Y, a distinct discontinuity imaged in the 3-D seismic data (see Fig. F5, p. 55, in the "Leg 204 Summary" chapter). However, the west-dipping strata above Horizon Y that downlap onto the flat, possibly erosional surface of Horizon Y (Fig. F3) were not detected in the stratigraphy recovered at Site 1245.

Smear slide analyses indicate that lithostratigraphic Unit II is primarily composed of 78% clay, 19% silt, and 3% sand (Fig. F4). The major nonbiogenic components of lithostratigraphic Unit II are feldspar, quartz, and clay and opaque minerals. Opaque grains, mostly sulfides in irregular and framboidal forms, are common in all grain sizes and typically comprise ~3% of the major and minor lithologies, although locally they reach 10% (e.g., Sections 204-1245B-4H-1 and 7H-4). Glauconite composes >2% of the sediment, and it reaches up to 15% in a 7-cm-thick sand layer located at 67.2 mbsf (Sample 204-1245B-8H-1, 112 cm) (Figs. F7A, F8). Volcanic glass–rich sand, containing 15%–30% glass, is present in Section 204-1245B-6H-3 at ~51.2 mbsf.

The total biogenic component of the sediment, which is composed of foraminifers, nannofossils, diatoms, radiolarians, and sponge spicules, ranges from 3% to 13% of the total sediment. Biogenic opal reaches up to 11%, is composed primarily of diatoms (Sample 204-1245B-8H-2, 67 cm), and is more abundant than the calcareous components (Figs. F2, F4).

Lithostratigraphic Unit II contained one authigenic carbonate nodule in interval 204-1245C-6H-4, 103–105 cm (~53 mbsf). Thin section analysis of the nodule indicates that it is primarily micritic carbonate, containing sparse foraminifers and nonbiogenic components (e.g., quartz, feldspar, and opaques). Two phases of calcite with differing Mg contents were recognized based on the XRD analyses.

Lithostratigraphic Unit III

Intervals: Sections 204-1245B-8H-7 through 24X-7 and Section 204-1245C-10H-7 to Core 204-1245C-28H.
Depths: Hole 1245B: 76.00–212.70 mbsf and Hole 1245C: 77.00–200.90 mbsf
Age: early–middle Pleistocene

Lithostratigraphic Unit III consists of dark greenish gray (5GY 4/1) clay and silty clay to nannofossil-rich and diatom-rich silty clay. The major silty clay lithology is commonly interbedded with fining-upward sandy silt and silt turbidites (Fig. F9). Most of the recovered cores preserve original sedimentary structures, with the exception of the gas

F6. Turbidite, Unit II, p. 44.

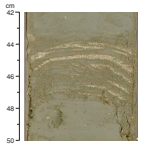

F7. Glauconite compared to carbonate content, p. 45.

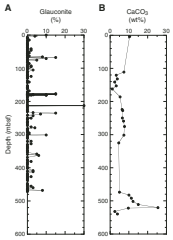

F8. Glauconite grains, p. 46.

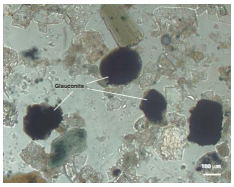

F9. Turbidite, Subunit IIIA, p. 47.

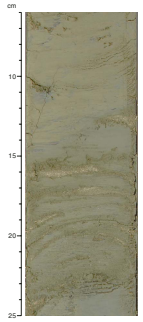

hydrate–bearing sediments, which are characterized by mousselike textures (Fig. **F10**) (see also **"Sedimentary Evidence of Gas Hydrate,"** p. 10). Sediments are slightly fractured, with subhorizontal cracks that are presumably caused by gas expansion. Core recovery was high in lithostratigraphic Unit III (90.3% in Hole 1245B and 89.1% in Hole 1245C), making it possible to correlate between the sequences recovered in Holes 1245B and 1245C.

The lower boundary of lithostratigraphic Unit III was placed above the first glauconite-bearing sand layers at ~212.7 mbsf in Core 204-1245B-24X (Figs. **F7, F8**). This boundary also corresponds to an increase in the MS of sediments (see **"Physical Properties,"** p. 19). Lithostratigraphic Unit III was subdivided into two subunits (Subunits IIIA and IIIB), based on the change in the abundance of biogenic components, variations in grain size, and correlation with 3-D seismic data.

Lithostratigraphic Subunit IIIA

Lithostratigraphic Subunit IIIA (76–183 mbsf in Hole 1245B and 77–189.5 mbsf in Hole 1245C) consists of nannofossil- and diatom-rich clay and silty clay (Figs. **F2, F11**) finely interbedded with thin (2–4 mm to <1 cm thick) sandy silt and silt layers, which we interpret as turbidites (Fig. **F9**). Mottles, patches, and nodules of dark gray (N3) iron sulfides and bioturbation are common to rare throughout the subunit. The base of lithostratigraphic Subunit IIIA is defined by an increase in mean grain size and the presence of volcanic glass–rich sediments and ashes, identified as Horizon A on the 3-D seismic data (Fig. **F3**) (see Figs. **F5,** p. 55, and **F6,** p. 56, both in the "Leg 204 Summary" chapter).

Smear slide analyses indicate that the major lithology of lithostratigraphic Subunit IIIA is typically composed of ~77% clay and ~23% silt. The texture of the minor lithology is dominated by sand and silt, and this grain size becomes more abundant with depth in this subunit (Fig. **F2**). The major mineral components of the subunit are feldspar, quartz, and clay and opaque minerals. Biogenic components (calcareous and opal) vary from 0% to 25% of the total sediments (Fig. **F2**).

Soft-sediment deformation features are locally observed in lithostratigraphic Subunit IIIA (e.g., Section 204-1245B-14H-2). Mousselike textures were observed near intervals where gas hydrate was sampled between 126 and 143 mbsf near the depth of the BSR (see **"Sedimentary Evidence of Gas Hydrate,"** p. 10). Iron sulfide precipitates and bioturbation range from common to rare throughout this subunit. A sequence of volcanic glass–rich sediments, located at ~180 mbsf in Hole 1245B, appears to correspond to Horizon A, a bright reflector identified in the 3-D seismic data.

Five distinct light-colored intervals containing volcanic glass–rich sediments and ash were found between 176 and 183 mbsf (Sections 204-1245B-21X-2 to 21X-4) (Fig. **F12**). These five intervals correlate with the approximate depth of Horizon A in the 3-D seismic data (Fig. **F3**) (see Figs. **F5,** p. 55, and **F6,** p. 56, both in the "Leg 204 Summary" chapter). A detailed analysis of more than 32 smear slides was conducted in conjunction with high-resolution color reflectance (b*) and MS measurements acquired at 1-cm spacing across these intervals (Fig. **F13**). Smear slide results are described on the barrel sheets and tabulated in smear slide summaries (see **"Site 1245 Smear Slides"**). The volcanic glass–rich sediment and ash sequences, ranging from 6 to 23 cm thick, are typically composed of volcanic glass–rich sands (dark beige color) that grade upward into sandy-silty volcanic ash (light beige color) and clayey-silty ash (pure white). The glass content of each layer

F10. Mousselike texture above the BSR, p. 48.

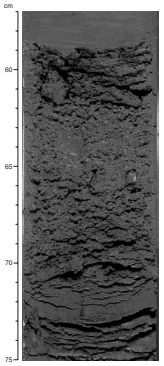

F11. Diatom-rich clay, p. 49.

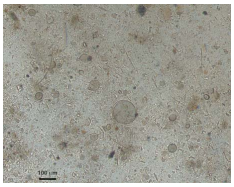

F12. Volcanic glass–rich sediment and ash sequences, p. 50.

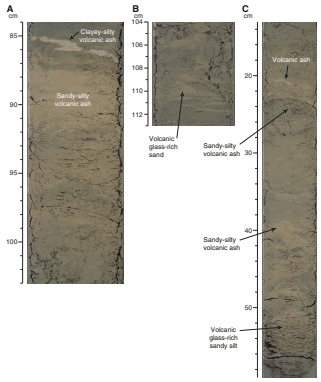

F13. Ash sequences around Horizon A, p. 51.

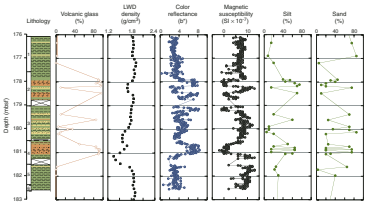

increases in the sequence from the basal sand containing 0%–20% glass, to the sandy to silty ash containing up to 80% glass, to the uppermost clayey-silty ash containing 80%–96% glass (Figs. F13, F14, F15). Both color reflectance data (b*; ranging from blue to yellow) and MS values are inversely correlated across the glass-rich sediment and ash intervals, where the sands at the bases of the ash layers have high MS and low color reflectance values compared to the surrounding major lithology (silty clay), and the intervals with the highest concentrations of ash appear to have low MS and high color reflectance values (Fig. F13). The intervals containing the volcanic glass–rich sediments and ashes are considered to represent the primary source of Horizon A in the 3-D seismic reflection data (Fig. F3).

Lithostratigraphic Subunit IIIB

Lithostratigraphic Subunit IIIB (183–212.7 mbsf in Hole 1245B and 189.5–200.9 mbsf in Hole 1245C) consists of both silty clay and nannofossil-rich silty clay interbedded with graded silt layers (see "Site 1245 Visual Core Descriptions"). Near the top of Subunit IIIB, biogenic opal, predominantly in the form of diatoms, composes up to 45% of the sediment (Fig. F4). Calcareous components increase slightly toward the base of the subunit (Figs. F2, F7B).

Lithostratigraphic Unit IV

Interval: Sections 204-1245B-24X-7 through 46X-2
Depth: 212.70–419.30 mbsf
Age: early Pleistocene

Lithostratigraphic Unit IV is primarily composed of dark greenish gray (5GY 4/1) to very dark gray (N3) indurated claystone and silty claystone. This unit has been subdivided into two lithostratigraphic subunits at 320 mbsf (Subunits IVA and IVB) on the basis of changes in both grain size and biogenic content (Figs. F2, F16, F17). Above 320 mbsf, the major lithology of lithostratigraphic Subunit IVA typically contains coarse-grained silt layers that fine upward into hemipelagic clay containing >10% nannofossils. Below 320 mbsf, lithostratigraphic Subunit IVB lacks silt horizons and typically contains <10% total biogenic components.

Glauconite-bearing sands, induration, and scaly clay fabric at 212.7 mbsf mark the upper boundary of lithostratigraphic Unit IV (Figs. F2, F4, F7A) and differentiates this unit from the graded sand-silt-clay sequences of lithostratigraphic Subunit IIIB. The base of lithostratigraphic Unit IV is defined by another shift in grain size and biogenic composition at 420 mbsf (Fig. F2). This shift correlates well with a change in the lithium profile at Site 1245 (see "Interstitial Water Geochemistry," p. 13; Fig. F28).

Lithostratigraphic Subunit IVA

Lithostratigraphic Subunit IVA (Hole 1245B; 212.7–320 mbsf) is composed of indurated silty claystone with a total biogenic content >10%. Minor lithologies are silt- to sand-sized interlayers that are unevenly spaced throughout the subunit at intervals ranging from 1 to 15 m. Glauconite-bearing sands are found at 213, 218, 226, and 256 mbsf, respectively (Fig. F7A). At other Leg 204 sites, the onset of the glauconite-bearing sand correlates with the top of the deeper accretionary complex. However, the glauconite found in the sand fraction of the fining-upward sequences at this site may have been transported to this loca-

F14. Volcanic glass within an ash sequence, p. 52.

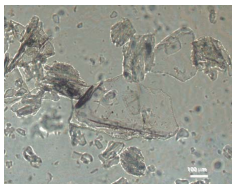

F15. XRD record from volcanic glass, p. 53.

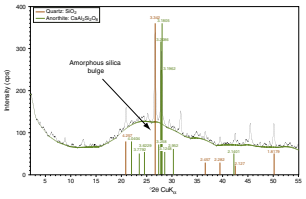

F16. Nannofossil-rich claystone, p. 54.

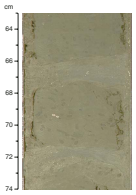

F17. Claystone, p. 55.

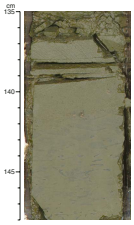

tion via turbidity currents and, therefore, may not reflect the original in situ diagenetic conditions. Sulfide and bioturbation are also common in lithostratigraphic Subunit IVA. Sulfide is found both as smeared interlayers <0.2 cm thick, which extend across the entire core, and as infill in bioturbated horizons.

Planar and subhorizontal bedding is visible throughout lithostratigraphic Subunit IVA. Scaly clay fabric was observed from 225 to 320 mbsf. This fabric was most commonly found in fractured drill biscuits and does not have a uniform orientation.

Calcareous nannofossils are the dominant biogenic component of lithostratigraphic Subunit IVA. The calcareous nannofossil content of the major lithology is >10% and >15% in Cores 204-1245B-31X, 32X, and 34X (Figs. F2, F4). Nannofossil abundance in the minor lithology is typically higher than that in the major lithology. Foraminifers are also present but typically compose 5%–15% of the minor lithologies from 263 to 320 mbsf and rarely exceed 10% of the major lithology (e.g., Core 204-1245B-34X). A slight increase in biogenic opal, from the background content of 1%–3% to 8% in Core 204-1245B-35X, occurs between 295 and 300 mbsf.

Lithostratigraphic Subunit IVB

Lithostratigraphic Subunit IVB (Hole 1245B; 320–419.3 mbsf) is composed of indurated claystone and silty claystone, which is the major lithology of lithostratigraphic Subunit IVA. The primary difference between these two lithostratigraphic subunits lies in the composition of the minor lithology. Lithostratigraphic Subunit IVB contains significantly fewer graded silt turbidite sequences than were found in lithostratigraphic Subunit IVA. The minor lithologies of lithostratigraphic Subunit IVB are typically composed of 30% silt and 70% clay; glauconite is absent, as is most sulfide and bioturbation. Where bioturbation is present, pyrrhotite and dispersed (millimeter scale) white precipitates, likely gypsum, are also found. These precipitates are found in Cores 204-1245B-39X, 40X, and 42X, are present as an inner lining on preserved burrows, and commonly surround sulfide-rich infilled burrows.

Planar bedding is only found at the top of lithostratigraphic Subunit IVB in Core 204-1245B-37X (Fig. F17). Scaly fabric is more common in lithostratigraphic Subunit IVA than lithostratigraphic Subunit IVB, although it was observed in Cores 204-1245B-37X through 41X as well as in Core 47X.

Both calcareous and siliceous biogenic components are less common in lithostratigraphic Subunit IVB than in IVA (Figs. F2, F4). Foraminifers are absent from the major lithology of lithostratigraphic Subunit IVB, but are present in sandy interlayers (minor lithology) in Cores 204-1245B-37X and 39X. Calcareous nannofossil content drops dramatically in lithostratigraphic Subunit IVB, with only Cores 204-1245B-37X and 43X composed of nannofossil-rich major lithologies; all other cores contain <6% nannofossils. Biogenic opal is slightly more abundant at the top of lithostratigraphic Subunit IVB. A smear slide analysis of Sample 204-1245B-37X-1, 38 cm, indicates that the dominant lithology contains 6% diatoms. Throughout the rest of lithostratigraphic Subunit IVB, the biogenic opal content ranges from 0% to 3% in both the major and minor lithologies (Fig. F4).

Lithostratigraphic Unit V

Intervals: Sections 204-1245B-48X-3 through 53X-CC and 204-1245E-1R-1 through 8R-2
Depths: Hole 1245B: 419.30–472.88 mbsf and Hole 1245E: 473.70–540.25 mbsf
Age: early Pleistocene

Lithostratigraphic Unit V, which was cored in Holes 1245B and 1245E, is composed of dark greenish gray (5GY 4/1) claystone and silty claystone (Fig. F2). Cores were highly disturbed by drilling, such that the drilling biscuits were heavily fractured in some intervals. Lithostratigraphic Unit V cannot be correlated between Holes 1245B and 1245E (Fig. F2) because the recovered intervals do not overlap.

Lithostratigraphic Unit V is composed of a highly lithified, nannofossil-rich clay and silty claystone (Fig. F18) that displays dispersed moderate bioturbation, parallel-bedded, fining-upward silt and sand turbidites, and macroscopic foraminifers (Fig. F19). The lithostratigraphic Unit IV/V boundary is placed at 419.3 mbsf, directly above the first occurrence (FO) of frequent thick turbidites that are rich in biogenic calcareous components (nannofossils and foraminifers) (Fig. F2). An increase in the pore water lithium concentration to significantly higher values at ~430 mbsf (see "Interstitial Water Geochemistry," p. 13) also correlates with the lithostratigraphic Unit IV/V boundary.

The major lithology of lithostratigraphic Unit V in Hole 1245B is clay and silty claystone that is nannofossil rich from 426 to 462 mbsf (Cores 204-1245B-49X and 52X) (Fig. F2). Based on smear slide analyses, the claystone contains up to 98% clay and the silty claystone up to 3% sand and 27% silt (Fig. F4). The major components of the clay and silty claystone, as determined by XRD analyses, are quartz, feldspar, muscovite, illite, other clay minerals, and minor amounts of calcite.

The major lithology of lithostratigraphic Unit V is further characterized by rare to moderate bioturbation, absent sulfides, macroscopic foraminifers, mollusk shell fragments, and wood fragments. Macroscopic foraminifers (Cores 204-1245B-49X and 204-1245E-2R, 5R, 6R, and 8R), mollusk shell fragments (Cores 204-1245B-49X and 52X and 204-1245E-2R, 6R, and 7R), and wood fragments (Sections 204-1245B-49X-3, 110 cm, and 204-1245E-6R-1, 64 cm) were all noted in visual core descriptions. Observed diagenetic features include dispersed white precipitates, likely gypsum, in Cores 204-1245E-4R through 5R and a sulfide precipitate (probably pyrrhotite) in Section 6R-2, 85 cm.

Minor lithologies in lithostratigraphic Unit V are highly varied and are typically found as interlayers within the major lithology (see Table T2). These interlayers are typically turbidites (4–30 cm thick) characterized by grading (Fig. F20) and planar laminations (Fig. F19A). Dark grains (~1 mm) are visible in Sections 204-1245E-3R-1, 48 cm; 3R-2, 13 and 106 cm; and 3R-CC, 14 cm. Foraminifer-rich clay and silty claystone are also minor lithologies within lithostratigraphic Unit V from 492 to 531 mbsf.

Intervals 204-1245B-51X-1, 54–60 cm, and 100–115 cm; and 53X-2, 95–99 cm; 53X-4, 8–7 cm; 53X-5, 66–150 cm; and 53X-6, 45–60 cm, contain mud clast layers ranging in thickness from 4 to 84 cm (Fig. F19B). The clasts are composed of well-rounded, unsorted mudstone and are slightly greener and browner than the surrounding lithology. A diatom-bearing silty claystone clast is found in Section 204-1245B-53X-

F18. Nannofossil-rich claystone, p. 56.

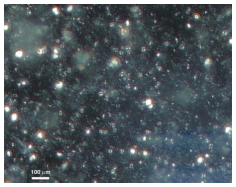

F19. Turbidite and mud clasts, p. 57.

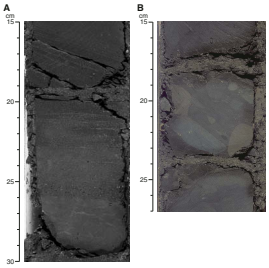

T2. Variation of minor lithologies, p. 103.

F20. Turbidite, p. 58.

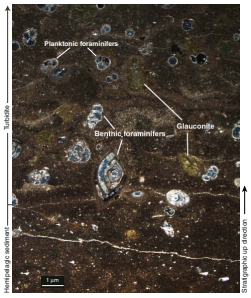

4 (smear slide Sample 53X-4, 30 cm). The size of the different clasts varies from 0.5 to 6 cm in diameter.

Sedimentary Evidence of Gas Hydrate

A total of 11 gas hydrate samples were taken from Site 1245 (Table T3). Mousselike textures were observed within lithostratigraphic Units II and III and correspond to intervals near the locations of gas hydrate samples. The observed disruption to the sedimentary structures is presumed to have been caused by the dissociation of gas hydrate and correlates well with cold anomalies detected in the infrared (IR) images (see "Physical Properties," p. 19).

Below 134 mbsf, the depth of the BSR at Site 1245, mousselike texture was observed in Cores 204-1245B-16H and 204-1245C-24H. However, no low chlorinity anomalies were detected in interstitial water (IW) geochemistry data, and no cold anomalies were observed with the IR thermal camera at these depths (see "Interstitial Water Geochemistry," p. 13, and "Physical Properties," p. 19). Therefore, the presence of mousselike texture below 134 mbsf is probably due to coring-related disturbance rather than to sediment disruption related to gas hydrate dissociation.

T3. Gas hydrate samples and depths, p. 104.

Environment of Deposition

Site 1245 is located on the western flank of the southern summit of Hydrate Ridge, where we recovered a thick (~540 m) sedimentary sequence of folded and uplifted Quaternary age strata (see Fig. F5, p. 55, in the "Leg 204 Summary" chapter). We divide the sequence into five lithostratigraphic units (Figs. F2, F3, F4), of which three (Units I–III) correlate with Sites 1250, 1249, 1248, and 1247 and two (Units I and II) with Site 1246 (see Fig. F10, p. 60, in the "Leg 204 Summary" chapter).

Lithostratigraphic Unit V is characterized by mud clast deposits and thick turbidites within a major lithology of nannofossil-rich clay and silty claystone and may include the top of the deeper accretionary complex of southern Hydrate Ridge (see Fig. F5, p. 55, in the "Leg 204 Summary" chapter). The abundant macrofossils and wood fragments in the turbidites of this unit suggest a shelf rather than a slope basin origin for these sediments. The proximal position of these sediments to the deformation front also suggests they were originally deposited on the abyssal plain and have since been accreted and uplifted during accretionary wedge formation.

Lithostratigraphic Unit IV consists of claystone and silty claystone with abundant calcareous nannofossils. Biostratigraphic data indicate a nannofossil zone boundary at ~280 mbsf (see "Biostratigraphy," p. 11), which may be reflected in the stratigraphy as a decrease in calcareous nannofossils (below ~280 mbsf). The reduced abundance of calcareous nannofossils in lithostratigraphic Subunit IVB could be caused by either dilution of biogenic materials by terrigenous sediment or a change in nannofossil productivity at the time of deposition.

The distinguishing features of lithostratigraphic Unit III are the abundance of biogenic opal, the volcanic glass–rich sediment and ash sequences, and frequent turbidites. The detailed record of volcanic glass–rich sediment and ash sequences around 180 mbsf in Hole 1245B is well correlated to Horizon A in the 3-D seismic data. The repeated association of graded sand- and silt-bearing volcanic glass and the high concentration of volcanic ash near the upper limit of the graded se-

quences suggests the volcanic glass and ash were deposited by turbidity currents. High-frequency turbidites throughout Unit III correspond to the slightly higher average sedimentation rate of 13 cm/k.y. compared to lithostratigraphic Unit II, which contains less coarse material and has a sedimentation rate of 10 cm/k.y. (see "Biostratigraphy," p. 11). The increased abundance of biogenic opal in lithostratigraphic Unit III with depth may suggest a high level of biological productivity, perhaps contributing to the higher sedimentation rate for this unit.

The boundary between lithostratigraphic Units III and II corresponds to a distinct seismic discontinuity (Horizon Y) at 75 mbsf. Horizon Y appears to be an angular unconformity (see Fig. F5, p. 55, in the "Leg 204 Summary" chapter); however, the stratigraphy above it is folded and the unconformity surface itself is not. The folded geometry above Horizon Y would be more consistent with that produced during folding above a ramp-flat thrust fault system. Although there is no evidence of fault gouge in the recovered cores, a fault origin for Horizon Y cannot be excluded.

The decrease in coarse material (sand) toward the base of lithostratigraphic Unit II suggests a decrease in the sedimentation rate, which is consistent with the biostratigraphically determined average sedimentation rate of 10 cm/k.y. just above Horizon Y at Site 1245 (see "Biostratigraphy," p. 11).

The presence of turbidites at the top of lithostratigraphic Unit II suggests that sedimentation rates were higher during deposition of the upper portion of lithostratigraphic Unit II, which is consistent with the last increases in sedimentation rate (23 cm/k.y.; from 0 to 60 mbsf) determined from the biostratigraphy (see "Summary," p. 12, in "Biostratigraphy"). The lack of obvious turbidites in lithostratigraphic Unit I may indicate that it was deposited as hemipelagic drape over an uplifted Hydrate Ridge. Alternatively, it may represent an older clay-rich section of the stratigraphy now exposed near the crest of Hydrate Ridge because of erosion.

BIOSTRATIGRAPHY

Five holes were drilled and four holes were cored at Site 1245 on the northwestern flank of the summit of south Hydrate Ridge. Hole 1245B was cored from the seafloor down to 473.7 mbsf, and Hole 1245E was cored from 473.7 to 540.3 mbsf, thereby obtaining a composite 540-m Quaternary sequence. The biostratigraphy determined for Site 1245 was based on examination of diatoms and calcareous nannofossils from all core catcher samples and a few discrete samples from cores in Holes 1245B and 1245E.

Diatoms

Diatoms are common to few and moderately preserved in the interval from 0 to 66 mbsf. In the interval from 66 to 470 mbsf in Hole 1245B they are rare to absent and poorly preserved, except in the interval from 128 to 163 mbsf, where common to few, poorly to moderately preserved diatoms are present. Samples from Hole 1245E do not contain diatoms, probably as a result of diagenetic dissolution of diatom valves. Diatom assemblages in Hole 1245B are dominated by species such as *Stephanopyxis dimorpha, Stephanopyxis* spp., *Neodenticula semi-*

nae, and *Thalassionema nitzschioides*. A warm-water taxa *Fragilariopsis doliolus* is present sporadically.

The interval from the seafloor to 38.7 mbsf in Hole 1245B contains *N. seminae* but lacks *Proboscia curvirostris*. This interval was assigned to North Pacific Diatom (NPD) Zone 12 (*N. seminae* Zone). The last occurrence (LO) of *P. curvirostris* was found in Sample 204-1245B-5H-CC (46.66 mbsf). This species is present sporadically down to Sample 204-1245B-53X-5, 68–70 cm (470.44–470.46 mbsf), indicating the age of this sample to be younger than 1.6 Ma. The FO of *Actinocyclus oculatus* (1.0 Ma) was not found in Hole 1245B; this is likely a result of the trace to rare presence and poor preservation of diatoms in the middle part of the hole.

Calcareous Nannofossils

The calcareous nannofossil biostratigraphy for Site 1245 was based on an investigation of core catcher samples from the 540-m composite sequence of cores recovered from Holes 1245B and 1245E. Common to rare and well- to moderately preserved calcareous nannofossils were observed in three intervals at Site 1245, from 127.79 to 144.82, from 174.47 to 319.72, and from 412.87 to 540.20 mbsf. They are poorly preserved or are infrequently present, with low abundance in the rest of the intervals. This agrees with sedimentological core description data from this site (see Fig. **F4**). An early Pleistocene–Holocene calcareous nannofossil assemblage was found in the composite 540-m sequence.

Emiliania huxleyi is present infrequently from the seafloor down to 55.58 mbsf (Sample 204-1245B-5H-CC). Common and well-preserved, large-sized (~4 µm) *E. huxleyi* were observed in Samples 204-1245B-5H-CC and 6H-CC (46.66–55.58 mbsf). As large-sized forms of *E. huxleyi* are present in the early evolutionary stage of this species (Pujos-Lamy, 1977), the interval from the seafloor to 55.58 mbsf was assigned to Zone NN21. Two samples below 55.58 mbsf (Samples 204-1245B-7H-CC and 8H-CC) contain a few poorly preserved small *Gephyrocapsa* species but lack either *E. huxleyi* or *Pseudoemiliania lacunosa*. Therefore, these samples were assigned to Zone NN20. *P. lacunosa* is continuously present from 84.79 to 540 mbsf. The LO of *P. lacunosa* was placed at 84.79 mbsf, which marks the NN19b/NN20 zonal boundary. Various small *Gephyrocapsa* species are abundant in the interval from 156.72 to 271.93 mbsf (Samples 204-1245B-18X-CC to 30X-CC), assigning this interval to the mid-Pleistocene small *Gephyrocapsa* spp. Acme Zone (1.0–1.2 Ma). Therefore, the LO of the small *Gephyrocapsa* spp. Acme was placed at 156.72 mbsf and the FO of the small *Gephyrocapsa* spp. Acme at 271.93 mbsf. The LO of *Calcidiscus macintyrei,* which was found in Sample 204-1245E-6R-CC (522.33 mbsf), suggests an age of 1.59 Ma (the lower part of Pleistocene Zone NN19) for this sample. Rare to common *Gephyrocapsa lumina* is present in the base sediments (540.20 mbsf) of Site 1245, indicating an age younger than 1.67 Ma.

Summary

The presence of age-diagnostic fossils is summarized in Figure **F21.** One diatom event and five nannofossil events were recognized at Site 1245 (Table **T4**). The diatom assemblage from 470.46 mbsf indicates the age at this depth to be younger than 1.6 Ma. This corresponds well to the nannofossil record, which suggests that the age of the bottom of Hole 1245E is younger than 1.67 Ma. Based on evidence from diatoms

F21. Diatom and nannofossil event marker species, p. 59.

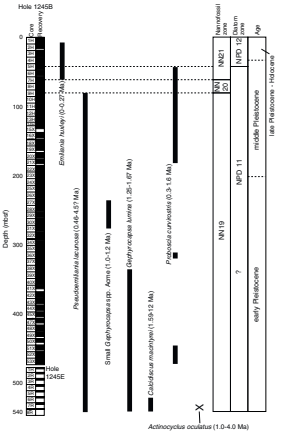

T4. Bioevents found, p. 105.

and calcareous nannofossils, the 540-m sequence recovered from Site 1245 is of Quaternary age (early Pleistocene–Holocene).

Linear sedimentation rates were estimated based on diatom and calcareous nannofossil events (Table T4; Fig. F22). Sedimentation rates at this site are generally higher than those at the other sites drilled during Leg 204, except for Site 1251. The sedimentation rate is estimated to be 23 cm/k.y. for the interval from 0 to 60 mbsf, 10 cm/k.y. for the interval from 60 to 80 mbsf, 13 cm/k.y. for the interval from 80 to 150.77 mbsf, and 62 cm/k.y. for the interval from 150.77 to 540.20 mbsf. The higher sedimentation rate below 150 mbsf is well correlated with the record of frequent turbidites observed within this interval (see "Lithostratigraphy," p. 3).

F22. Age-depth plots, p. 60.

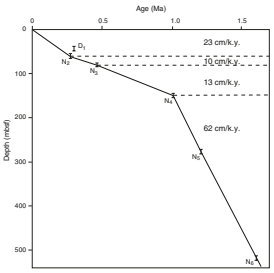

INTERSTITIAL WATER GEOCHEMISTRY

A total of 120 IW samples were collected from Site 1245. We collected 70 whole-round samples in Hole 1245B, with a sample spacing of approximately 2 per core in the upper 125 mbsf, followed by a sampling resolution of 1 whole-round sample per core below this depth. Hole 1245C was dedicated to microbiological studies (see "Microbiology," p. 18). Thirteen whole-round samples were collected from this hole; these samples were taken adjacent to core sections sampled for postcruise studies of microbiological processes below the sulfate/methane interface (SMI). In addition, nine samples were taken from 53.12 to 53.38 mbsf from the working half of the core to evaluate Cl^- distribution around a 2-cm-thick hydrate layer. In Hole 1245D, we used a high-resolution whole-round sampling protocol within the anaerobic methane oxidation (AMO) zone (approximately 2 whole-round samples per section for a total of 19 samples) in a coordinated program with the shipboard microbiologists. The deep sedimentary sequence at this site was sampled by rotary coring in Hole 1245E, from which we collected seven samples. The IW geochemistry data are tabulated in Table T5 and are illustrated in Figure F23.

T5. Concentrations of dissolved species in pore waters, p. 106.

F23. Concentration profiles of dissolved species, p. 61.

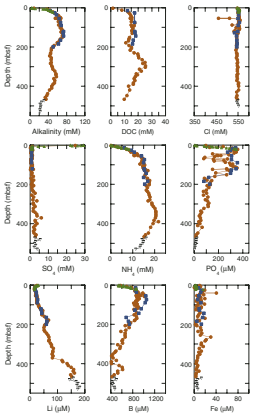

Chloride Concentration and the Presence of Gas Hydrate

The chloride distribution in pore fluids above the BSR at Site 1245 shows similar features to that observed at Site 1244, namely, the presence of excursions with anomalous low chloride values above the BSR that are thought to represent gas hydrate dissociation during core retrieval. These chloride anomalies can be used to infer the presence and amount of gas hydrate in the sediments (detailed in "Interstitial Water Geochemistry," p. 13, in the "Explanatory Notes" chapter and "Interstitial Water Geochemistry," p. 13, in the "Site 1244" chapter). Based on the chloride distribution, we predict that the onset of gas hydrate at Site 1245 occurs at ~55 mbsf, a depth that is controlled by interactions among methane concentration, temperature, and pressure conditions. Indeed, the methane content of the sediments at this site approaches that needed to form methane hydrate at ~57 mbsf (see "Hydrocarbon Gases," p. 16, in "Organic Geochemistry"), which is in excellent agreement with the chloride estimate. Similarly, this depth corresponds to the onset of variability in the LWD resistivity data (see "Downhole Logging," p. 26) and the first occurrence of temperature anomalies measured with the IR camera (see "Physical Properties," p. 19). The

percent hydrate in the pore space of sediments calculated from the Cl^- anomalies ranges from 0% to 25% and is limited to the zone between 55 and 130 mbsf (Fig. F24).

To further characterize the relationship between the observed chloride anomalies and the presence of gas hydrate, we conducted an experiment from the working half of Core 204-1245C-7H, from which samples were collected ~90 min after the core arrived on deck. Temperature anomalies observed with the IR camera while the core was on the catwalk indicate the presence of gas hydrate in Section 204-1245C-7H-5. This section was transferred immediately to the core laboratory, where it was split in half. Hydrate was, indeed, observed as a 2-cm-thick layer between 35 and 45 cm and oriented at a high angle to bedding. Approximately 10 cm^3 of sediment was collected from the hydrate layer and at various distances from it. Pore waters were extracted from these samples to measure interstitial chloride concentration (shipboard) and isotopic composition of the water (shore based). Shipboard results from this experiment are listed in Table T6 and illustrated in Figure F25. As shown in this figure, samples collected within 5 cm of the hydrate layer show significant anomalies in the chloride content, whereas samples collected at distances >10 cm from the hydrate layer do not show any deviation from the background chloride values.

Sulfate, Methane, and the Sulfate/Methane Interface

High-resolution sampling in Hole 1245D allows firm characterization of sulfate and methane profiles as well as the identification of the position of SMI (Fig. F26). Sulfate generally decreases downcore and is consumed most rapidly between 4 and 6 mbsf. Minimal sulfate values combined with rapidly increasing methane headspace concentration (see "Hydrocarbon Gases," p. 16, in "Organic Geochemistry") locate the SMI at ~7 mbsf.

The shape of the sulfate profile is nonlinear. Strong curvature is present at the top of the profile, and there is no definitive linear portion of the sulfate concentration data. The strong curvature may be due to the oxidation of sedimentary organic matter through the process of sulfate reduction, as well as to the effect of fluid advection. These processes can be better quantified with knowledge of the isotopic composition of the methane gas and of the dissolved inorganic carbon, sulfate, and sulfide. All these analyses will be carried out postcruise. As a consequence, no shipboard assessment of sulfate flux (e.g., see "Interstitial Water Geochemistry," p. 13, in the "Site 1244" chapter) can be presented for this site.

Major and Minor Element Distributions

Pore fluids from the 190- to 300-mbsf zone show a decrease in the concentrations of calcium, magnesium, and strontium, which is accompanied by a decrease in alkalinity (Fig. F27). This observation suggests that there is a CO_2 sink within this depth interval, which would most likely be caused by authigenic carbonate formation. Carbonate ($CaCO_3$) is observed to increase within this zone, predominantly resulting from an increase of biogenic $CaCO_3$ in the sediments (see "Lithostratigraphy," p. 3). It is possible that this biogenic component provides nucleation sites for authigenic carbonate formation.

F24. Chloride estimates of gas hydrates, p. 63.

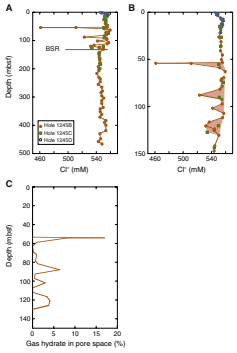

T6. Concentration of dissolved chloride, p. 109.

F25. High-resolution analyses of chloride content, p. 64.

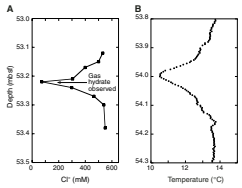

F26. Sulfate and methane concentration profiles, p. 65.

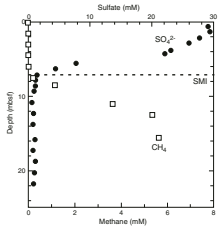

F27. Authigenic carbonate formation zone, p. 66.

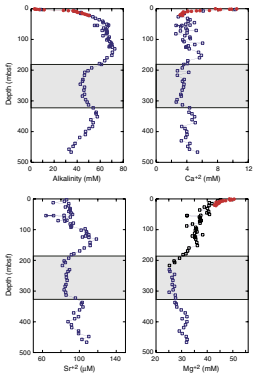

The effects of diagenetic reactions within accreted sediments are usually documented by the distribution of chloride, lithium, and strontium as well as by the isotopic composition of these elements. At Site 1244 (see "Interstitial Water Geochemistry," p. 13, in the "Site 1244" chapter) and at other sites previously drilled on the Cascadia margin (Kastner et al., 1995), reactions at depth are characterized by an increase in dissolved lithium and strontium, accompanied by a decrease in dissolved chloride concentration. Site 1245 sediments do not show the marked chloride gradient with depth below the BSR observed at Site 1244, suggesting that the thick package of young, uplifted, and folded strata lying below the BSR at this site has not undergone significant dehydration of hydrous silicates. However, there is an increase in dissolved lithium (Fig. F28) that indicates removal of this element from aluminosilicates at temperatures >70°C, as predicted from laboratory experiments (e.g., Edmond et al., 1979; Seyfred et al., 1984) and previous field observations in accretionary margins (Kastner et al., 1995; Chan and Kastner, 2002). The increase in dissolved lithium with depth in the upper 350 mbsf at both Sites 1244 and 1245 has a similar gradient, which is consistent with the similar geothermal gradient observed at these two sites (see "Downhole Tools and Pressure Coring," p. 22).

Superimposed on its linear increase with depth, dissolved lithium shows excursions to higher concentrations at 180 and 420 mbsf, respectively (Fig. F28). The first of these excursions corresponds to the depth of the seismic reflector known as Horizon A (180 mbsf) (see "Introduction," p. 1). This increase suggests migration of lithium-enriched fluids from depths below 1 km, where burial temperature reaches the 70°–100°C threshold needed for lithium release from alumnosilicates. Horizon A was identified in the sediments to correspond to a thick interval (~174–181 mbsf) of volcanic ash, with two distinct ashes observed as sandy layers near 180 mbsf (see "Lithostratigraphy," p. 3). Presumably, the sand layers represent a migration path for fluids coming from deeper intervals within the accretionary wedge. Gases collected from the sediments between the BSR (131 mbsf) and Horizon A (180 mbsf) also show enrichment of heavy hydrocarbons (see "Hydrocarbon Gases," p. 16, in "Organic Geochemistry"), which is consistent with the postulated migration of fluids from a deep-seated source.

The second lithium maximum is present from 420 to 440 mbsf (Fig. F28). This interval corresponds to the boundary between lithostratigraphic Units III and IV (see "Lithostratigraphy," p. 3.) and perhaps represents another zone of lateral fluid migration. Analysis of the isotopic composition of lithium in the dissolved and solid phases from this site will enhance our understanding of the fluid sources and pathways and fluid migration patterns in the complex hydrogeological system at Site 1245. These data will help to constrain processes pertaining to the gas composition and fluid flux to the GHSZ.

F28. Lithium concentrations, p. 67.

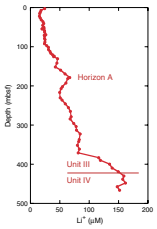

ORGANIC GEOCHEMISTRY

Site 1245 is located on the western flank of Hydrate Ridge. The shipboard organic geochemistry program at Site 1245 included analyses of hydrocarbon gases, carbonate and organic carbon, and total sulfur and nitrogen content. Descriptions of the methods used for these analyses are summarized in "Organic Geochemistry," p. 16, in the "Explanatory Notes" chapter.

Hydrocarbon Gases

Concentrations of methane (C_1), ethane (C_2), ethylene ($C_{2=}$), and propane (C_3) were measured using the headspace technique. Sediments were sampled in every section of the first core and with decreasing frequency in subsequent cores, to a minimum of one sample per available core. The results are reported in parts per million by volume (ppmv) in Table **T7** and plotted against depth in Figure **F29.** Methane content in Hole 1245B varies from 11 to 42 ppmv in the upper 6 mbsf. It rapidly increases to 1,321 ppmv at 7.5 mbsf and 9,964 ppmv at 8.5 mbsf and remains in the range of 10,000–60,000 ppmv to the base of the cored section. In addition to the relative concentration of methane in the headspace vial, the C_1 values are expressed in millimoles per liter (mM) of pore water in Table **T7** and illustrated in Figure **F30.** Based on the methane concentration profile, the onset of methanogenesis occurs at a depth of ~8 mbsf in Holes 1245B and 1245D. Dissolved sulfate is also essentially depleted in the pore water in the uppermost 8 mbsf (see **"Sulfate, Methane, and the Sulfate/Methane Interface,"** p. 14, in "Interstitial Water Geochemistry").

Small amounts of ethane (0.5–18.2 ppmv) are detected in the headspace vials above 130 mbsf. Ethane contents increase between 130 and 200 mbsf, ranging from 70 to a maximum value of 557 ppmv at 142 mbsf. Propane is also abundant in this interval, ranging from 76 to 430 ppmv. Enrichment of ethane and propane gases in this interval probably reflects the presence of migrated thermogenic hydrocarbons (Fig. **F29**). Ethylene is present sporadically throughout the cored section (0.5–1.4 ppmv) (Table **T7**) and is probably related to biological activity in the shallow sediments.

The compositions of light hydrocarbon and nonhydrocarbon gases from voids or expansion gaps in the core liner are shown in Table **T8** and illustrated in Figure **F31.** Methane contents in the voids sampled from Hole 1245B are generally >900,000 ppmv (>90% by volume) (Fig. **F31**), except for a few samples contaminated with air. The depth interval between 130 and 200 mbsf is characterized by a thousand-fold increase in the amount of C_2–C_5 hydrocarbons present (Fig. **F31**). A similar trend is also apparent in the headspace gas analysis. The presence of these thermogenic hydrocarbons between depths of 130 and 200 mbsf is due to the cores intersecting a zone of migrated thermogenic hydrocarbons, presumably originating from deeper in the accretionary complex. Horizon A or other permeable layers may act as a migration conduit for these hydrocarbons. Beneath the zone of maximum wet gas hydrocarbon enrichment at ~150 mbsf, the level of C_2–C_5 hydrocarbons in the cores gradually decreases and reaches "normal" background levels below depths of ~300 mbsf.

Gas composition as expressed by the C_1/C_2 ratio of headspace and void gas is plotted vs. depth in Figure **F32.** The C_1/C_2 ratios for either sample type show little systematic change above the BSR. The C_1/C_2 ratios of the void gas samples show a shift to lower values at 50–80 mbsf, indicating a relative enrichment in ethane of the void gas. This shift is possibly related to gas hydrate decomposition during core recovery. Below the depth where the buildup of methane enables gas hydrates to form, the void gas samples contain, mainly, gas released from gas hydrate dissociation during core recovery. The decrease of the C_1/C_2 ratio resulting from the presence of migrated thermogenic wet gases is distinctive at depths between 130 and 200 mbsf. An anomalous de-

T7. Concentrations of C_1, C_2, and C_3, p. 110.

F29. Concentrations of C_1, C_2, and C_3 vs. depth, p. 68.

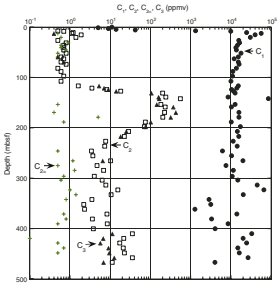

F30. Dissolved methane and sulfate, p. 69

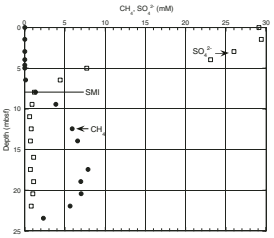

T8. Concentrations of light hydrocarbon and nonhydrocarbon gases, p. 112.

F31. Light hydrocarbons from void gas vs. depth, p. 70.

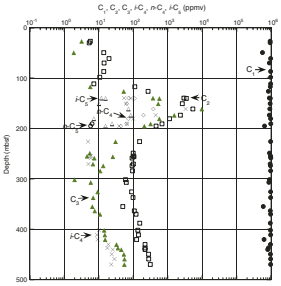

F32. C_1/C_2 ratio vs. depth, p. 71.

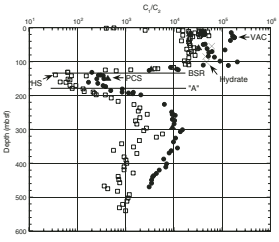

crease of the C_1/C_2 ratio is also distinctive between the depths that correlate with the seismic features identified as the BSR and Horizon A.

The C_1/C_2 ratio is plotted vs. estimated sediment temperature in Figure **F33.** The C_1/C_2 plots show evidence for migrated hydrocarbons in the depth interval from ~130 to 300 mbsf (temperatures of 12°–17°C), which results in ratios that are lower than expected for the prevailing sediment temperature. Sediment temperatures were estimated from a seafloor temperature of 4.5°C and a geothermal gradient of 52°C/km (see **"Downhole Tools and Pressure Coring,"** p. 22).

F33. C_1/C_2 ratio vs. temperature, p. 72.

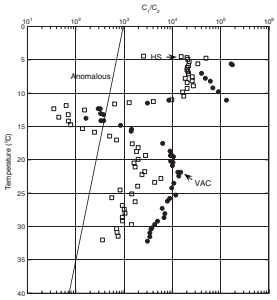

Gas Hydrate and Pressure Cores

Gas hydrate pieces and gas hydrate–bearing sediments were recovered from cores on the catwalk and analyzed. Four gas samples from decomposed pieces of gas hydrate were analyzed from Samples 204-1245B-6H-5, 103 cm; 9H-CC; 204-1245C-7H-5, 40 cm; and 13H-4 56–74 cm (Table **T9**). The concentration of methane varies from 227,000 to 945,000 ppmv (22.7%–94.5% by volume) as a result of air contamination during sampling. The C_1/C_2 ratios of the gas from the dissociated gas hydrate from Samples 204-1245B-9H-CC and 204-1245C-13H-4, 56–76 cm, show enrichment of ethane in the gas hydrate relative to the adjacent void gas samples (Fig. **F32**). However, ethane was not enriched in gas from Sample 204-1245B-6H-5, 103 cm, and was below detection levels in the gas hydrate sample from Sample 204-1245C-7H-5, 40 cm.

T9. Gas from decomposed gas hydrate, p. 114.

Five deployments of the pressure core sampler (PCS) successfully retrieved full (1 m long) cores from depths of 17.0–291.2 mbsf. The composition of gas samples obtained during controlled PCS degassing experiments are listed in Table **T10.** One PCS sample from Core 204-1245C-16P provided a pressure curve and gas content that confirms the subsurface presence of methane hydrate (see **"Downhole Tools and Pressure Coring,"** p. 22). Based on the volume-averaged composition, the C_1/C_2 ratios for gas in the PCS cores fall within the trend defined by vacutainer (VAC) void gas samples (Fig. **F32**), except for the sample recovered from 17.0 mbsf.

T10. Composition of PCS gas samples, p. 115.

Carbon Analyses, Elemental Analyses, and Rock-Eval Characterization

A total of 27 sediment samples (one per core except for special tool cores) were analyzed for carbonate carbon (IC), total carbon (TC), OC, total nitrogen (TN), and total sulfur (TS). The results are listed in Table **T11** and plotted in Figure **F34.** IC content varies from 0.14 to 2.19 wt%. Concentration of IC is relatively high at 520.68 mbsf, where biogenic calcareous material is present in high amounts (see **"Lithostratigraphy,"** p. 3). When calculated as $CaCO_3$, the carbonate contents of the sediments vary from 1.19 to 25.48 wt% (Fig. **F34**).

OC content varies from 0.71 to 1.46 wt% (average = 1.11 wt%) (Table **T11;** Fig. **F34**). The C/N ratio is <10, suggesting that marine organic matter is dominant in the sediment. C/N ratios are mainly controlled by variation in the OC content of the sediments, with nitrogen being relatively uniform throughout the section at levels of 0.11–0.22 wt% (Table **T11;** Fig. **F34**). The nitrogen data show no apparent trends vs. either depth or OC content. The TS contents vary from 0.12 to 1.23 wt% (Table **T11**), with a consistent relationship between TS and OC content (Fig. **F34**).

T11. IC, TOC, TN, and TS, and C/N ratios in sediments, p. 116.

F34. Contents of IC, $CaCO_3$, OC, TS, and TN and C/N ratios, p. 73.

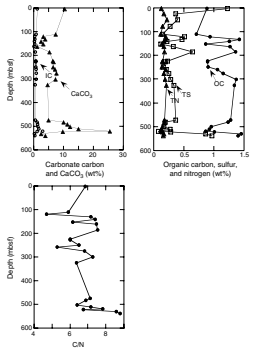

The results of Rock-Eval pyrolysis of selected samples are given in Table T12. This analysis was performed in part to evaluate the possible presence of migrated liquid hydrocarbons. Although the production index values seem moderately elevated (i.e., >0.1), they are fairly typical for continental margin sediments cored by ODP. There is no correlation between increased C_{2+} gas components and higher production index values and no definitive evidence for oil staining.

T12. Rock-Eval pyrolysis of samples, p. 117.

MICROBIOLOGY

Site 1245 is located on the northern slope of the southern summit of Hydrate Ridge. This site provided the opportunity to sample an environment influenced by wet gas hydrocarbon input (see "Organic Geochemistry," p. 15) as well as high methane fluxes. As at Site 1244, the overall goals were to quantify and describe methanogenesis, methanotrophy, and general microbial community structure in the presence of methane and methane hydrate. Chloride gradients at this site are markedly different than those on the eastern side of Hydrate Ridge and may reflect a difference in tectonic and depositional environments. Although subtle, these differences may noticeably influence the structure and activity of associated microbial communities.

Microbiological Sampling

AMO appears to dominate the sulfate and methane signals in the upper sediments at Site 1245. The SMI is at ~7 mbsf (see "Sulfate, Methane, and the Sulfate/Methane Interface," p. 14, in "Interstitial Water Geochemistry" and "Hydrocarbon Gases," p. 16, in "Organic Geochemistry"). The top three cores from Hole 1245D were sampled intensively (one to two samples per section) in coordination with the IW investigations (Table T13).

T13. Intervals sampled for microbiology, p. 118.

To examine methanogenesis at Site 1245, we sampled regularly downhole past the base of the GHSZ and well into the zone where free methane gas may be present (Table T13). Deeper sampling was spread over Holes 1245B and 1245C (the deepest sample was from 435 mbsf). Below 130 mbsf, ethane and longer-chain hydrocarbons became more prominent (see "Hydrocarbon Gases," p. 16, in "Organic Geochemistry"), indicating a thermogenic source of methane combining with a biological source of undetermined magnitude.

Sediments associated with hydrates were not deliberately sampled at Site 1245; however, IR temperature anomalies, indicating small amounts of disseminated or veined hydrates, were present in the GHSZ in Hole 1245C.

A series of ash layers at ~180 mbsf (see "Lithostratigraphy," p. 3) likely correspond to seismic Horizon A (see "Introduction," p. 1). Ash layers also have longer-chain hydrocarbons (see "Hydrocarbon Gases," p. 16, in "Organic Geochemistry") and increased lithium concentration (see "Major and Minor Element Distributions," p. 14, in "Interstitial Water Geochemistry"), which are indications that these ash layers may act as a conduit for migration of deeper gases and pore water. Because these sections of ash were precious, we sampled with particular care. Before the core sections were split, visible ash layers were identified and the section to be sampled was cut in two, allowing the microbiologists to take plugs of sediment directly from the cut ends of the core. The

two pieces of the core section were then rejoined and passed through the multisensor track (MST) and the regular core flow procedure. Samples were taken from inside and outside of the ash layers.

Contamination Tests

Perfluorocarbon Tracer

Most core sections sampled for microbiology had 5-g subsamples taken from outer and inner layers for gas chromatography analysis as described in "Perfluorocarbon Tracer," p. 20, in "Shipboard Microbiological Procedures and Protocols" in "Microbiology" in the "Explanatory Notes" chapter. Samples were analyzed as described, and raw data are presented in Table T14. Differences between outside and inside samples generally indicate minimal penetration of tracer. Notable exceptions may reflect penetration along fractures in sediments or discrepancies in handling and sampling, particularly when dealing with XCB cores.

T14. Core quality indicators, p. 119.

Fluorescent Microspheres

A comparison of fluorescent microsphere penetration in core interiors and exteriors is summarized in Table T14. Except on the few occasions that deployment of microspheres failed (the Whirl-Pak bag did not break), microscopic analysis of outer core layers showed numbers of microspheres ranging up to 10^5/g of sediment, whereas microsphere numbers in inner core layers were generally below the detection limit of 10/g of sediment. Microsphere deployment was unsuccessful in the Hole 1245D mudline core. Future legs employing microsphere quality assurance methods may wish to consider experimenting with different bag types and core catcher attachment when coring mudlines or soft sediment.

PHYSICAL PROPERTIES

At Site 1245, three holes were used for physical property analyses: Holes 1245B (0–473 mbsf), 1245C (0–221 mbsf), and 1245E (473–540 mbsf). Routine physical property measurements were performed on the recovered core sections from these holes, except for Hole 1245E where the RCB coring technique was used. RCB cores were not suitable for high-quality MST measurements; however, discrete samples were taken for moisture and density (MAD) analyses. The data quality for these RCB core samples is generally comparable to those obtained from APC and XCB cores, but there is a larger uncertainty in the coring depth of samples from these RCB cores because of the poor core recovery.

Standard IR imaging was performed at Site 1245 on cores from Holes 1245B and 1245C. RCB cores from Hole 1245E were not imaged. The first cold-spot anomalies associated with the presence of gas hydrate were detected in cores from Holes 1245B and 1245C, just below 50 mbsf. The deepest occurrence of cold anomalies in Hole 1245B (129.4 mbsf) matches well with the depth of the BSR at 134 mbsf, as estimated from seismic data.

Infrared Scanner

IR imaging of cores drilled at Site 1245 provided on-catwalk identification of hydrate zones in each core, as described in the Site 1244 chapter and in the Explanatory Notes chapter (see "Physical Properties," p. 24, in the "Site 1244" chapter and "Physical Properties," p. 22, in the "Explanatory Notes" chapter). This information was used to facilitate hydrate sampling and preservation for all cores. The IR thermal anomalies for Holes 1245B and 1245C are cataloged in Table T15 and include an interpretation of the overall hydrate texture for each anomaly. The majority of the hydrates detectable by IR imaging for Hole 1245B (75%) are present as apparently disseminated layers. Nodular textures account for the remainder of hydrate occurrences (25%). For Hole 1245C, 66% of the IR images indicate disseminated hydrate; nodular and vein hydrate each account for 17%. The preponderance of both disseminated and stratigraphically conformable layers of hydrate in Holes 1245B and 1245C suggests that differences in permeability and porosity related to bedding may control the presence of hydrate at Site 1245.

Cores from both holes show strong cold anomalies between ~5 and 120 mbsf (Figs. F35, F36). Hole 1245B also has a single cold anomaly at 129 mbsf corresponding to the BSR depth (134 mbsf). Figure F36A shows the magnitude of the temperature anomalies as function of depth for both Holes 1245B and 1245C plotted back to back. Anomalies in the two holes are similar, with a sharp onset at 49.9–51.5 mbsf and cessation of anomalies at 119.5 to 121.3 mbsf, except for the single anomaly near the BSR in Hole 1245B. Although individual anomalies cannot be correlated between the holes, the depths at which clusters are observed are consistent, suggesting that hydrate occurrence is stratigraphically controlled.

The IR thermal anomalies associated with hydrate are also consistent with pore water saturation (S_w) estimated from LWD data (Fig. F36B) (see "Downhole Logging," p. 26) except near the BSR, where LWD logging indicates greater presence of hydrate than observed using IR imaging. This difference may be explained by the possible inability of IR imaging to detect low concentrations of hydrate disseminated over a relatively large zone and by heterogeneity in the actual concentrations of hydrate between the two holes.

Sediment Density from Multisensor Track and Moisture and Density Data

The sediment densities derived from MAD, GRA, and LWD data all generally increase downhole, which is the trend caused by normal compaction of the marine sediments (Fig. F37). Density values at the seafloor are ~1.6 g/cm³, but these increase downhole to ~2.0 g/cm³ at 540 mbsf, resulting from the effect of sediment compaction (Table T16). Porosities decrease from values of ~65%–70% at the seafloor to <50% at 540 mbsf. Grain densities do not show any apparent trend with depth and have an average value of 2.69 g/cm³.

Lithostratigraphic Units I and II have lower boundaries at 31 and 76 mbsf, respectively, and coincide with seismic Reflectors X and Y (Figs. F37, F38). These boundaries are also visible in the physical properties, especially in the LWD and MAD bulk density data. However, physical property anomalies cannot be correlated to the boundary between

T15. IR anomalies, p. 120.

F35. Downcore IR temperature profile, p. 74.

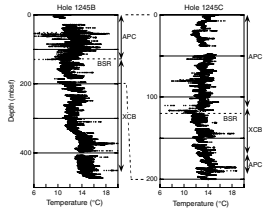

F36. IR temperature anomalies and S_w, p. 75.

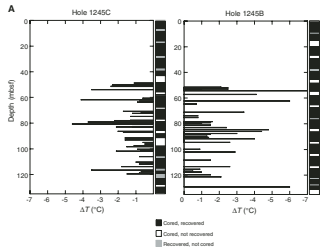

F37. Overview of physical properties, p. 77.

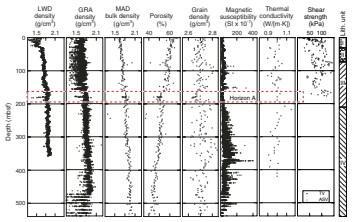

T16. MAD data, p. 122.

F38. Physical properties and the seismic record, p. 78.

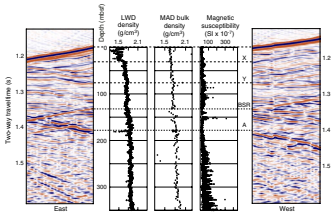

lithostratigraphic Units III and IV, which was defined at a depth of 212 mbsf (see "Lithostratigraphy," p. 3).

A distinctive feature at this site is the Horizon A density anomaly at a depth of 180 mbsf. This horizon is characterized by very low sediment densities of <1.4 g/cm³ as determined from GRA and LWD measurements. However, the discrete MAD samples only show a change of 0.1 g/cm³ across this interval, possibly due to the spacing of discrete samples. Porosity is slightly reduced by ~5%, and grain density is slightly lower at 2.65 g/cm³. The decrease in GRA and LWD density is mainly caused by the presence of abundant ash layers (see "Lithostratigraphy," p. 3). Horizon A shows two distinctive intervals of reduced density (Fig. F39). This double low-density feature is also seen at Site 1248, where Horizon A was cored at a depth of 128 mbsf (see "Physical Properties," p. 14, in the "Site 1248" chapter).

F39. Physical properties across Horizon A, p. 79.

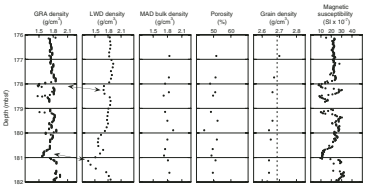

Magnetic Susceptibility

The MS record in the upper 200 mbsf is characterized by small variations with the exception of three major events at 86, 108, and 150 mbsf, respectively (Fig. F37). All three spikes are associated with turbidite events, as determined from core descriptions (see "Lithostratigraphy," p. 3). Below 200 mbsf, the overall magnitude of the MS increases and the record is characterized by many individual spikes over relatively short intervals. The most prominent spike at 372 mbsf does not clearly correlate to a seismic event or major lithostratigraphic boundary. Observation of the split core section at this depth, there is no indication of a turbidite layer or a greater abundance of sulfides.

The prominent Horizon A, clearly defined in the sediment density record, is not associated with large MS variations. Small variations in MS, however, can be correlated to the observed individual ash layers (see "Lithostratigraphy," p. 3). The ash layers are associated with low MS, whereas the sandy/silty layers show higher MS values.

Non Contact Resistivity System

Resistivity was determined using the Non Contact Resistivity (NCR) system on cores recovered from Holes 1245B and 1245C (Fig. F40). However, the measurements are dominated by the gas expansion cracks, which act as electrical insulators. It is interesting to note that the degree of cracking as determined by the noncontact resistivity (NCR) decreases dramatically below the BSR at 134 mbsf. Where gas cracks are less abundant, the measured sediment resistivity values vary around 1 Ωm.

F40. NCR, p. 80.

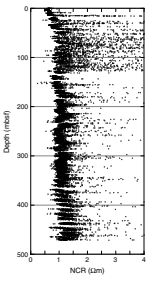

Compressional Wave Velocity from the Multisensor Track and Hamilton Frame

At Site 1245, compressional (*P*)-wave velocity (V_P) was measured on shallow cores recovered from all holes. In Hole 1245B, velocities were measured using the MST on Core 204-1245B-1H from seafloor to a maximum depth of 8.5 mbsf. On the split half sections, measurements were carried out using all three V_P sensors mounted on the Hamilton Frame up to a maximum depth of 10 mbsf (Fig. F41).

At shallow depths from the seafloor to 10 mbsf, there is a good correlation among the MST, V_P, NCR, and the GRA density (Fig. F41). Gas

F41. V_P, bulk density, NCR, and shear strength, p. 81.

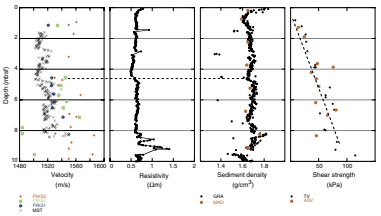

expansion cracks started at ~8.5 mbsf and made further measurements impossible. From cores recovered from Hole 1245E, individual small samples were selected and trimmed with a saw for V_P measuring using the PWS3 sensor only (Table T17). The V_P values at depths greater than 470 mbsf vary between 1700 and 2090 m/s, and have an average value of 1994 m/s. Because of the higher noise level in the velocity measurements, the automated picker of the Hamilton Frame was not able to determine reliable velocity picks, and all V_P values were determined based on handpicks of the waveforms.

T17. V_P measurements, p. 124.

Thermal Conductivity

Thermal conductivity was measured in Hole 1245B only (Table T18). Values range from 0.9 to 1.12 W/(m·K) (average = 0.978 W/[m·K]). No distinct downhole trend is evident, and no major correlation with bulk density variations was observed.

T18. Thermal conductivity data, p. 125.

Shear Strength

Shear strength was measured in Holes 1245B and 1245C using the automated shear vane and the handheld Torvane (Fig. F37; Table T19). Shear strength shows a linear increase with depth in the upper 10 mbsf (Fig. F41) but is dominated by large scatter at depth. This is partially the result of gas expansion cracks, which caused relatively unreliable measurements, in spite of the care taken to select the intervals with minimum disturbance.

T19. Shear-strength measurements, p. 126.

Summary and Discussion

At Site 1245, cores were recovered up to a total depth of 540 mbsf, which is the deepest hole penetration of this leg. Physical properties have been correlated to major seismic events, such as Horizons X, Y, and A. Horizons X and Y mark boundaries between the lithostratigraphic Units I, II, and III, respectively. Horizon A is the most prominent seismic reflector at this site (besides the BSR) and is characterized by low sediment densities. This horizon is characterized by sand and silt layers including large amounts of volcanic ash components. There is no MS anomaly associated with Horizon A, which is in contrast to other turbidite sequences observed during this leg.

IR imaging provided a robust and fast method of detecting gas hydrate at this site. In Hole 1245B, the deepest thermal anomaly at 129.4 mbsf is in good agreement with the seismically defined depth of the BSR at 134 mbsf.

T20. Temperature measurements, p. 128.

F42. In situ temperatures, p. 82.

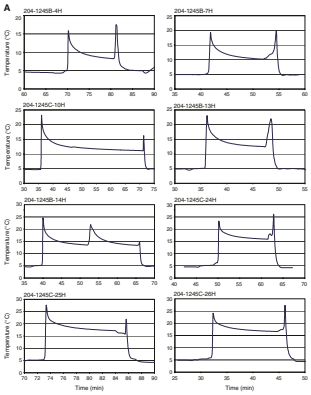

DOWNHOLE TOOLS AND PRESSURE CORING

Downhole Temperature Measurements

Twelve measurements of in situ temperature were made at this site: ten with the APCT tool and three with the DVTP. A detailed sequence of four measurements was made in Hole 1245C at approximately the depth of Horizon A, although there is some uncertainty about hole-to-hole depth correlation. Measurements span the depth range of 38–350 mbsf (Table T20). Raw data are shown in Figure F42. Only the portion

of the data from the immediate time period before, during, and after tool insertion is shown.

APCT data were modeled using the software program TFIT (as described in the "Downhole Tools and Pressure Coring," p. 34, in the "Explanatory Notes" chapter) using measured thermal conductivities (see "Physical Properties," p. 19). Uncertainty in the extrapolated value of in situ temperature as a result of subjective analyst picking of t_p, t_i, and t_f is <0.05°C for these high-quality records. Uncertainty resulting from possible errors in measured values of thermal conductivity is estimated to also be ~0.05°C. Instrument calibration uncertainties are present but are poorly quantified (see "Downhole Tools and Pressure Coring," p. 29, in the "Site 1244" chapter). No in situ temperatures were derived from DVTP data because the time series suggest that the probe did not penetrate the seafloor properly.

The subsurface temperature data from the APCT tool are shown in Figure F43 along with the best-fit temperature gradient. Solutions with and without inclusion of the mudline temperature are shown and are not significantly different. The dark gray horizontal line at 134 mbsf marks the position of the BSR as determined from seismic reflection data and confirmed by wireline acoustic logging data (see "Downhole Logging," p. 26). The dashed horizontal line shows the predicted depth to the base of the GHSZ, assuming the temperature gradient determined for Site 1245 and hydrostatic pressure for a pure methane and seawater system (Maekawa et al., 1995). The temperature at the BSR, indicated by the downhole measurements, is 0.5°C colder than predicted. Possible explanations for this mismatch will be discussed elsewhere.

F43. Subsurface temperatures, p. 84.

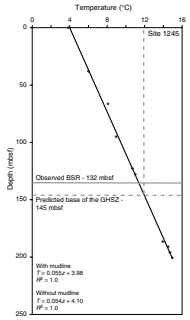

In Situ Pressure Measurements

No in situ pressure measurements were made at this site.

Pressure Core Sampler

The ODP PCS was deployed five times at Site 1245. All deployments were successful (i.e., a core under pressure was recovered). The main objectives of the deployments were (1) to construct a detailed profile of concentration and composition of natural gases in the upper part of the section (0–300 mbsf) and (2) to identify the presence/absence and concentration of gas hydrate within the GHSZ.

Specific depth intervals were targeted for deployment of the PCS. Three cores (Cores 204-1245C-3P [17–18 mbsf], 8P [57–58 mbsf], and 16P [120–121 mbsf]) were recovered from above the BSR. The other two cores (Cores 204-1245B-17P [147.1–148.1 mbsf] and 33P [291.2–292.2 mbsf]) were recovered from below the BSR.

The PCS chambers were degassed for 334–4685 min after recovery (Table T21). Pressure was recorded during degassing experiments (Fig. F44). Gas was collected in a series of sample increments (splits), and most were analyzed for molecular composition (see "Organic Geochemistry," p. 15). In addition, gas splits were subsampled for shore-based analyses. After degassing, the PCS chambers were disassembled. The lengths of the cores were measured (Table T21), and samples were taken for analysis of physical properties (see "Physical Properties," p. 19).

Gas was collected in 20- to 1070-mL increments. The measured incremental and cumulative volumes are plotted vs. time in Figure F44. The cumulative volume of released gas varies from 315 (Core 204-1245C-3P)

T21. Results from degassing experiments, p. 129.

F44. Volume-pressure-time plots for the PCS, p. 85.

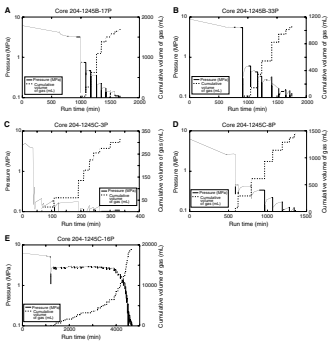

to 19,025 mL (Core 16P) (Table T21). The volume of the last gas splits varies from 10 (Core 204-1245C-8P) to 20 mL (Cores 17P and 16P). This observation suggests that almost all gas present in the cores was collected.

Gases released from the PCS are mixtures of air (N_2 and O_2), CH_4, CO_2, and C_{2+} hydrocarbon gases (see "Gas Hydrate and Pressure Cores," p. 17, in "Organic Geochemistry"). The abundance of air components in the PCS gas samples (2.6%–29.3% of gas mixtures) suggests that air was not always properly displaced from the PCS by seawater during deployments. Methane is the dominant natural gas present in collected gas splits. The molecular composition of gases from the PCS is similar to the composition of gas voids at adjacent depths (see Fig. F45).

Sediments in cores recovered with the PCS have lithologies that are similar to sediments recovered by the APC and XCB at adjacent depths (see "Physical Properties," p. 19). However, the porosity of sediments from the PCS is often different from the porosity of sediments at adjacent depths (Fig. F45) for reasons that are not yet understood. Porosity values measured in samples from APC and XCB cores taken near the PCS were used to estimate the in situ methane concentration (Table T21).

The concentration of in situ methane was estimated based on data from the degassing experiments (i.e., total volume of methane) and core examination (i.e., length of recovered core and the porosity of sediments). The calculation yields equivalent concentrations varying from 10.2 to 1,116.6 mM of methane in pore water (Table T21). These concentrations have been compared with the theoretical methane-solubility curve extrapolated from values calculated for higher pressures (greater depths) (Handa, 1990; Duan et al., 1992) (Fig. F46).

Preliminary analysis suggests that gas hydrates have been present in relatively high concentrations (12%–16% of pore volume) in Core 204-1245C-16P recovered from above the BSR. In addition to high gas concentrations, strong evidence of the presence of gas hydrate was found in the pressure record of core degassing (Fig. F44E). The estimate of gas hydrate saturation is consistent with those based on well logging data (see "Downhole Logging," p. 26). However, other cores retrieved from above the BSR (Cores 204-1245C-3P and 8P) suggest that only dissolved methane is present in many intervals within the GHSZ. No free gas seems to be present in intervals ~15 and ~160 m below the BSR (Cores 204-1245B-17P and 33P, respectively). Additional comparisons of measured methane concentrations with theoretical methane solubility, both above and below the BSR, will be performed on shore to better estimate if methane was present in situ in solution, in free phase, or as gas hydrate.

F45. Porosity of sediments in APC, XCB, and PCS cores, p. 86.

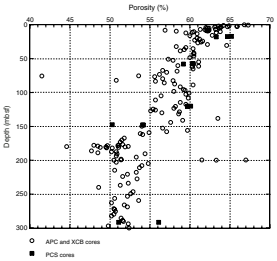

F46. Methane concentrations, p. 87.

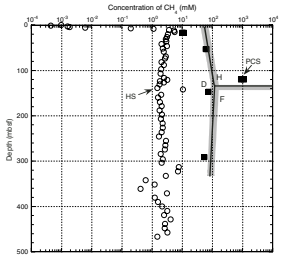

HYACINTH Pressure Core Sampling

Coring Summary

Four deployments of the HYACINTH pressure coring tools were made at Site 1245, two each with the HRC and FPC (see "Operations," p. 2). The HRC cores (Cores 204-1245B-46E [HRC 5] and 204-1245C-29E [HRC 6]) were at 407 and 201 mbsf, respectively. The FPC cores (Cores 204-1245C-18Y [FPC 7] and 27Y [FPC 8]) were at 129 and 195 mbsf, respectively. All the cores were located below the BSR (located at ~134 mbsf), apart from Core 204-1245C-18Y (FPC 7), which was ~5 m above the BSR. Technical and operational difficulties prevented any cores

from being recovered under full pressure for further analysis. The FPC recovered a good core (90 cm) from 129 mbsf but apparently had difficulty penetrating the stiffer lithology at 195 mbsf and only recovered a 15-cm-long section. We recovered a 38-cm core (Core 204-1245B-46E; HRC 5) in indurated claystone, but recovery of Core 204-1245C-29E (HRC 6) was hampered by operational difficulties when the active heave compensator (AHC) failed and only a 20-cm-long core was recovered.

HYACE Rotary Corer Operations

Two HRC deployments, Cores 204-1245B-46E (HRC 5) and Core 204-1245C-29E (HRC 6) were made at depths of 407 and 201 mbsf, respectively (see Table T22). The first attempt to run Core 204-1245B-46E (HRC 5) was aborted after difficult hole conditions required high pump rates, which were incompatible with the HRC operation.

T22. HYACINTH pressure coring summary, p. 130.

On the second attempt, the tool was lowered at 50–70 m/min and stopped at 1245 m with the drill string already at TD to minimize the risk of borehole instability. It was lowered on the wireline to the landing position, and 5 m of slack wire was paid out before closing the blowout preventer (BOP). Pumping began at 80 gallons per minute (gpm), and a pressure peak was observed at 620 psi (first shear pin sheared). Pumping continued at 110 gpm, but a second pressure peak (which would have indicated full stroke) was not observed after 24 min. Pumping was stopped, and the BOP was opened. The drill string was picked up to 1285.3 m before pumping was continued for 1 min at 90 gpm, in an attempt to ensure a full stroke. After pumping stopped, the tool was raised on the wireline, at first slowly and then at 60–70 m/min, to the surface. When broken out of the drill string, it was observed that the central rod was not fully retracted until several jerks on the tugger line had occurred. The DSA tool was removed and was returned to the trestles on the pipe racker for disassembly.

We observed that the liner had broken above the core catcher, the piston cap had unscrewed, high loads had damaged a bearing, and the valve had not closed. Despite this, 38 cm (recovery = 38%) of stiff indurated claystone was recovered. We concluded that a variety of factors could have caused the problems encountered, including poor motor performance, but these problems were attributed to insufficient heave compensation and poor hole conditions. The HRC was completely overhauled and the motor replaced before the next deployment (Core 204-1245C-29E [HRC 6]).

The HRC was deployed in Hole 1245C as Core 204-1245C-29E (HRC 6) at 201 mbsf. The tool was run into the hole at 40–70 m/min and stopped at 1030 m. Pumping was stopped, the tool was lowered onto the landing shoulder, and 5 m of slack wire was paid out. The drill string was then lowered to TD and held with 15 klb (weight on bit). The BOP was closed, and pumping began slowly with both passive and active heave compensation activated. A pressure peak was observed at 650 psi (first shear pin sheared) and pumping continued at 85 gpm. However, at this stage a sudden problem with the AHC occurred (the string was bouncing with weight on bit changing rapidly between 5 and 45 klb), and it was switched off while the passive compensator remained on. Coring could not continue, and the drill string was picked up ~5 m while pumping at 100 gpm. After pumping was stopped, the tool was lifted on the wireline slowly for the first 20 m (7 m/min) and then at 110 m/min while circulating. The tool was broken out of the string, the

DSA tool was removed, the strongbacks replaced, and the DSA tool was returned to the trestles on the piperacker. We found that a full stroke had been achieved and the core liner had retracted into the autoclave with a 20-cm-long core (Core 204-1245C-29E) at the top, but the autoclave flapper valve had not closed. The inner sleeve had become stuck at the valve, which may have been caused by the sudden motions when the AHC failed.

Fugro Pressure Corer Operations

Two FPC deployments, Core 204-1245C-18Y (FPC 7) and Core 204-1245C-27Y (FPC 8), were made at depths of 129 and 195 mbsf, respectively. During the coring procedure for Core 204-1245C-18Y (FPC 7), the AHC was turned off because it appeared to increase the variability of the weight on bit. A full core (90 cm long) was recovered, but the lower autoclave valve had not fully closed. The fall path of the valve was modified before the next deployment. During recovery of Core 204-1245C-27Y (FPC 8), the AHC was used. However, the inner rod failed to stroke out completely, indicating that the formation was too stiff for the hammer mechanism. This resulted in the recovery of a short core (15 cm long) and an imploded liner with inverted catcher fingers. It should be noted that the APC cores taken on either side of Core 204-1245C-27Y (FPC 8), namely Cores 204-1245C-26H and 28H, only recovered 4.8 and 3.8 m, respectively. Consequently, the working hypothesis that the operational limit of the FPC hammer mechanism is similar to the working limit of the APC appears to have been confirmed in this type of silty clay formation.

DOWNHOLE LOGGING

Logging While Drilling

Operations

LWD operations in Hole 1245A began at 0900 hr UTC on 18 July 2002, with tool initialization at the rig floor. LWD tools included the GeoVision Resistivity (resistivity at the bit [RAB]) with $9^1/_8$-in button sleeve, measurement while drilling (MWD), NMR-MRP tool, and Vision Neutron Density tool (VND). Memory and battery life were increased to allow for up to 70 hr of continuous drilling. Hole 1245A was spudded at 0945 hr at 886.50 meters below rig floor (mbrf) water depth (drillers depth) on the western flank of Hydrate Ridge. Drilling proceeded at ~25 m/hr to TD at 380 mbsf without difficulty, and real-time data were transmitted to the surface at a rate of 6 Hz. Given calm heave conditions, the real-time data record was changed to increase the vertical resolution of the formation evaluation logs with less emphasis on high-resolution weight-on-bit and torque measurements. Mud pump noise affected the data transmission to a lesser extent than at Site 1244. LWD tools were pulled to 85 m clear of the seafloor at 0745 hr on 19 July for the dynamic positioning move to Site 1246. Total bit run was ~23 hr.

Logging Quality

Figure F47 shows the quality control logs for Hole 1245A. The target rate of penetration (ROP) of 25 m/hr (±5 m/hr) in the interval from the

F47. Quality control LWD logs, p. 88.

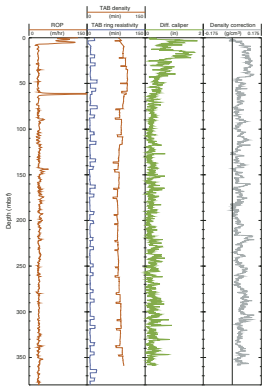

seafloor to TD was generally achieved. This is sufficient to record one sample per 4-cm interval (~25 samples per meter), which was obtained over 86% of the total section of the hole. The quality of RAB images is, thus, quite high, and no significant resolution loss is observed with variation in ROP in Hole 1245A. However, the quality of the RAB images in the interval from 17 to 25 mbsf in Hole 1245A (Fig. F48) is degraded by an apparent problem associated with low rates of bit rotation. The NMR-MRP porosity data were enhanced by using slow drilling rates, but the data-sampling resolution is less than that of the RAB, with one measurement every ~15 cm.

The differential caliper log (DCAL), which gives the distance between the tool sensor and the wall of the borehole, as recorded by the LWD density tool, is the best indicator of borehole conditions. The differential caliper values are <1 in over 96% of the total section in Hole 1245A. Only the uppermost 24 mbsf of the hole shows washouts >1 in. The density correction, calculated from the difference between the short- and long-spaced density measurements, generally varies from 0 to 0.12 g/cm³ (Fig. F47), which shows the good quality of the density measurements. A standoff of <1 in between the tool and the borehole wall indicates high-quality density measurements, with an accuracy of ±0.017 g/cm³. The interval below 280 mbsf shows minor washouts resulting from borehole breakouts, with DCAL measurements up to 1 in; density measurements in this interval are slightly degraded.

Time-after-bit (TAB) measurements are 10 ± 3 min for ring resistivity and gamma ray logs. However, the TAB for the density and neutron porosity logs was more variable, ranging from 70 to 100 min (Fig. F47). In general, the TAB values remain relatively constant, coinciding with steady ROP while drilling over most of the hole, although some large variations in ROP are observed just below the seafloor and again at a depth of 62 mbsf.

The depths relative to seafloor were fixed for all of the LWD logs by identifying the gamma ray signal associated with the seafloor and shifting the logging data to the appropriate depth as determined by the drillers pipe tallies. For Hole 1245A, it was determined that the gamma ray logging pick for the seafloor was at a depth of 882.0 mbrf. The rig floor logging datum was located 10.9 m above sea level.

F48. Summary of LWD log data, p. 89.

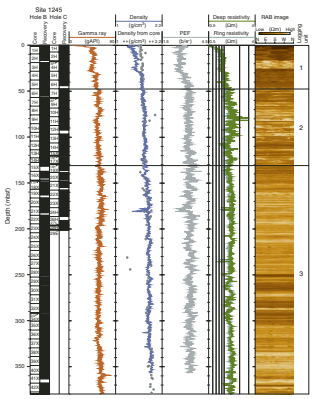

Wireline Logging

Operations

Hole 1245E was originally planned to be RCB drilled and cored to a depth of 600 mbsf. With increasing hole stability problems, we decided to stop drilling at 550 mbsf and proceed with conventional wireline logging (CWL). The drill string became stuck shortly after starting the hole-conditioning program. The drill string was eventually freed after more than 14 hr of effort. It was determined that the hole should be safe and open to a depth of ~350 mbsf, which became the target depth for logging. Rig-up for logging operations began at 0300 hr on 15 August and final rig-down for the CWL operations was complete by 1630 on 16 August. See Table T23 for detailed information on the Hole 1245E CWL program.

CWL operations in Hole 1245E began with the deployment of the triple combo tool string (Temperature/Acceleration/Pressure [TAP] tool/Dual Induction Tool [DIT]/Hostile Environment Litho-Density Tool [HLDT]/Accelerator Porosity Sonde [APS]/Hostile Environment Gamma

T23. Conventional wireline logging, p. 131.

Ray Sonde [HNGS]/Inline Checkshot tool [QSST]) (Table T23). The triple combo tool string initially encountered a borehole bridge at a depth of ~320 mbsf that the tool string could not pass; TD of Hole 1245E was therefore redefined to be ~320 mbsf. Good quality data were acquired during the main uphole log pass (see below), and the tool was run back down to TD for a second pass. Before the start of the second log pass, several checkshots were performed with the QSST tool, but the signal-to-noise ratio was poor. QSST shot attempts were made with the WHC on and off, and the tool was lowered up and down and reseated at TD to improve coupling with the borehole wall, while at the same time extra cable slack was added. After stacking several QSST checkshots, the signal-to-noise ratio showed some improvement and a one-way traveltime of 758 ms was recorded at the TD of Hole 1245E (320 mbsf). To calculate an interval velocity with depth, a 32-m uphole shift is necessary to take into account the positioning of the QSST tool at the top of the triple combo tool string. The repeat pass of the triple combo tool string was performed over an interval from 320 mbsf up into the drill pipe at 73 mbsf. TAP tool data and associated depth data were recorded without any problems. The triple combo logging run ended with the rig-down of the tool string, which was completed at 1100 hr on 15 August.

For the second CWL run in Hole 1245E, the FMS-sonic tool string (FMS/Dipole Sonic Imager [DSI]/Scintillation Gamma Ray Tool [SGT]) was deployed. The FMS-sonic tool string reached a maximum depth of 319 mbsf on two consecutive passes. For the first pass, the FMS button electrical current setting was too high and FMS images appeared very dark during real-time acquisition; this was rectified for the second pass. The FMS calipers showed that parts of the hole were elliptical in shape, one arm reading an average of ~12 in and the other up to 16 in, consistent with the density log caliper recorded on the triple combo run. Both passes of the FMS-sonic tool string appeared to track the same path up the borehole. DSI modes used for the first pass were standard-frequency monopole, low-frequency lower dipole, and standard frequency for the upper dipole. DSI modes used for the second pass were the same, except that the monopole was run at low frequency. The recorded sonic waveforms are of very high quality, particularly the dipole recordings, but the very low velocity of this formation made it difficult for the automatic slowness/time coherence (STC) picking program to select accurate compressional velocities. The lower-frequency monopole used in the second pass improved the quality of the automatic STC selections, but further reprocessing was still required.

A final run was made for seismic experiments, which will be discussed elsewhere.

Logging Quality

All logging data from the triple combo and FMS-sonic tool string runs in Hole 1245E are of high quality (Figs. F49, F50, F51, F52). The hole conditions were generally good with density caliper measurement readings around 12 in, on average. Numerous relatively short washed-out intervals up to 16 in diameter are evident throughout the hole. Comparison of logs from successive passes shows good repeatability of the data, with only several notable small depth mismatches.

The absolute depths, relative to seafloor, for all of the CWL logs were fixed by identifying the gamma ray signal associated with the seafloor

F49. CWL logging data, p. 90.

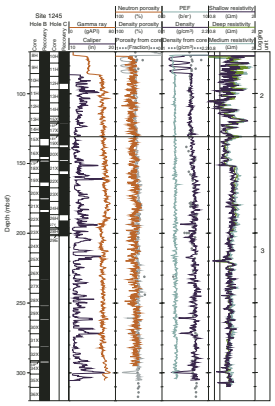

F50. CWL gamma ray logging data, p. 91.

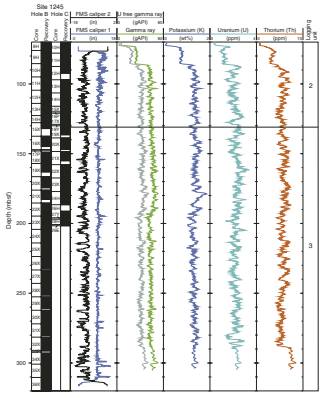

F51. Comparison of LWD and CWL data, p. 92.

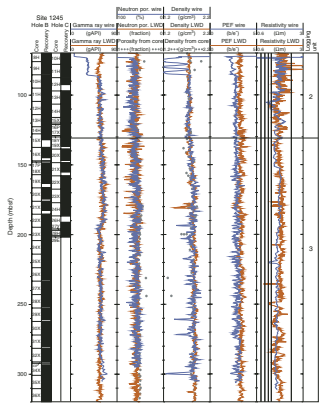

and depth shifting the log data appropriately. The gamma ray pick for the seafloor in Hole 1245E was 883 mbrf for all of the CWL runs.

Interpretation of Logging-While-Drilling and Wireline Logging

Data from Holes 1245A and 1245E show excellent quality LWD and CWL logs. The presence of gas hydrate was identified from ~50 to 131 mbsf by high resistivities and acoustic velocities and RAB image anomalies, allowing quantitative estimates of gas hydrate saturations. Interbedded layers of low and high density and variable natural gamma ray intensity are observed within and below the GHSZ, which may indicate lithologic changes associated with turbidites and the presence of a relatively thick free gas–saturated sand.

Logging-While-Drilling and Wireline Logging Comparison

Figure F51 shows a comparison of downhole LWD and CWL data from Holes 1245A and 1245E, using the gamma ray, neutron porosity, density, photoelectric factor, and deep resistivity logs. The highly variable CWL log data within the upper 85 mbsf of Hole 1245E was obtained through the drill pipe. In general, the LWD and CWL data from each hole, as depicted in Figure F51, match relatively well, exhibiting similar curve shapes and absolute logging values. The CWL (Hole 1245E) and LWD (Hole 1245A) GRA density logs, however, are characterized by numerous low density anomalies that do not correlate between the two holes. However, both density logs in Figure F51 still compare favorably with the core-derived density data. In addition, the CWL (Hole 1245E) and LWD (Hole 1245A) resistivity logs exhibit differences in measured values with depth and a difference in the apparent vertical resolution of each device, with the RAB (LWD) tool yielding a log with a higher vertical resolution.

Logging Units

The logged section in Holes 1245A and 1245E is divided into three "logging units," based on obvious changes in the LWD and CWL gamma ray, density, electrical resistivity (Figs. F48, F49, F50), and acoustic transit-time measurements (Fig. F52).

Logging Unit 1 (0–48 mbsf) is characterized by increasing resistivities and densities with depth as measured by the LWD tools. However, this trend in the downhole logging data is probably in part due to degraded log measurements within the enlarged portion of the near surface borehole as shown in Figure F47. The base of logging Unit 1 does not exactly coincide with the base of lithostratigraphic Unit I (0–31 mbsf), which is mainly composed of clay. The transition from logging Unit 1 to 2 is defined by a sharp increase in electrical resistivity.

Logging Unit 2 (48–131 mbsf) is characterized by zones of distinct high resistivities and moderate to high V_P, with peak resistivity values exceeding 2 Ωm and V_P recorded at >1.61 km/s. The LWD-measured densities increase with depth in logging Unit 2 (1.65 g/cm³ at the top to near 1.80 g/cm³ at the bottom). In Hole 1245E (Fig. F52), the acoustic transit-time log has been used to precisely select the depth of the boundary between logging Units 2 and 3, which is marked by a drop in

F52. CWL acoustic logging data, p. 93.

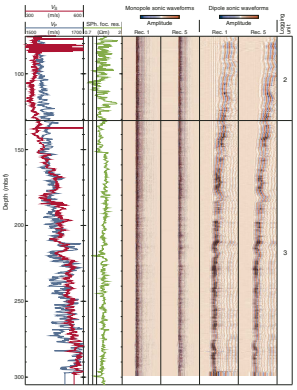

V_P to <1.56 km/s and corresponds to the depth of the BSR at this site. Logging Unit 2 is included in lithostratigraphic Unit II (31–212 mbsf), which is characterized as a diatom-bearing clay to silty clay interval with some sand-rich sections (see **"Lithostratigraphic Unit II,"** p. 4, in "Lithostratigraphic Units" in "Lithostratigraphy").

Logging Unit 3 (131–380 mbsf; TD of Hole 1245A) correlates with the lower part of lithostratigraphic Unit II (31–212 mbsf) and the upper part of lithostratigraphic Unit III (212–419 mbsf), both of which contain clay to silty clay turbidite sequences (see **"Lithostratigraphic Units,"** p. 4, in "Lithostratigraphy"). The gamma ray logs from this unit show a characteristic cyclicity that reflects the interbedded sand-silt-clay turbidite sequences. A 4-m-thick anomalous interval, characterized by variable V_P (ranging from 1.57 to 1.65 km/s), variable resistivity (ranging from ~0.8 to ~1.8 Ωm), and low density (<1.5 g/cm^3) is present in logging Unit 3 within the depth interval from 177 to 181 mbsf, which suggests the presence of a free gas–bearing sand. This apparent free gas–bearing interval corresponds to the seismic Horizon A (see **"Introduction,"** p. 1). Toward the bottom of the hole (below 220 mbsf), the RAB resistivity images (Fig. **F48**) show borehole breakouts consistently at northwest-southeast orientations in the borehole.

Resistivity-at-the-Bit and Formation MicroScanner Images

Both the RAB and FMS tools produce high-resolution images of the electrical resistivity characteristics of the borehole wall that can be used for detailed sedimentological and structural interpretations. It is also possible to use the RAB and FMS tools to make high-resolution electrical images of gas hydrates in the borehole, thus yielding information about the nature and texture of gas hydrate in sediments. The resolution of the images from the RAB tool is considerably lower than the resolution of the images from the FMS. For example, the RAB images have about a 5- to 10-cm vertical resolution, whereas the FMS tool can resolve features such as microfractures with widths <1 cm. However, the RAB tool provides 360° coverage of the borehole, whereas FMS images cover only ~30% of the hole.

The RAB image in Figure **F53** is characterized by light (high resistivity) to dark (low resistivity) bands, which in many cases can be traced across the display. The light continuous high-resistivity bands likely indicate that gas hydrate fills low- to high-angle fractures and nearly flat-lying stratigraphic horizons in Hole 1245A.

In Figure **F54,** we have cross correlated a RAB image (Hole 1245A) and a FMS image (Hole 1245E) from the stratigraphic interval that contains Horizon A, which has been identified as a prominent regional seismic reflector (see **"Introduction,"** p. 1). As shown on the FMS and RAB images in Figure **F54,** Horizon A appears as a complex interbedded zone of high and low resistivities. More detailed examination of the FMS image shows distinct lateral variability within this interval and apparent fine-scale sedimentologic structures. The comparison of the deep- and shallow-measuring RAB images in Figure **F54** also shows evidence of geologic controls on the infiltration of conductive drilling fluids into the formation, which appears more prevalent in the shallow-measuring RAB image.

As described above, logging Unit 3 (131–380 mbsf) correlates with the lower part of lithostratigraphic Unit II (31–212 mbsf) and the upper

F53. RAB image showing the possible presence of gas hydrate, p. 94.

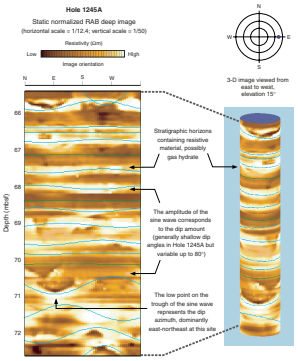

F54. RAB and FMS images showing seismic Horizon A, p. 95.

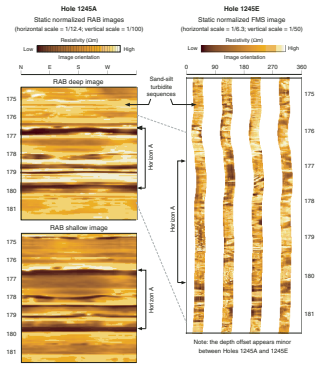

part of lithostratigraphic Unit III (212–419 mbsf), which are described as interbedded clay to silty clay turbidite sequences (see "Lithostratigraphic Units," p. 4, in "Lithostratigraphy"). The RAB and FMS images in Figure F55, from logging Unit 3 in Holes 1245A and 1245E, are characterized by interbedded light (resistive) and dark (conductive) layers. The darker, more conductive layers usually represent the more porous, coarser-grained fraction of the turbidite sequence, in which the conductive drilling fluids have penetrated more deeply into the formation.

F55. RAB and FMS images showing turbidites, p. 96.

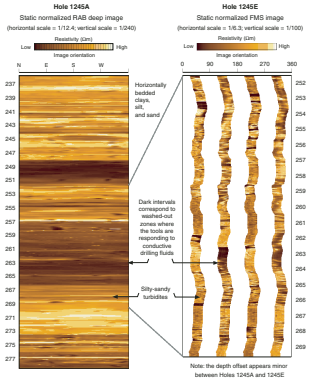

Logging Porosities

Sediment porosities can be determined from analyses of recovered cores and from numerous borehole measurements (see "Physical Properties," p. 22, and "Downhole Logging," p. 43, both in the "Explanatory Notes" chapter). Data from the LWD density, neutron, and nuclear magnetic resonance logs have been used to calculate sediment porosities from Hole 1245A. Core-derived physical property data, including porosities (see "Physical Properties," p. 19), have been used to both calibrate and evaluate the log-derived sediment porosities.

The VND LWD-derived measurements of bulk density in Hole 1245A (Fig. F48) are relatively consistent within logging Units 2 and 3, with values ranging from ~1.7 g/cm^3 near the top of logging Unit 2 (depth = 48 mbsf) to >1.9 g/cm^3 at the bottom of logging Unit 3 (depth = 380 mbsf). The LWD log-derived density measurements (ρ_b) from Hole 1245A were used to calculate sediment porosities (ϕ) using the standard density-porosity relation,

$$\phi = (\rho_m - \rho_b)/(\rho_m - \rho_w).$$

Water density (ρ_w) was assumed to be constant and equal to 1.05 g/cm^3; however, variable core-derived grain/matrix densities (ρ_m) were assumed for each logging density porosity calculation. The core-derived grain densities (ρ_m) in Hole 1245A ranged from an average value at the seafloor of 2.69 to ~2.71 g/cm^3 at the bottom of hole (see "Physical Properties," p. 19). The density log-derived porosities from Hole 1245A range from ~70% near the seafloor to ~50% at the bottom of logging Unit 3 (Fig. F56).

F56. Comparison of LWD and core-derived porosities, p. 97.

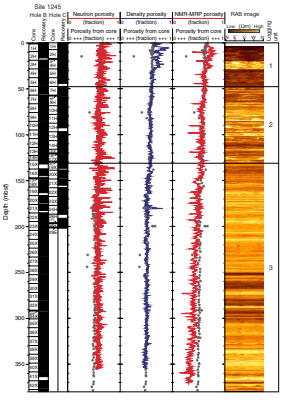

The LWD neutron porosity log from Hole 1245A (Fig. F56) yielded sediment porosities ranging from an average value at the top of the logged section of ~70% to ~60% in logging Unit 3. The "total" sediment porosities derived by the NMR-MRP tool in Hole 1245A (Fig. F56) ranged from ~70% near the seafloor to ~30% near the bottom of the hole.

In studies of downhole logging data, it is common to compare porosity data from different sources to evaluate the results of particular measurements. The comparison of core- and LWD-derived porosities in Figure F56 reveals that the density log-derived porosities are generally similar to the core porosities in logging Units 2 through 3 (48–380 mbsf). However, the density log-derived porosities are generally higher than the core-derived porosities in logging Unit 1. The neutron and NMR-MRP–derived log porosities are generally similar to the core-derived porosities in logging Unit 2, but the neutron log porosities are higher than the core-derived porosities throughout most of logging Unit 3, whereas the NMR-MRP–log porosities are lower than the core-derived porosities in most of logging Unit 3.

Gas Hydrate

The presence of gas hydrate at Site 1245 was documented by direct core sampling, with 11 gas hydrate samples recovered from Holes 1245B and 1245C within the depth interval from 54.10 to 129.26 mbsf. It was inferred, based on geochemical core analyses (see "Interstitial Water Geochemistry," p. 13), IR image analysis of cores (see "Physical Properties," p. 19), and downhole logging data, that disseminated gas hydrate is present in logging Unit 2 and, possibly, in logging Unit 1. As previously discussed in "Downhole Logging," p. 43, in the "Explanatory Notes" chapter, the presence of gas hydrate is generally characterized by increases in log-measured electrical resistivities and acoustic velocities. Logging Unit 2 at Site 1245 is characterized by a distinct stepwise increase in both electrical resistivities and acoustic velocities. In addition, the LWD resistivity tool reveals several thin high-resistivity zones within logging Unit 1 (0–48 mbsf), suggesting possible presence of gas hydrate.

Resistivity log data have been used to quantify the amount of gas hydrate at Site 1245. For the purpose of discussion, it is assumed that the high resistivities and velocities measured in logging Unit 2 are due to the presence of gas hydrate. Archie's Relation,

$$S_w = (aR_w/\phi^m R_t)^{1/n}$$

(see "Downhole Logging," p. 43, in the "Explanatory Notes" chapter), was used with resistivity data (R_t) from the LWD RAB tool and porosity data (ϕ^m) from the LWD density tool to calculate water saturations in Hole 1245A. It should be noted that gas hydrate saturation (S_h) is the measurement of the percentage of pore space in sediment occupied by gas hydrate, which is the mathematical complement of Archie-derived S_w, with

$$S_h = 1 - S_w.$$

For Archie's Relation, the formation water resistivity (R_w) was calculated from recovered core-water samples and the Archie a and m variables were calculated using a crossplot technique, which compares the downhole log-derived resistivities and density porosities. See Collett and Ladd (2000) for the details on how to calculate the required formation water resistivities and Archie variables. The values used at Site 1245 were a = 1, m = 2.8, and n = 1.9386.

Archie's Relation yielded water saturations (Fig. F57) ranging from an average minimum value of ~70% to a maximum of 100% in logging Unit 2 (48–131 mbsf) from Hole 1245A, which implies the gas hydrate saturations in logging Unit 2 range from 0% to 30%. It also appears that logging Unit 1 may contain several thin gas hydrate–bearing intervals. However, the low water saturations shown in logging Unit 3 (Fig. F57) correspond to zones that exhibit low acoustic velocities on the downhole recorded acoustic wireline logs (Fig. F52), which are indicative of free gas–bearing sediments.

Temperature Data

The LDEO TAP tool was deployed on the triple combo tool string in Hole 1245E (Fig. F58). During the process of coring and drilling, cold

F57. LWD-derived water saturations, p. 98.

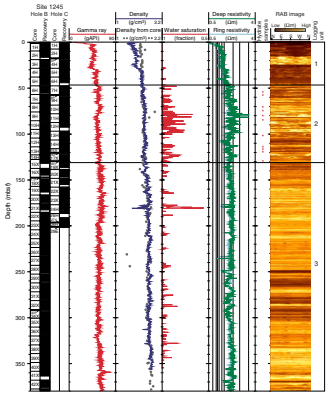

F58. Borehole temperatures recorded with the TAP tool, p. 99.

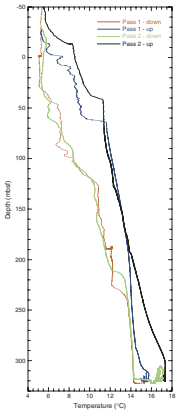

seawater is circulated in the hole, cooling the formation surrounding the borehole. Once drilling ceases, the temperature of the fluids in the borehole gradually rebounds to the in situ equilibrium formation temperature. Thus, the temperature data from the TAP tool cannot be easily used to assess the nature of the in situ equilibrium temperatures. However, the plot of the first pass downgoing temperature profile in Figure F58 reveals several gradient changes that were caused by borehole temperature anomalies. The temperature anomaly at 88 mbsf is the base of the drill pipe during the initial descent of the triple combo tool string. The break in the slope of first pass downgoing temperature log at a depth ~120 mbsf is near the depth of the BSR (131 mbsf) at this site. The anomalous temperature measurement at a depth of ~185 mbsf on the first pass downgoing temperature log is near the depth of seismic Horizon A, which may indicate gas flowing into the borehole.

REFERENCES

Chan, L.-H., and Kastner, M., 2000. Lithium isotopic compositions of pore fluids and sediments in the Costa Rica subduction zone: implications for fluid processes and sediment contribution to the arc volcanoes. *Earth Planet. Sci. Lett.,* 183:275–290.

Clague, D., Maher, N., and Paull, C.K., 2001. High-resolution multibeam survey of Hydrate Ridge, offshore Oregon. *In* Paul, C.K., and Dillon, W.P. (Eds.), *Natural Gas Hydrates: Occurrence, Distribution, and Detection.* Am. Geophys. Union, Geophys. Monogr. Ser., 124:297–306.

Collett, T.S., and Ladd, J., 2000. Detection of gas hydrate with downhole logs and assessment of gas hydrate concentrations (saturations) and gas volumes on the Blake Ridge with electrical resistivity log data. *In* Paull, C.K., Matsumoto, R., Wallace, P.J., and Dillon, W.P. (Eds.), *Proc. ODP, Sci. Results,* 164: College Station, TX (Ocean Drilling Program), 179–191.

Duan, Z., Møller, N., Greenberg, J., and Weare, J.H., 1992. The prediction of methane solubility in natural waters to high ionic strengths from 0° to 250°C and from 0 to 1600 bar. *Geochim. Cosmochim. Acta,* 56:1451–1460.

Edmond, J.M., Measures, C., McDuff, R.E., Chan, L.H., Collier, R., and Grant, B., 1979. Ridge crest hydrothermal activity and the balances of the major and minor elements in the ocean: the Galapagos data. *Earth Planet. Sci. Lett.,* 46:1–18.

Handa, Y.P., 1990. Effect of hydrostatic pressure and salinity on the stability of gas hydrates. *J. Phys. Chem.,* 94:2652–2657.

Kastner, M., Kvenvolden, K.A., Whiticar, M.J., Camerlenghi, A., and Lorenson, T.D., 1995. Relation between pore fluid chemistry and gas hydrates associated with bottom-simulating reflectors at the Cascadia margin, Sites 889 and 892. *In* Carson, B., Westbrook, G.K., Musgrave, R.J., and Suess, E. (Eds.), *Proc. ODP, Sci. Results,* 146 (Pt 1): College Station, TX (Ocean Drilling Program), 175–187.

Maekawa, T., Itoh, S., Sakata, S., Igari, S., and Imai, N., 1995. Pressure and temperature conditions for methane hydrate dissociation in sodium chloride solutions. *Geochem. J.,* 29:325–329.

Pujos-Lamy, A., 1977. *Emiliania* et *Gephyrocapsa* (nannoplancton calcaire): biometrie et interet biostratigraphique dans le Pleistocene superieur marin des Acores. *Rev. Esp. Micropaleontol.,* 9:69–84.

Seyfried, W.E., Jr., Janecky, D.R., and Mottl, M.J., 1984. Alteration of the oceanic crust: implications for geochemical cycles of lithium and boron. *Geochim. Cosmochim. Acta,* 48:557–569.

Figure F1. Bathymetric map showing locations of holes drilled at Site 1245. Bathymetry from EM300 data acquired by Monterey Bay Aquarium Research Institute (MBARI) (Clague et al., 2001).

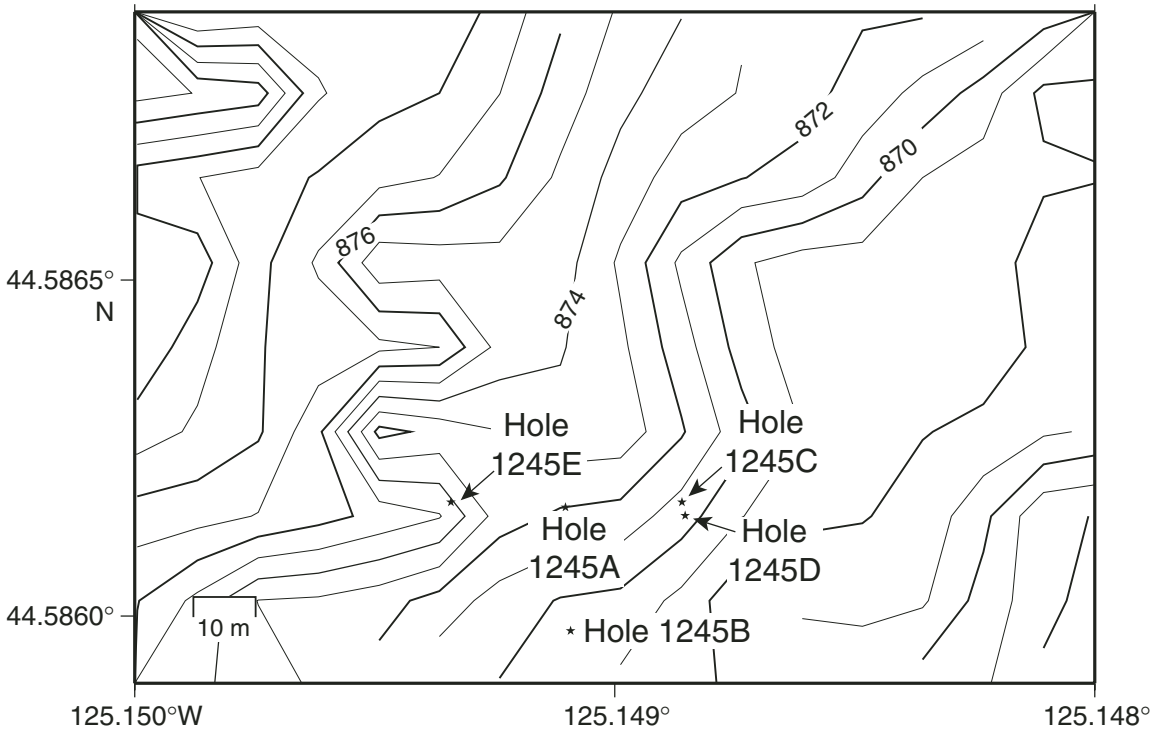

Figure F2. Lithostratigraphic summary for Holes 1245B and 1245E. (Continued on next four pages.)

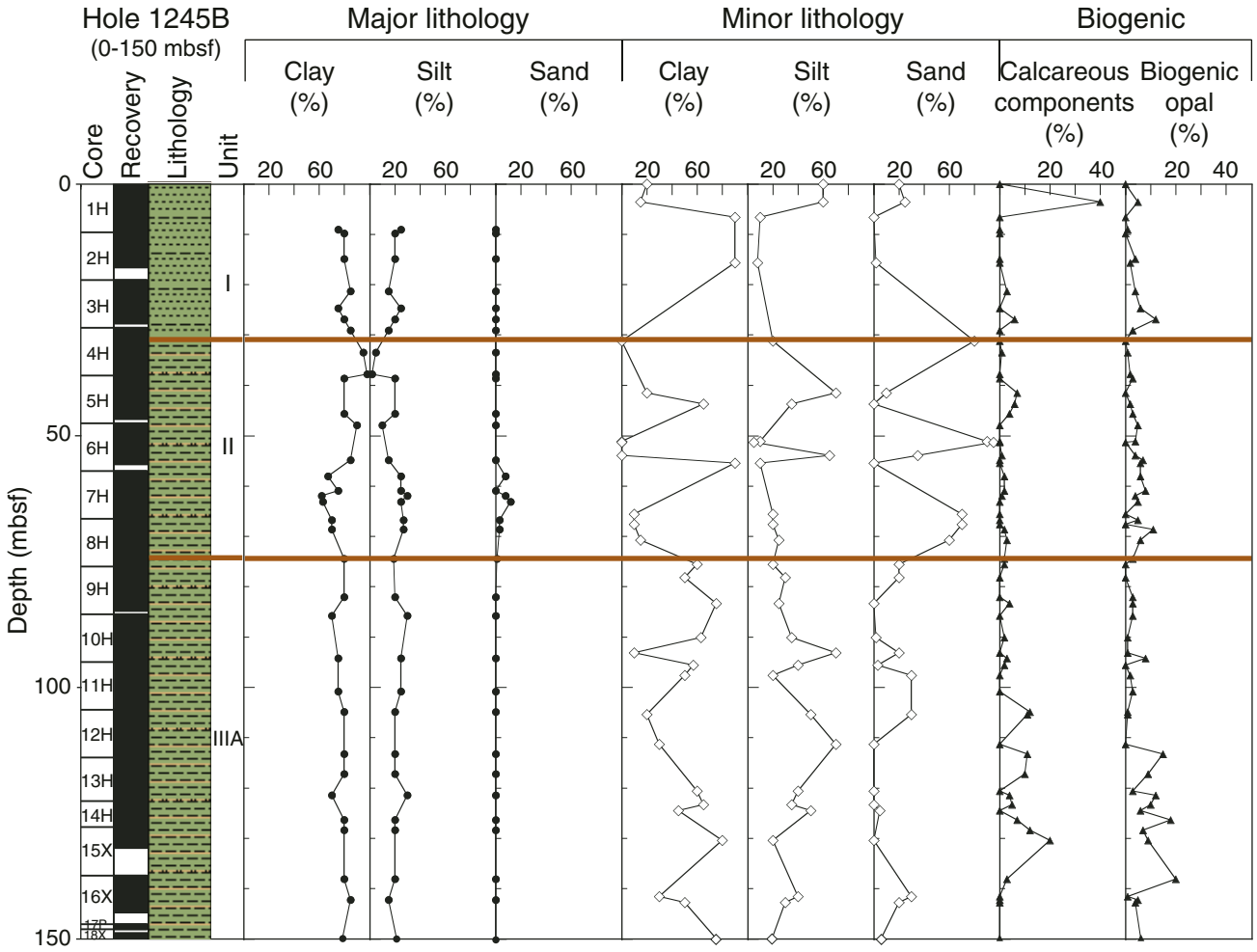

Figure F2 (continued).

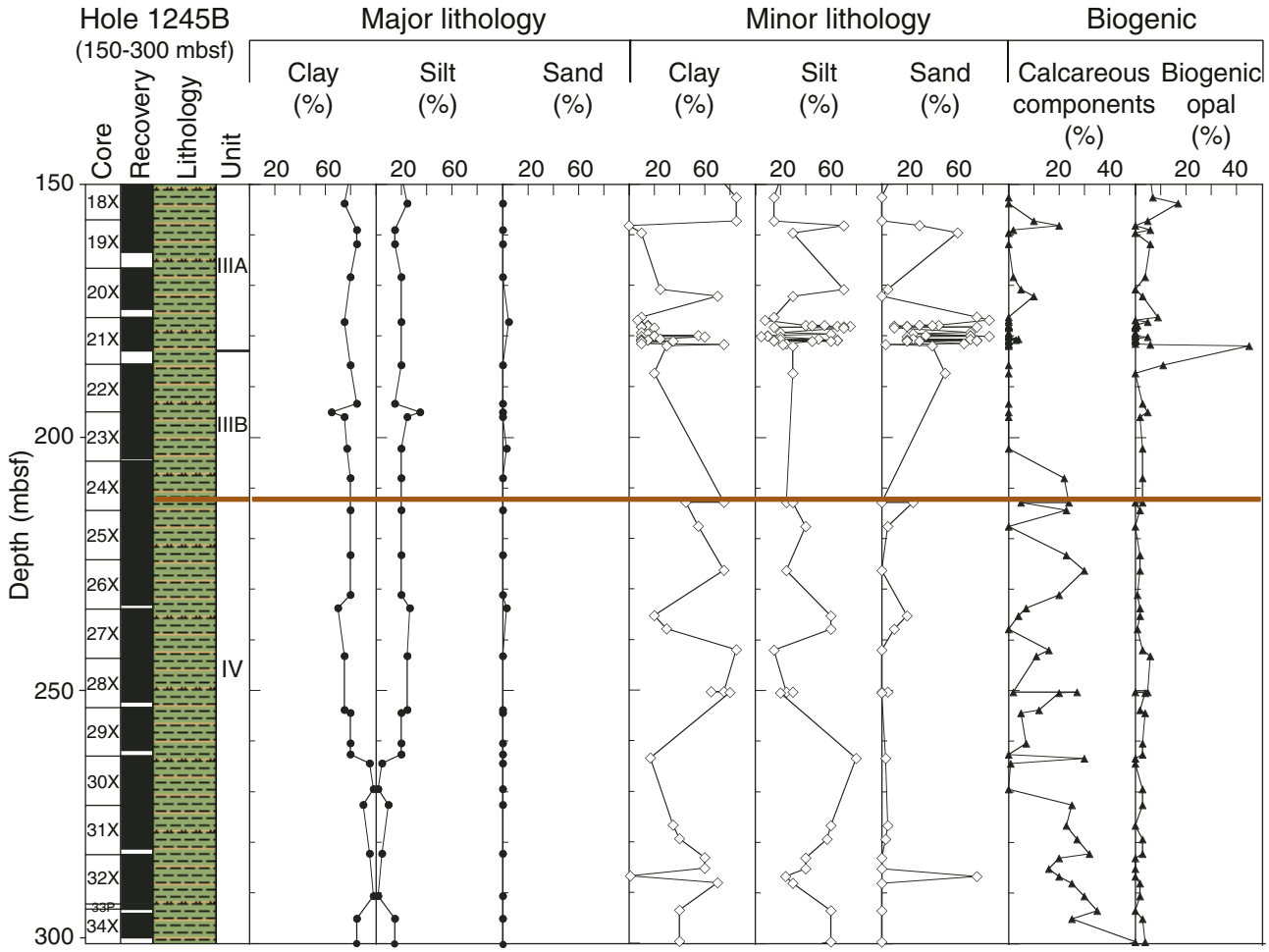

Figure F2 (continued).

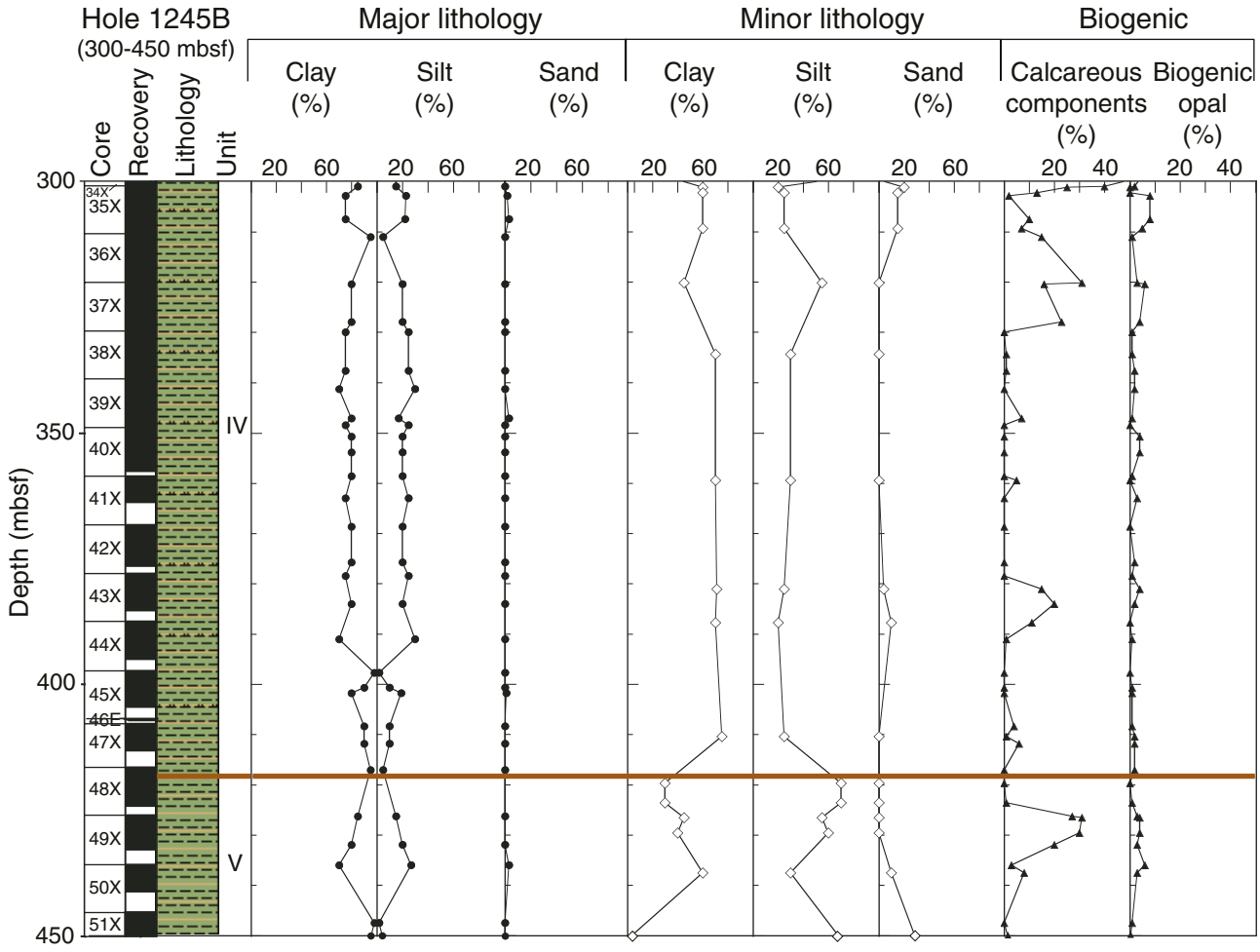

Figure F2 (continued).

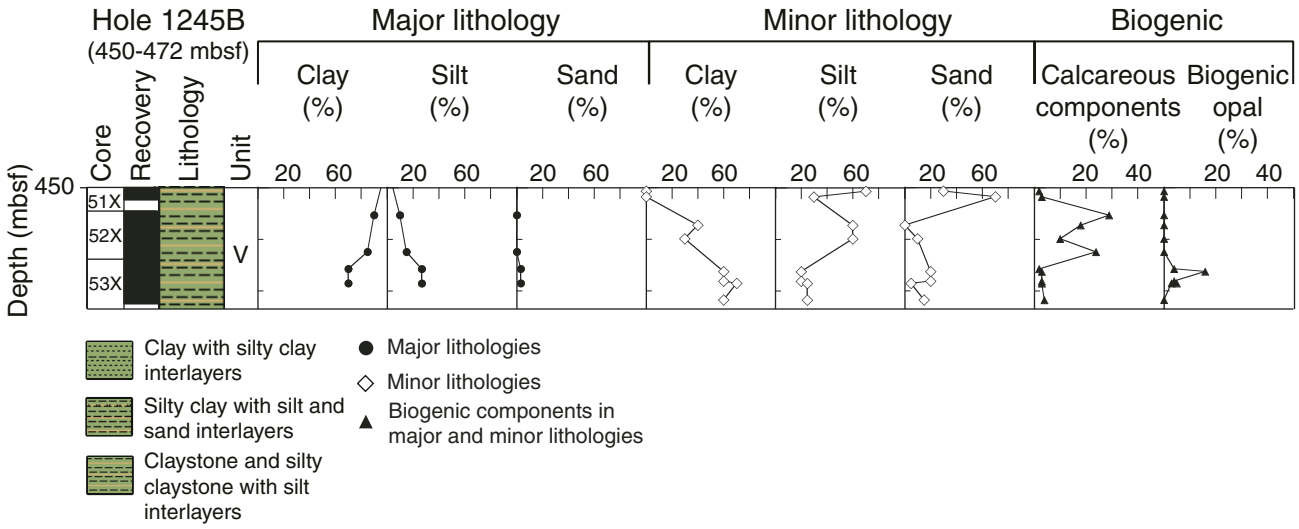

Figure F2 (continued).

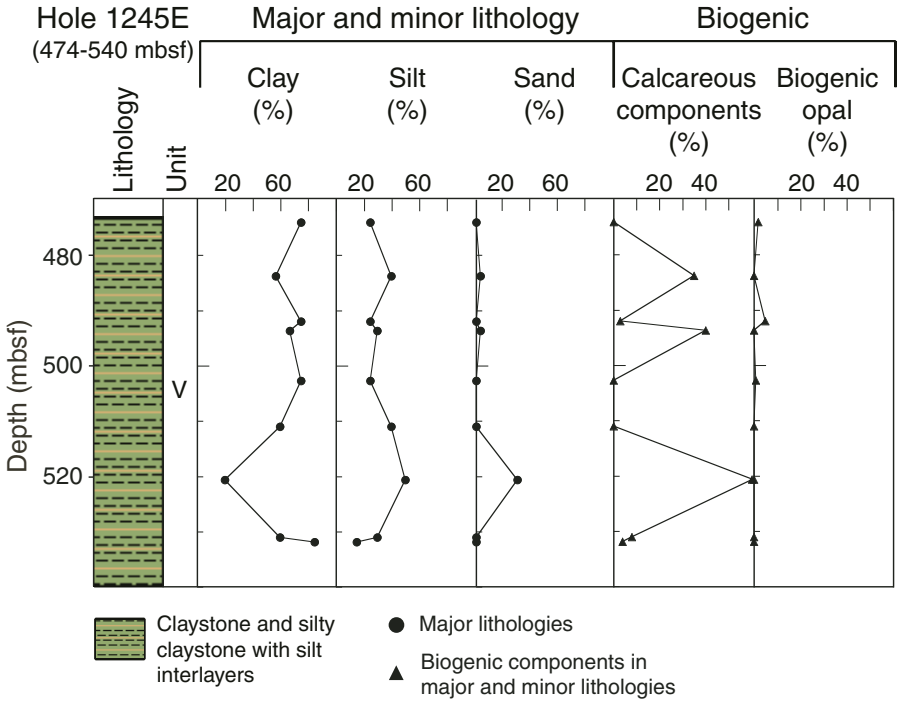

Figure F3. Seismic reflection profile from west (left) to east (right) at Site 1245. Lithostratigraphic units and subunits are shown as well as the location of Site 1245. Lithostratigraphic Unit V is located below 419 mbsf and, thus, is not represented on this figure. LWD density and electrical ring resistivity data are included. Seismic Horizons Y and A are also shown. SF = seafloor, BSR = bottom-simulating reflector.

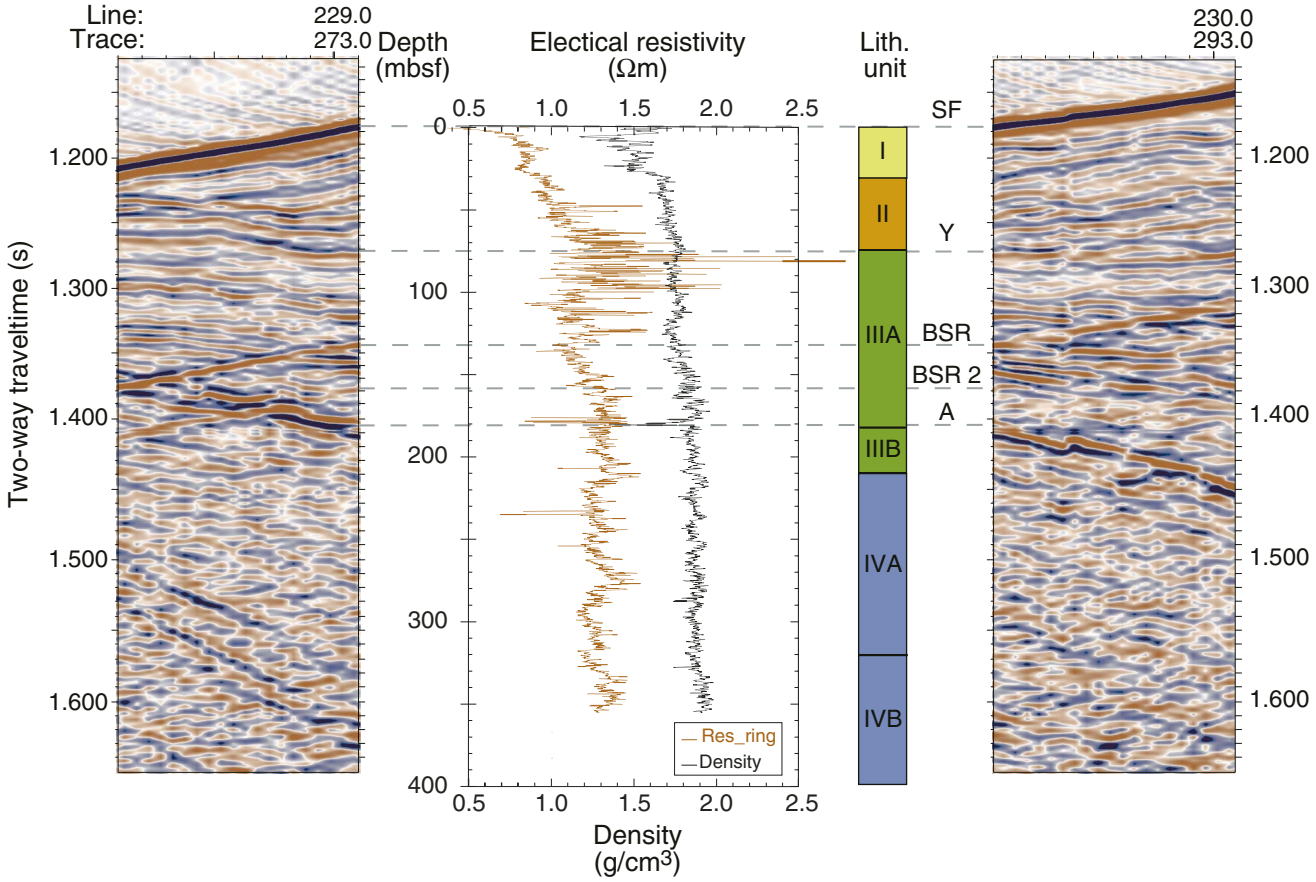

Figure F4. Abundance of clay, silt, sand, calcareous components, and biogenic opal in the major and minor lithologies (deep section) determined from smear slide descriptions of Holes 1245B and 1245E.

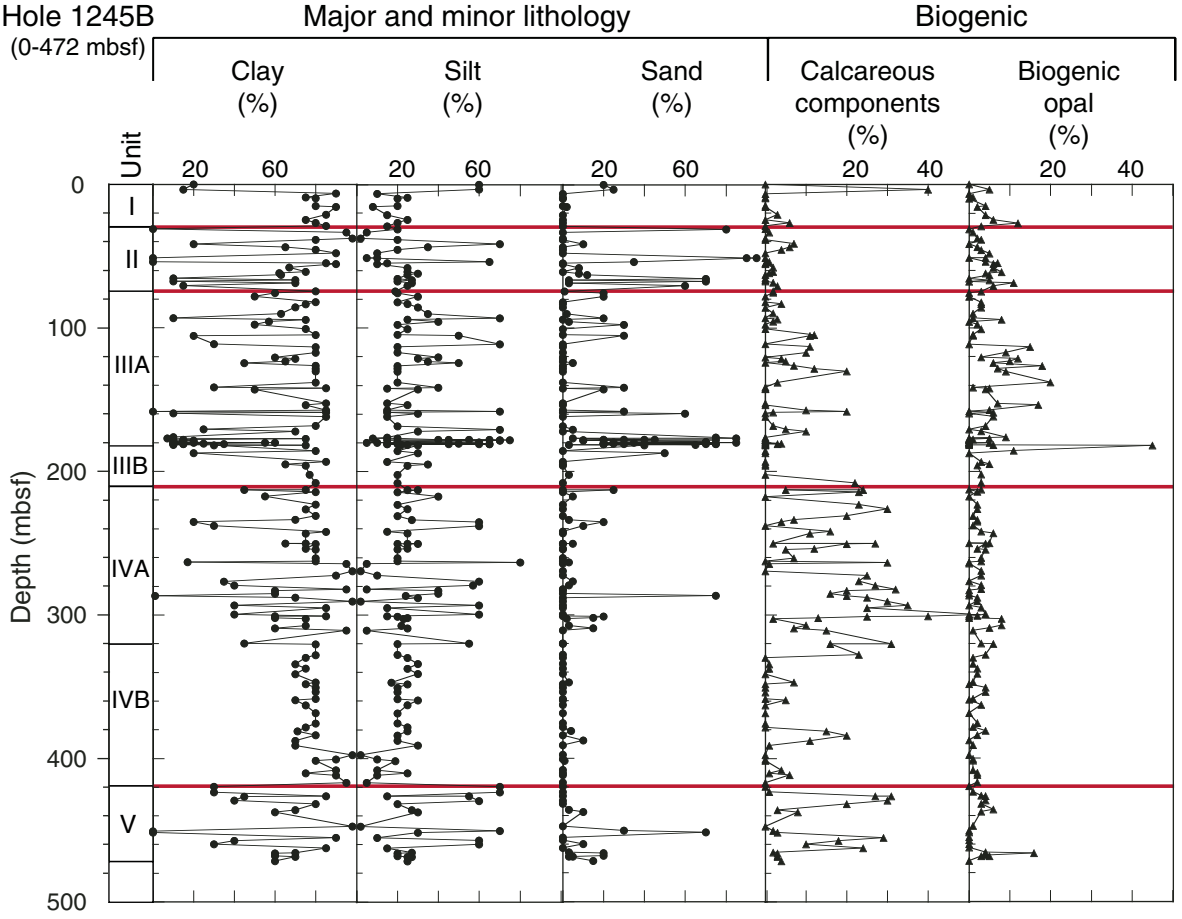

Figure F5. Close-up photograph of a carbonate nodule in lithostratigraphic Unit I (interval 204-1245B-2H-4, 35–42 cm [~14.35 mbsf]).

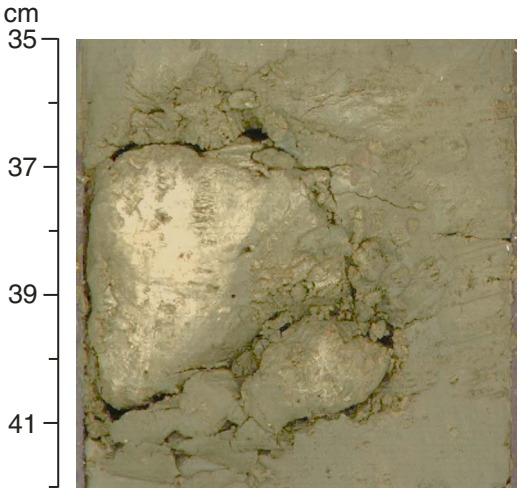

Figure F6. Close-up photograph of a turbidite in lithostratigraphic Unit II (interval 204-1245B-8H-7, 42–50 cm [75.79 mbsf]).

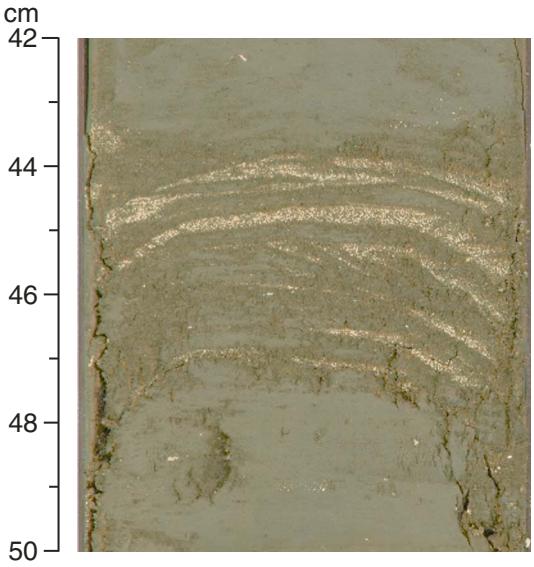

Figure F7. A. Abundance of glauconite estimated from smear slides taken from Hole 1245B. **B.** Calcium carbonate content in Holes 1245B and 1245E determined by coulometry (see **"Organic Geochemistry,"** p. 16, in the "Explanatory Notes" chapter).

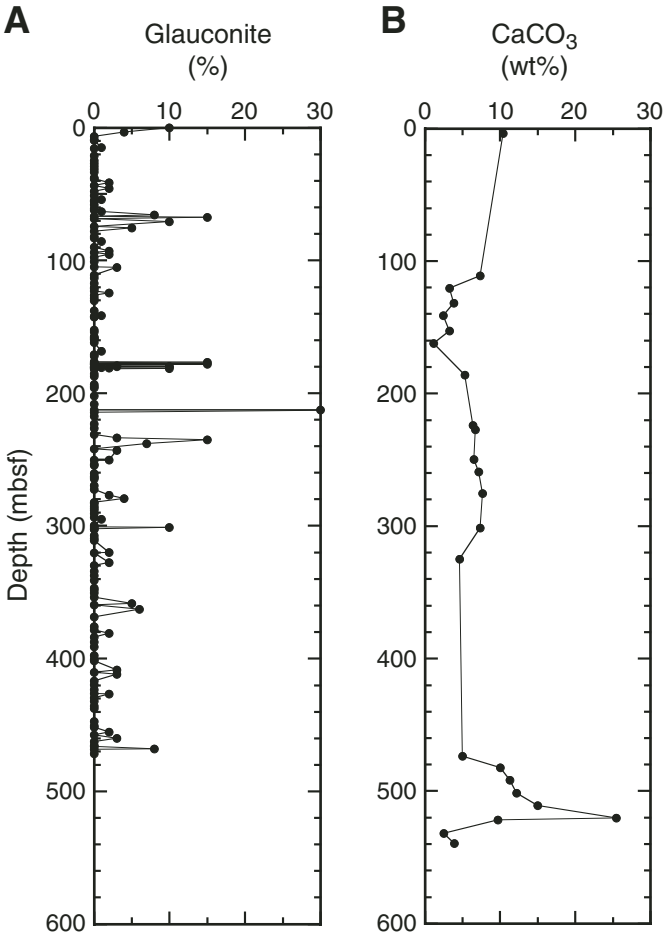

Figure F8. Photomicrograph showing glauconite grains in lithostratigraphic Unit II (Sample **204-1245B-8H-1, 112 cm** [67.2 mbsf]) (magnification = 200×).

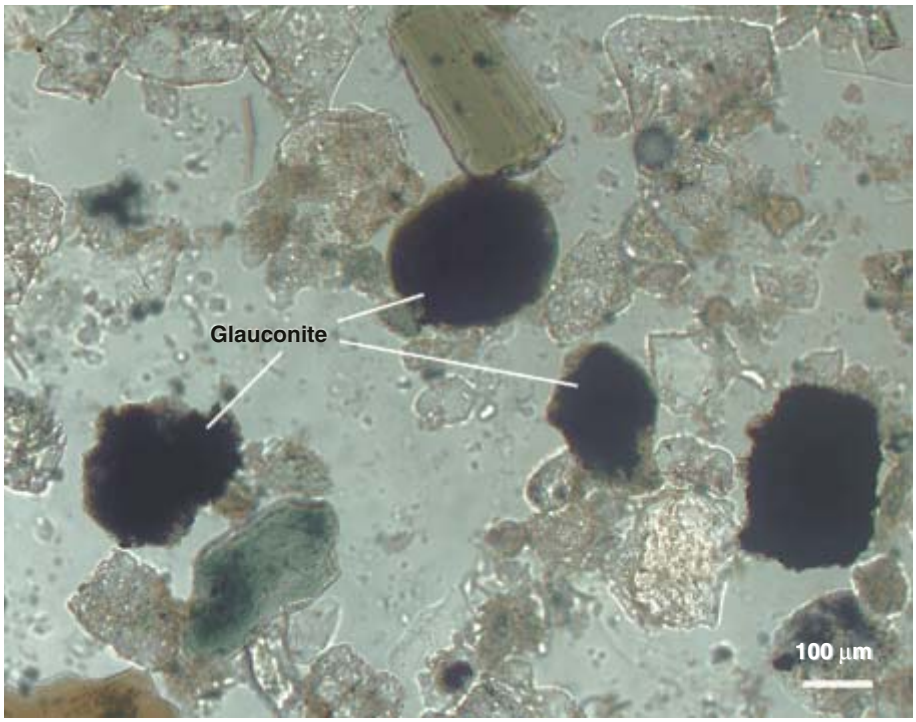

Figure F9. Close-up photograph of a turbidite from lithostratigraphic Subunit IIIA (interval 204-1245B-12H-3, 6–25 cm [~107.5 mbsf]).

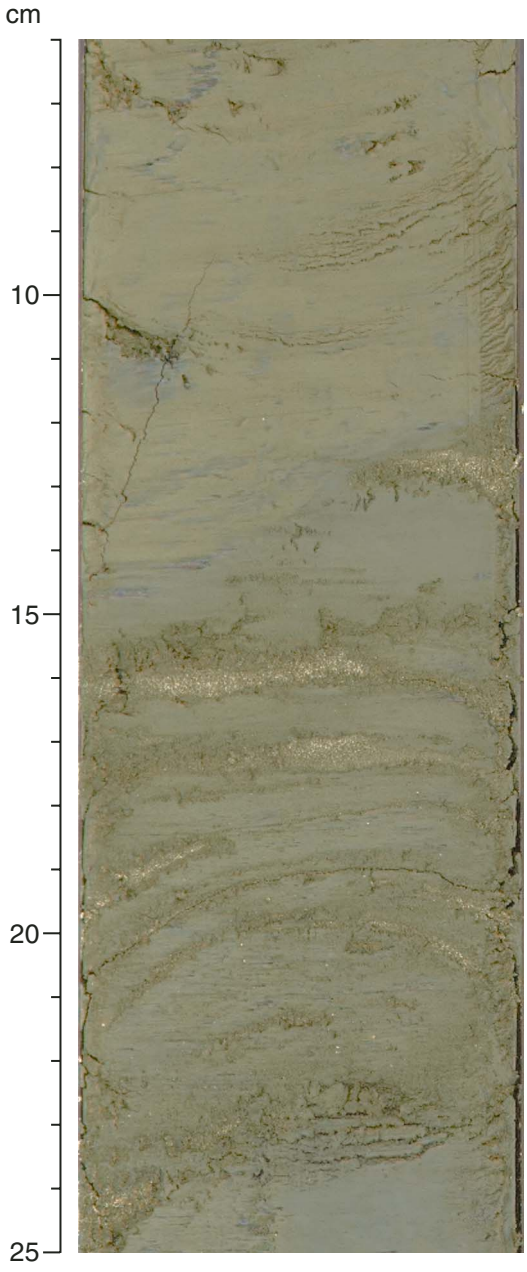

Figure F10. Close-up photograph of a mousselike texture above the BSR at 131 mbsf in lithostratigraphic Subunit IIIB (interval 204-1245B-11H-1, 57–75 cm [~95.65 mbsf]).

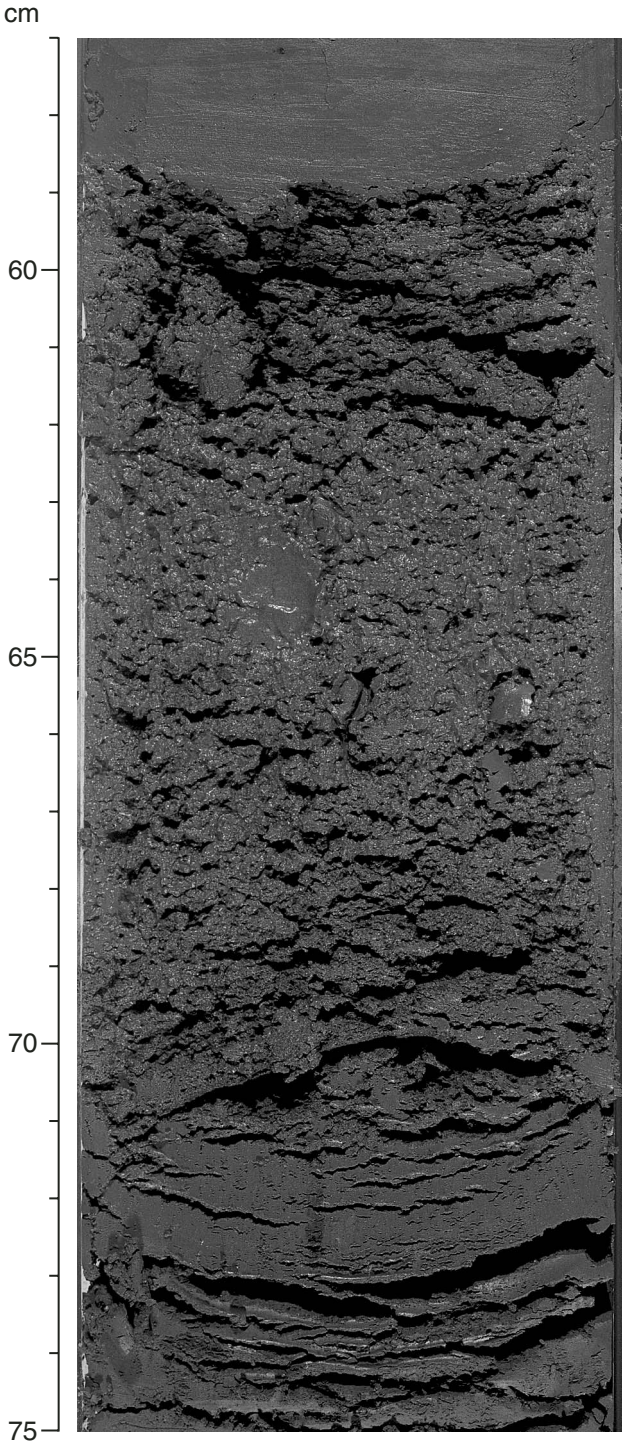

Figure F11. Photomicrograph of diatom-rich clay, which is typical of the lithostratigraphic Subunit IIIA (Sample **204-1245B-14H-3, 80 cm** [139 mbsf]) (200×).

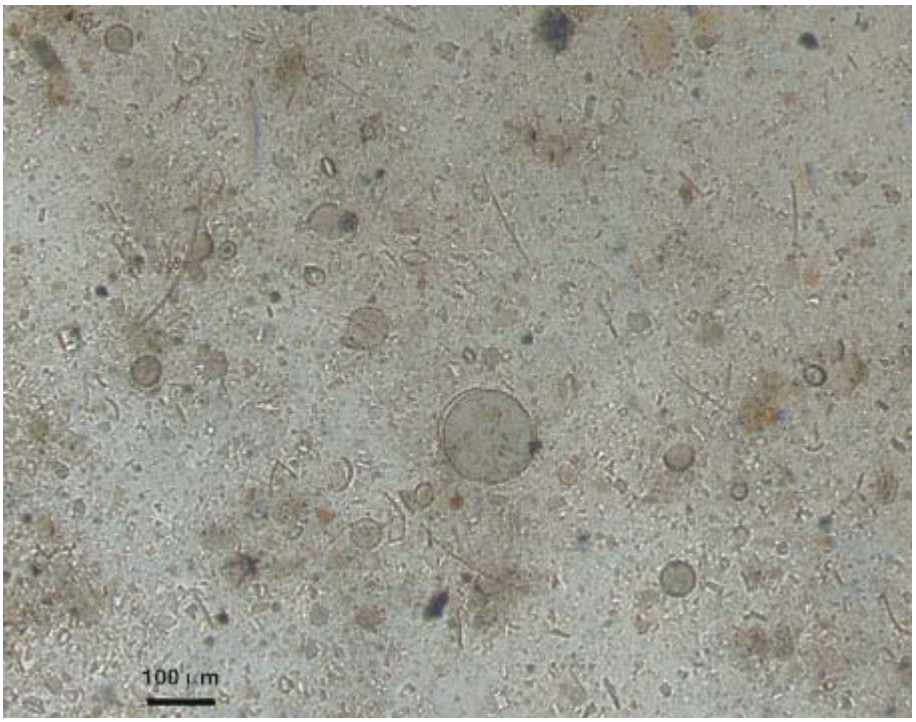

Figure F12. Close-up photograph of volcanic glass–rich sediment and ash sequences in lithostratigraphic Subunit IIIA. **A.** Volcanic glass–rich sediment and ash sequence (interval 204-1245B-21X-2, 84–103 cm [~178 mbsf]). **B.** Graded volcanic glass–rich sand (interval 204-1245B-21X-3, 104–113 cm [~180 mbsf]). **C.** Volcanic glass–rich sediment and ash sequence (interval 204-1245B-21X-4, 13–59 cm [~181 mbsf]).

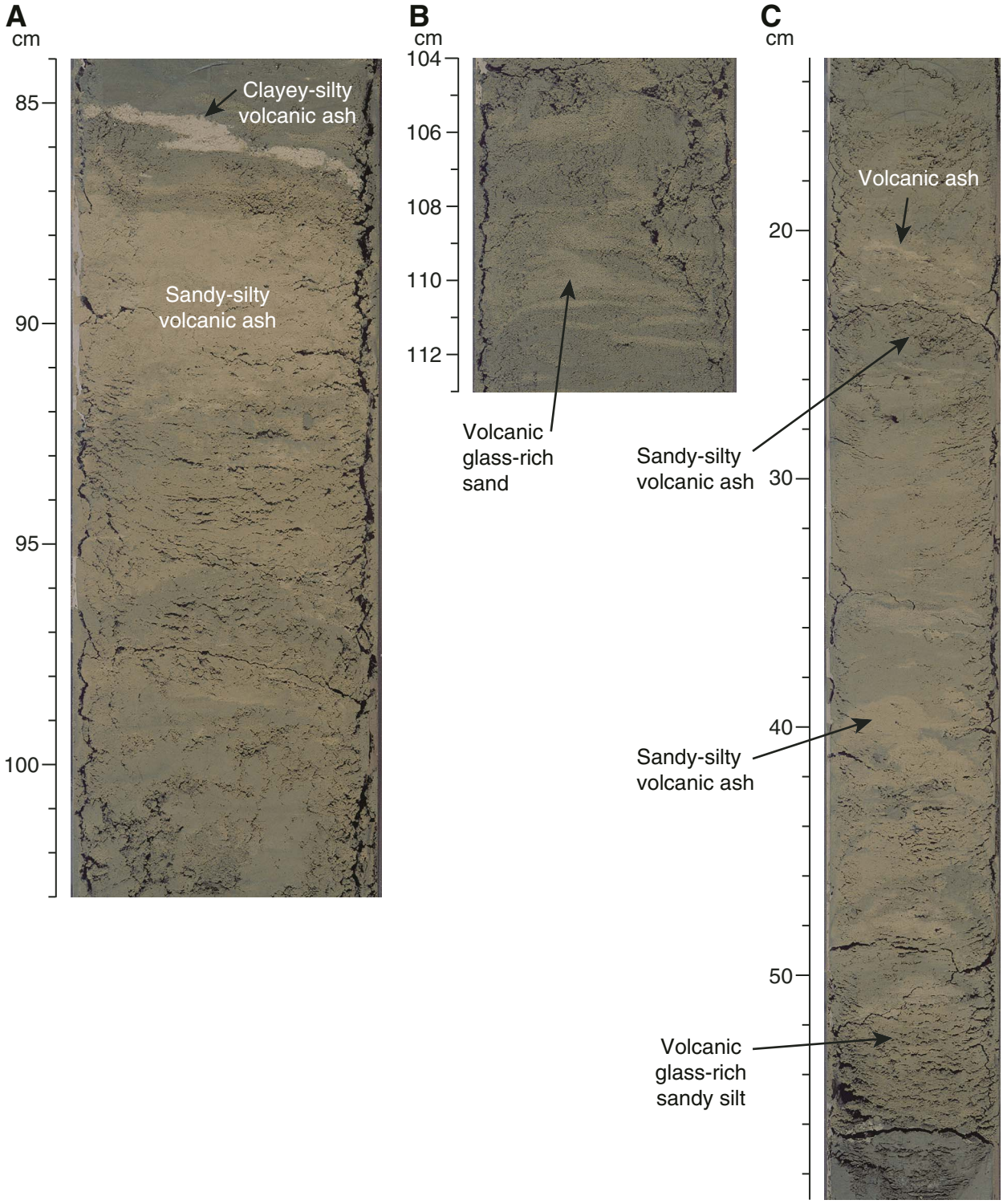

Figure F13. A summary of the volcanic glass–rich sediment and ash sequences of Horizon A in Hole 1245B. Note the high MS values for the sandy and silty layers and the low MS values and lighter color reflectance (lower b*) values for the more pure ash occurrences. LWD = logging while drilling.

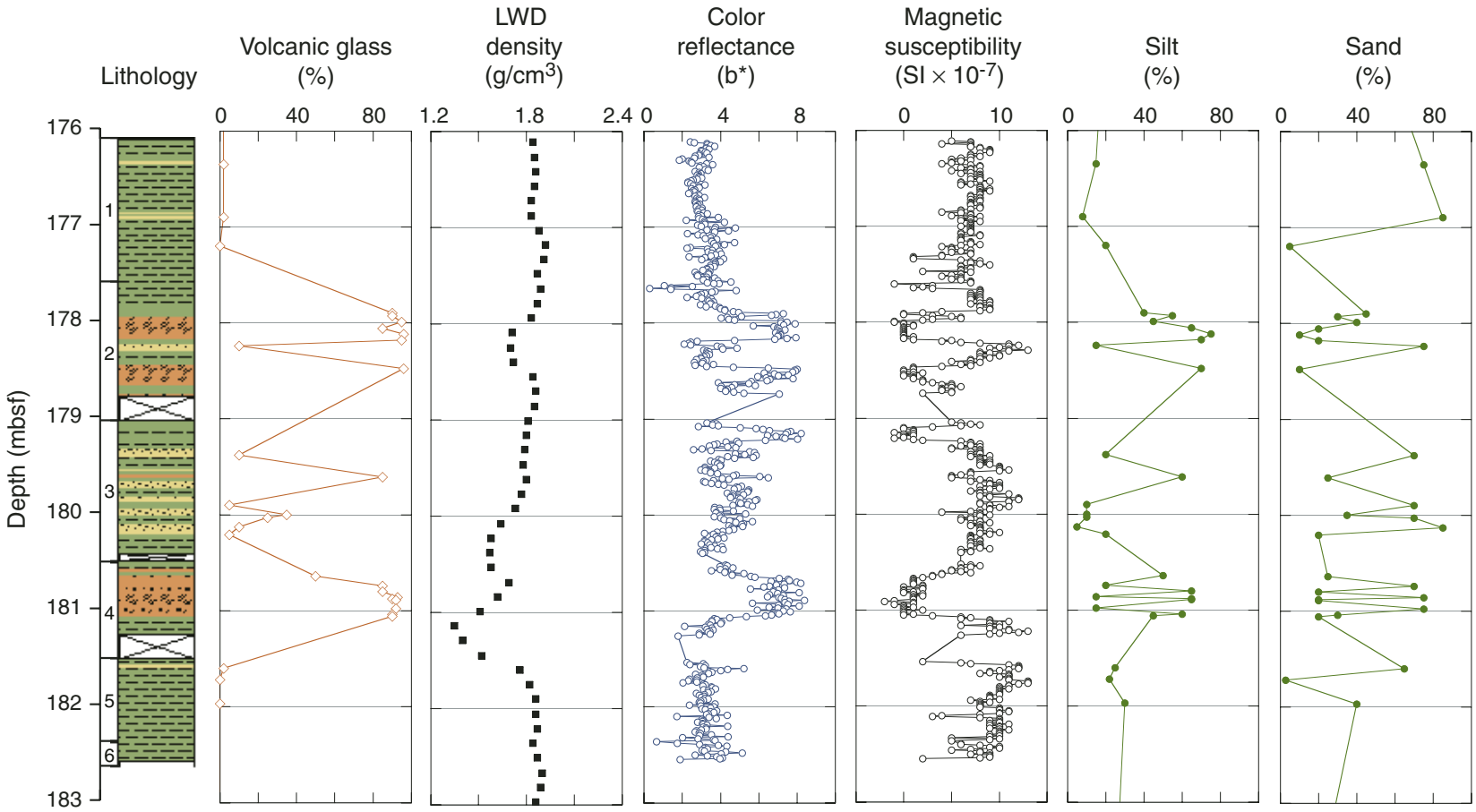

Figure F14. Photomicrograph of sand-sized volcanic glass within the Horizon A volcanic glass–rich sediment and ash sequence in lithostratigraphic Subunit IIIA (Sample **204-1245B-21X-4, 36 cm** [180.86 mbsf]) (200×).

Figure F15. XRD record from a volcanic glass sample in lithostratigraphic Subunit IIIA (Sample 204-1245B-21X-4, 35–36 cm [180.85 mbsf]) (200×).

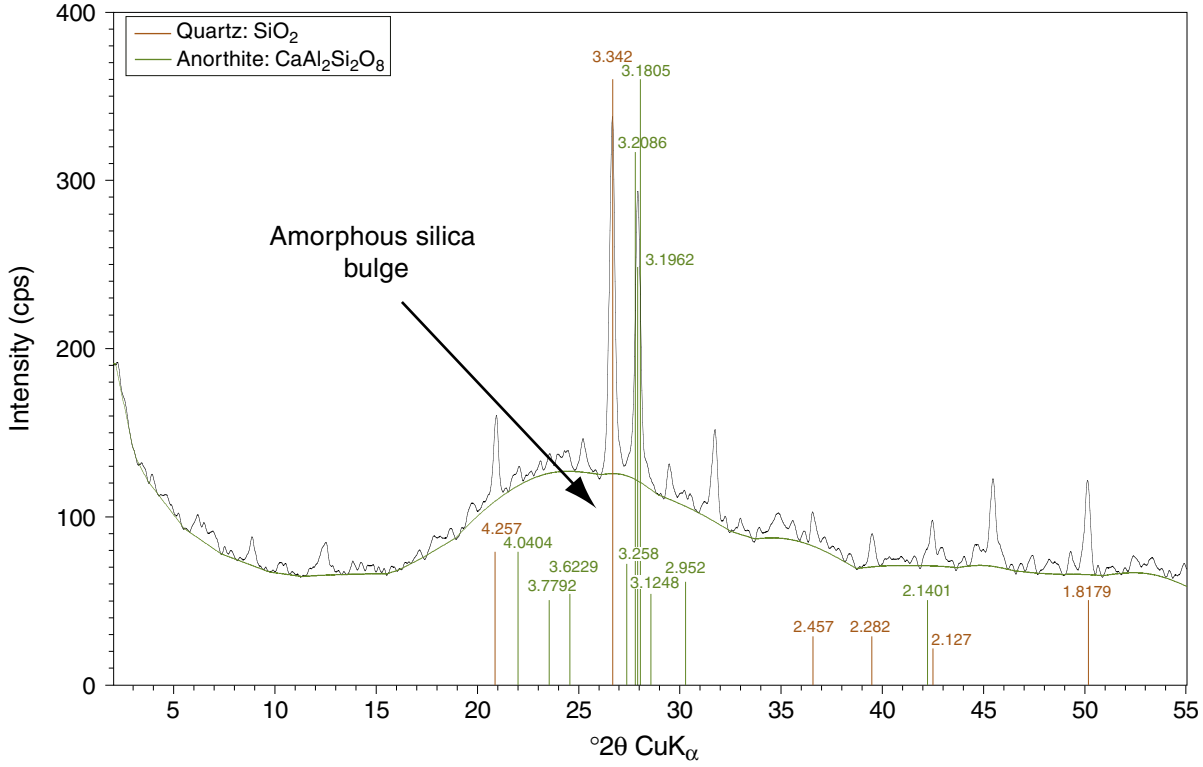

Figure F16. Close-up photograph of nannofossil-rich claystone with abundant bioturbation, typical of lithostratigraphic Subunit IVA (interval 204-1245B-34X-5, 63–74 cm [299.80 mbsf]).

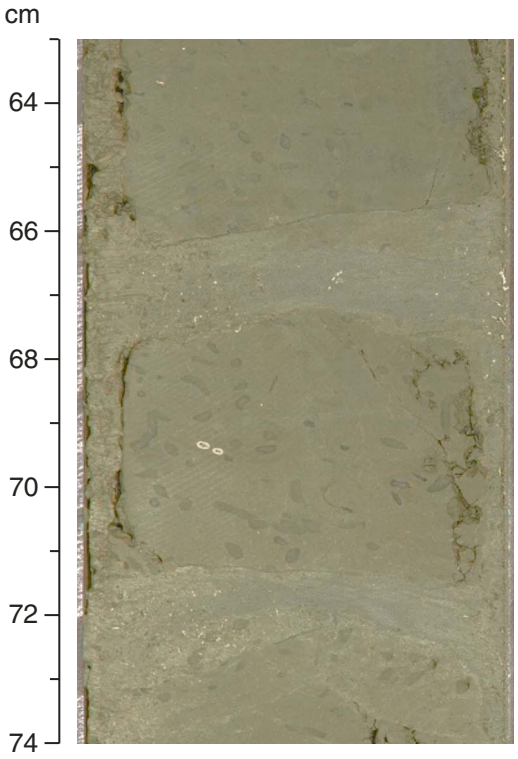

Figure F17. Close-up photograph of claystone with abundant bioturbation below a turbidite with planar laminations from lithostratigraphic Subunit IVB (interval 204-1245B-37X-1, 135–148 cm [~321 mbsf]).

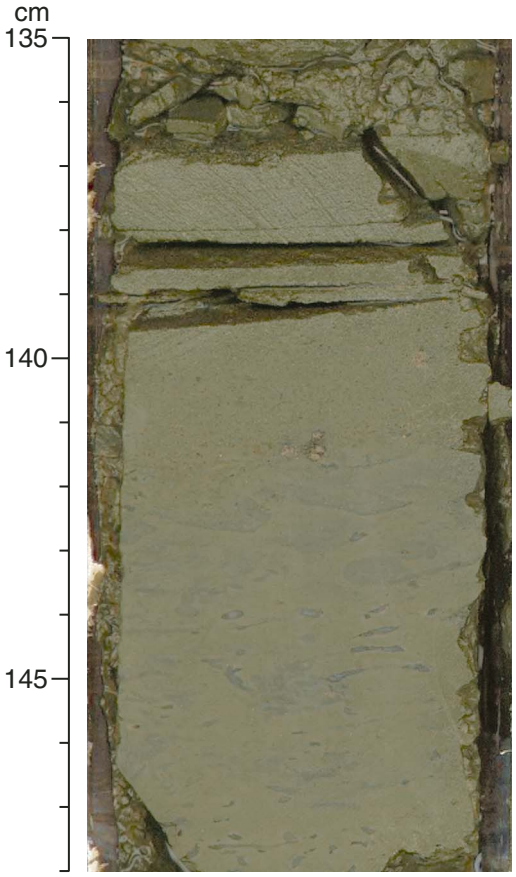

Figure F18. Photomicrograph of a smear slide sample from the nannofossil-rich claystone in the upper part of lithostratigraphic Unit V (Sample **204-1245B-49X-1, 37 cm** [426.27 mbsf]) (1000×; crossed nicols).

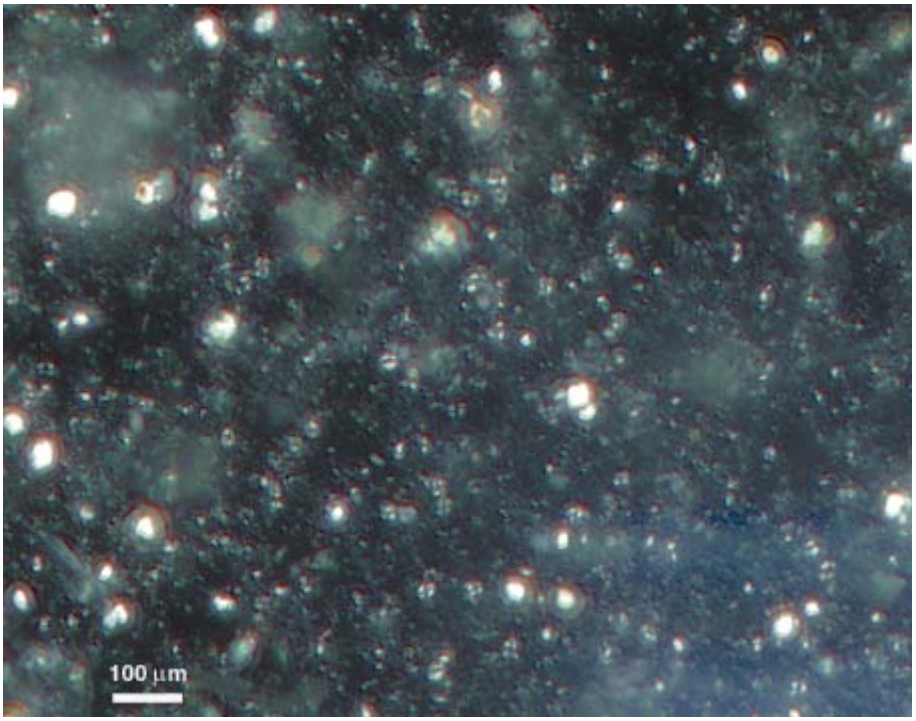

Figure F19. Close-up photographs of lithostratigraphic Unit V. **A.** A thick turbidite (interval 204-1245B-51X-3, 15–30 cm [~448.45 mbsf]). Notice the visible foraminifers near the coarse base of the turbidite, the parallel laminations, and the cross bedding. **B.** Mud clasts within the conglomerate of Unit V (interval 204-1245B-53X-4, 15–27 cm [~468.48 mbsf]).

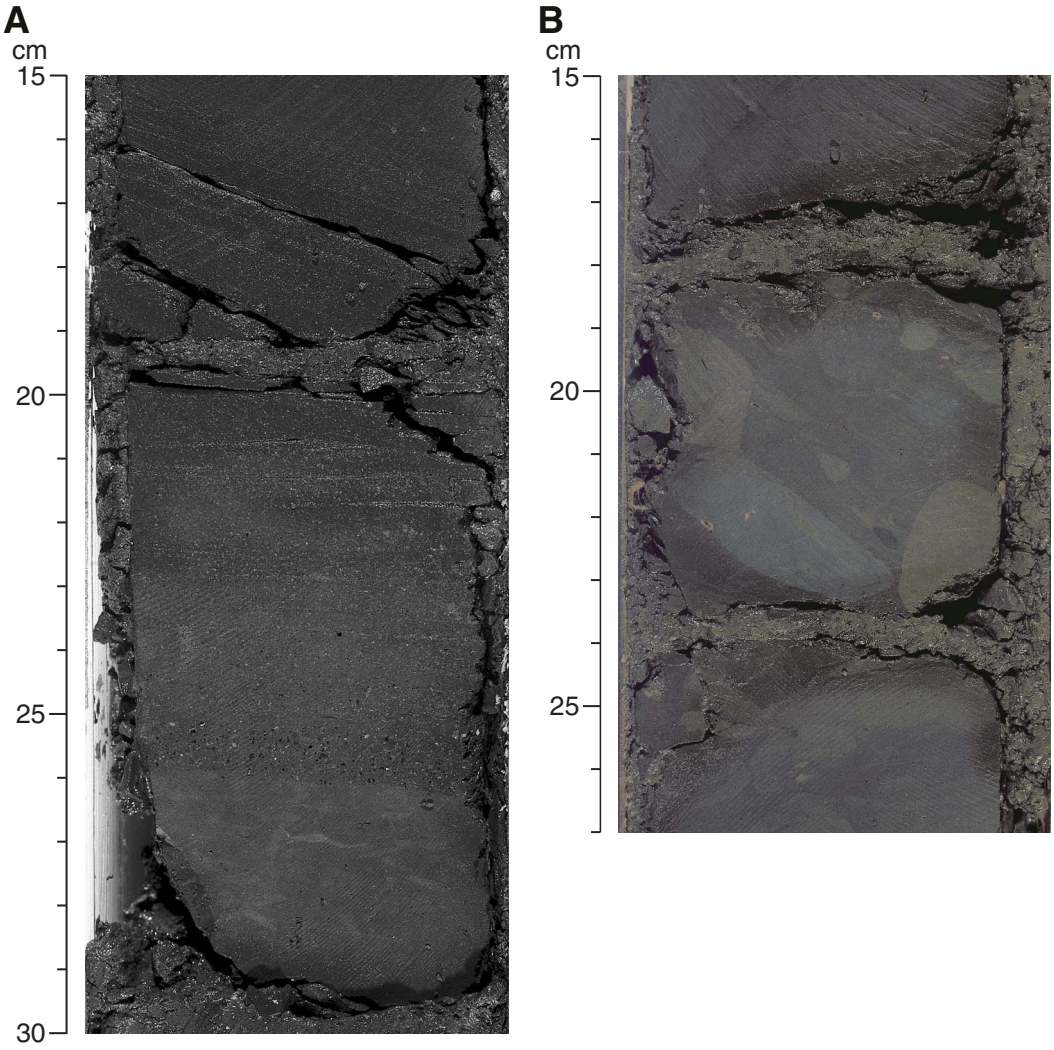

Figure F20. Photomicrograph across the base of a turbidite observed in a thin section from lithostratigraphic Unit V (Sample **204-1245B-51X-3, 24–28 cm** [~448 mbsf]) (25×). Notice the grading, visible by the foraminifers.

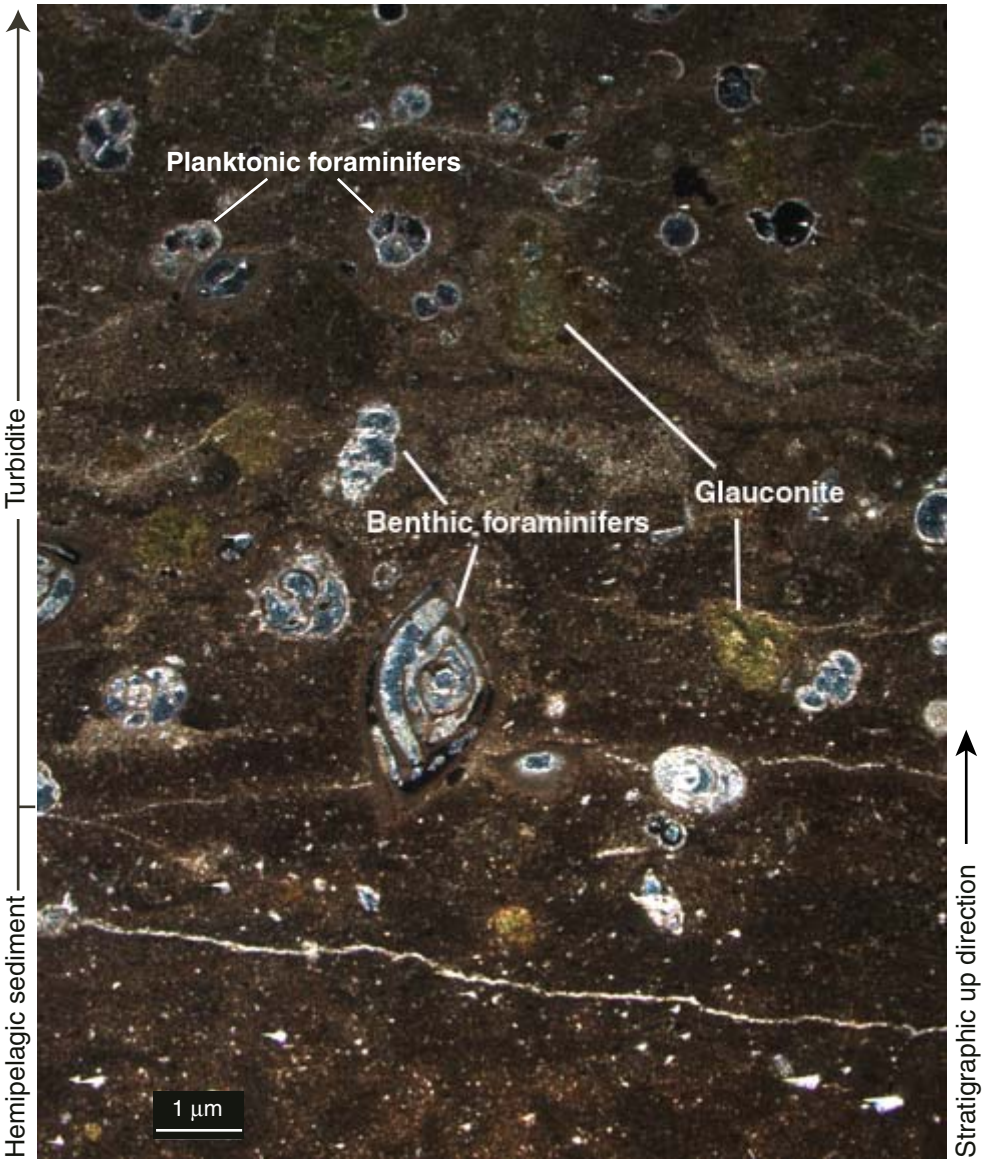

Figure F21. Chart of diatom and nannofossil event marker species in Holes 1245B and 1245E.

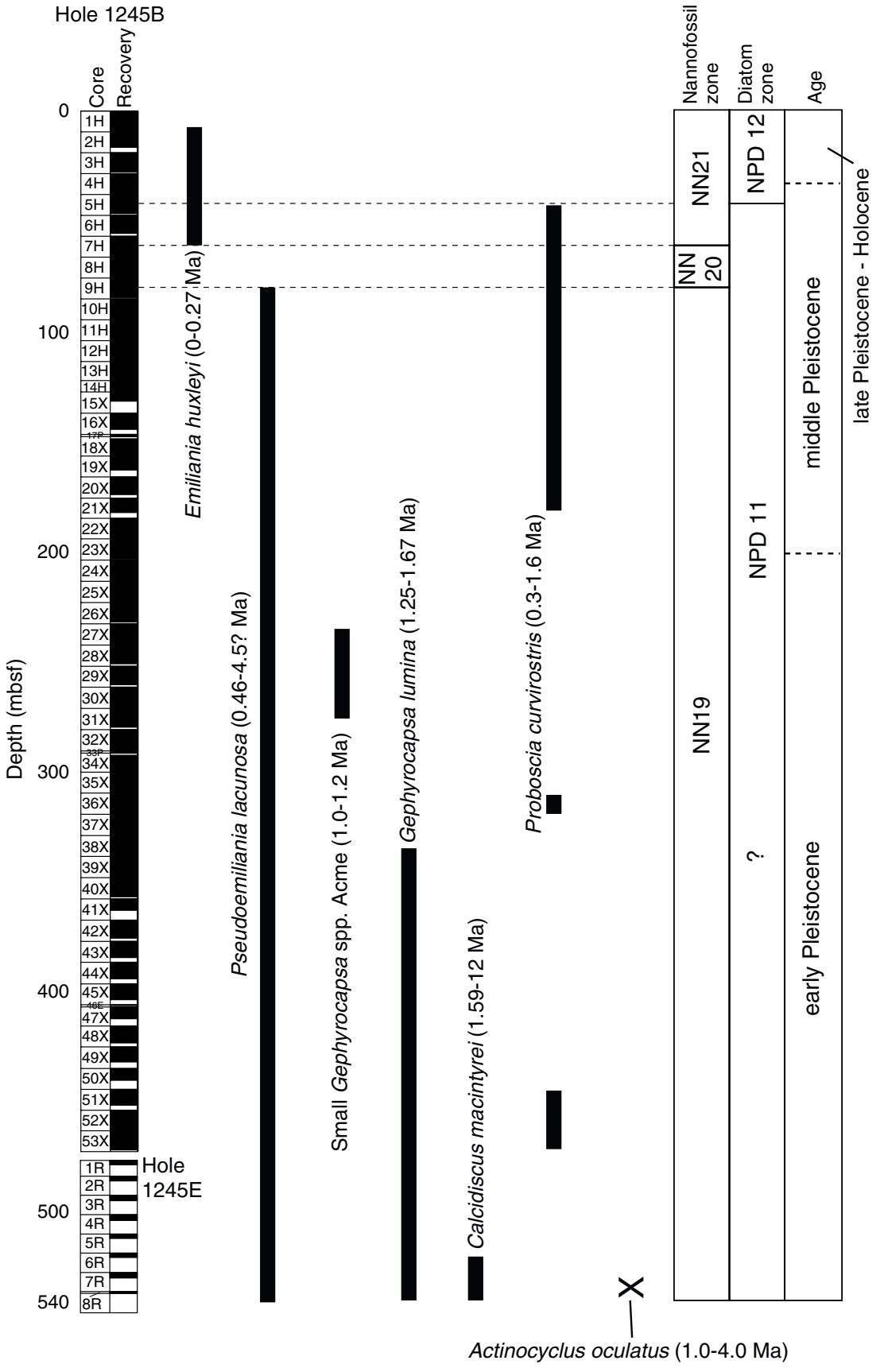

Figure F22. Age-depth plots based on diatom and calcareous nannofossil bioevents for Holes 1245B and 1245E. The detailed age and depth of control points are given in Table T4, p. 105. D = diatom event; N = nannofossil event.

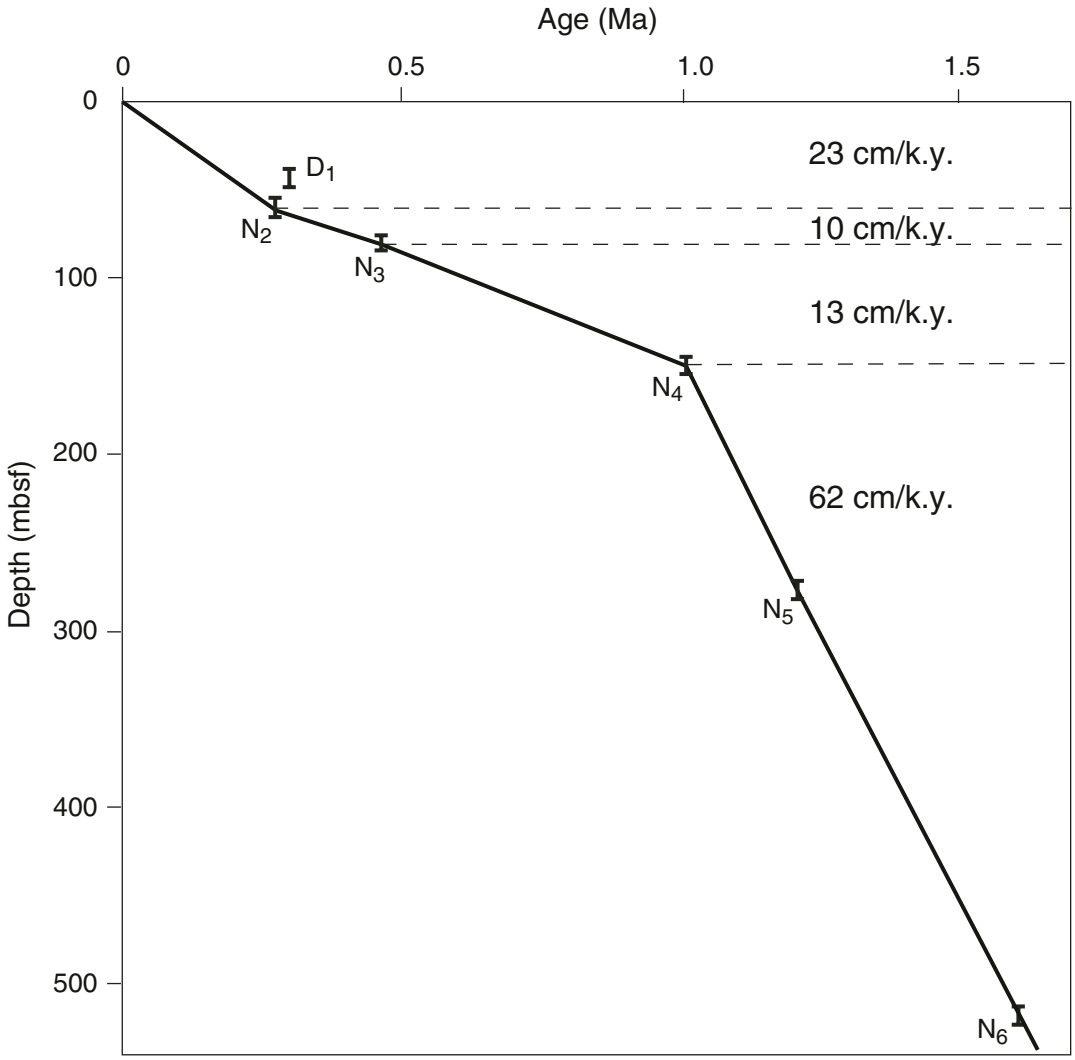

Figure F23. Concentration profiles of various dissolved species in pore waters. DOC = dissolved organic carbon. (Continued on next page.)

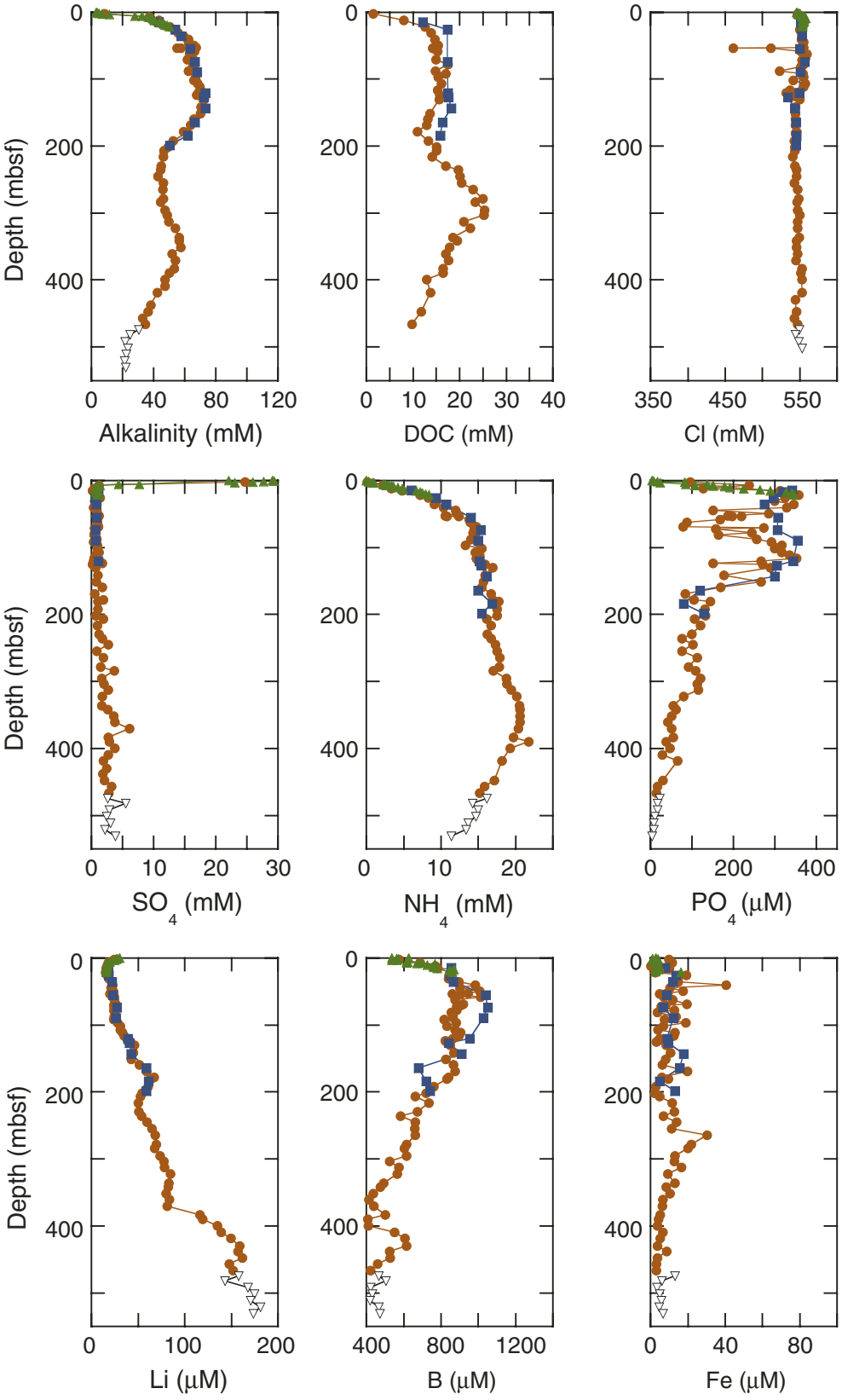

Figure F23 (continued).

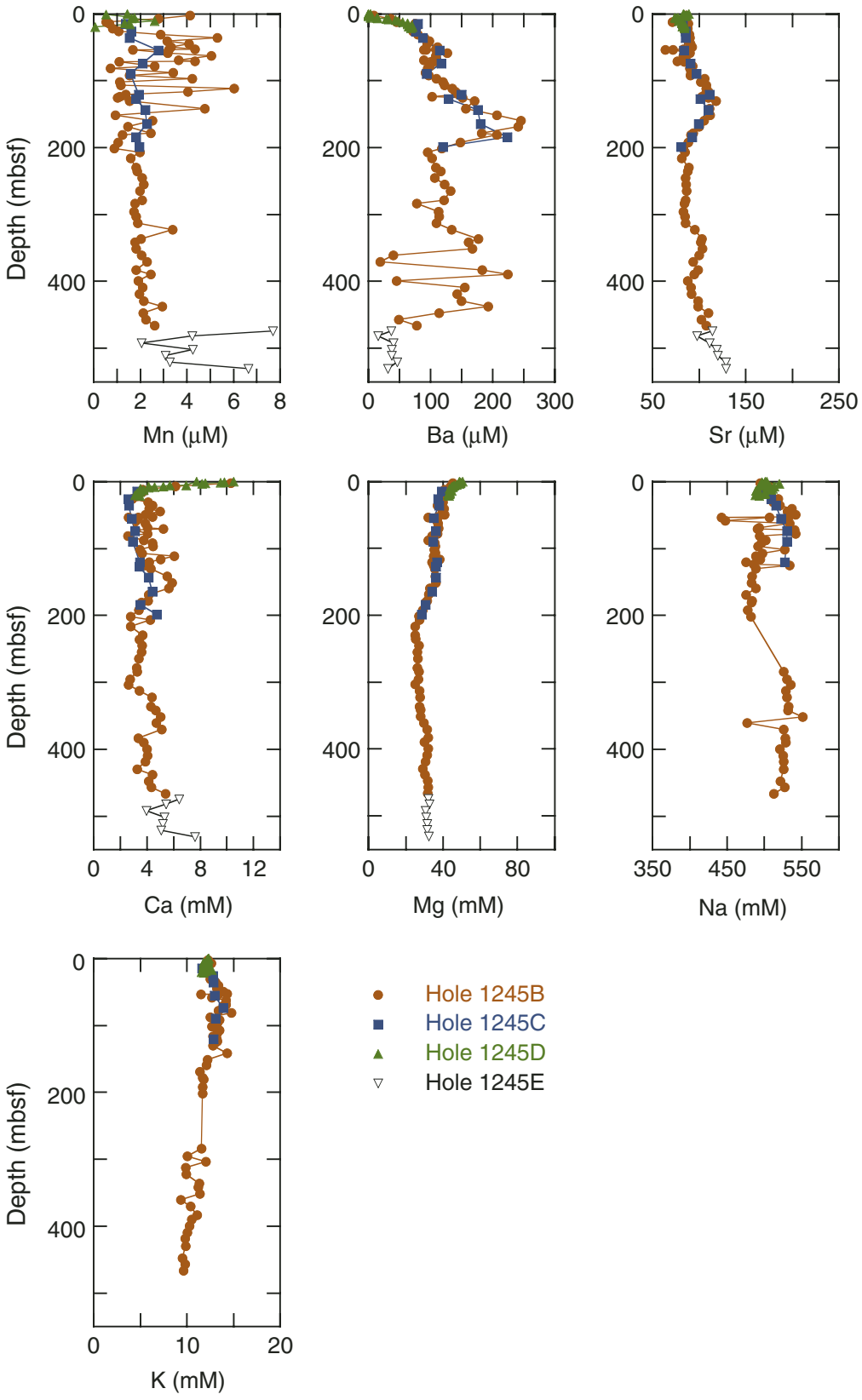

Figure F24. Chloride (Cl^-) concentration profile and estimates of gas hydrate amounts using these chloride data. **A.** Chloride concentration profiles from Holes 1245B, 1245C, and 1245D with the precruise estimate of the depth of the bottom-simulating reflector (BSR). **B.** Interpretation of the location of gas hydrates (red shading) within the GHSZ. Note that the baseline used for this interpretation is established by connecting the highest chloride concentration values within the GHSZ, which presumably represent in situ Cl^- concentration. **C.** Interpretation of the amount of gas hydrate as a percentage of pore space. Note that the sample with the freshest chloride concentration predicts 18% gas hydrate, whereas other occurrences of gas hydrate occupy from 0% to 6% of the pore space.

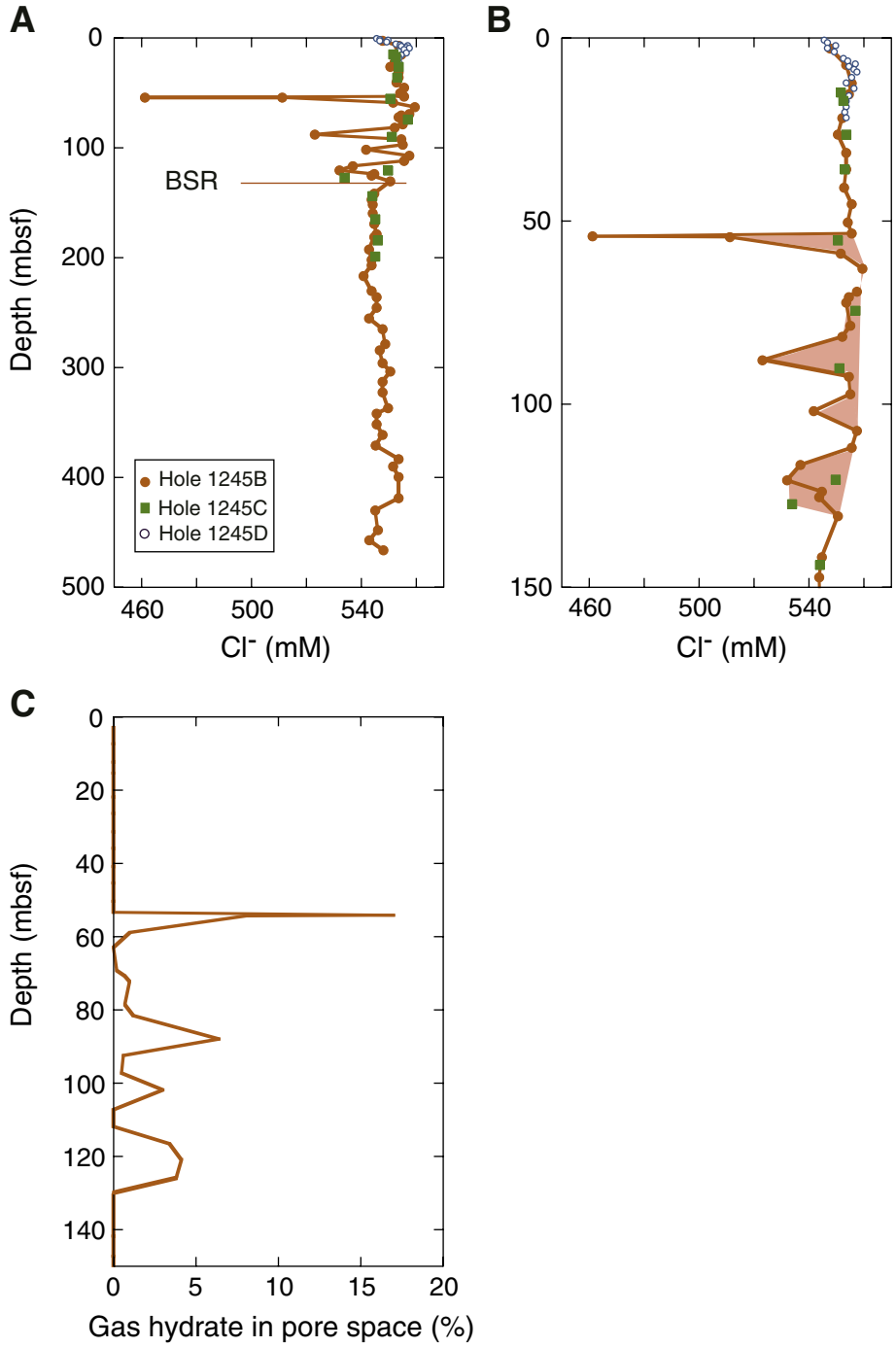

Figure F25. High-resolution analyses of chloride (Cl^-) content in a core containing a discrete 2-cm layer of gas hydrate. **A.** Graph showing the influence of gas hydrate dissociation on the chloride concentration of the pore water. Gas hydrate was observed in Sample 204-1245C-7H-5, 42–44 cm (see arrow), and dissociated to yield freshwater to the sediment. Note that the lowest chloride concentration (73 mM) is present in this sample. As the distance from the gas hydrate increases, so does interstitial chloride concentration. **B.** Temperature measurements obtained with the IR camera, showing a well-defined temperature anomaly corresponding to a discrete hydrate layer subsequently observed in the core. The differences in depth between the anomaly observed in the catwalk (minimum temperature at 54.0 mbsf) and the presence of gas hydrate (53.22 mbsf) reflects the differences in curatorial depth before and after the core was cut into sections. Matching the depths before and after cutting the core is particularly challenging when dealing with gas-saturated cores, where expansion in the liner results in rapid formation of voids. However, within this section of the core, there is only one distinct hydrate layer; thus, we are confident that the temperature anomaly measured on the catwalk at 54 mbsf corresponds to dissociation of the hydrate layer identified in the core at 53.22 mbsf.

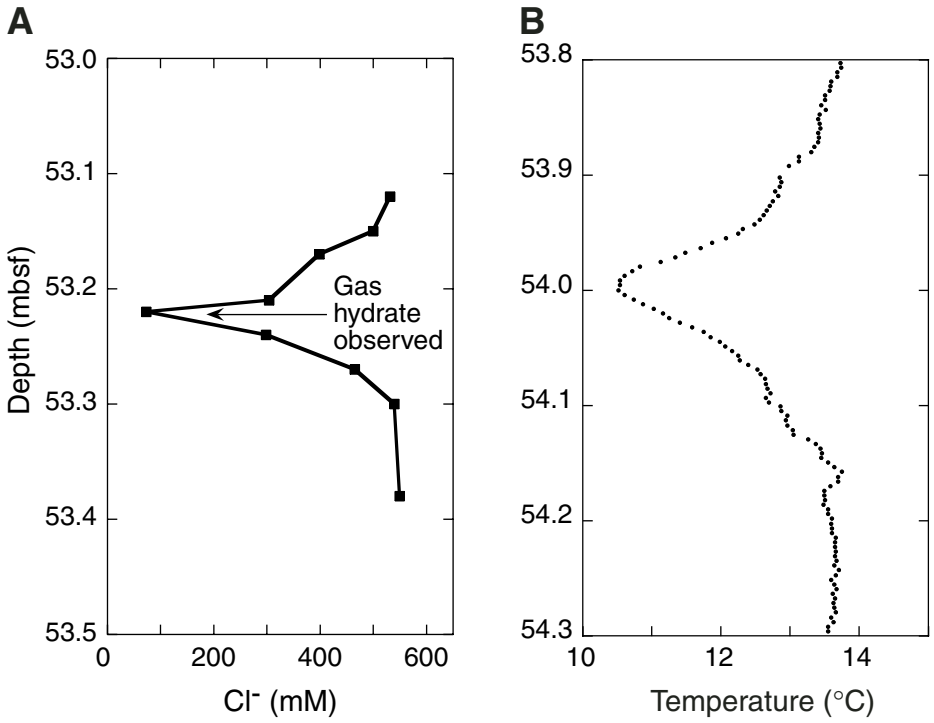

Figure F26. Sulfate (SO_4^{2-}) and methane (CH_4) concentration profiles at Site 1245. Sulfate concentration data (solid circles) were measured in Hole 1245D and show a nonlinear profile. Methane concentration data (open squares) are from headspace gas measurements in Hole 1245B. Using both profiles, the sulfate/methane interface (SMI) is present at ~7 mbsf.

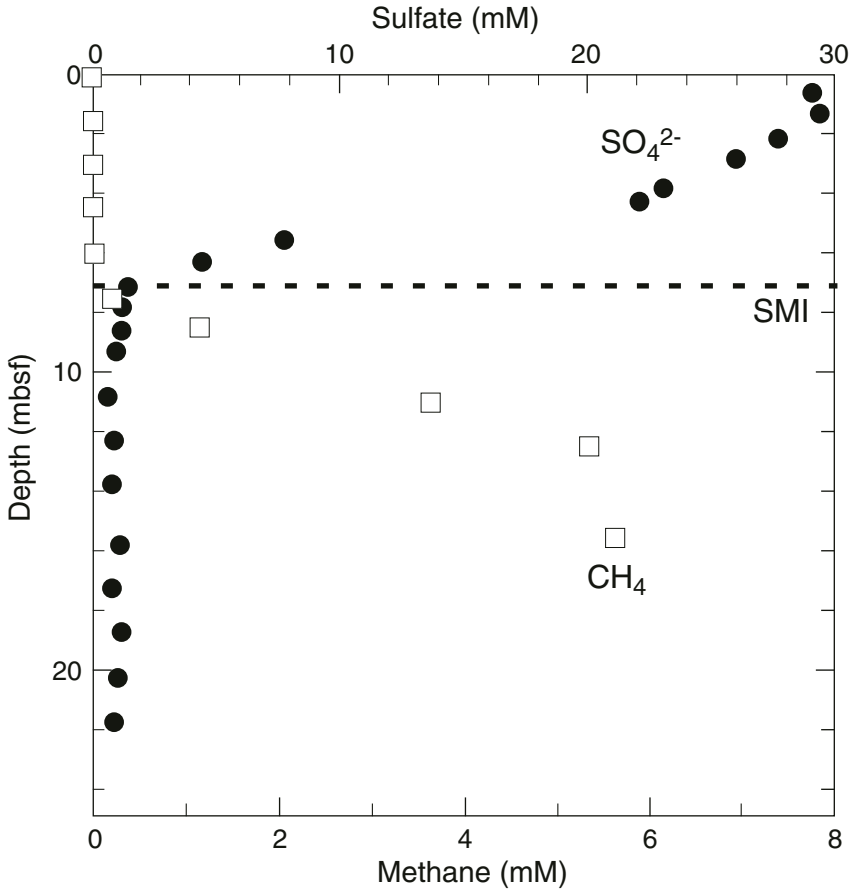

Figure F27. A zone of authigenic carbonate formation from 190 to 310 mbsf (green shading) is inferred from the downhole distribution of alkalinity, calcium, magnesium, and strontium. Sediments within this zone are also characterized by an increase of biogenic $CaCO_3$.

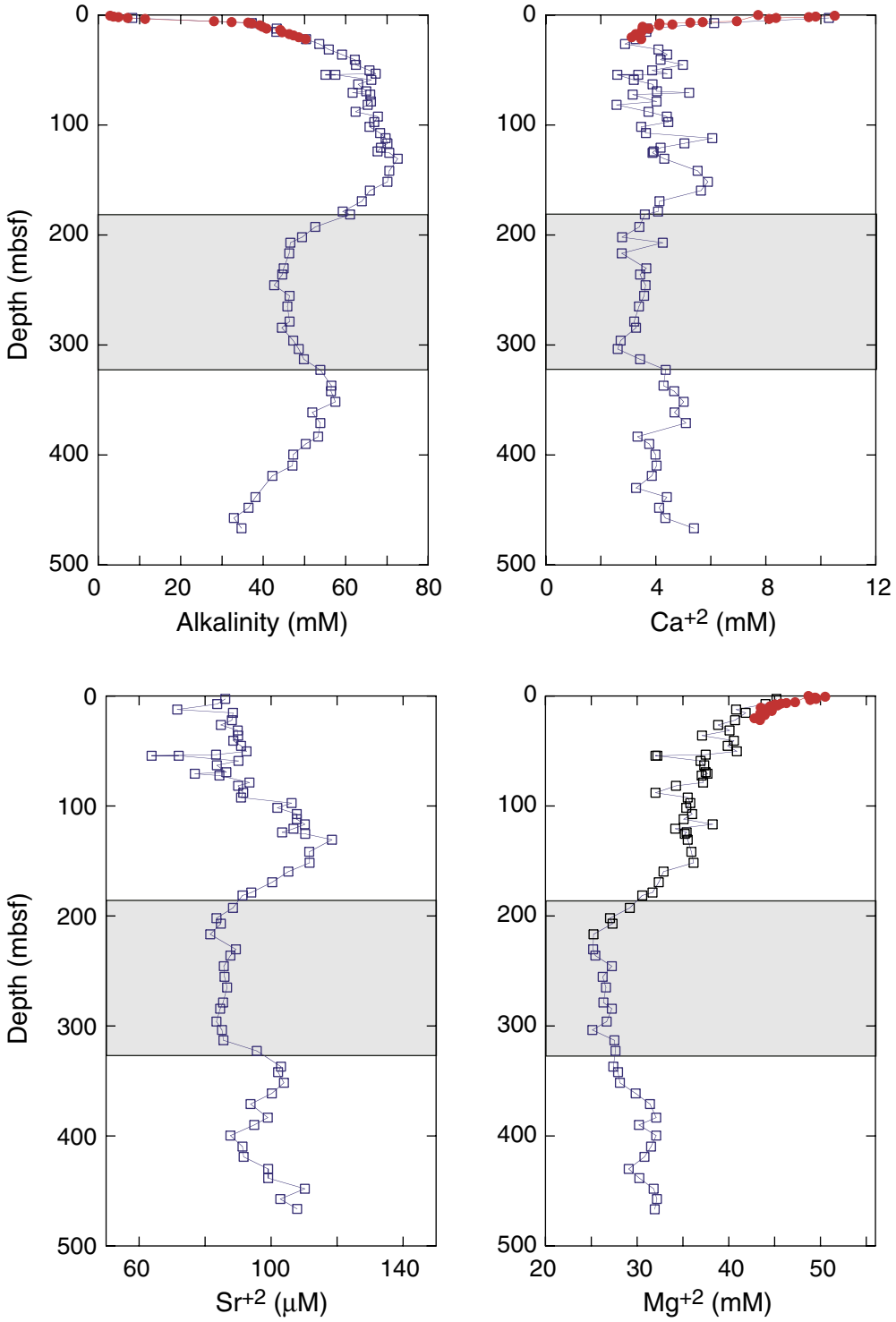

Figure F28. Interstitial lithium (Li^+) concentration data from Site 1245 shown with the stratigraphic location of Horizon A and the boundary between lithostratigraphic Units III and IV (see **"Lithostratigraphy,"** p. 3). At Horizon A (180 mbsf), there is a localized increase of lithium, which perhaps represents fluid movement through this zone. Maximum concentration of lithium are present at the boundary between lithostratigraphic Units III and IV (420 mbsf), which may represent another fluid conduit.

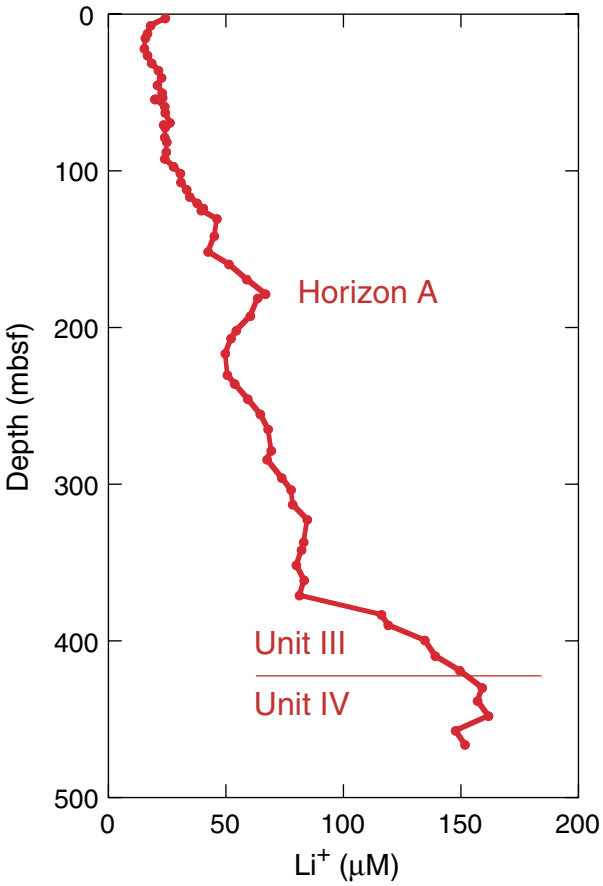

Figure F29. Concentrations of C_1, C_2, and C_3 from the headspace method vs. depth for Hole 1245B.

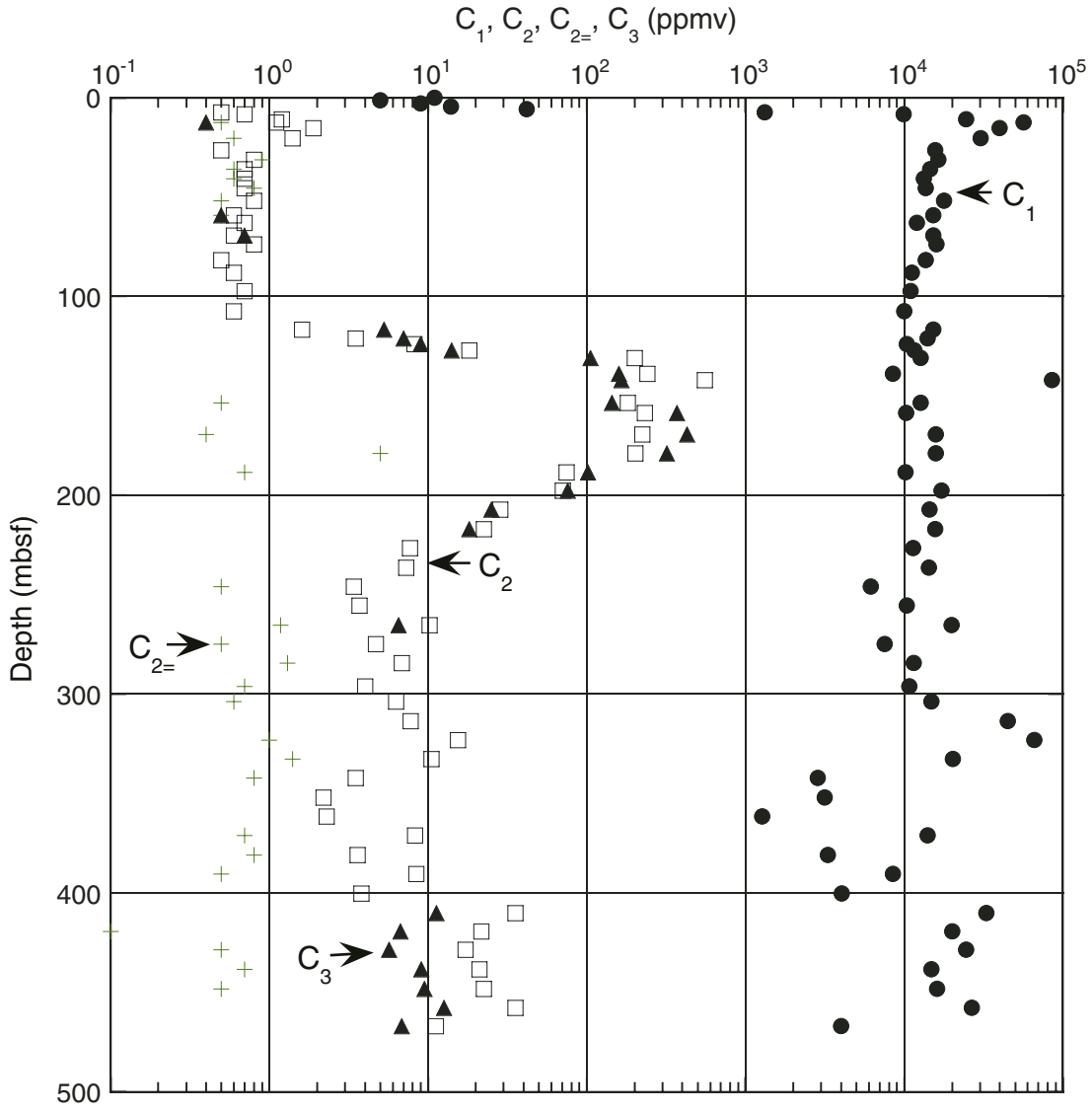

Figure F30. Dissolved residual methane (CH_4) and sulfate (SO_4^{2-}) in pore water. Methane concentration increases at the depth where sulfate concentration is depleted. SMI = sulfate/methane interface.

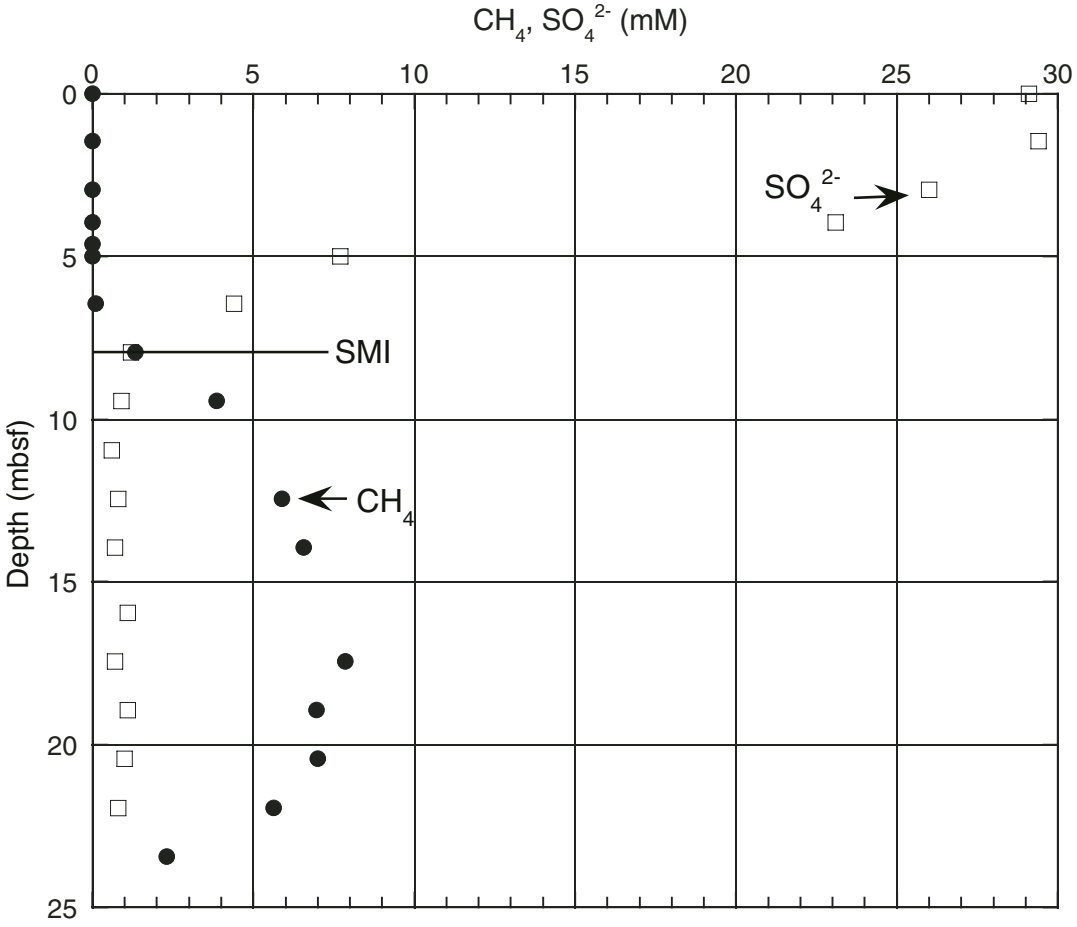

Figure F31. C_1, C_2, C_3, *i*-C_4, *n*-C_4, and *i*-C_5 from void gas vs. depth in Hole 1245B.

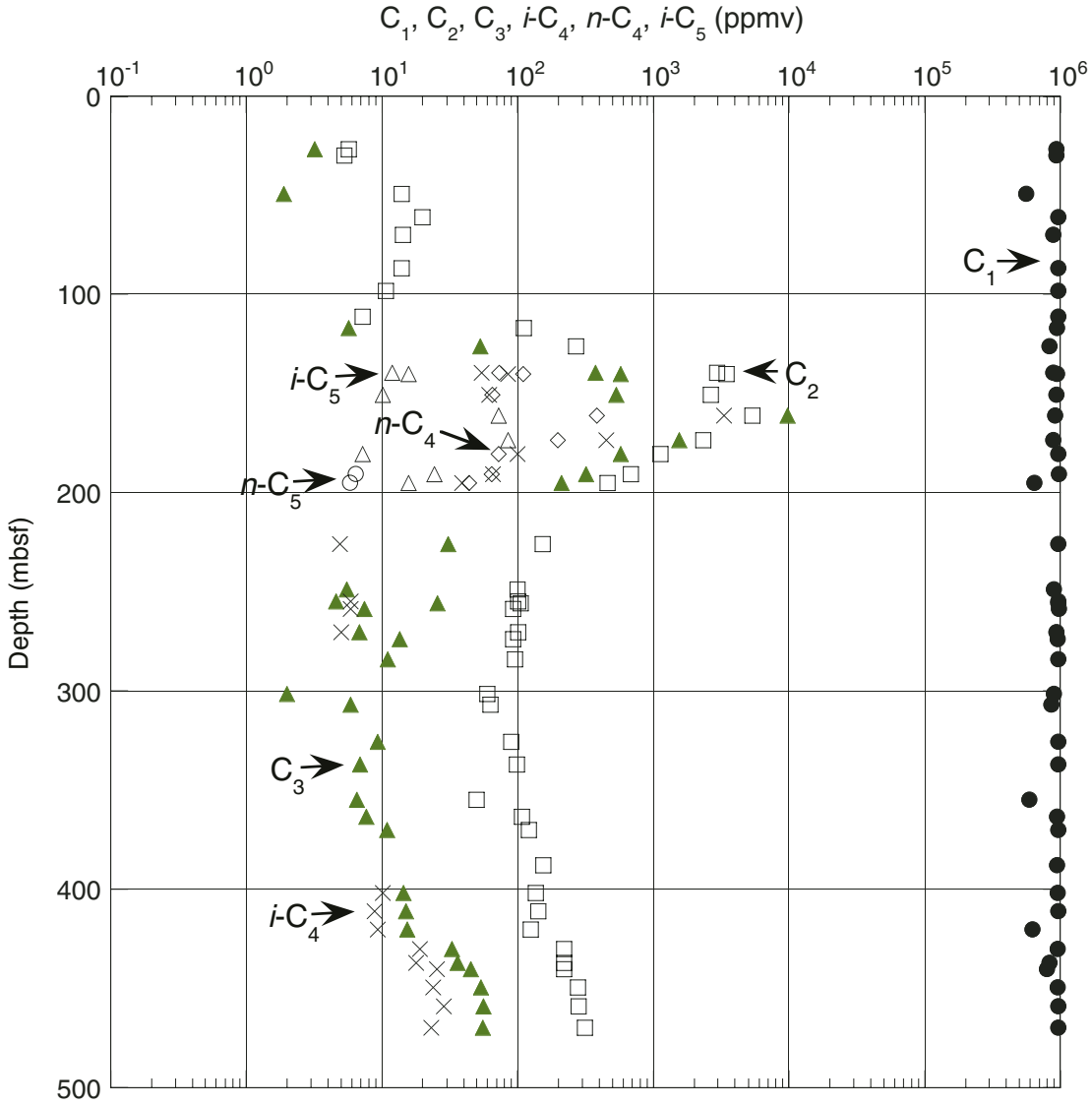

Figure F32. C_1/C_2 ratio vs. depth in Holes 1245B, 1245C, 1245D, and 1245E. HS = headspace, PCS = pressure core sampler, BSR = bottom-simulating reflector, VAC = vacutainer.

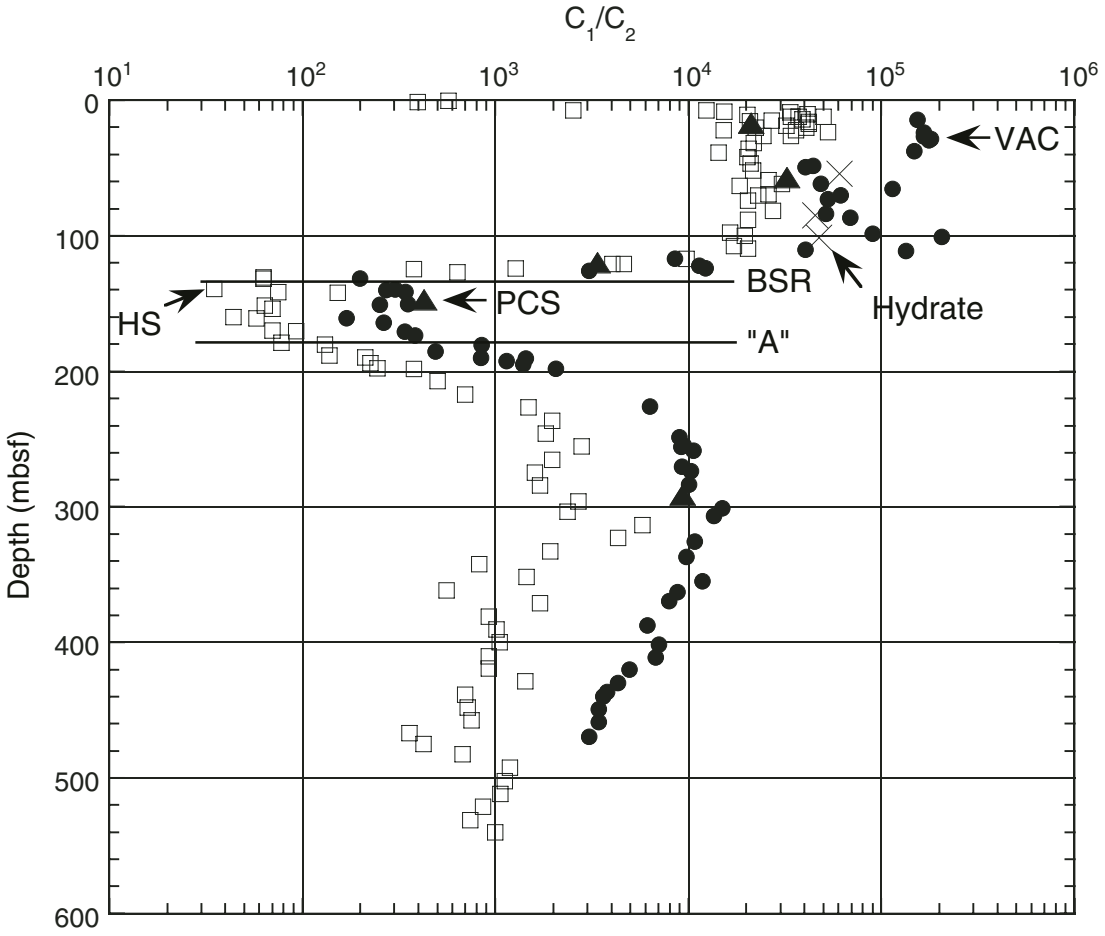

Figure F33. C_1/C_2 ratio vs. temperature in Hole 1245B. HS = headspace, VAC = vacutainer.

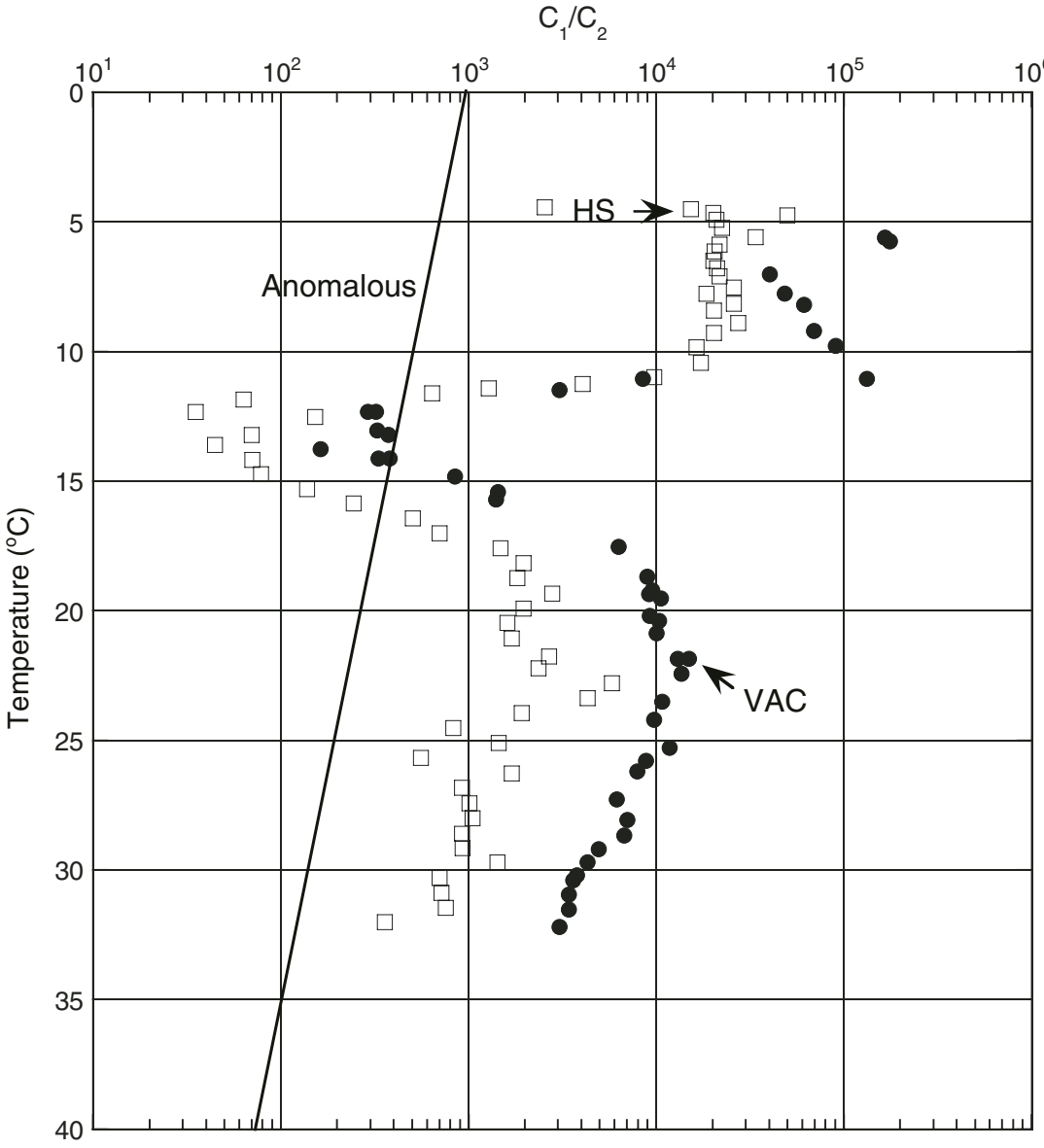

Figure F34. Contents of carbonate carbon (IC), calcium carbonate, organic carbon (OC), total sulfur (TS), and total nitrogen (TN) and C/N ratios in sediments from Holes 1245B and 1245E.

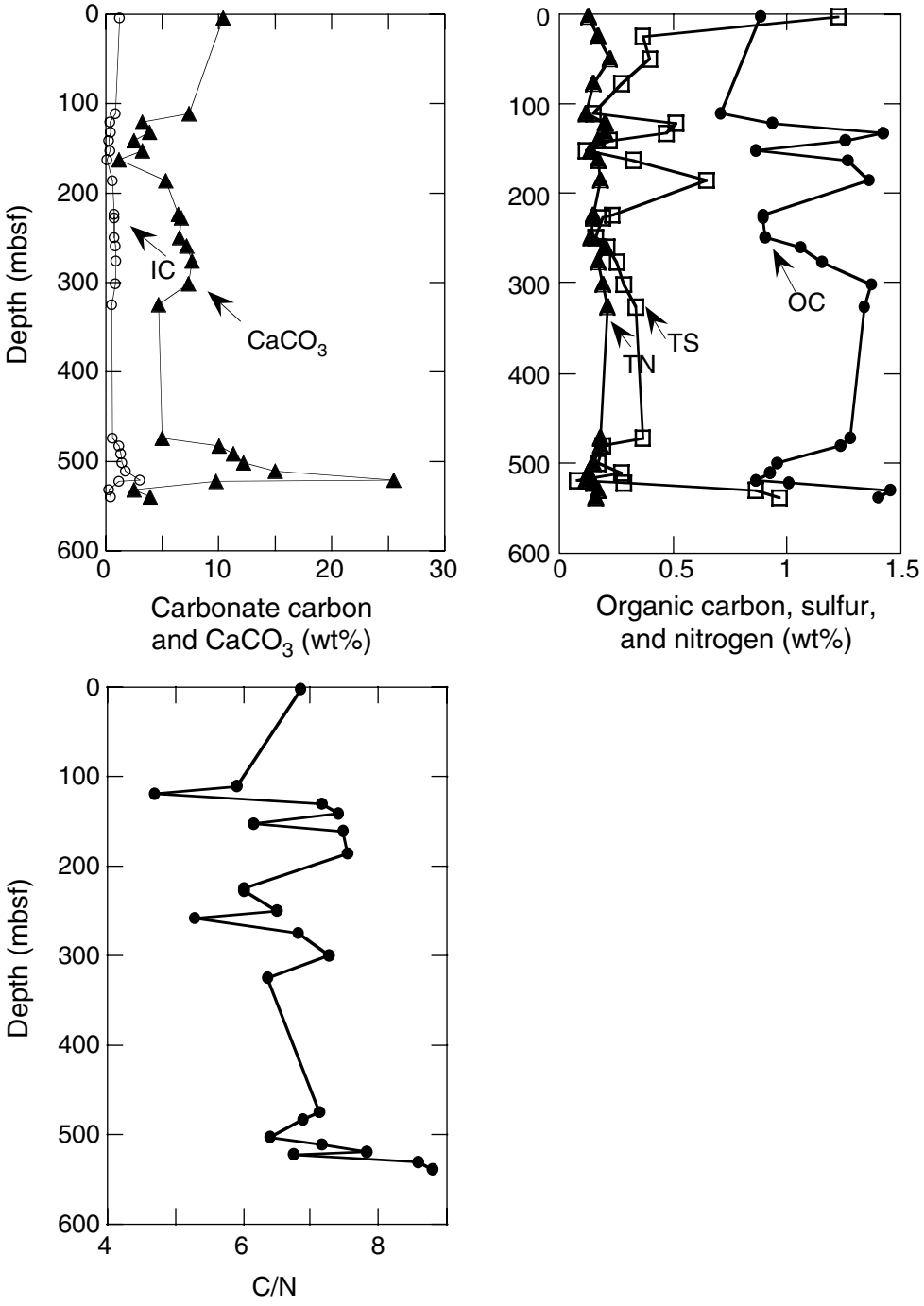

Figure F35. Downcore IR temperature profile in Holes 1245B and 1245C. APC = advanced piston corer, XCB = extended core barrel, BSR = bottom-simulating reflector.

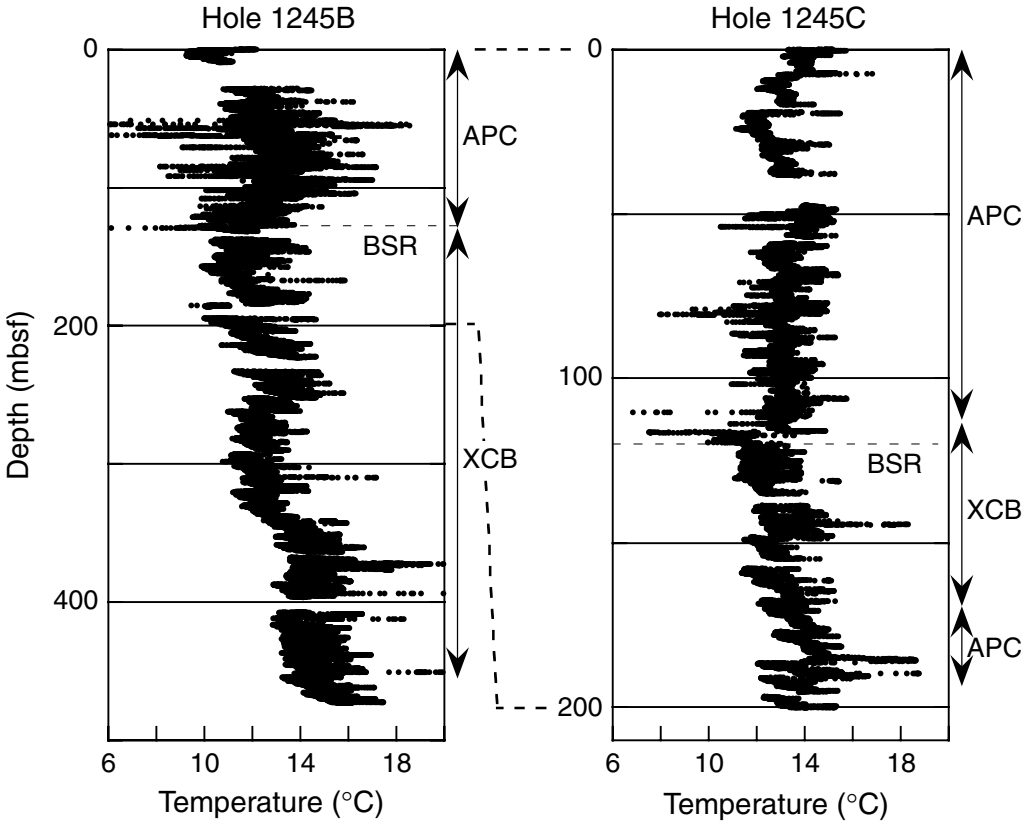

Figure F36. A. Comparison of temperature anomalies from IR imaging between Holes 1245B and 1245C. (Continued on next page.)

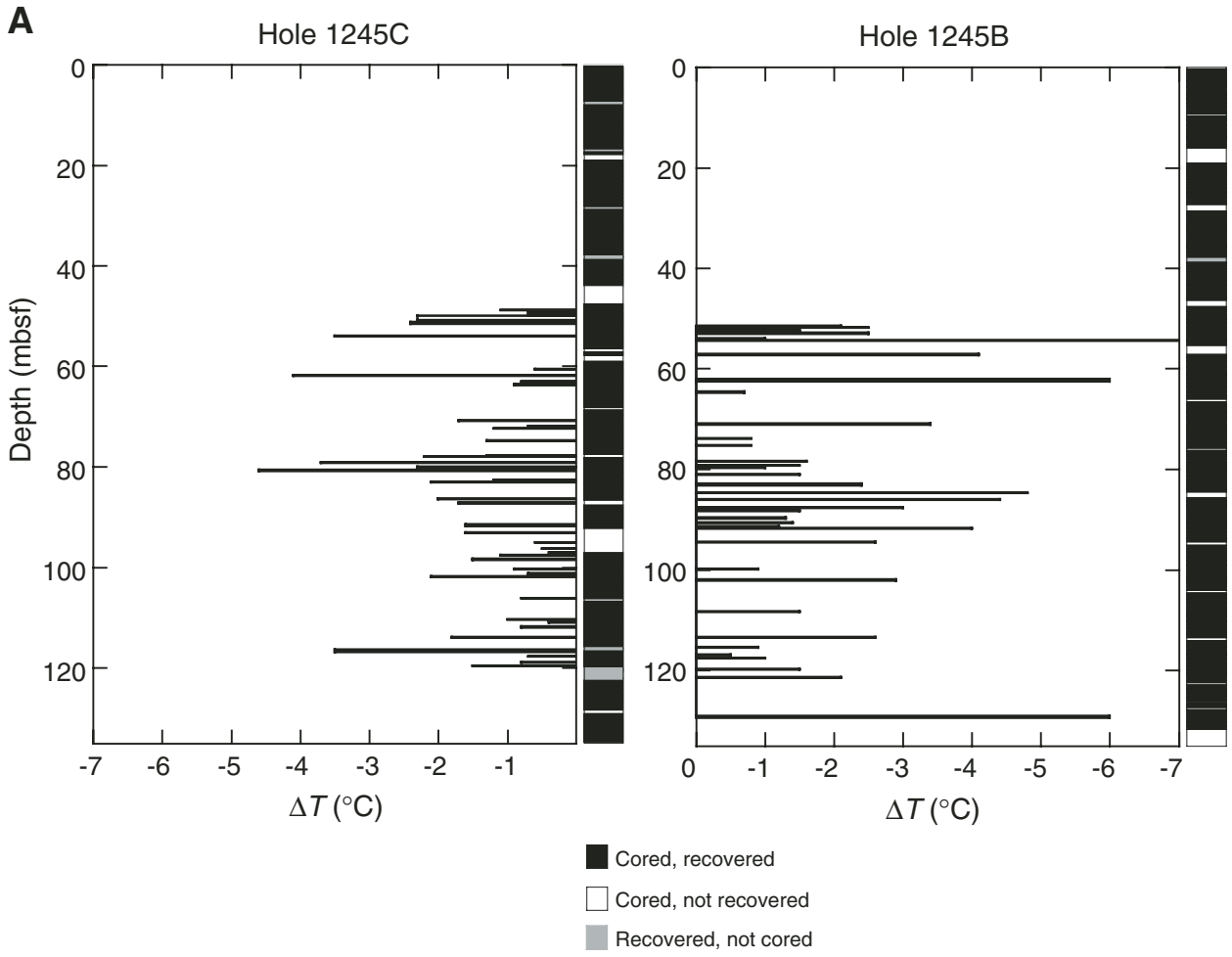

Figure F36 (continued). B. Comparison of IR temperature anomalies in Hole 1245B and pore water saturation as determined from LWD resistivity in Hole 1245A (see "Downhole Logging," p. 26).

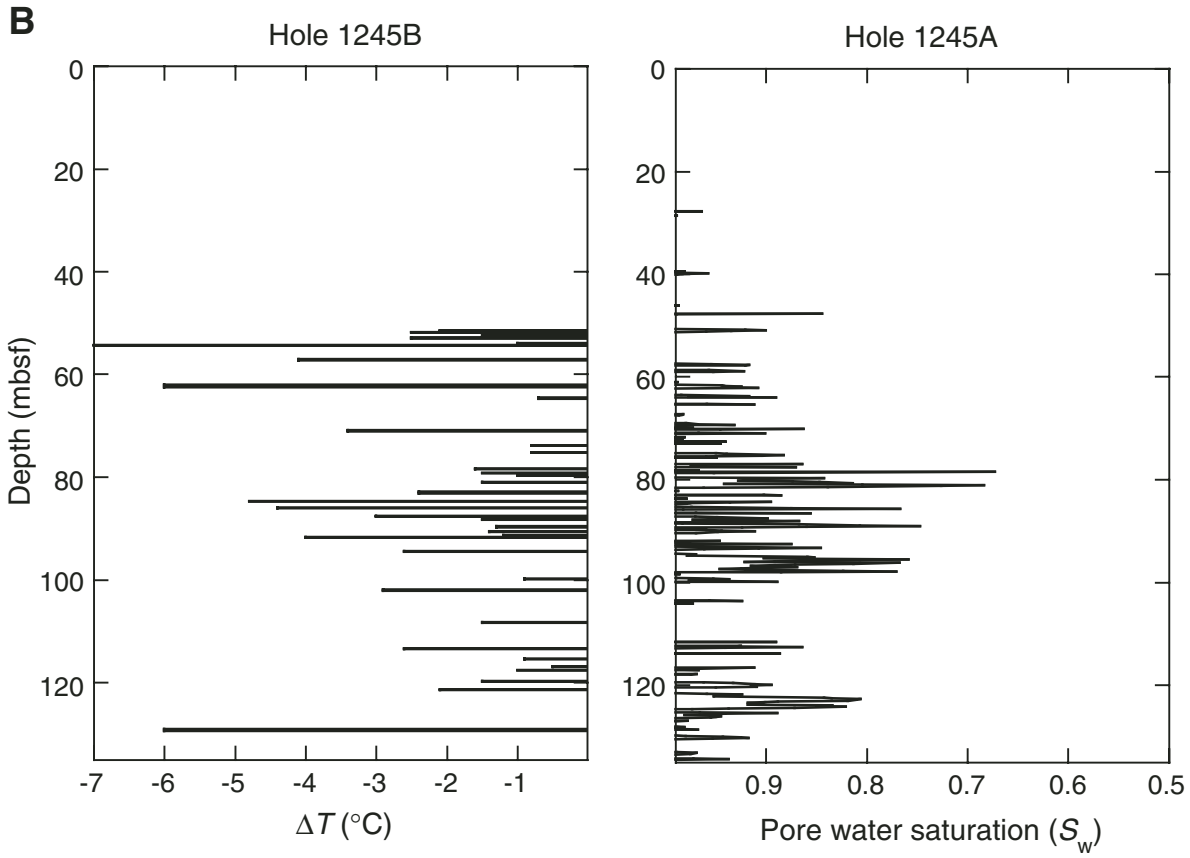

Figure F37. Overview of physical properties measured at Site 1245. LWD = logging while drilling, GRA = gamma ray attenuation, MAD = moisture and density. TV = Torvane, ASV = automated shear vane.

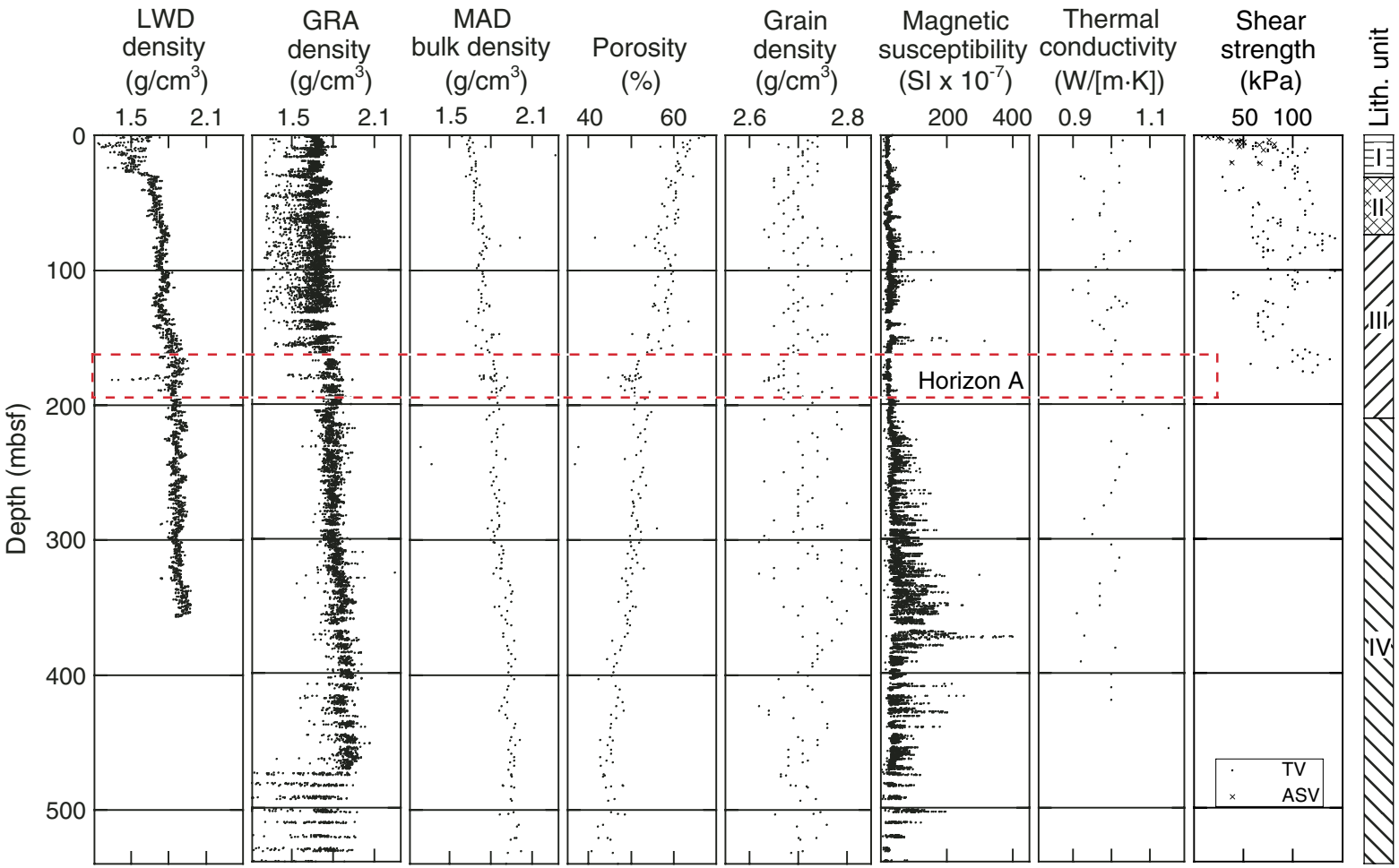

Figure F38. Correlation between physical properties and the seismic record at Site 1245. LWD = logging while drilling, MAD = moisture and density, BSR = bottom-simulating reflector.

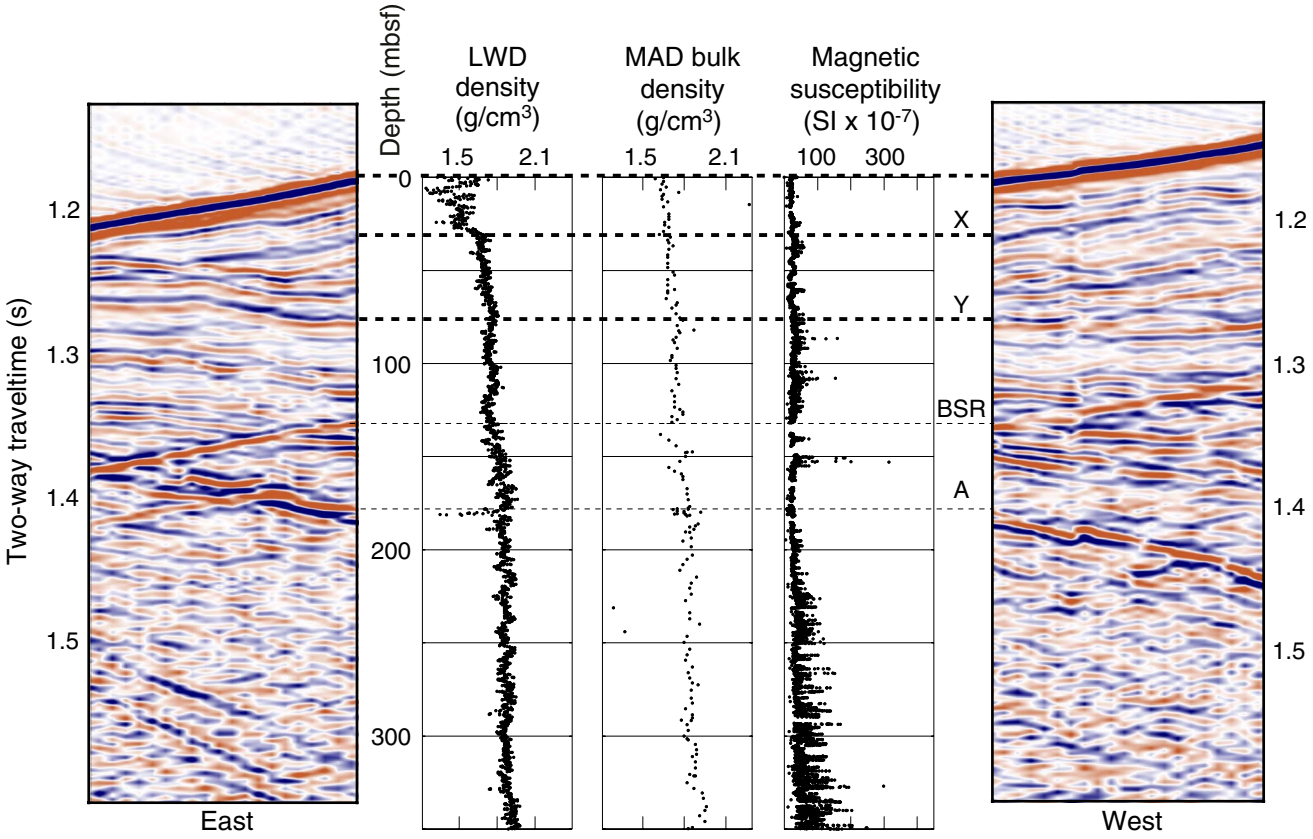

Figure F39. Physical properties across Horizon A at Site 1245. GRA = gamma ray attenuation, LWD = logging while drilling, MAD = moisture and density.

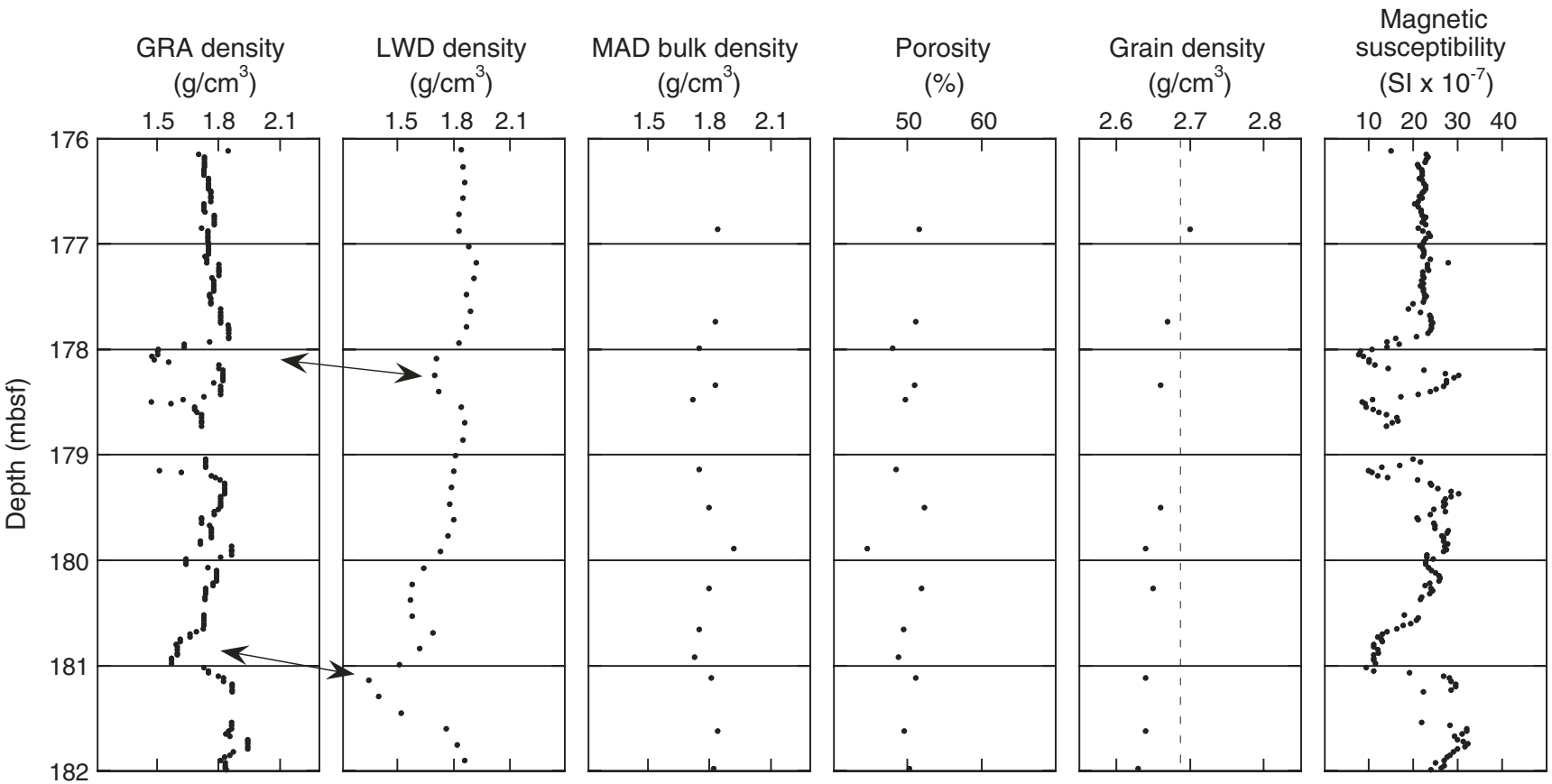

Figure F40. Noncontact resistivity (NCR) in Hole 1245B.

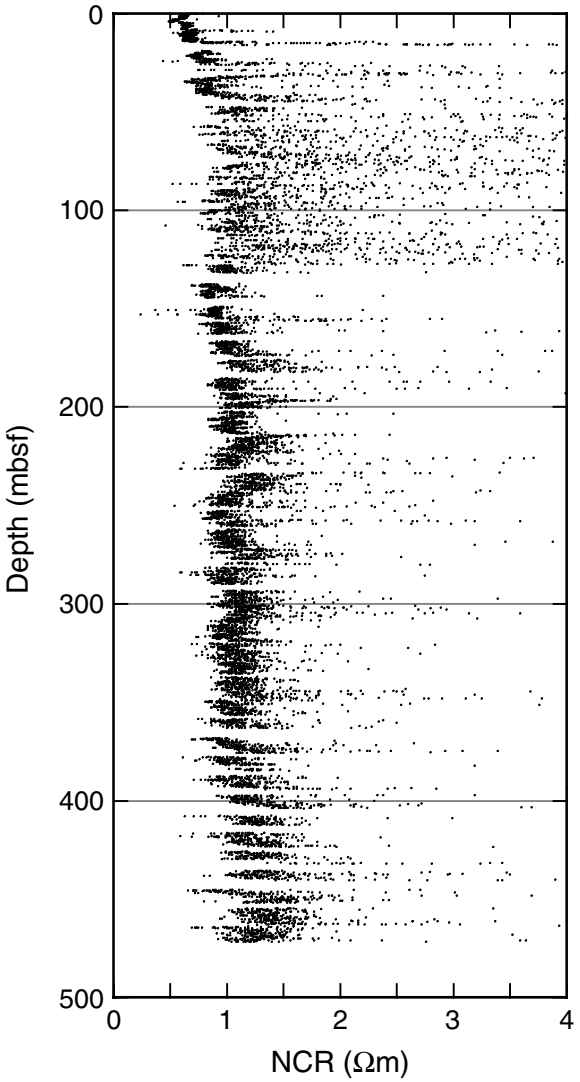

Figure F41. Comparison of V_P, bulk density, NCR, and shear strength at Site 1245. GRA = gamma ray attenuation, MAD = moisture and density, TV = Torvane, ASV = automated shear vane, MST = multisensor track.

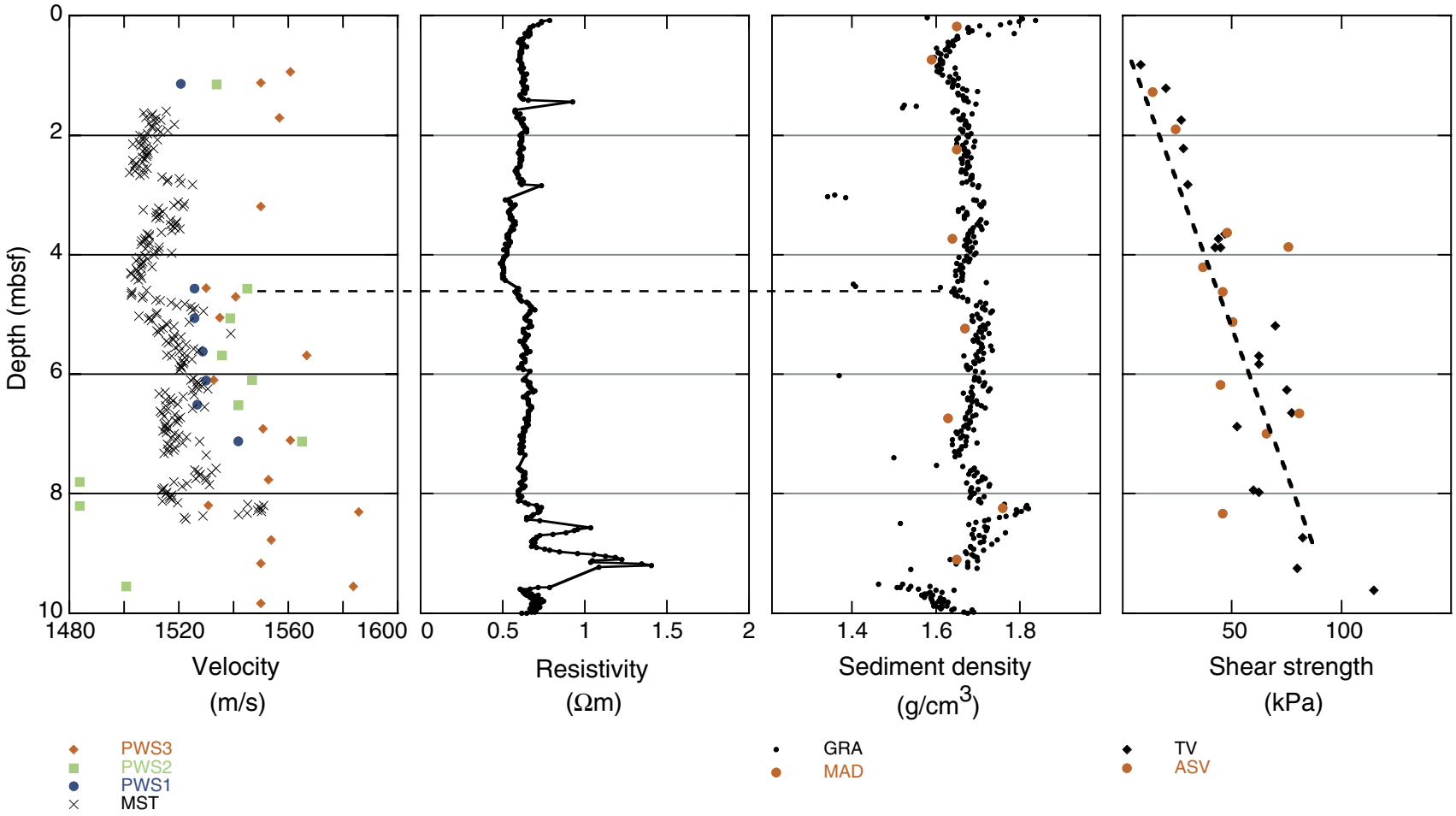

Figure F42. Raw data for estimating in situ temperatures. **A.** APCT tool data. Only the portion of data immediately before, during, and immediately after penetration of the probe into the subsurface is shown. For an example of the entire temperature history of a deployment, see **"Downhole Tools and Pressure Coring,"** p. 34, in the "Explanatory Notes" chapter. The ODP core identification number associated with each run of the APCT tool is indicated in the upper left corner of the graph. (Continued on next page.)

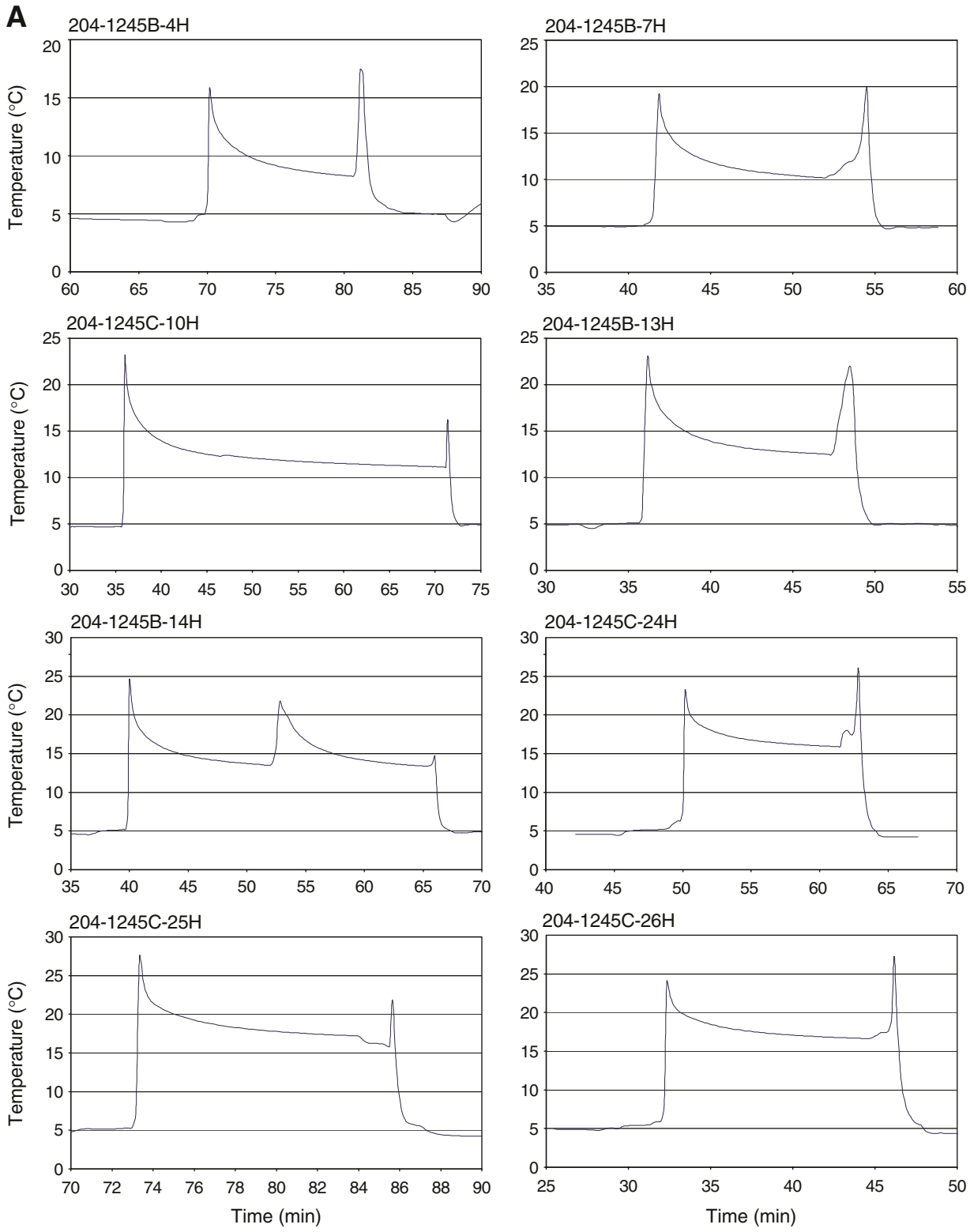

Figure F42 (continued). B. DVTP temperature data. The ODP identification for the core preceding tool deployment, the deployment depth (mbsf), and the measured equilibrium temperature are indicated.

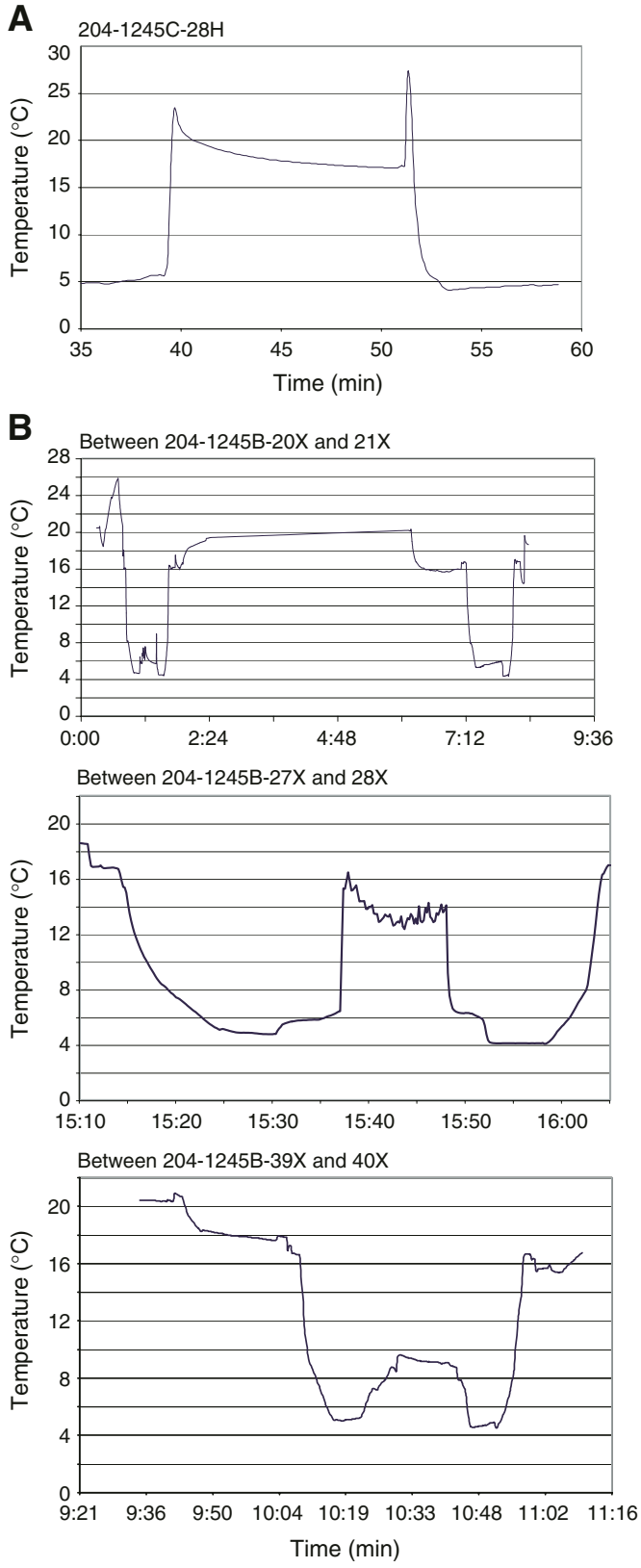

Figure F43. Subsurface temperatures plotted vs. depth beneath the seafloor at Site 1245. The equation for the best-fitting linear thermal gradient is also shown. BSR = bottom-simulating reflector, GHSZ = gas hydrate stability zone.

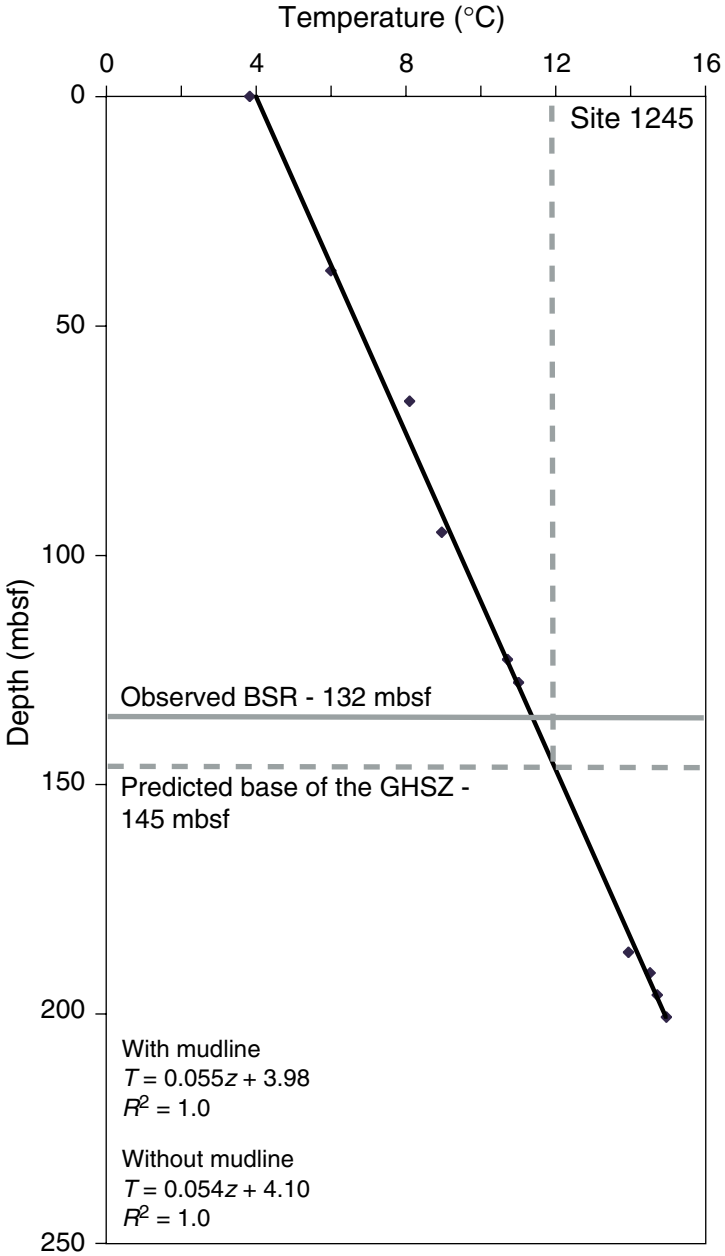

Figure F44. A–E. Volume-pressure-time plots for PCS deployments at Site 1245. Note that in Core 204-1245C-16P, pressure kept increasing to values equal to or above the pressure measured in the previous gas release, until ~4000 min of the run, suggesting the decomposition of gas hydrate.

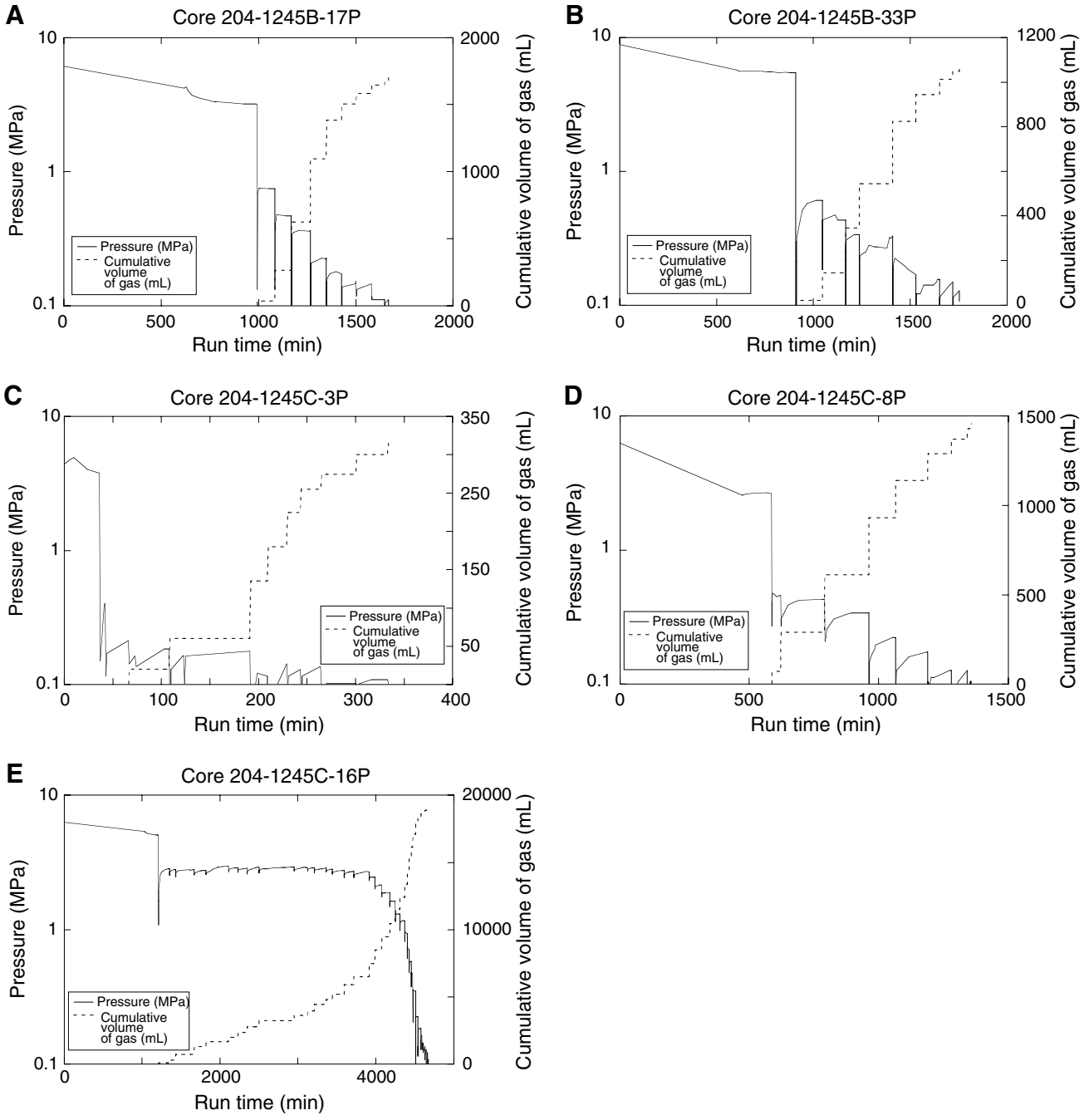

Figure F45. Porosity of sediments in advanced piston corer (APC), extended core barrel (XCB), and pressure core sampler (PCS) cores at Site 1245. Note that porosity measured in samples from the PCS cores is often different from the general porosity trend at Site 1245.

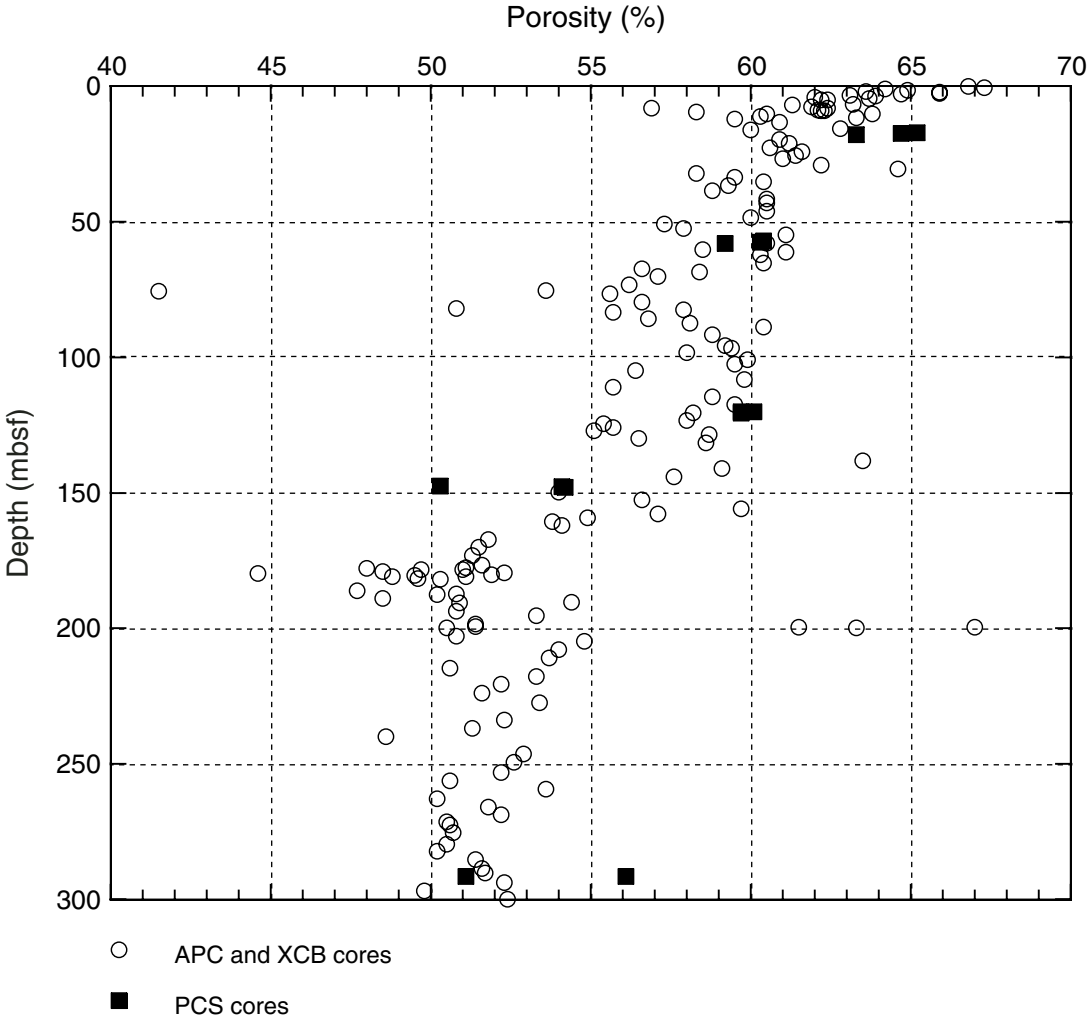

Figure F46. Methane (CH_4) concentration in sediments based on headspace (HS) and pressure core sampler (PCS) data at Site 1245. Estimated theoretical solubility of methane in pore water (extrapolated from values calculated for higher pressures [depths]) (Handa, 1990; Duan et al., 1992) is shown, and fields of dissolved methane (D), methane hydrate (H), and free methane (F) are depicted. Shaded area = uncertainties in the position of the boundaries. Note that the headspace technique fails to determine accurate concentration values above ~2 mM because methane is relatively abundant in situ and it rapidly escapes from sediments upon core retrieval.

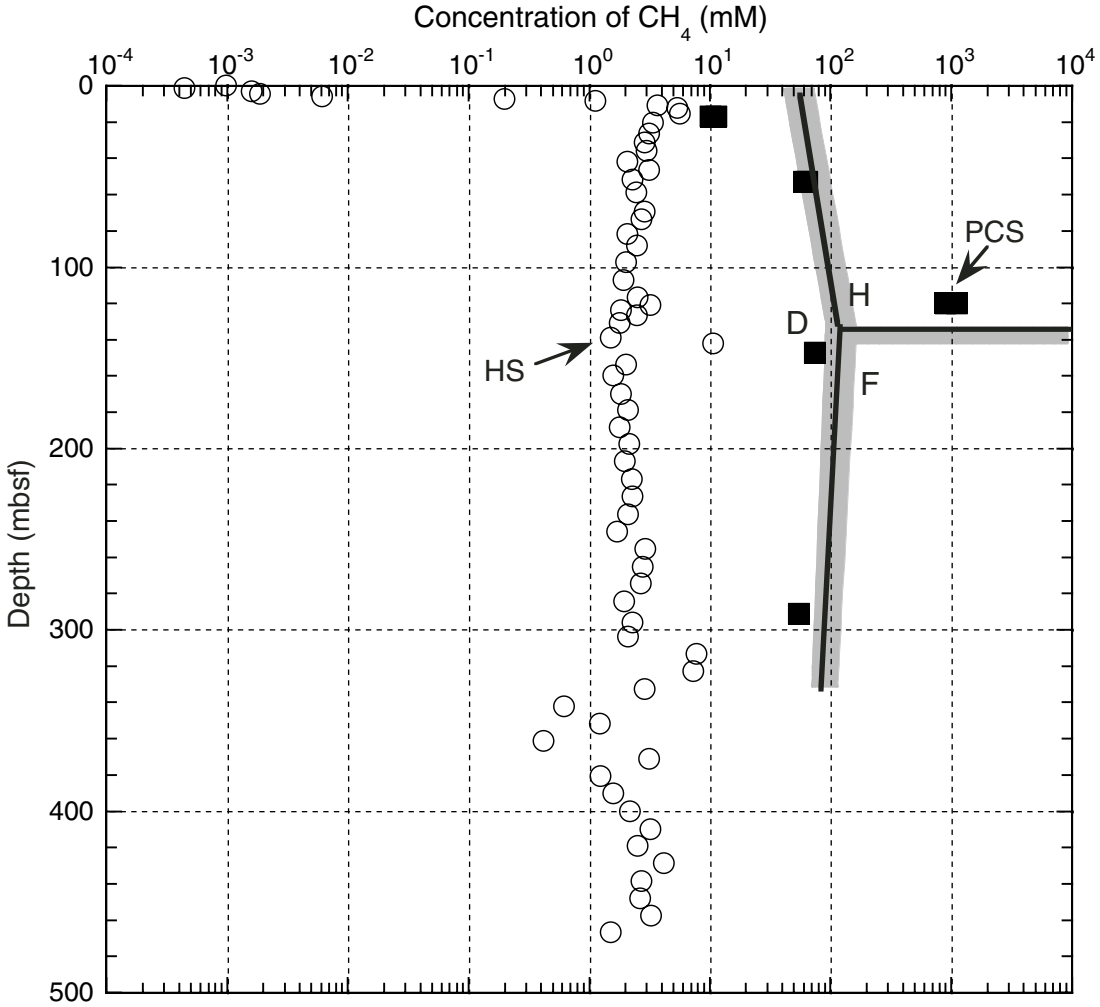

Figure F47. Quality control LWD logs from Hole 1245A. ROP = rate of penetration, TAB = time after bit, Diff. = differential.

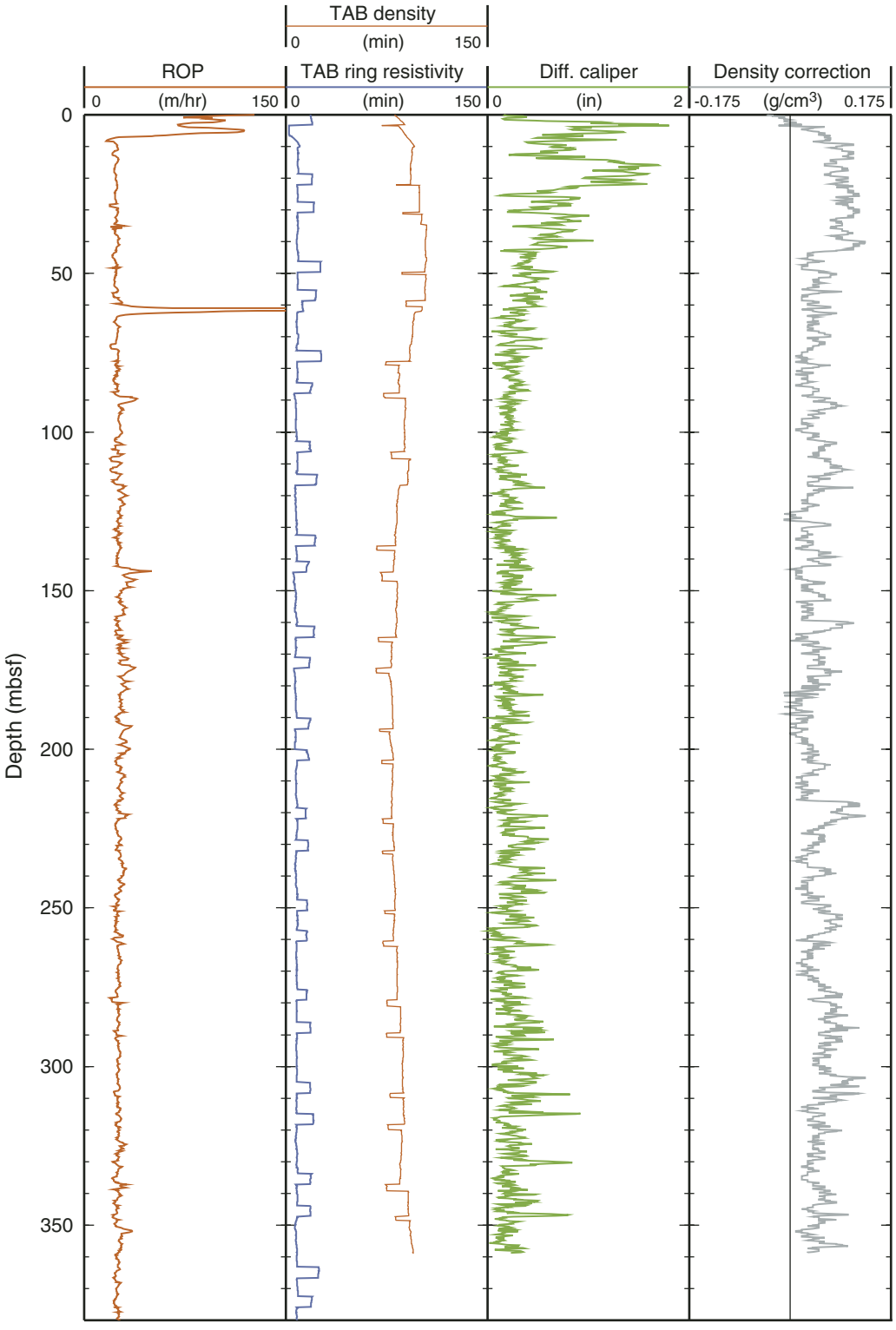

Figure F48. Summary of LWD log data from Hole 1245A. gAPI = American Petroleum Institute gamma ray units, PEF = photoelectric effect factor, RAB = resistivity at the bit.

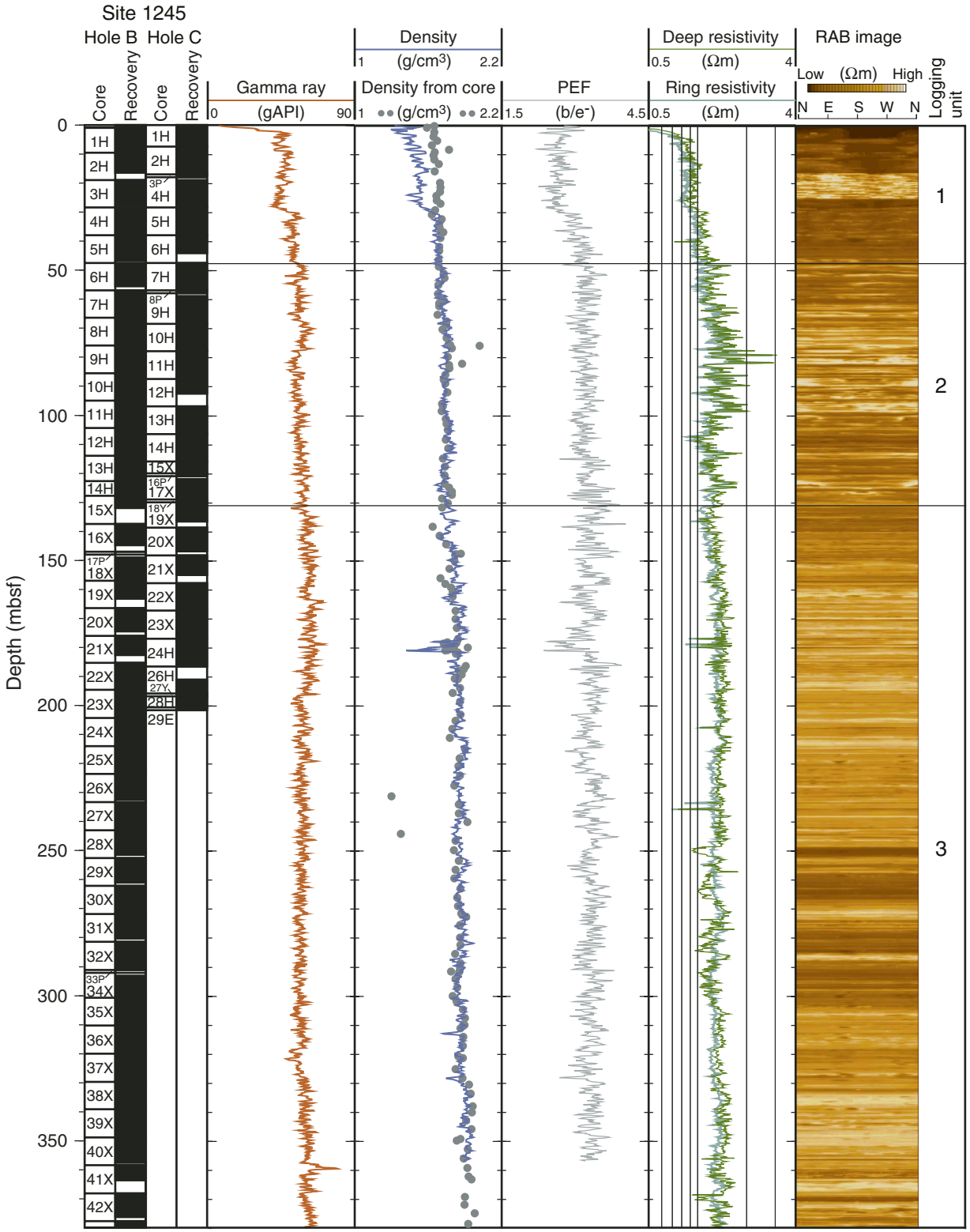

Figure F49. Summary of CWL logging data from Hole 1245E. gAPI = American Petroleum Institute gamma ray units, PEF = photoelectric effect factor.

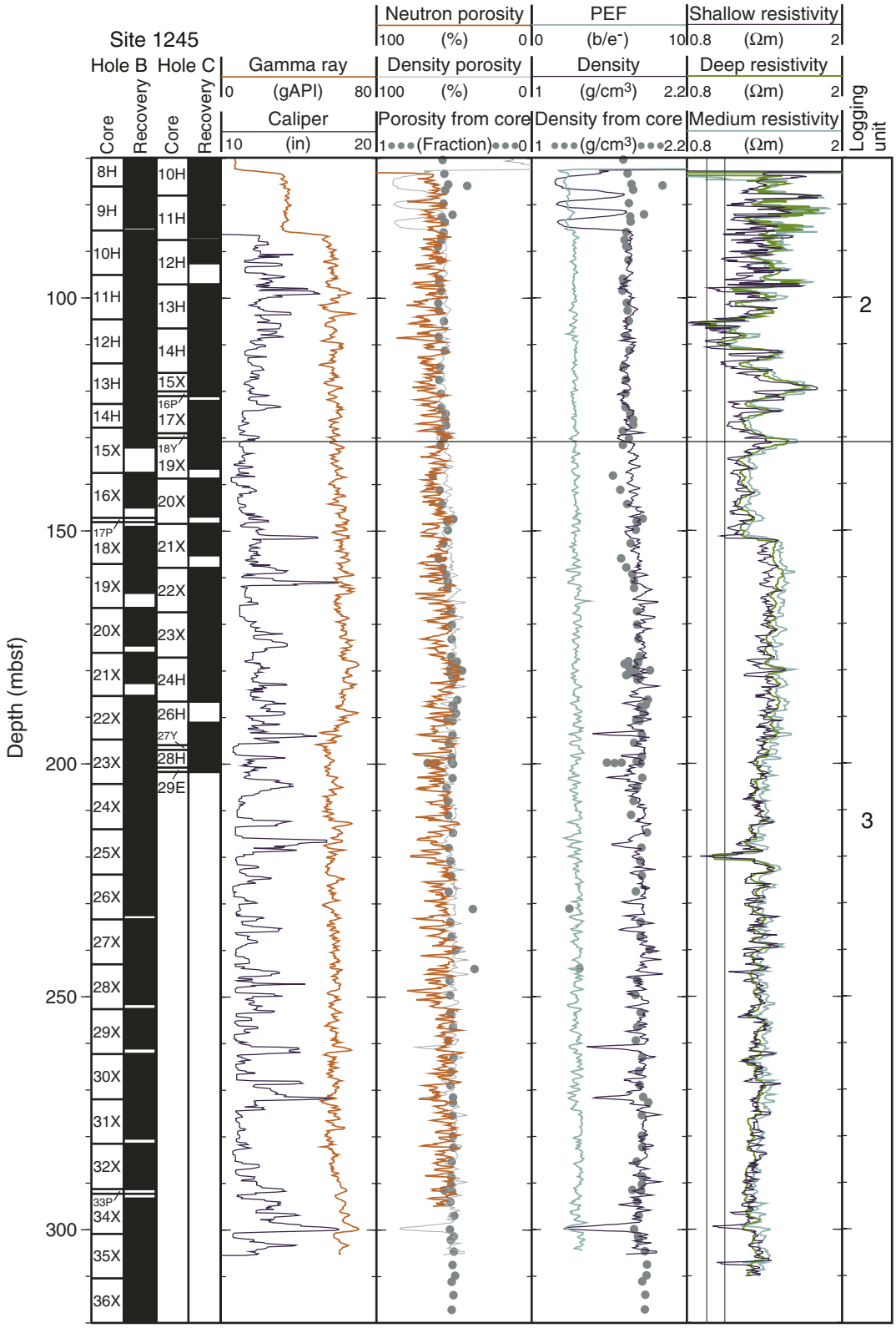

Figure F50. CWL gamma ray logging data from Hole 1245E. FMS = Formation MicroScanner, gAPI = American Petroleum Institute gamma ray units.

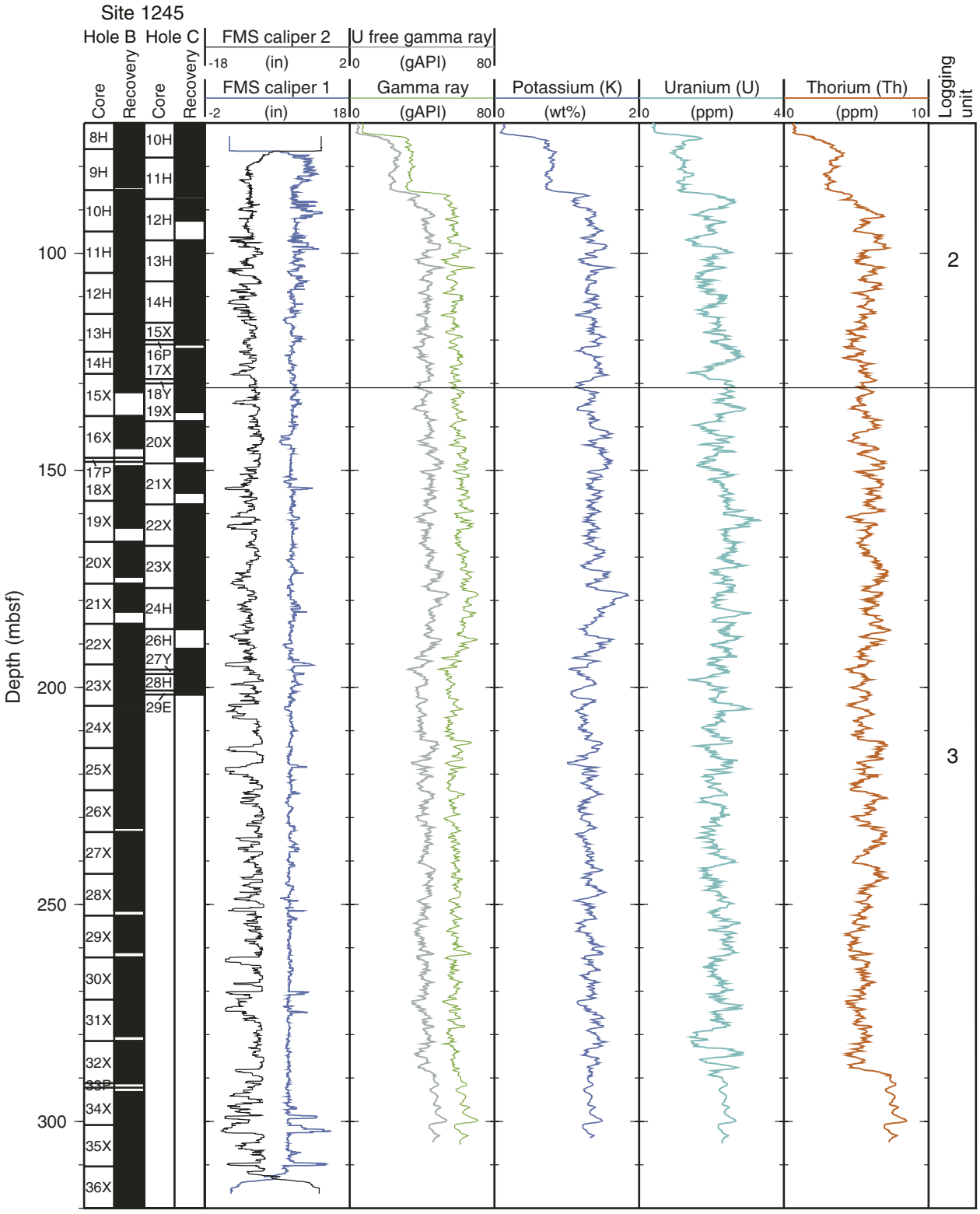

Figure F51. Comparison of logging-while-drilling (LWD) and conventional wireline logging (CWL) downhole logging data from Holes 1245A and 1245E. gAPI = American Petroleum Institute gamma ray units, por. = porosity, PEF = photoelectric effect factor.

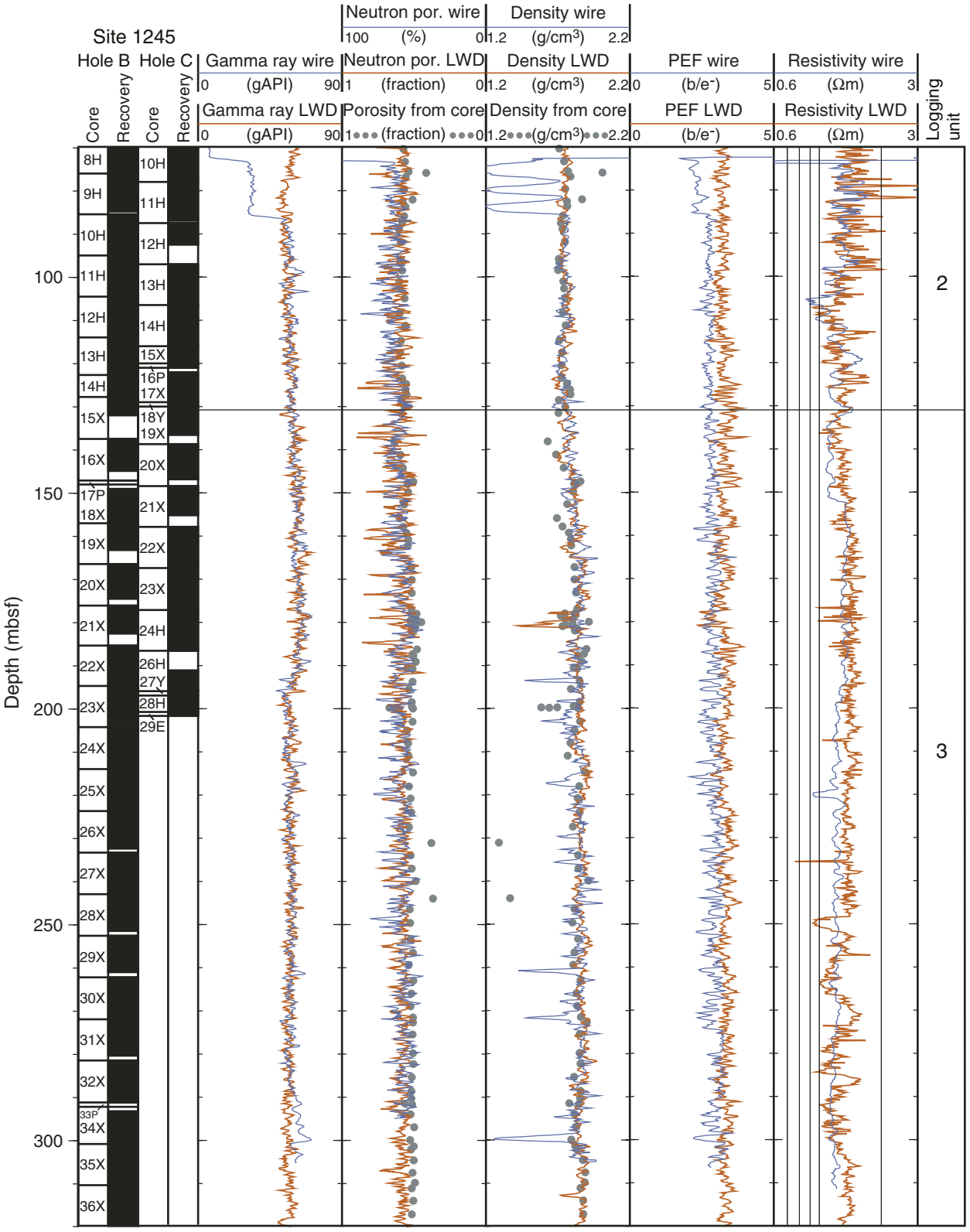

Figure F52. CWL acoustic logging data from Hole 1245E. The resistivity log is used as a reference indicator of the presence of gas hydrate. Low acoustic waveform amplitudes are also possible indicators of gas hydrate. SPh. foc. res. = spherically focused resistivity.

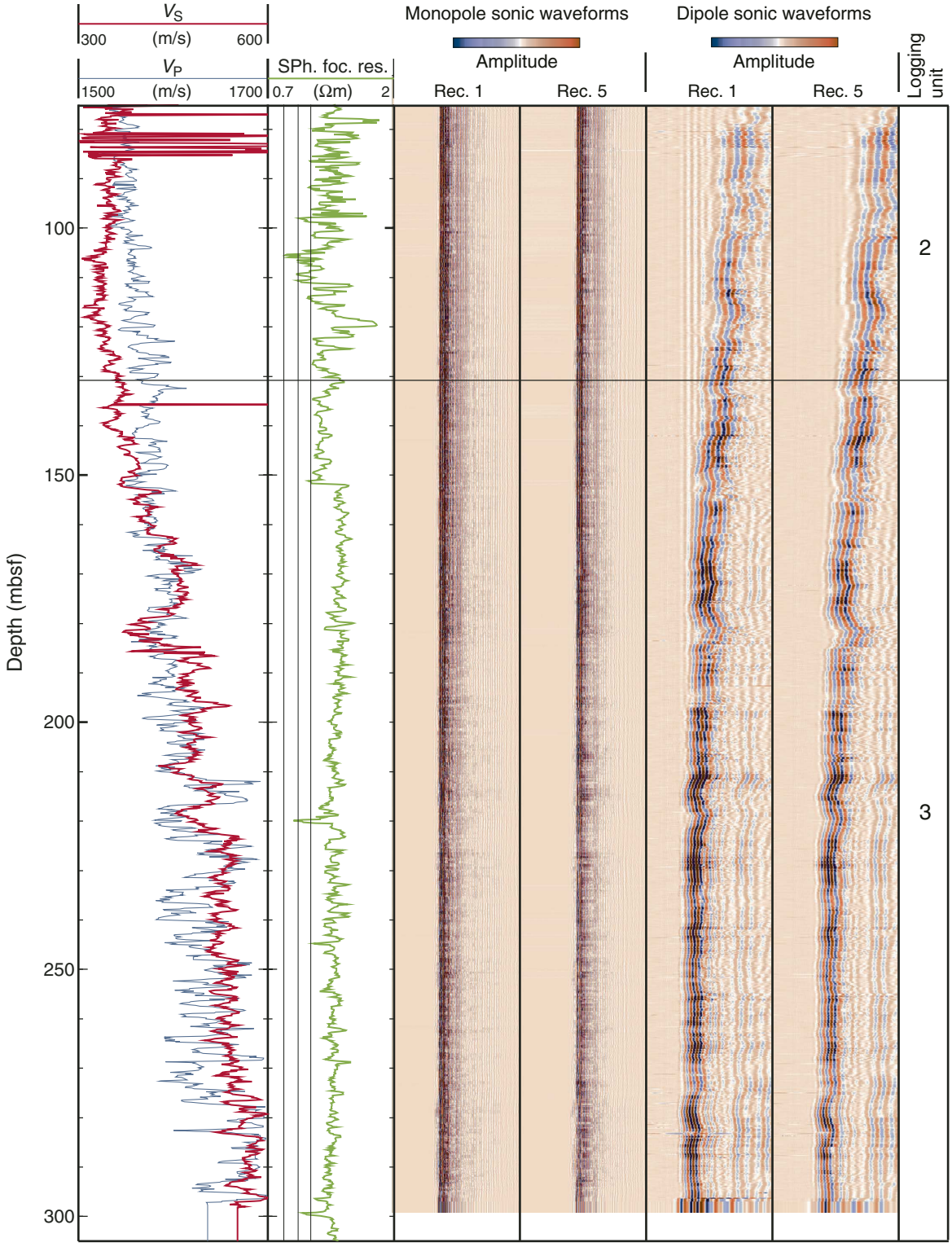

Figure F53. Resistivity-at-the-bit (RAB) image showing the possible presence of gas hydrate as bright resistive material occupying low-to-high angle fractures and nearly flat lying stratigraphic horizons in Hole 1245A. 3-D = three-dimensional.

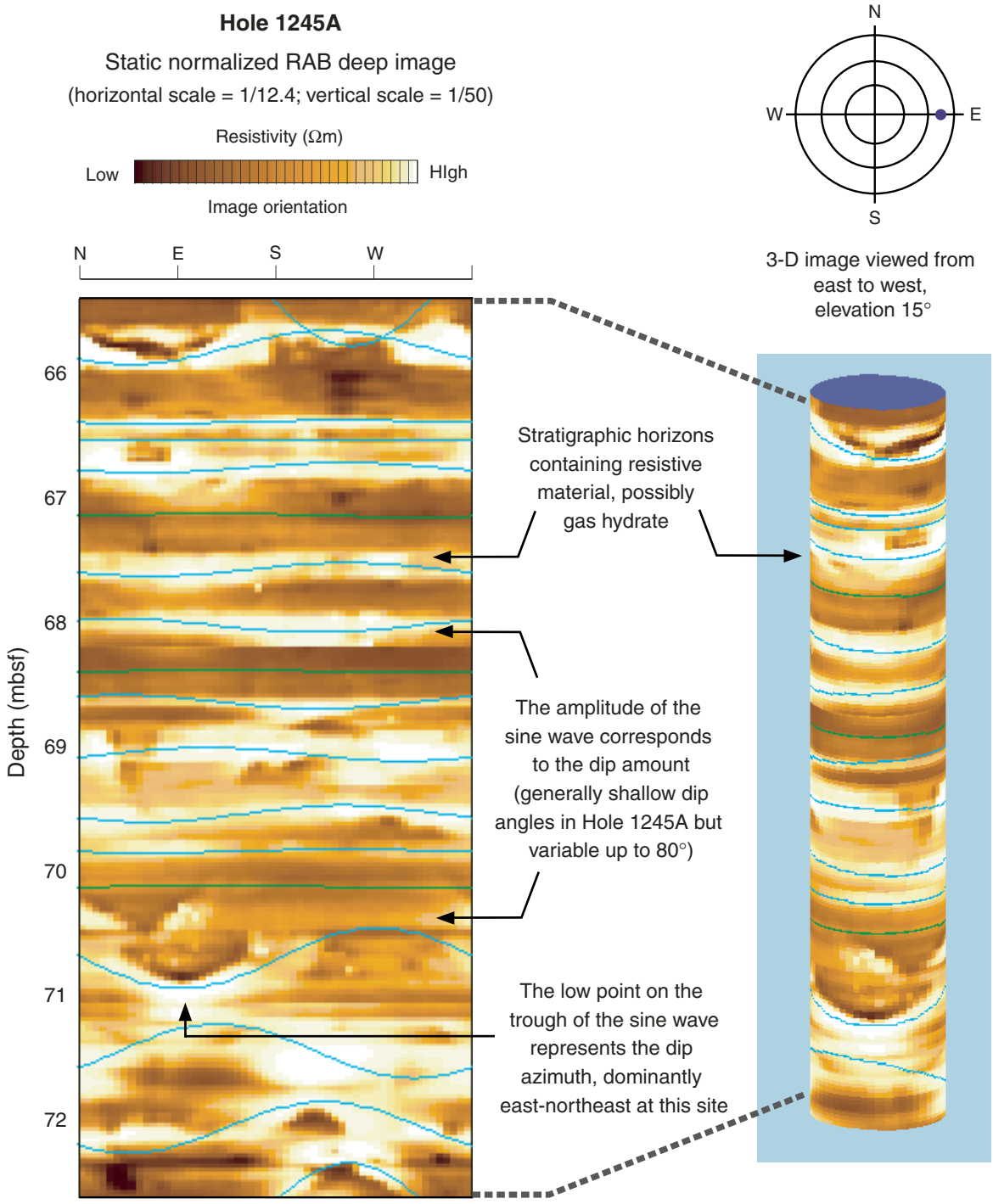

Figure F54. Resistivity-at-the-bit (RAB) and Formation MicroScanner (FMS) images showing seismic Horizon A present as alternating bright, resistive, and dark conductive layers of sand and ash in Holes 1245A and 1245E.

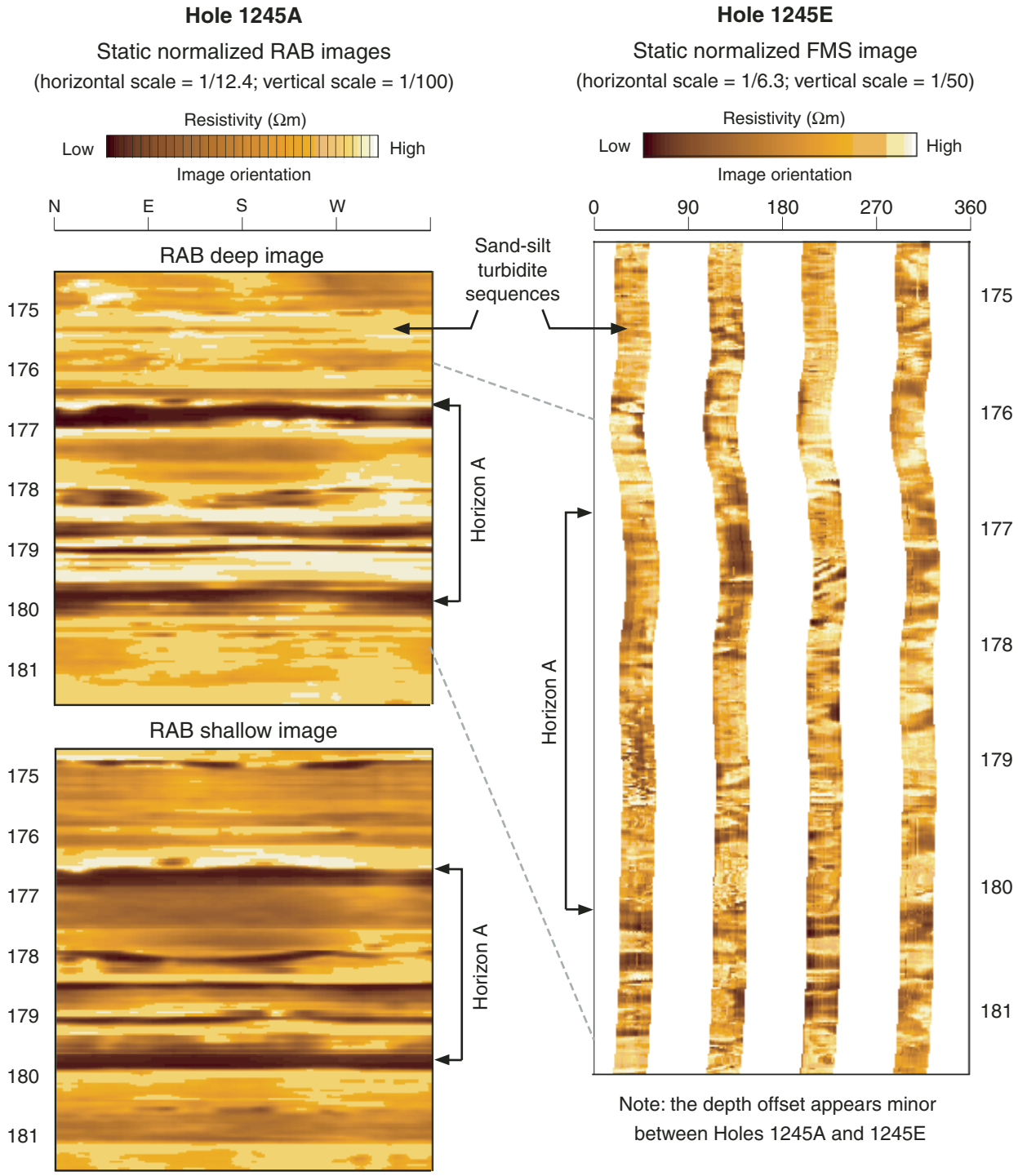

Figure F55. Resistivity-at-the-bit (RAB) and Formation MicroScanner (FMS) images showing turbidites characterized by interbedded bright resistive and dark conductive layers in Holes 1245A and 1245E.

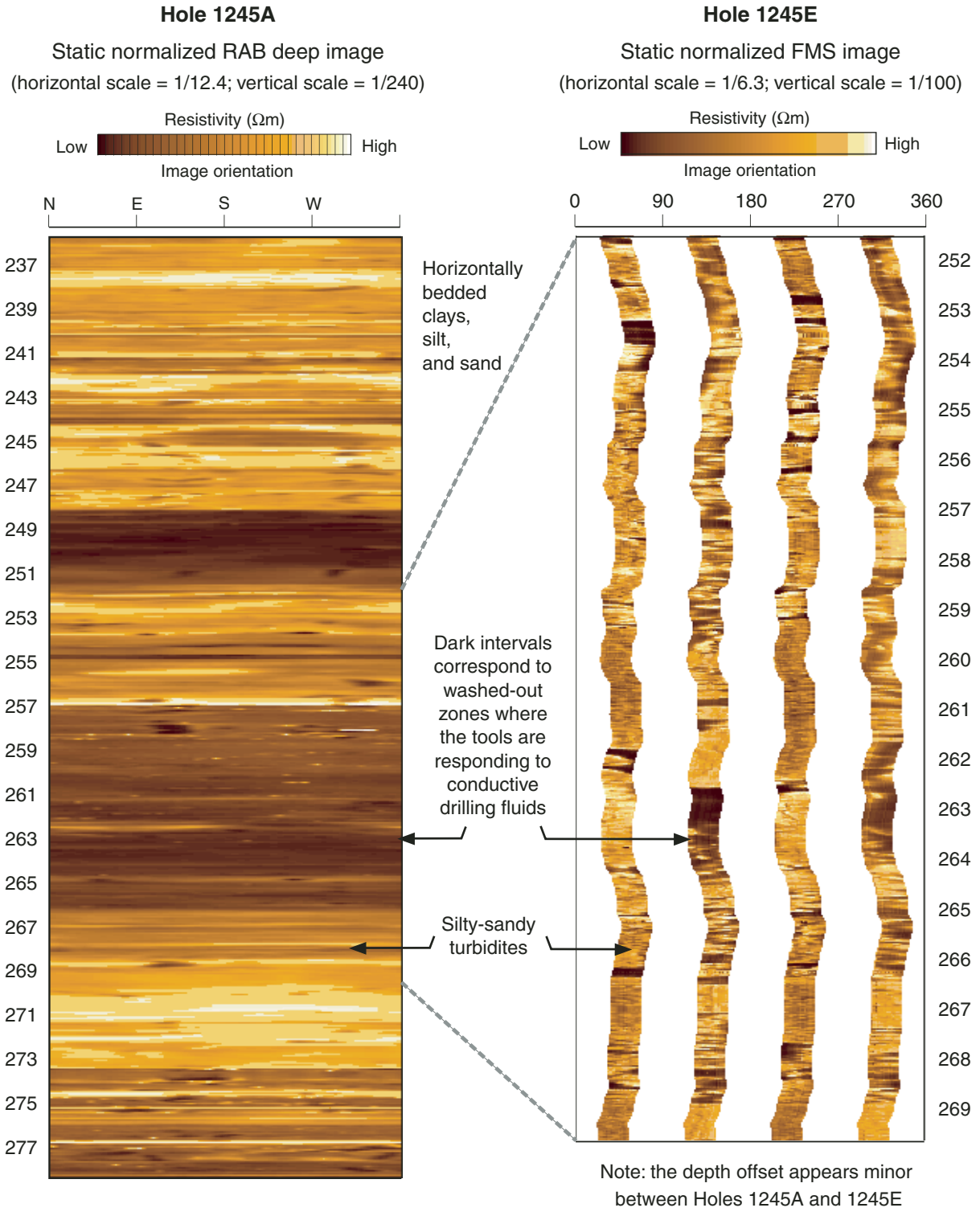

Figure F56. Comparison of LWD- and core-derived porosities from Hole 1245A. NMR-MRP = Nuclear Magnetic Resonance, RAB = resistivity at the bit.

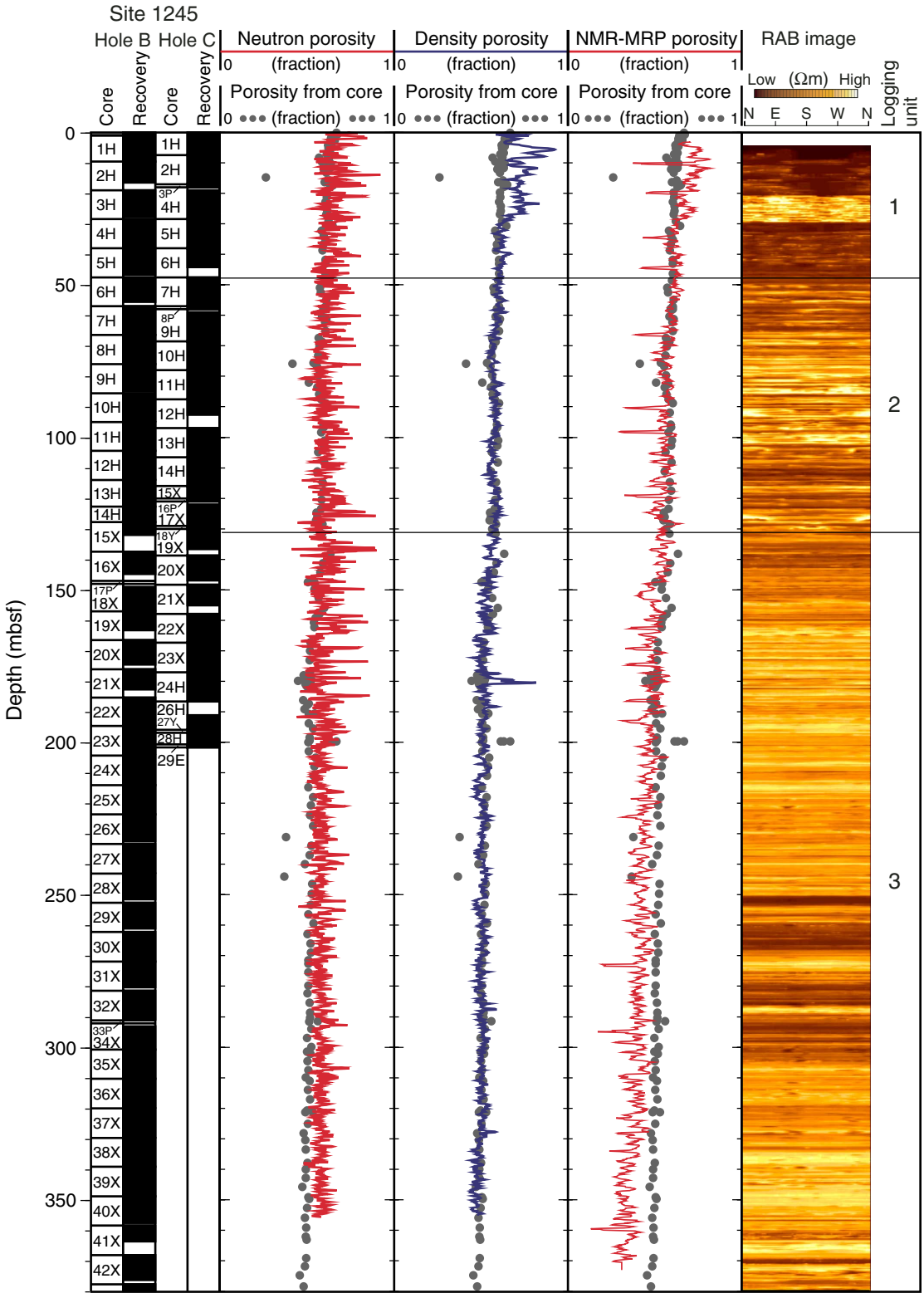

Figure F57. LWD-derived water saturations from Hole 1245A. gAPI = American Petroleum Institute gamma ray units, RAB = resistivity at the bit.

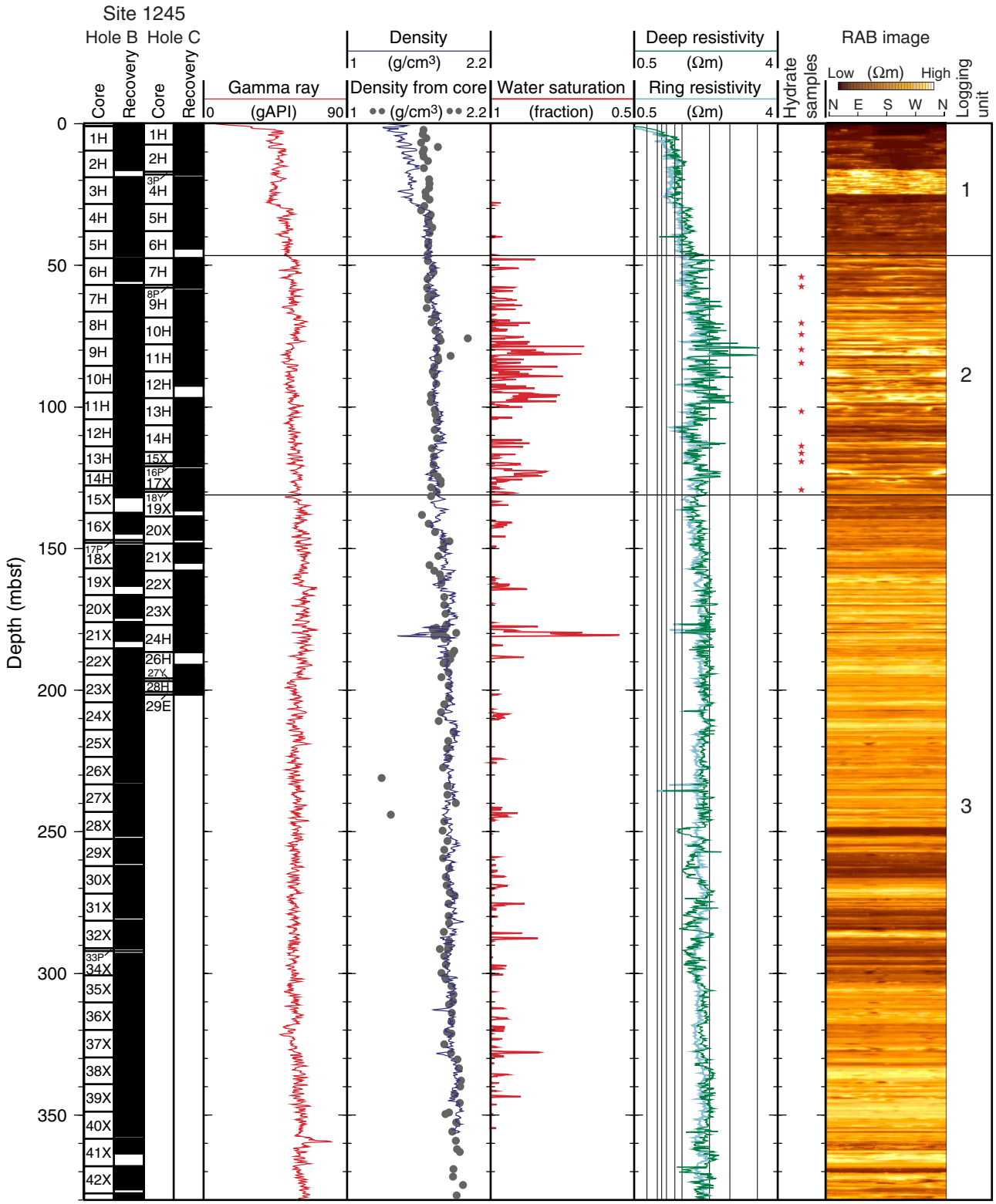

Figure F58. Borehole temperatures recorded with the TAP tool on the downward run of the triple combo tool string in Hole 1425E.

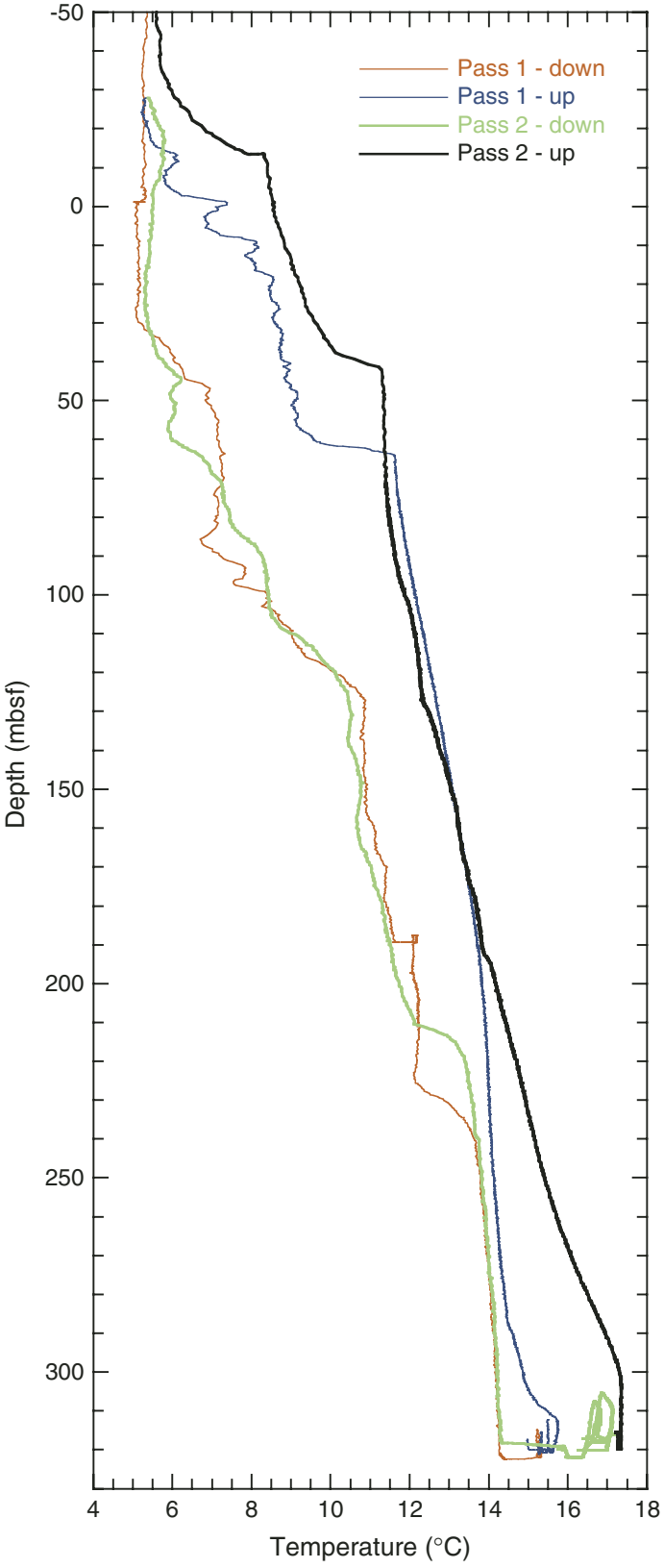

Table T1. Coring summary, Site 1245. (Continued on next two pages.)

Hole 1245A
Latitude: 44°35.1697′N
Longitude: 125°8.9462′W
Time on site (hr): 250.0 (1900 hr, 17 Jul–2345 hr, 18 Jul 2002)
Time on hole (hr): 28.75 (1900 hr, 17 Jul–2345 hr, 18 Jul 2002)
Seafloor (drill pipe measurement from rig floor, mbrf): 886.5
Distance between rig floor and sea level (m): 10.9
Water depth (drill pipe measurement from sea level, m): 875.6
Total depth (drill pipe measurement from rig floor, mbrf): 1266.5
Total penetration (meters below seafloor, mbsf): 380
Total number of cores: 0
Total number of drilled intervals: 1
Total length of cored section (m): 0.0
Total core recovered (m): 0.00
Core recovery (%): 0.0

Hole 1245B
Latitude: 44°35.1587′N
Longitude: 125°8.9455′W
Time on hole (hr): 80.5 (0715 hr, 6 Aug–1545 hr, 9 Aug 2002)
Seafloor (drill pipe measurement from rig floor, mbrf): 881.0
Distance between rig floor and sea level (m): 11.3
Water depth (drill pipe measurement from sea level, m): 869.7
Total depth (drill pipe measurement from rig floor, mbrf): 1354.7
Total penetration (meters below seafloor, mbsf): 473.7
Total number of cores: 53
Total number of drilled intervals: 2
Total length of cored section (m): 471.7
Total core recovered (m): 418.02
Core recovery (%): 88.6

Hole 1245C
Latitude: 44°35.1702′N
Longitude: 125°8.9316′W
Time on hole (hr): 32.75 (1545 hr, 9 Aug–0030 hr, 11 Aug 2002)
Seafloor (drill pipe measurement from rig floor, mbrf): 880.0
Distance between rig floor and sea level (m): 11.3
Water depth (drill pipe measurement from sea level, m): 868.7
Total depth (drill pipe measurement from rig floor, mbrf): 1081.7
Total penetration (meters below seafloor, mbsf): 201.7
Total number of cores: 29
Total number of drilled intervals: 3
Total length of cored section (m): 198.7
Total core recovered (m): 185.31
Core recovery (%): 93.3

Hole 1245D
Latitude: 44°35.1690′N
Longitude: 125°8.9312′W
Time on hole (hr): 3.5 (0030 hr, 11 Aug–0400 hr, 11 Aug 2002)
Seafloor (drill pipe measurement from rig floor, mbrf): 881.5
Distance between rig floor and sea level (m): 11.4
Water depth (drill pipe measurement from sea level, m): 870.1
Total depth (drill pipe measurement from rig floor, mbrf): 905.5
Total penetration (meters below seafloor, mbsf): 24.0
Total number of cores: 3
Total number of drilled intervals: 0
Total length of cored section (m): 24.0
Total core recovered (m): 24.82
Core recovery (%): 103.4

Table T1 (continued).

Hole 1245E
Latitude: 44°35.1702′N
Longitude: 125°8.9605′W
Time on hole (hr): 104.5 (2245 hr, 11 Aug–0715 hr, 16 Aug 2002)
Seafloor (drill pipe measurement from rig floor, mbrf): 881.0
Distance between rig floor and sea level (m): 11.5
Water depth (drill pipe measurement from sea level, m): 869.5
Total depth (drill pipe measurement from rig floor, mbrf): 1421.3
Total penetration (meters below seafloor, mbsf): 540.3
Total number of cores: 8
Total number of drilled intervals: 2
Total length of cored section (m): 66.6
Total core recovered (m): 18.48
Core recovery (%): 27.8

Core	Date (Aug 2002)	Local time (hr)	Depth (mbsf) Top	Depth (mbsf) Bottom	Length (m) Cored	Length (m) Recovered	Recovery (%)
204-1245A-							
			*****Drilled from 0 to 380.0 mbsf*****				
204-1245B-							
1H	6	1040	0.0	9.5	9.5	9.61	101.2
2H	6	1145	9.5	19.0	9.5	6.94	73.1
3H	6	1225	19.0	28.5	9.5	8.68	91.4
4H	6	1340	28.5	38.0	9.5	10.25	107.9
5H	6	1425	38.0	47.5	9.5	8.71	91.7
6H	6	1505	47.5	57.0	9.5	8.13	85.6
7H	6	1605	57.0	66.5	9.5	9.38	98.7
8H	6	1655	66.5	76.0	9.5	9.70	102.1
9H	6	1750	76.0	85.5	9.5	8.84	93.1
10H	6	1905	85.5	95.0	9.5	9.26	97.5
11H	6	1935	95.0	104.5	9.5	9.36	98.5
12H	6	2015	104.5	114.0	9.5	9.39	98.8
13H	6	2105	114.0	122.7	8.7	8.75	100.6
14H	6	2240	122.7	127.8	5.1	5.14	100.8
15X	7	0020	127.8	137.5	9.7	4.28	44.1
16X	7	0135	137.5	147.1	9.6	7.37	76.8
17P	7	0315	147.1	148.1	1.0	1.00	100.0
			*****Drilled from 148.1 to 149.1 mbsf*****				
18X	7	0445	149.1	157.0	7.9	7.67	97.1
19X	7	0545	157.0	166.5	9.5	6.28	66.1
20X	7	0715	166.5	176.1	9.6	8.02	83.5
21X	7	0910	176.1	185.4	9.3	6.53	70.2
22X	7	1015	185.4	194.7	9.3	9.75	104.8
23X	7	1115	194.7	204.3	9.6	9.10	94.8
24X	7	1210	204.3	214.0	9.7	9.70	100.0
25X	7	1310	214.0	223.7	9.7	9.69	99.9
26X	7	1410	223.7	233.3	9.6	8.74	91.0
27X	7	1510	233.3	243.0	9.7	9.53	98.2
28X	7	1715	243.0	252.6	9.6	8.46	88.1
29X	7	1850	252.6	262.2	9.6	8.46	88.1
30X	7	2005	262.2	271.9	9.7	9.78	100.8
31X	7	2130	271.9	281.5	9.6	8.48	88.3
32X	7	2305	281.5	291.2	9.7	9.38	96.7
33P	8	0010	291.2	292.2	1.0	1.00	100.0
			*****Drilled from 291.2 to 293.2 mbsf*****				
34X	8	0210	293.2	300.8	7.6	9.42	123.9
35X	8	0330	300.8	310.4	9.6	9.76	101.7
36X	8	0515	310.4	320.0	9.6	9.37	97.6
37X	8	0655	320.0	329.7	9.7	9.65	99.5
38X	8	0830	329.7	339.2	9.5	9.82	103.4
39X	8	1005	339.2	348.9	9.7	9.78	100.8
40X	8	1225	348.9	358.5	9.6	8.66	90.2
41X	8	1355	358.5	368.2	9.7	5.21	53.7
42X	8	1535	368.2	377.8	9.6	8.16	85.0
43X	8	1730	377.8	387.4	9.6	7.36	76.7
44X	8	1925	387.4	397.1	9.7	7.35	75.8
45X	8	2300	397.1	406.7	9.6	7.24	75.4
46E	9	0020	406.7	407.7	1.0	0.38	38.0
47X	9	0200	407.7	416.3	8.6	5.22	60.7

Table T1 (continued).

Core	Date (Aug 2002)	Local time (hr)	Depth (mbsf) Top	Depth (mbsf) Bottom	Length (m) Cored	Length (m) Recovered	Recovery (%)
48X	9	0350	416.3	425.9	9.6	7.74	80.6
49X	9	0535	425.9	435.6	9.7	6.72	69.3
50X	9	0800	435.6	445.2	9.6	5.25	54.7
51X	9	0925	445.2	454.7	9.5	7.21	75.9
52X	9	1100	454.7	464.0	9.3	9.72	104.5
53X	9	1255	464.0	473.7	9.7	8.64	89.1
			Cored totals:		471.7	418.02	88.6
			Drilled total:		2.0		
			Total:		473.7		
204-1245C-							
1H	9	1740	0.0	7.5	7.5	7.84	104.5
2H	9	1850	7.5	17.0	9.5	9.78	102.9
3P	9	2005	17.0	18.0	1.0	1.00	100.0
			*****Drilled from 18.0 to 19.0 mbsf*****				
4H	9	2030	19.0	28.5	9.5	9.74	102.5
5H	9	2100	28.5	38.0	9.5	10.12	106.5
6H	9	2145	38.0	47.5	9.5	6.23	65.6
7H	9	2230	47.5	57.0	9.5	9.27	97.6
8P	9	2350	57.0	58.0	1.0	1.00	100.0
			*****Drilled from 58.0 to 59.0 mbsf*****				
9H	10	0020	59.0	68.5	9.5	9.47	99.7
10H	10	0055	68.5	78.0	9.5	9.40	98.9
11H	10	0130	78.0	87.5	9.5	8.92	93.9
12H	10	0210	87.5	97.0	9.5	5.04	53.1
13H	10	0250	97.0	106.5	9.5	9.75	102.6
14H	10	0330	106.5	116.0	9.5	10.09	106.2
15X	10	0455	116.0	120.0	4.0	6.48	162.0
16P	10	0605	120.0	121.0	1.0	1.00	100.0
			*****Drilled from 121.0 to 122.0 mbsf*****				
17X	10	0715	122.0	129.0	7.0	6.75	96.4
18Y	10	0830	129.0	130.0	1.0	0.90	90.0
19X	10	0925	130.0	138.7	8.7	6.61	76.0
20X	10	1035	138.7	148.4	9.7	8.17	84.2
21X	10	1115	148.4	157.9	9.5	6.76	71.2
22X	10	1220	157.9	167.4	9.5	9.36	98.5
23X	10	1325	167.4	177.1	9.7	9.39	96.8
24H	10	1450	177.1	186.6	9.5	8.70	91.6
25H	10	1640	186.6	191.1	4.5	4.56	101.3
26H	10	1750	191.1	195.9	4.8	4.83	100.6
27Y	10	1935	195.9	196.9	1.0	0.15	15.0
28H	10	2030	196.9	200.7	3.8	3.80	100.0
29E	10	2220	200.7	201.7	1.0	0.20	20.0
			Cored totals:		198.7	185.31	93.3
			Drilled total:		3.0		
			Total:		201.7		
204-1245D-							
1H	11	0125	0.0	5.0	5.0	5.00	100.0
2H	11	0205	5.0	14.5	9.5	9.90	104.2
3H	11	0245	14.5	24.0	9.5	9.92	104.4
			Cored totals:		24.0	24.82	103.4
204-1245E-							
			*****Drilled from 0 to 251.5 mbsf*****				
			*****Drilled from 251.5 to 473.7 mbsf*****				
1R	13	1040	473.7	481.6	7.9	2.22	28.1
2R	13	1210	481.6	491.2	9.6	2.44	25.4
3R	13	1340	491.2	500.9	9.7	2.69	27.7
4R	13	1500	500.9	510.5	9.6	2.91	30.3
5R	13	1620	510.5	520.2	9.7	2.28	23.5
6R	13	1750	520.2	529.8	9.6	2.15	22.4
7R	13	1930	529.8	539.3	9.5	2.84	29.9
8R	13	2300	539.3	540.3	1.0	0.95	95.0
			Cored totals:		66.6	18.48	27.8
			Drilled total:		473.7		
			Total:		540.3		

Table T2. Variation of minor lithologies, lithostratigraphic Unit V.

Core	Section	Minor lithology
204-1245B-		
48X	3, 4, 5	Clayey siltstone
49X	1, 2, 3, 5	Nannofossil-rich, foraminifer-bearing siltstone or silty claystone
50X	2	Foraminifer-bearing sandstone-siltstone-claystone
50X	3, 4	Sandstone
51X	2, 3, 4, 5	Sandy siltstone to silty sandstone
52X	1, 2, 3, 4, 5, 6	Nannofossil-rich, foraminifer-bearing siltstone
53X	3	Glauconite and foraminifer-bearing sandstone-siltstone-claystone
204-1245E-		
1R	All	Foraminifer-rich silty claystone and silty sandstone
2R	All	Foraminifer-rich silty claystone and silty sandstone
6R	All	Foraminifer-rich silty claystone and silty sandstone
7R	1	Glauconite and foraminifer-bearing silty claystone

Table T3. Gas hydrate samples and their depths, Holes 1245B and 1245C.

Hole, core	Depth (mbsf)	Lithostratigraphic unit/subunit
204-		
1245B-6H	54.10	II
1245B-7H	57.44	II
1245C-10H	70.32	II
1245C-10H	74.38	II
1245C-11H	79.60	IIIA
1245B-9H	84.42	IIIA
1245C-13H	101.43	IIIA
1245C-14H	113.75	IIIA
1245C-15X	116.28	IIIA
1245C-15X	119.22	IIIA
1245B-15X	129.26	IIIA

Table T4. Bioevents, Holes 1245B and 1245E.

Age (Ma)	Bioevent	Top		Bottom		Average depth (mbsf)	Event number*	Comment
		Core, section	Depth (mbsf)	Core, section	Depth (mbsf)			
		204-1245B-		204-1245B-				
0.30	LO *Proboscia curvirostris*	4H-CC	38.70	5H-CC	46.66	42.68	1	Diatom
0.27	FO *Emiliania huxleyi*	6H-CC	55.58	7H-CC	66.33	60.96	2	Nannofossil
0.46	LO *Pseudoemiliania lacunosa*	8H-CC	76.15	9H-CC	84.79	80.47	3	Nannofossil
1.00	LO small *Gephyrocapsa* spp. Acme	16X-CC	144.82	18X-CC	156.72	150.77	4	Nannofossil
1.20	FO small *Gephyrocapsa* spp. Acme	30X-CC	271.93	31X-CC	280.33	276.13	5	Nannofossil
		204-1245E-		204-1245E-				
1.59	FO *Calcydiscus macintyrei*	5R-CC	512.73	6R-CC	522.30	517.52	6	Nannofossil

Notes: * = number in Figure F22, p. 60. FO = first occurrence, LO = last occurrence.

Table T5. Interstitial water data, Holes 1245B, 1245C, 1245D, and 1245E. (See table notes. Continued on next two pages.)

Core, section, interval (cm)	Depth (mbsf)	pH	Alkalinity (mM)	Salinity (g/kg)	Cl (mM)	SO_4 (mM)	NH_4 (mM)	PO_4 (µM)	Na (mM)	K (mM)	Mg (mM)	Ca (mM)	B (µM)	Ba (µM)	Fe (µM)	Li (µM)	Mn (µM)	Sr (µM)	DOC (mM)
204-1245B-																			
1H-2, 140–150	2.90	7.69	8.26	35	548	24.7	0.1	96	495	12.3	45.2	10.3	574	8.5	10.0	24.2	4.15	86.1	1.50
1H-5, 140–150	7.40	7.76	37.25	34	554	1.2	2.2	238	506	12.6	44.0	6.1	688	35.7	11.5	18.1	2.78	83.7	—
2H-2, 140–150	12.40	7.79	43.32	34	556	0.4	3.4	127	494	11.9	40.8	3.7	771	45.8	0.2	16.7	0.54	71.6	8.05
2H-4, 140–150	15.40	7.69	43.21	34	555	0.2	4.8	313	497	12.0	41.8	3.7	784	74.8	10.2	15.9	0.67	88.5	—
3H-2, 140–150	21.90	7.53	50.47	34	552	0.8	7.2	358	509	12.3	40.7	3.3	854	77.0	2.6	15.3	0.80	88.1	12.64
3H-5, 140–150	26.40	7.51	53.63	35	551	1.4	8.3	325	519	12.8	38.8	2.9	845	71.9	19.2	16.8	1.06	84.8	—
4H-2, 140–150	31.40	7.54	55.90	35	554	0.5	9.4	300	512	12.5	40.1	4.1	841	79.3	14.4	18.4	2.87	90.0	13.94
4H-5, 140–150	35.90	7.44	59.14	35	554	0.9	9.1	346	521	13.1	37.1	4.4	896	90.1	14.7	21.4	5.31	90.0	—
5H-2, 140–150	40.90	7.45	62.28	35	553	0.3	10.4	329	537	13.4	40.6	4.2	984	97.8	40.6	22.7	3.16	88.6	14.74
5H-5, 140–150	45.40	7.48	62.52	35	556	0.8	12.0	150	531	13.2	39.9	5.0	903	95.0	10.6	21.0	4.09	90.9	—
6H-2, 140–150	50.40	7.42	65.82	36	554	0.8	12.1	286	542	13.9	40.9	3.9	1008	111.6	17.6	23.0	3.32	92.6	15.38
6H-4, 140–150	53.40	7.60	67.29	36	556	1.2	10.6	187	533	14.3	37.5	4.4	946	109.0	9.4	23.2	4.36	83.4	—
6H-5, 78–88	54.28	7.52	55.13	30	461	0.7	10.8	219	443	11.5	32.0	3.4	909	89.3	8.2	19.9	3.22	63.8	14.22
6H-5, 88–103	54.38	7.67	57.54	33	511	0.8	12.4	197	507	13.4	32.2	2.6	863	93.1	5.1	20.4	1.69	72.1	14.38
7H-2, 140–150	58.95	7.52	66.27	35	552	0.8	13.8	168	448	12.7	36.9	3.2	1015	126.7	7.1	24.2	3.18	90.2	15.36
7H-5, 140–150	62.98	7.74	63.04	35	560	0.9	14.0	87	534	14.2	37.3	3.9	878	108.5	11.9	24.4	5.06	83.5	—
8H-2, 132–142	69.32	7.79	64.99	34	558	1.2	14.8	79	493	14.2	37.5	4.1	919	89.5	19.4	26.3	3.64	86.4	—
8H-3, 140–150	70.82	7.47	61.67	35	555	0.5	14.5	273	491	13.9	37.7	5.2	908	109.6	8.1	23.7	4.35	76.9	14.92
8H-4, 140–150	72.32	7.70	65.93	36	554	0.5	14.6	157	541	13.9	37.0	3.2	886	103.2	5.7	24.4	1.10	84.4	—
9H-2, 134–144	78.66	7.71	66.14	35	555	0.5	14.3	244	542	13.4	37.2	4.0	884	99.5	12.9	24.1	2.61	93.4	17.56
9H-4, 140–150	81.62	7.78	65.39	35	552	0.4	14.5	164	494	14.8	34.3	2.6	855	95.7	3.8	24.9	0.71	90.0	—
10H-2, 103–113	88.03	7.59	62.43	34	523	0.8	14.0	257	502	12.5	32.0	3.7	864	91.5	13.8	24.7	3.41	91.6	14.90
10H-5, 140–150	92.53	7.63	67.83	35	555	0.3	15.0	292	496	13.5	35.5	4.4	818	97.1	7.5	24.0	1.53	90.9	17.10
11H-2, 140–150	97.37	7.57	66.99	36	555	1.0	13.3	317	492	13.3	35.8	4.5	883	109.8	19.1	27.8	4.22	106.3	15.44
11H-5, 140–150	101.87	7.65	65.82	35	542	0.9	15.5	300	528	12.7	35.4	3.5	833	120.1	7.0	30.7	1.12	102.0	—
12H-2, 140–150	107.37	7.53	68.35	36	558	1.2	14.6	317	498	13.5	36.0	3.7	877	122.3	4.1	31.0	1.16	107.8	16.09
12H-5, 140–150	111.87	7.42	69.74	36	556	0.7	15.2	336	489	13.3	35.1	6.1	907	134.8	13.0	33.4	6.03	107.9	—
13H-2, 111–126	116.61	7.36	70.14	35	537	0.4	14.8	353	495	12.8	38.2	5.0	897	140.3	12.6	34.8	4.04	110.3	15.26
13H-5, 104–119	120.80	7.48	68.56	34	532	0.3	15.1	267	476	13.2	34.2	4.2	865	145.2	5.0	37.8	1.37	106.9	—
14H-1, 125–140	123.95	7.51	67.75	35	545	1.7	15.2	151	486	13.3	35.4	3.9	823	102.4	3.9	40.5	1.13	103.3	15.75
14H-2, 135–150	125.45	7.50	70.63	35	544	0.2	15.9	272	534	13.1	35.2	3.9	832	151.8	3.3	39.7	1.02	110.4	—
15X-3, 130–150	130.66	7.37	72.65	35	551	0.7	16.9	289	489	12.8	35.5	4.3	851	170.8	8.3	46.2	1.55	118.4	15.69
16X-3, 130–150	141.80	7.41	70.60	35	545	1.1	15.9	178	484	14.3	35.9	5.5	870	157.1	10.8	45.1	4.78	111.5	—
17P-1, 10–30	147.20	—	—	—	544	—	—	—	—	—	—	—	—	—	—	—	—	—	—
18X-2, 113–138	151.73	7.38	70.19	35	544	0.8	15.7	268	483	12.2	36.2	5.9	828	207.0	8.1	42.4	0.92	111.7	13.71
19X-2, 125–150	159.75	7.32	65.92	35	544	1.7	15.5	170	489	12.1	32.9	5.6	867	245.7	6.3	51.4	2.52	105.2	13.24
20X-2, 125–150	169.25	7.36	63.93	35	545	0.5	16.8	84	476	11.4	32.4	4.1	878	241.5	20.0	59.0	1.46	100.4	13.02
21X-2, 117–142	178.77	7.53	59.30	35	546	1.9	16.9	105	484	11.7	31.7	4.1	841	182.5	6.2	67.0	2.46	94.0	10.99
21X-4, 77–102	181.27	7.39	61.07	34	545	1.0	17.8	145	483	11.8	30.6	3.6	834	206.7	9.6	63.6	1.23	91.4	—
22X-5, 125–150	192.65	7.46	52.62	34	543	1.1	17.5	131	478	11.7	29.2	3.4	763	148.2	2.9	60.5	1.04	88.5	13.30
23X-5, 125–150	201.95	7.51	49.46	34	544	0.6	17.5	133	482	11.7	27.1	2.8	722	118.2	2.4	54.5	0.88	83.5	15.04
24X-2, 125–150	206.95	7.36	46.57	34	544	1.9	16.1	106	—	—	27.3	4.3	662	95.2	4.9	52.2	1.99	84.8	15.09
25X-2, 125–150	216.74	7.39	46.31	34	541	0.9	16.7	121	—	—	25.2	2.8	737	102.4	11.7	49.9	1.58	81.6	14.19
26X-5, 75–100	230.33	7.40	44.95	34	544	1.2	16.3	100	—	—	25.2	3.7	674	108.9	12.8	50.8	1.81	89.4	17.03
27X-2, 125–150	236.05	7.48	44.64	34	546	1.7	16.8	76	—	—	25.4	3.4	585	116.6	6.9	53.8	1.87	87.7	19.73
28X-2, 125–150	245.68	7.38	42.69	34	546	2.7	17.3	103	—	—	27.2	3.6	663	106.6	14.0	59.3	2.08	85.7	20.07
29X-2, 125–150	255.35	7.42	46.44	34	543	0.9	17.5	77	—	—	26.2	3.6	660	122.9	11.2	64.7	2.15	85.9	20.51
30X-2, 125–150	264.95	7.33	45.87	34	548	1.9	17.9	114	—	—	26.6	3.4	662	132.7	30.4	68.2	1.99	86.7	22.88

Table T5 (continued).

Core, section, interval (cm)	Depth (mbsf)	pH	Alkalinity (mM)	Salinity (g/kg)	Cl (mM)	SO_4 (mM)	NH_4 (mM)	PO_4 (µM)	Na (mM)	K (mM)	Mg (mM)	Ca (mM)	B (µM)	Ba (µM)	Fe (µM)	Li (µM)	Mn (µM)	Sr (µM)	DOC (mM)
31X-5, 125–150	278.76	7.39	46.37	34	549	1.5	17.8	92	—	—	26.3	3.2	616	122.1	21.8	69.4	2.08	85.4	25.01
32X-2, 125–150	284.25	7.33	44.57	33	547	3.6	17.1	110	526	11.6	27.2	3.3	605	77.7	20.2	67.6	1.78	84.6	23.43
33P-1, 80–100	292.00	—	—	—	—	—	—	—	—	—	—	—	—	—	—	—	—	—	—
34X-2, 125–150	295.95	7.38	47.32	34	548	1.6	18.8	121	531	10.0	26.7	2.7	617	113.1	12.9	73.8	1.73	83.5	25.39
35X-2, 125–150	303.55	7.64	48.63	34	551	2.0	18.9	113	536	12.0	25.1	2.6	525	114.3	12.9	77.8	1.83	85.1	25.22
36X-2, 125–150	313.15	7.39	49.91	34	548	2.7	19.4	116	529	9.9	27.5	3.4	576	109.4	16.6	78.5	1.90	85.6	20.94
37X-2, 125–150	322.75	7.27	53.88	34	548	1.7	20.1	80	530	9.9	27.7	4.4	565	134.5	9.2	84.8	3.39	95.7	22.35
38X-5, 125–150	336.95	7.59	56.57	34	550	1.7	20.5	55	533	11.3	27.4	4.3	493	177.4	13.1	83.1	2.02	103.1	18.60
39X-2, 125–150	341.95	7.37	56.44	35	546	2.6	20.6	61	532	11.2	27.9	4.7	475	161.1	8.4	82.3	1.77	102.1	19.50
40X-2, 125–150	351.65	7.33	57.50	34	546	3.5	20.6	51	552	11.4	28.1	5.0	437	167.9	10.5	80.1	1.81	103.9	17.85
41X-2, 125–150	361.25	7.41	51.94	34	548	3.7	20.6	42	477	9.3	29.9	4.7	414	40.5	6.8	83.3	2.06	100.2	17.11
42X-2, 125–150	370.95	7.34	53.90	34	545	6.1	20.4	52	526	10.4	31.4	5.1	440	18.8	6.4	81.3	2.29	93.8	17.69
43X-4, 125–150	383.55	7.35	53.31	35	554	2.7	19.7	55	528	11.1	32.1	3.3	500	183.4	5.1	116.3	1.81	99.0	16.51
44X-2, 125–150	390.15	7.52	50.28	35	552	2.8	21.8	38	529	10.5	30.2	3.8	409	224.3	4.4	119.2	2.46	94.9	16.48
45X-2, 125–150	399.85	7.35	47.32	35	554	3.8	19.3	47	521	10.3	32.1	4.0	411	45.9	3.7	134.8	1.91	87.7	13.02
47X-2, 125–150	409.80	7.31	47.16	34	—	2.7	—	28	526	10.1	31.5	4.0	553	155.0	6.7	139.2	2.09	91.3	—
48X-2, 125–150	419.05	7.27	42.24	34	554	1.9	18.2	65	526	9.9	30.8	3.9	606	142.9	5.4	149.5	1.97	91.7	13.85
49X-4, 0–25	430.11	—	—	—	545	2.5	—	—	526	9.9	29.1	3.3	616	149.9	3.7	159.0	2.14	99.1	—
50X-2, 125–150	438.27	7.37	38.16	34	—	1.9	—	—	—	—	30.3	4.4	524	192.5	8.6	157.1	2.95	99.2	—
51X-2, 125–150	447.95	7.48	36.45	34	546	2.1	17.1	30	522	9.5	31.8	4.1	528	113.9	3.9	161.8	2.13	110.2	11.84
52X-2, 125–150	457.45	7.34	32.92	34	543	3.2	15.9	17	527	9.8	32.2	4.4	462	49.0	3.2	147.7	2.24	102.8	—
53X-2, 125–150	466.51	7.53	34.78	34	548	2.8	15.2	14	513	9.7	31.9	5.4	423	77.8	3.2	151.9	2.61	107.9	9.79
204-1245C-																			
2H-5, 140–150	14.90	7.61	43.46	34	552	1.1	6.0	342	503	11.6	39.3	3.3	856	79.7	7.9	18.0	1.37	82.9	12.19
3P-1, 20–30	17.20	—	—	—	553	1.1	—	320	—	—	—	—	—	—	—	—	—	—	—
4H-5, 140–150	26.40	7.51	53.96	35	554	0.6	9.3	298	509	12.8	37.4	2.6	850	76.4	13.7	18.7	1.61	85.8	17.37
5H-5, 140–150	35.90	7.53	57.67	35	553	0.7	10.7	274	516	12.9	38.1	2.7	867	87.9	11.9	22.0	1.55	85.8	—
7H-6, 98–108	55.28	7.39	63.65	35	551	0.8	14.0	308	522	13.0	35.0	2.9	1040	114.7	8.8	23.3	2.78	84.0	—
10H-6, 0–30	74.48	7.47	66.47	36	557	0.7	15.3	306	531	14.0	36.1	3.1	1053	117.5	6.8	27.2	2.09	91.1	17.44
12H-2, 125–140	90.25	7.45	68.10	35	551	0.7	15.0	356	531	13.1	34.7	2.9	1029	94.1	12.2	26.1	1.58	97.6	—
15X-4, 130–150	120.62	7.36	73.31	36	550	1.1	15.2	345	528	12.9	36.9	3.5	955	150.3	9.1	39.3	1.94	111.5	17.58
17X-4, 110–130	127.35	7.47	72.18	35	534	—	15.4	305	—	—	36.2	3.4	841	129.0	9.6	40.5	1.82	101.2	17.65
20X-4, 75–100	143.95	7.42	73.31	36	544	—	16.1	301	—	—	36.2	4.1	912	176.2	17.7	42.5	2.21	110.3	18.23
22X-5, 125–150	165.15	7.44	66.74	35	545	—	15.0	119	—	—	34.0	4.4	679	180.7	15.7	59.1	2.29	99.3	16.39
24H-5, 125–150	184.35	7.60	62.11	35	546	—	16.9	81	—	—	30.6	3.5	721	224.0	5.0	61.4	1.82	92.5	15.93
28H-2, 80–100	199.20	7.46	50.43	34	545	—	15.5	129	—	—	28.7	4.8	743	119.8	13.0	59.2	1.96	80.8	—
204-1245D-																			
1H-1, 60–70	0.60	7.25	2.95	35	546	29.1	0.0	4	503	12.4	50.5	10.5	627	0.0	2.7	30.2	1.45	89.1	—
1H-1, 135–150	1.35	7.50	3.66	35	547	29.4	—	7	497	12.2	49.4	9.8	564	0.0	1.1	27.8	0.54	83.7	—
1H-2, 65–75	2.15	7.47	4.89	34	550	27.7	0.3	17	497	12.2	49.5	9.6	572	0.0	4.1	26.9	BDL	87.0	—
1H-2, 135–150	2.85	7.56	7.07	35	547	26.0	—	83	498	12.1	49.5	8.4	538	0.0	3.6	24.9	BDL	85.4	—
1H-3, 40–50	3.40	7.59	11.44	34	549	23.1	0.8	23	520	12.3	48.9	8.1	563	0.0	3.3	24.7	BDL	85.2	—
1H-3, 85–100	3.85	—	—	—	550	22.1	1.0	—	502	12.3	48.7	7.7	537	2.9	1.4	24.5	BDL	83.2	—
2H-1, 65–75	5.65	7.46	28.06	34	553	7.7	2.2	85	500	12.2	47.2	7.0	617	3.5	1.7	19.6	1.74	77.5	—
2H-1, 135–150	6.35	7.65	32.42	34	554	4.4	2.5	137	494	11.8	46.3	5.7	622	14.1	3.5	18.5	BDL	74.1	—
2H-2, 65–75	7.15	7.58	36.33	34	557	1.4	2.9	108	508	12.2	45.7	5.3	615	15.0	3.4	17.9	1.62	75.6	—
2H-2, 135–150	7.85	7.96	37.22	34	555	1.2	3.1	150	514	12.1	45.1	4.1	695	29.0	3.2	17.7	BDL	79.5	—
2H-3, 65–75	8.65	—	—	—	556	1.1	3.4	150	504	11.9	45.3	4.6	671	32.4	3.8	17.3	BDL	79.8	—

Table T5 (continued).

Core, section, interval (cm)	Depth (mbsf)	pH	Alkalinity (mM)	Salinity (g/kg)	Cl (mM)	SO_4 (mM)	NH_4 (mM)	PO_4 (µM)	Na (mM)	K (mM)	Mg (mM)	Ca (mM)	B (µM)	Ba (µM)	Fe (µM)	Li (µM)	Mn (µM)	Sr (µM)	DOC (mM)
2H-3, 135–150	9.35	7.88	39.23	34	558	0.9	3.6	178	506	11.9	44.5	4.1	769	43.9	3.3	17.5	BDL	80.6	—
2H-4, 135–150	10.85	7.67	39.88	34	556	0.6	4.2	192	511	11.9	43.5	3.5	726	48.4	4.7	15.8	2.62	78.0	—
2H-5, 135–150	12.35	7.49	40.82	34	554	0.8	4.8	225	510	11.8	43.9	3.8	759	55.5	3.5	16.9	BDL	81.2	—
2H-6, 135–150	13.85	7.58	44.14	34	556	0.7	5.0	265	489	12.4	44.7	3.5	762	63.2	4.9	16.1	1.34	81.3	—
3H-1, 135–150	15.85	7.46	44.60	34	555	1.1	6.7	290	493	12.5	43.5	3.5	780	63.0	4.6	16.2	1.56	82.5	—
3H-2, 135–150	17.35	7.49	46.31	34	554	0.7	7.2	328	502	12.7	43.9	3.3	871	70.3	4.3	16.6	BDL	85.1	—
3H-3, 135–150	18.85	7.51	47.39	35	554	1.1	7.5	340	501	12.1	43.6	3.3	846	64.8	2.7	15.7	BDL	81.9	—
3H-4, 135–150	20.35	7.74	48.66	35	553	1.0	8.0	346	488	11.6	42.8	3.1	862	70.7	2.5	16.6	0.06	84.3	—
3H-5, 135–150	21.85	7.41	50.32	35	554	0.8	8.4	344	494	11.8	43.4	3.5	859	68.1	16.4	15.9	—	84.4	—
204-1245E-																			
1R-1, 120–135	474.90	7.47	30.33	33	550	2.6	16.2	22	—	—	32.1	6.4	467	36.8	13.0	158.0	7.69	114.0	—
2R-1, 69–89	482.29	7.28	24.77	32	545	5.5	14.2	17	—	—	32.8	5.5	504	15.8	6.2	143.0	4.24	98.0	—
3R-1, 114–144	492.34	7.33	21.87	32	549	2.9	15.0	17	—	—	30.5	3.9	424	39.7	3.5	168.0	2.06	111.0	—
4R-1, 130–150	502.20	7.36	23.44	33	554	2.5	14.7	11	—	—	31.0	5.3	430	37.2	5.0	175.0	4.25	119.0	—
5R-1, 122–144	511.72	7.37	22.44	33	—	3.0	13.7	7	—	—	31.5	5.2	420	37.2	5.9	171.0	3.09	120.0	—
6R-1, 85–105	521.05	7.33	21.48	33	—	2.1	13.3	7	—	—	31.4	5.1	467	46.2	4.6	181.0	3.27	129.0	—
7R-1, 132–150	531.12	7.00	22.22	32	—	3.8	11.4	3	—	—	32.3	7.6	471	31.0	6.6	174.0	6.65	129.0	—

Notes: DOC = dissolved organic carbon. — = no sample was available. BDL = below detection limit.

Table T6. Concentrations of dissolved chloride in pore fluids, Hole 1245C.

Core, section, interval (cm)	Depth (mbsf)	Cl (mM)
204-1245C-		
7H-5, 32–34	53.12	531
7H-5, 35–37	53.15	500
7H-5, 37–39	53.17	399
7H-5, 41–43	53.21	304
7H-5, 42–44	53.22	73
7H-5, 44–46	53.24	298
7H-5, 47–49	53.27	466
7H-5, 50–52	53.30	539
7H-5, 58–60	53.38	550

Note: All samples collected in the vicinity of a gas hydrate layer from interval 204-1245C-7H-5, 42–44 cm.

Table T7. Concentrations of methane, ethane, ethylene, and propane in headspace gas, Holes 1245B, 1245C, 1245D, and 1245E. (See table note. Continued on next page.)

Core, section, interval (cm)	Depth (mbsf)	C_1 (ppmv)	C_2 (ppmv)	$C_{2=}$ (ppmv)	C_3 (ppmv)	C_1/C_2	C_1 (mM)
204-1245B-							
1H-1, 0–5	0.0	11.0					0.001
1H-2, 0–5	1.5	5.3					0.000
1H-3, 0–5	3.0	8.7					0.002
1H-4, 0–5	4.5	14.1					0.002
1H-5, 0–5	6.0	42.0					0.01
1H-6, 0–5	7.5	1,321	0.5			2,540	0.20
1H-7, 0–5	8.5	9,964	0.7			15,329	1.13
2H-2, 0–5	11.0	24,698	1.2			20,244	3.66
2H-3, 0–5	12.5	56,500	1.1	0.5	0.4	50,000	5.34
2H-5, 0–5	15.5	39,855	1.9			20,866	5.64
3H-2, 0–5	20.5	30,224	1.4	0.6		22,388	3.39
3H-6, 0–5	26.5	15,643	0.5			34,007	3.13
4H-3, 0–5	31.5	16,351	0.8	0.9		21,801	2.89
4H-6, 0–5	36.0	14,612	0.7	0.6		20,580	3.01
5H-3, 0–5	41.0	13,356	0.7	0.6		20,236	2.08
5H-6, 0–5	45.5	13,687	0.7	0.8		21,057	3.14
6H-4, 0–5	52.0	17,831	0.8	0.5		21,745	2.27
7H-3, 0–5	59.1	15,347	0.6	0.5	0.5	26,012	2.46
7H-6, 0–5	63.1	12,012	0.7			18,480	
8H-3, 0–5	69.4	15,354	0.6		0.7	26,024	2.89
8H-6, 0–5	73.9	16,066	0.8			20,337	2.72
9H-5, 0–5	81.7	13,713	0.5			27,426	2.06
10H-3, 0–5	88.1	11,178	0.6			20,324	2.49
11H-3, 0–5	97.5	10,995	0.7			16,410	2.03
12H-3, 0–5	107.5	10,000	0.6			17,241	1.92
13H-3, 0–5	116.8	15,338	1.6		5.3	9,769	2.53
13H-6, 0–5	121.0	14,049	3.5		7.0	4,049	3.23
14H-2, 0–5	124.1	10,437	8.2		9.0	1,279	1.83
14H-4, 0–5	127.0	11,575	18.2		14.1	637	2.49
15X-4, 0–5	130.9	12,689	200		106	63	1.78
16X-2, 0–5	139.0	8,491	242		159	35	1.52
16X-4, 0–5	142.0	85,022	557		166	153	10.57
18X-4, 0–5	153.5	12,731	182	0.5	144	70	2.02
19X-2, 0–5	158.5	10,320	232		370	44	1.59
20X-3, 0–5	169.5	15,862	225	0.4	430	70	1.84
21X-3, 0–5	179.0	15,891	203	5.0	320	78	2.11
22X-3, 0–5	188.4	10,261	74.6	0.7	101	138	1.80
23X-3, 0–5	197.7	17,222	70.3		75.8	245	2.15
24X-3, 0–5	207.2	14,388	28.6		25.1	504	1.98
25X-3, 0–5	217.0	15,707	22.4		18.2	700	2.27
26X-3, 0–5	226.6	11,405	7.7			1,485	2.27
27X-3, 0–5	236.3	14,328	7.3			1,971	2.09
28X-3, 0–5	245.9	6,166	3.4	0.5		1,830	1.70
29X-3, 0–5	255.6	10,400	3.7			2,796	2.91
30X-3, 0–5	265.2	19,945	10.2	1.18	6.5	1,965	2.79
31X-3, 0–5	274.8	7,521	4.7	0.5		1,607	2.67
32X-3, 0–5	284.5	11,519	6.8	1.3		1,699	1.94
34X-3, 0–5	296.2	10,809	4.0	0.7		2,696	2.28
35X-3, 0–5	303.8	14,797	6.3	0.6		2,360	2.09
36X-3, 0–5	313.4	44,994	7.8			5,798	7.72
37X-3, 0–5	323.0	66,367	15.4	1.0		4,324	7.30
38X-3, 0–5	332.7	20,203	10.5	1.4		1,931	2.89
39X-3, 0–5	342.2	2,868	3.5	0.8		827	0.62
40X-3, 0–5	351.9	3,170	2.2			1,447	1.23
41X-3, 0–5	361.5	1,278	2.3			561	0.42
42X-3, 0–5	371.2	14,071	8.3	0.7		1,706	3.12
43X-3, 0–5	380.8	3,305	3.6	0.8		923	1.24
44X-3, 0–5	390.4	8,502	8.4	0.5		1,016	1.58
45X-3, 0–5	400.1	4,042	3.8			1,053	2.17
47X-3, 0–5	410.1	32,965	35.6		11.3	925	3.24
48X-3, 0–5	419.3	20,050	21.6	0.1	6.7	927	2.54
49X-3, 0–5	428.6	24,534	17.2	0.5	5.7	1,428	4.18
50X-3, 0–5	438.5	14,841	21.2	0.7	9.1	701	2.71
51X-3, 0–5	448.2	16,085	22.4	0.5	9.5	720	2.65
52X-3, 0–5	457.7	26,830	35.6		12.6	754	3.26

Table T7 (continued).

Core, section, interval (cm)	Depth (mbsf)	C_1 (ppmv)	C_2 (ppmv)	$C_{2=}$ (ppmv)	C_3 (ppmv)	C_1/C_2	C_1 (mM)
53X-3, 0–5	466.8	3,998	11.2		6.8	359	1.51
204-1245C-							
1H-1, 0–5	0.0	110,278	193			573	15.6
1H-2, 15–16	1.6	443	1.1			396	0.1
1H-3, 110–111	4.0	33.0					0.0
1H-6, 61–66	7.5	7,086	0.6			12,432	1.6
2H-2, 0–5	9.0	36,225	1.1			33,855	5.1
2H-3, 0–5	10.5	58,291	1.4			41,341	7.2
2H-4, 0–5	12.0	40,818	1.2			34,015	7.2
2H-6, 0–5	15.0	27,002	1.0	0.4		27,002	3.4
4H-3, 0–5	22.0	23,683	1.6	0.4		15,279	3.9
4H-6, 0–5	26.5	27,079	1.1	0.7		24,395	4.1
5H-3, 0–5	31.5	12,696					1.9
5H-6, 0–5	36.0	17,341		0.6			2.9
6H-2, 0–5	38.7	12,901	0.9			14,334	2.0
7H-3, 0–5	50.5	10,928		0.5			2.0
9H-3, 0–5	62.0	15,583	0.5	0.4		30,555	2.4
10H-3, 0–5	70.5	13,363	0.6	0.3		23,040	2.4
11H-5, 0–5	82.8	13,329					2.1
12H-3, 0–5	90.5	5,456					0.9
13H-3, 0–5	99.9	23,672	1.2	0.6	1.1	19,564	3.4
14H-3, 0–5	109.5	14,637	0.7	0.3		20,329	2.2
15X-5, 0–5	120.8	12,676	2.7		6.4	4,626	2.0
17X-3, 0–5	124.8	14,448	38.2	1.1	42.8	379	2.0
19X-2, 0–5	131.5	10,651	170	0.8	123	63	2.3
20X-3, 0–5	141.7	12,655	169	0.6	83.9	75	2.7
21X-3, 0–5	151.4	13,334	208	0.5	127	64	2.3
22X-3, 0–5	160.9	10,189	175	0.4	170	58	2.1
23X-3, 0–5	170.4	11,144	120	0.4	118	93	2.6
24H-3, 0–5	180.1	25,673	195	0.5	172	131	4.7
25H-3, 0–5	189.6	11,288	53.2		54.1	212	2.7
26H-3, 0–5	194.1	21,203	93.7	1.3	92.6	226	4.1
28H-2, 0–5	198.4	15,348	40.5		29.8	379	2.8
204-1245D-							
1H-1, 0–5	0.0	3.7					0.0
1H-1, 145–150	1.5	4.7					0.0
1H-2, 145–150	3.0	11.1					0.0
1H-3, 95–100	4.0	18.3					0.0
1H-4, 63–68	4.6	44.5					0.0
2H-1, 0–5	5.0	45.8					0.0
2H-1, 145–150	6.5	574					0.1
2H-2, 145–150	8.0	5,547					1.3
2H-3, 145–150	9.5	18,973					3.9
2H-4, 145–150	11.0	32,631					
2H-5, 145–150	12.5	35,015	0.9			37,250	5.9
2H-6, 145–150	14.0	50,188	1.3			38,905	6.6
3H-1, 145–150	16.0	27,268	0.7			41,951	
3H-2, 145–150	17.5	46,175	1.1			41,977	7.9
3H-3, 145–150	19.0	31,980	1.0			32,303	7.0
3H-4, 145–150	20.5	37,036	0.9			40,699	7.0
3H-5, 145–150	22.0	42,508	1.2			36,024	5.6
3H-6, 145–150	23.5	18,016	0.3			52,988	2.3
204-1245E-							
1R-2, 0–5	475.1	29,596	69.5		60.1	426	
2R-2, 0–5	482.5	62,035	91.7		68.4	676	
3R-2, 0–5	492.6	101,321	85.3		51.8	1,188	
4R-2, 0–5	502.4	59,595	53.2		25.8	1,121	
5R-2, 0–5	511.9	93,043	87.7		41.9	1,061	
6R-2, 0–5	521.3	63,888	73.8		37.0	865	
7R-2, 0–5	531.3	36,334	48.9		18.4	742	
8R-1, 75–80	540.1	89,538	89.9		30.8	996	

Note: C_1 = methane, C_2 = ethane, $C_{2=}$ = ethylene, C_3 = propane.

Table T8. Concentrations of light hydrocarbon and nonhydrocarbon gases in VAC samples of core gas voids, Holes 1245B, 1245C, and 1245D. (**See table note.** Continued on next page.)

Core, section, interval (cm)	Depth (mbsf)	C_1 (ppmv)	C_2 (ppmv)	C_3 (ppmv)	*i*-C_4 (ppmv)	*n*-C_4 (ppmv)	*i*-C_5 (ppmv)	*n*-C_5 (ppmv)	H_2S (ppmv)	CO_2 (ppmv)	O_2 (ppmv)	N_2 (ppmv)	C_1/C_2
204-1245B-													
3H-6, 46	26.96	936,942	5.7	3.2						23,478	224	19,601	165,830
4H-1, 135	29.85	940,837	5.3							20,024	278	25,114	176,849
6H-2, 50	49.50	562,155	13.9	1.9						57,723	8,289	298,502	40,327
7H-4, 78	61.22	965,611	19.9							5,250	190	6,191	48,548
8H-3, 80	70.22	883,221	14.3							7,477	9,528	73,285	61,591
10H-1, 133	86.83	965,871	14.0							7,914	213	7,526	69,238
11H-3, 97	98.44	965,618	10.7							7,855	191	7,675	90,160
12H-5, 81	111.28	969,764	7.2							12,375	110	4,911	133,945
13H-3, 33	117.09	941,924	110.6	5.7						3,989	1,275	36,421	8,516
14H-3, 50	126.10	827,709	269.7	53.1						24,087	3,621	120,542	3,069
16X-2, 57	139.57	891,225	2,935.6	377.0	54.0	73.0	11.9						304
16X-2, 122	140.22	948,659	3,480.0	574.0	85.4	109.2	15.8			22,683		11,093	273
18X-2, 3	150.63	939,130	2,643.0	532.1	61.5	65.1	10.1			25,842		12,345	355
19X-3, 121	161.21	918,094	5,394.0	9,794.0	3,333.0	385.0	72.5			31,134		16,270	170
20X-5, 99	173.49	892,334	2,318.0	1,548.0	450.5	197.9	85.0			36,576	2,320	86,117	385
21X-4, 15	180.65	965,919	1,136.0	576.1	99.7	72.7	7.2						850
22X-4, 80	190.70	977,833	679.7	318.0	66.0	64.1	24.2	6.4		3,561	751	7,224	1,439
23X-1, 50	195.20	643,870	459.4	210.7	38.9	43.9	15.8	5.8		188,550	3,696	46,789	1,401
26X-2, 91	225.99	971,736	153.4	30.7	4.9					6,232	130	1,080	6,333
28X-4, 139	248.82	898,915	99.9	5.5						17,951	96	1,065	8,999
29X-2, 81	254.91	966,721	101.3	4.6	5.9					12,091	119	1,074	9,539
29X-3, 16	255.76	970,926	105.2	25.8									9,229
29X-5, 15	258.75	981,051	92.4	7.4	5.9					4,885	64	776	10,616
30X-6, 84	270.48	937,660	101.1	6.8	5.0					15,511	4,771	20,246	9,279
31X-2, 48	273.88	957,410	92.3	13.6						16,996	124	1,283	10,372
32X-2, 94	283.94	960,673	95.4	11.0						15,681	138	1,302	10,066
34X-6, 68	301.38	894,180	59.8	2.0						4,815	117	1,311	14,953
35X-5, 0	306.80	856,612	62.8	5.9									13,640
37X-4, 112	325.62	966,746	89.6	9.3						11,395	2,169	1,473	10,788
38X-5, 125	336.95	961,609	98.4	6.9						16,284	665	1,080	9,770
40X-5, 0	354.87	590,713	50.0	6.5						2,619	87,056	324,228	11,826
41X-5, 1	363.34	952,457	108.1	7.7						16,912	416	23,985	8,808
42X-2, 48	370.00	962,674	121.3	10.9						20,270	239	9,290	7,934
44X-1, 39	387.79	947,680	154.1	0.0						29,245	307	11,802	6,150
45X-4, 17	401.77	952,909	135.3	14.4	10.1					11,600	357	18,281	7,043
47X-4, 1	411.23	964,361	142.3	15.1	8.8					10,921	163	7,144	6,777
48X-3, 77	420.07	622,715	125.6	15.4	9.3					12,235	77,028	288,860	4,958
49X-4, 3	430.14	953,359	220.8	32.8	19.1					15,346	2,563	5,107	4,318
50X-1, 130	436.90	829,521	219.0	36.1	17.8					21,069	30,516	110,859	3,789
50X-4, 40	440.13	796,911	220.2	45.4	25.3					18,614	37,480	139,494	3,619
51X-3, 125	449.45	956,303	277.8	53.6	23.9					17,033	1,540	1,593	3,443
52X-3, 140	459.10	970,149	281.9	55.8	28.6					6,495	487	1,161	3,442
53X-5, 14	469.90	962,618	314.3	55.3	23.1								3,063
204-1245C-													
5H-1, 47	28.97	928,871	5.1	7.9						29,371	2,677	18,564	181,066
5H-7, 37	37.83	725,273	4.9	6.9						24,317	49,792	187,843	148,015
7H-1, 126	48.76	968,029	21.8							6,169	228	1,053	44,446
9H-5, 61	65.61	963,272	8.4	1.7						9,841	458	1,144	114,403
10H-4, 100	72.97	959,006	18.1	1.2						2,956	783	5,650	53,101
11H-5, 105	83.85	963,897	18.7							3,832	467	1,188	51,600
13H-4, 26	101.13	942,990	4.6							16,719	646	2,529	205,444
14H-3, 70	110.20	962,399	23.7	10.7						5,255	1,969	1,739	40,556
15X-5, 123	122.05	880,627	77.2	82.6	6.8					49,192	8,429	32,105	11,401
17X-2, 50	124.00	950,254	428.0	110.9	5.5					15,702	1,204	1,995	12,303
19X-2, 12	131.62	912,946	4,554.4	1,211.7	274.4	416.4	134.0			46,053	1,880	6,530	200
20X-3, 3	141.73	947,880	2,774.0	515.7	45.4	52.8	6.8			14,319	1,916	1,557	342
21X-2, 131	151.21	923,161	3,651.4	966.5	139.2	155.8	42.1			46,128	2,173	1,610	253
22X-5, 49	164.39	964,767	3,092.3	1,282.5	232.4	228.9	75.7			7,878	318	825	264
23X-3, 70	171.10	951,404	2,786.4	1,148.9	190.7	223.7	80.8			22,521	798	1,006	341
24H-6, 69	185.29	935,185	1,909.3	861.1	170.8	174.2	66.6			32,448	1,677	2,491	490
25H-3, 63	190.23	756,895	897.1	373.0	36.9	38.1				30,656	41,050	157,698	844
26H-1, 135	192.45	952,034	831.6	287.0	26.7	22.0	7.7			15,269		618	1,145
28H-1, 113	198.03	887,177	429.3	116.4	13.2	12.7				5,025	512	961	2,067

Table T8 (continued).

Core, section, interval (cm)	Depth (mbsf)	C_1 (ppmv)	C_2 (ppmv)	C_3 (ppmv)	*i*-C_4 (ppmv)	*n*-C_4 (ppmv)	*i*-C_5 (ppmv)	*n*-C_5 (ppmv)	H_2S (ppmv)	CO_2 (ppmv)	O_2 (ppmv)	N_2 (ppmv)	C_1/C_2
204-1245D-													
3H-1, 12	14.62	753,607	4.9						1,478.0	15,851	40,864	179,913	154,428
3H-7, 51	24.01	902,132	5.4							30,030	8,263	37,866	166,445

Note: C_1 = methane, C_2 = ethane, C_3 = propane, *i*-C_4 = isobutane, *n*-C_4 = normal butane, *i*-C_5 = iso-pentane, *n*-C_5 = normal pentane, H_2S = hydrogen sulfide, CO_2 = carbon dioxide, O_2 = oxygen, N_2 = nitrogen.

Table T9. Composition of gas from analyses of decomposed samples of gas hydrate, Holes 1245B and 1245C.

Core, section, interval (cm)	Depth (mbsf)	C_1 (ppmv)	C_2 (ppmv)	C_3 (ppmv)	*i*-C_4 (ppmv)	*n*-C_4 (ppmv)	*n*-C_5 (ppmv)	*n*-C_6 (ppmv)	CO_2 (ppmv)	O_2 (ppmv)	N_2 (ppmv)	C_1/C_2
204-1245B-												
6H-5, 103	53.5	811,962	13.4						3,737	28,288	132,907	60,730
9H-CC	84.8	939,965	20.7						2,238	10,643	36,935	45,431
204-1245C-												
7H-5, 40	53.2	226,987							3,222	157,857	606,919	
13H-4, 56–76	101.4	945,471	19.9						3,674	4,442	9,742	47,463

Note: C_1 = methane, C_2 = ethane, C_3 = propane, *i*-C_4 = isobutane, *n*-C_4 = normal butane, *n*-C_5 = normal pentane, *n*-C_6 = normal hexane, CO_2 = carbon dioxide, O_2 = oxygen, N_2 = nitrogen.

Table T10. Composition of gas samples from PCS experiments, Holes 1245B and 1245C.

Sample	Volume (mL)	C_1 (ppm)	C_2 (ppm)	C_3 (ppm)	*i*-C_4 (ppm)	*n*-C_4 (ppm)	*i*-C_5 (ppm)	*n*-C_5 (ppm)	O_2 (ppm)	N_2 (ppm)	CO_2 (ppm)	C_1/C_2
204-1245B-17P (147.1 mbsf)												
G1	35	162,032	255	77.9					532,114	179,217	661	427
G2	230	914,168	2,388	226	20.9	19.7			401	61,760	1,039	
G3	360	959,519	2,293	276	28.0	26.5			89	14,400	2,370	
G4	470	841,609	1,867	346	34.2	30.2			5,004	56,562	3,051	
G5	290	891,726	1,947	378	39.6	36.7			1,828	82,777	5,422	
G6	120	739,309	1,649	305	29.9	29.3			7,401	105,229	3,908	
G7	195	688,167	1,778	406	44.9	40.0			63,930	219,608	4,406	
204-1245B-33P (291.2 mbsf)												
G1	145	815,141	185	38.3					23,239	159,993	3,404	9,366
G2	200	954,143	85.9	6.4					584	28,592	1,339	
G3	200	959,964	72.0	9.0					317	22,379	1,599	
G4	280	964,083	80.5	12.9					281	18,982	2,470	
G5	120	956,861	87.1	13.9					578	25,174	5,714	
G6	120	954,431	88.3	14.6					1,510	20,389	4,480	
204-1245C-3P (17.0 mbsf)												
G1	315	700,557	14.4	8.5					24,385	267,649	2,475	21,187
204-1245C-8P (57.0 mbsf)												
G1	70	450,834	6.1						87,858	456,942	976	32,594
G2	220	896,327	5.0						11,002	79,838	869	
G3	320	870,778	148	8.8		5.7			20,647	83,941	793	
G4	320	887,127	6.0						11,134	76,030	885	
G5	210	899,704	6.3						5,821	65,291	2,096	
G6	150	887,386	16.0						4,470	62,667	2,509	
G7	80	880,800	7.7						5,652	71,857	2,677	
G8	90	850,832	8.1						6,677	76,732	2,759	
1245C-16P (120.0 mbsf)												
G1	110	435,628	53.4	9.4					57,711	497,409	761	3,372
G2	210	909,066	172	17.6					10,046	58,948	567	
G3	420	961,719	228	19.1					95	9,206	322	
G4	600	962,915	230	18.6					696	8,437	259	
G5	350	944,449	233	17.5					7,452	21,038	366	
G6	340	949,772	245	18.4					5,339	17,380	310	
G7	350	923,146	216	19.6					2,985	12,514	279	
G8	420	953,261	279	19.0					2,173	10,454	301	
G9	440	952,527	255	18.6					1,829	8,895	309	
G10	390	941,006	258	18.8					7,382	21,831	375	
G11	340	951,346	263	20.1					3,345	12,881	384	
G12	480	934,755	258	17.5					10,025	23,803	385	
G13	370	957,017	290	17.7					2,012	8,399	402	
G14	390	955,475	267	15.3					1,850	8,947	331	
G15	720	959,518	276	19.6					760	3,852	324	
G16	600	941,737	284	19.5					6,949	13,277	447	
G17	940	922,488	285	21.2					11,771	26,376	459	
G18	1,010	948,264	306	18.9					3,636	9,736	536	
G19	1,015	954,929	298	16.0					1,011	5,831	703	
G20	970	951,118	311	14.2					802	5,441	866	
G21	1,070	954,353	310	18.6					107	5,172	1,215	
G22	870	936,476	292	23.8					137	6,384	1,227	
G23	990	954,042	314	19.1					164	6,432	1,698	
G24	1,050	928,148	330	21.8					5,523	30,934	2,239	
G25	970	941,091	301	23.1					2,784	17,927	3,217	
G26	730	916,747	290	24.4					7,000	40,721	3,443	
G27	950	924,615	302	23.0					1,996	34,843	4,962	
G28	910	905,325	297	23.3					6,324	50,350	6,093	
G29	420	902,677	317	21.1					5,676	53,774	7,291	
G30	190	912,392	354	30.8					1,156	20,435	13,608	
G31	410	909,907	366	32.0					1,486	23,965	14,481	

Note: C_1 = methane, C_2 = ethane, C_3 = propane, *i*-C_4 = iso-butane, *n*-C_4 = normal butane, *i*-C_5 = iso-pentane, *n*-C_5 = normal pentane, O_2 = oxygen, N_2 = nitrogen, CO_2 = carbon dioxide.

Table T11. Carbonate carbon, calcium carbonate, total carbon, organic carbon, total nitrogen, and total sulfur contents and C/N ratios, Holes 1245B and 1245E.

Core, section, interval (cm)	Depth (mbsf)	Carbonate carbon (wt%)	$CaCO_3$ (wt%)	Total carbon (wt%)	Organic carbon (wt%)	Total nitrogen (wt%)	Total sulfur (wt%)	C/N
204-1245B-								
1H-3, 77–78	3.77	1.25	10.41	2.14	0.89	0.13	1.23	6.85
3H-5, 77–78	25.77	NA	NC	2.09	NC	0.17	0.36	NC
6H-3, 48–49	50.98	NA	NC	1.69	NC	0.22	0.40	NC
9H-1, 75–76	76.75	NA	NC	1.57	NC	0.15	0.27	NC
12H-5, 76–77	111.23	0.89	7.39	1.60	0.71	0.12	0.15	5.92
13H-5, 77–78	120.53	0.39	3.29	1.33	0.94	0.20	0.51	4.70
15X-3, 77–78	130.13	0.47	3.90	1.90	1.43	0.20	0.47	7.15
16X-3, 77–78	141.27	0.30	2.49	1.56	1.26	0.17	0.22	7.41
18X-3, 77–78	152.75	0.39	3.28	1.25	0.86	0.14	0.12	6.14
19X-4, 77–78	162.27	0.14	1.19	1.41	1.27	0.17	0.32	7.47
22X-1, 76–77	186.16	0.64	5.34	2.00	1.36	0.18	0.65	7.56
26X-1, 30–31	224.00	0.77	6.44	1.67	0.90	0.15	0.23	6.00
26X-3, 84–85	227.42	0.81	6.71	1.71	0.90	0.15	0.19	6.00
28X-5, 73–74	249.66	0.79	6.56	1.70	0.91	0.14	0.16	6.50
29X-5, 77–78	259.37	0.86	7.20	1.92	1.06	0.20	0.21	5.30
31X-3, 74–75	275.54	0.92	7.68	2.08	1.16	0.17	0.25	6.82
35X-1, 61–62	301.41	0.88	7.34	2.26	1.38	0.19	0.28	7.26
37X-4, 66–67	325.16	0.56	4.67	1.90	1.34	0.21	0.33	6.38
204-1245E-								
1R-1, 17–18	473.87	0.60	5.00	1.88	1.28	0.18	0.37	7.11
2R-2, 12–13	482.61	1.21	10.08	2.45	1.24	0.18	0.19	6.89
3R-1, 69–70	491.89	1.36	11.29	NA	NC	NA	NA	NC
4R-1, 74–75	501.64	1.47	12.22	2.43	0.96	0.15	0.17	6.40
5R-1, 49–50	510.99	1.80	15.00	2.73	0.93	0.13	0.27	7.15
6R-1, 48–49	520.68	3.06	25.48	3.92	0.86	0.11	0.07	7.82
6R-2, 64–65	521.89	1.17	9.76	2.18	1.01	0.15	0.28	6.73
7R-2, 77–78	532.07	0.30	2.51	1.76	1.46	0.17	0.87	8.59
8R-1, 45–46	539.75	0.47	3.95	1.88	1.41	0.16	0.97	8.81

Notes: NA = not analyzed, NC = not calculated. $CaCO_3$ = calcium carbonate.

Table T12. Rock-Eval pyrolysis of samples, Holes 1245B and 1245E.

Core, section, interval (cm)	Depth (mbsf)	Organic carbon (wt%)	S_1 (mg/g)	S_2 (mg/g)	Production index ($S_1/[S_1+S_2]$)	Hydrogen index (mg S_2/g C)	T_{max} (°C)
204-1245B-							
1H-3, 77–78	3.77	0.89	0.27	1.61	0.14	181	394
13H-5, 77–78	120.53	0.94	0.24	1.98	0.11	211	519
15X-3, 77–78	130.13	1.43	0.35	1.83	0.16	128	413
16X-3, 77–78	141.27	1.26	0.36	2.17	0.14	172	468
18X-3, 77–78	152.75	0.86	0.12	1.58	0.07	184	547
19X-4, 77–78	162.27	1.27	0.15	1.80	0.08	142	414
22X-1, 76–77	186.16	1.36	0.29	1.61	0.15	118	412
26X-1, 30–31	224.00	0.90	0.12	0.92	0.12	102	410
28X-5, 73–74	249.66	0.91	0.10	0.88	0.10	97	418
35X-1, 61–62	301.41	1.38	0.28	1.84	0.13	133	411
204-1245E-							
2R-2, 12–13	482.61	1.24	0.28	2.75	0.09	222	412
7R-2, 77–78	532.07	1.46	0.37	3.06	0.11	210	410

Notes: NA = not analyzed. S_1 and S_2 are as defined in "Organic Matter Characterization," p. 18, in "Organic Geochemistry" in the "Explanatory Notes" chapter.

Table T13. Intervals sampled for microbiology, Holes 1245B, 1245C, and 1245D.

Core, section, interval (cm)	Depth (mbsf)
204-1245B-	
22X-5, 0–125	191.40
23X-5, 0–95	200.70
26X-5, 0–75	229.58
31X-5, 0–125	277.51
38X-5, 0–125	335.70
43X-4, 0–125	382.30
49X-4, 25–144	430.36
204-1245C-	
2H-5, 0–140	13.50
4H-5, 100–140	26.00
5H-5, 81–140	35.31
7H-6, 0–77	54.30
10H-6, 30–100	74.78
12H-2, 50–125	89.50
15X-4, 0–130	119.32
17X-4, 0–110	126.25
20X-4, 0–75	143.20
22X-5, 0–125	163.90
24H-5, 0–125	183.10
28H-2, 0–80	198.40
204-1245D-	
1H-1, 0–60	0.00
1H-1, 70–135	0.70
1H-2, 0–65	1.50
1H-2, 75–135	2.25
1H-3, 0–85	3.00
1H-4, 0–68	4.00
2H-1, 0–65	5.00
2H-1, 75–135	5.75
2H-2, 0–65	6.50
2H-2, 75–135	7.25
2H-3, 0–65	8.00
2H-3, 75–135	8.75
2H-4, 0–135	9.50
2H-5, 0–135	11.00
2H-6, 0–135	12.50
2H-7, 0–60	14.00
3H-1, 0–135	14.50
3H-2, 0–135	16.00
3H-3, 0–135	17.50
3H-4, 0–135	19.00
3H-5, 0–135	20.50
3H-6, 0–135	22.00

Table T14. PFT concentration in intervals sampled for microbiology, Holes 1245B, 1245C, and 1245D.

Core, section, interval (cm)	Depth (mbsf)	PFT per sample (ag)		Microspheres per gram	
		Inside core	Outer edge	Inside core	Outer edge
204-1245B-					
23X-5, 85–95	201.55	NS	NS	51	17,800
26X-5, 65–75	230.23	NS	NS	58	10,300
31X-5, 130–140	278.81	0.00032	94	BDL	6,100
38X-5, 0–125	335.70	570	11	BDL	7,720
43X-4, 100–110	383.30	BDL	11,000	543	16,000
204-1245C-					
2H-5, 130–140	14.80	NS	NS	BDL	3,810
4H-5, 130–140	26.30	NS	NS	BDL	20,000
5H-5, 130–140	35.80	BDL	30,000	15	18,000
7H-6, 90–100	55.20	1,500	490	BDL	4,340
10H-6, 30–40	74.78	NS	NS		BDL
12H-2, 115–125	90.15	0.0018	26	BDL	16,400
15X-4, 0–135	119.32	NS	NS		BDL
17X-4, 0–130	126.25	NS	NS		BDL
20X-4, 75–100	143.95	9,200	65	BDL	5,380
22X-5, 25–45	164.15	0.000064	0.0028	BDL	5,570
24H-5, 120–130	184.30	310	0.96	BDL	135,000
28H-2, 45–50	198.85	0.52	2.6	BDL	17,108
204-1245D-					
1H-3, 65–75	3.65	BDL	0.0018	UD	UD
2H-2, 115–125	7.65	BDL	0.00025	UD	UD
3H-2, 120–135	17.20	0.0051	6.5	BDL	1,000
3H-5, 140–150	21.90	BDL	3,200	BDL	3,750

Notes: PFT = perfluorocarbon tracer. ag = attograms. NS = not sampled, BDL = below detection limit, UD = unsuccessful deployment.

Table T15. Presence of gas hydrate based on infrared images of cores in liners, Holes 1245B and 1245B. (**See table notes.** Continued on next page.)

Core, section	ΔT (°C)	Gas hydrate texture*	Depth interval (mbsf)† Top	Depth interval (mbsf)† Bottom	Anomaly designation‡	Hydrate sample Top (cm)	Hydrate sample Bottom (cm)	Hydrate sample Depth (mbsf)
204-1245B-								
6H	–2.1	Disseminated	51.50	51.60	IR218			
6H	–2.5	Disseminated; nodular	51.80	51.85	IR219			
6H	–1.5	Disseminated	52.40	52.50	IR220			
6H	–2.5	Disseminated	52.80	53.10	IR221			
6H	–1.0	Nodular	53.95	54.00	IR222			
6H-5	–9.4	Nodular on steeply dipping plane	54.35	54.50	IR223	60	78	54.10
7H-1	–4.1	Nodular; two separate pieces	57.10	57.30	IR224	44	55	57.44
7H	–6.0	Nodular or vein overlying disseminated	62.10	62.60	IR225			
7H	–0.7	Disseminated	64.50	64.80	IR226			
8H	–3.4	Disseminated	70.85	71.20	IR227			
8H	–0.8	Disseminated	73.90	73.95	IR228			
8H	–0.8	Disseminated; fracture in middle	75.20	75.27	IR229			
9H	–1.6	Disseminated	78.30	78.55	IR230			
9H	–1.5	Disseminated	79.20	79.25	IR231			
9H	–1.0	Disseminated	79.65	79.80	IR232			
9H	–1.5	Disseminated	81.00	81.10	IR233			
9H	–2.4	Disseminated and dipping vein	82.90	83.25	IR234			
9H-CC	–4.8	Nodular or vein	84.70	84.75	IR235	0	10	84.42
10H	–2.6	Disseminated	94.40	94.50	IR236			
10H	–4.4	Disseminated	85.95	86.15	IR237			
10H	–3.0	Disseminated	87.60	87.70	IR238			
10H-4	–1.5	Disseminated	88.20	88.35	IR239			
10H	–1.3	Disseminated	89.60	89.80	IR240			
10H	–1.4	Disseminated	90.55	90.75	IR241			
10H	–1.2	Nodular	91.35	91.40	IR242			
10H	–4.0	Nodular	91.70	91.80	IR243			
11H	–0.9	Disseminated	99.80	99.87	IR244			
11H	–2.9	Disseminated	101.90	102.15	IR245			
12H	–1.5	Disseminated	108.25	108.40	IR246			
12H	–2.6	Nodular	113.40	113.55	IR247			
13H	–0.9	Disseminated	115.38	115.42	IR248			
13H	–0.5	Disseminated	116.90	116.95	IR249			
13H	–1.0	Disseminated	117.55	117.65	IR250			
13H	–1.5	Disseminated	119.75	119.85	IR251			
13H	–2.1	Disseminated with voids	121.30	121.50	IR252			
15X-3	–6.0	Nodular adjacent to void and steeply dipping fracture (?)	129.10	129.40	IR253	46	56	129.26
204-1245C-								
7H	–1.1	Disseminated	48.88	48.91	IR254			
7H	–0.7	Disseminated; layered	49.30	49.80	IR255			
7H	–2.3	Disseminated; layered; nodular	50.00	50.80	IR256			
7H	–2.4	Disseminated	51.25	51.60	IR257			
7H	–3.5	Vein; parallel to bedding	53.90	54.10	IR258			
9H	–0.6	Disseminated	60.58	60.62	IR259			
9H	–4.1	Disseminated; vein	61.80	61.87	IR260			
9H	–0.8	Vein parallel to bedding	63.03	63.10	IR261			
9H	–0.9	Disseminated	63.50	63.83	IR262			
10H-2	–1.7	Nodular	70.80	70.92	IR263	40	55	70.32
10H	–0.7	Disseminated	71.85	71.89	IR264			
10H-5	–1.2	Vein; low dip sharp top; gradational bottom	72.38	72.41	IR265	99	105	74.38
10H	–1.3	Disseminated; parting in center	74.80	74.95	IR266			
10H	–1.3	Vein; multiple layers	77.79	77.85	IR267			
11H	–2.2	Vein; moderate dip	78.01	78.02	IR268			
11H	–3.7	Nodular; parting both sides	79.10	79.20	IR269			
11H-2	–2.3	Disseminated	79.99	80.11	IR270	52	72	79.60
11H	–4.6	Nodular	80.59	80.82	IR271			
11H	–1.2	Disseminated	82.65	82.72	IR272			
11H	–2.1	Disseminated	82.97	83.05	IR273			
11H	–2.0	Disseminated	86.38	86.49	IR274			
11H	–1.7	Nodular; two separate parts	87.10	87.30	IR275			
12H	–1.6	Disseminated	91.47	91.85	IR276			
12H	–1.6	Disseminated	93.11	93.21	IR277			
12H	–0.6	Disseminated	95.05	95.11	IR278			
12H	–0.5	Nodular	96.29	96.32	IR279			
13H	–0.4	Disseminated	97.02	97.02	IR280			
13H	–1.1	Disseminated	97.55	97.65	IR281			

Table T15 (continued).

Core, section	ΔT (°C)	Gas hydrate texture*	Depth interval (mbsf)† Top	Depth interval (mbsf)† Bottom	Anomaly designation‡	Hydrate sample Top (cm)	Hydrate sample Bottom (cm)	Hydrate sample Depth (mbsf)
13H	–1.5	Disseminated	98.27	98.61	IR282			
13H	–0.9	Disseminated	100.30	100.41	IR283			
13H	–0.7	Disseminated	101.20	101.48	IR284			
13H-4	–2.1	Nodular on dipping plane	101.79	101.90	IR285	56	76	101.43
13H	–0.8	Disseminated	106.09	106.19	IR286			
14H	–1.0	Disseminated; mud worm may be source	110.39	110.42	IR287			
14H	–0.4	Disseminated	110.80	111.00	IR288			
14H-3	–0.8	Disseminated	111.80	111.98	IR289			
14H-5	–1.8	Vein parallel to bedding	113.89	113.98	IR290	125	135	113.75
15X-1	–3.5	Nodular; core top hydrate sample missing	116.40	116.80	IR291	28	64	116.28
15X	–0.7	Disseminated	117.71	117.75	IR293			
15X	–0.8	Disseminated	118.81	118.92	IR294			
15X-3	–1.5	Vein; parallel bedding	119.54	119.60	IR295	108	118	119.22

Notes: * = from uncut core liner. † = difference between these depth intervals and the equivalent curated section depth intervals is typically <1m. ‡ = designation used for reference to specific anomalies in text and figures.

Table T16. Moisture and density, Holes 1245B, 1245C, and 1245E. (Continued on next page.)

Core, section, interval (cm)	Depth (mbsf)	Density (g/cm³)		Porosity (%)
		Bulk	Grain	
204-1245B-				
1H-1, 18–20	0.18	1.645	2.893	66.8
1H-1, 74–76	0.74	1.585	2.741	67.3
1H-2, 74–76	2.24	1.645	2.846	65.9
1H-3, 74–76	3.74	1.637	2.724	63.9
1H-4, 74–76	5.24	1.667	2.727	62.2
1H-5, 74–76	6.74	1.625	2.658	63.2
1H-6, 74–76	8.24	1.762	2.737	56.9
1H-7, 60–62	9.10	1.647	2.677	62.3
2H-1, 74–76	10.24	1.637	2.717	63.8
2H-2, 74–76	11.74	1.644	2.714	63.3
2H-3, 74–76	13.24	1.681	2.705	60.9
2H-4, 74–76	14.74	2.268	2.706	26.1
2H-5, 29–31	15.79	1.647	2.701	62.8
3H-1, 74–76	19.74	1.689	2.724	60.9
3H-2, 74–76	21.24	1.692	2.744	61.2
3H-3, 74–76	22.74	1.689	2.710	60.6
3H-4, 74–76	24.24	1.661	2.684	61.6
3H-5, 74–76	25.74	1.664	2.681	61.4
3H-6, 34–36	26.84	1.693	2.741	61.0
4H-1, 57–59	29.07	1.649	2.678	62.2
4H-2, 74–76	30.74	1.622	2.715	64.6
4H-3, 74–76	32.24	1.703	2.652	58.3
4H-4, 74–76	33.74	1.683	2.649	59.5
4H-5, 74–76	35.24	1.688	2.699	60.4
4H-6, 74–76	36.74	1.718	2.730	59.3
5H-1, 74–76	38.74	1.694	2.649	58.8
5H-3, 74–76	41.74	1.682	2.688	60.5
5H-4, 55–57	43.05	1.682	2.689	60.5
5H-6, 77–79	46.27	1.677	2.680	60.5
6H-1, 108–110	48.58	1.680	2.665	60.0
6H-3, 48–50	50.98	1.720	2.655	57.3
6H-4, 54–56	52.54	1.728	2.697	57.9
6H-6, 38–40	54.91	1.678	2.704	61.1
7H-2, 43–45	57.98	1.675	2.672	60.5
7H-3, 131–133	60.36	1.725	2.714	58.5
7H-4, 77–79	61.21	1.682	2.714	61.1
7H-5, 69–71	62.27	1.684	2.688	60.3
7H-7, 65–67	65.23	1.669	2.652	60.4
8H-1, 96–98	67.46	1.745	2.683	56.6
8H-2, 74–76	68.74	1.739	2.743	58.4
8H-3, 82–84	70.24	1.710	2.625	57.1
8H-5, 82–84	73.24	1.744	2.667	56.2
8H-7, 17–19	75.53	1.773	2.638	53.6
8H-7, 45–47	75.81	2.012	2.715	41.5
9H-1, 74–76	76.74	1.788	2.747	55.6
9H-3, 87–89	79.63	1.754	2.707	56.6
9H-5, 31–33	82.03	1.870	2.745	50.8
9H-5, 74–76	82.46	1.763	2.778	57.9
9H-6, 36–38	83.58	1.766	2.701	55.7
10H-1, 36–38	85.86	1.735	2.670	56.8
10H-2, 50–52	87.50	1.721	2.689	58.1
10H-3, 74–76	88.87	1.732	2.814	60.4
10H-5, 74–76	91.87	1.750	2.789	58.8
11H-1, 80–82	95.80	1.707	2.699	59.2
11H-2, 74–76	96.71	1.712	2.717	59.4
11H-3, 94–96	98.41	1.702	2.636	58.0
11H-5, 56–58	101.03	1.738	2.806	59.9
11H-6, 74–76	102.71	1.744	2.799	59.5
12H-1, 42–44	104.92	1.753	2.695	56.4
12H-3, 74–76	108.21	1.737	2.796	59.8
12H-5, 74–76	111.21	1.756	2.677	55.7
13H-1, 74–76	114.74	1.712	2.694	58.8
13H-3, 74–76	117.50	1.730	2.767	59.5
13H-5, 74–76	120.50	1.728	2.709	58.2
14H-1, 74–76	123.44	1.726	2.695	58.0
14H-2, 60–62	124.70	1.765	2.687	55.4
14H-3, 50–52	126.10	1.787	2.749	55.7
14H-4, 22–24	127.18	1.788	2.724	55.1
15X-1, 74–76	128.54	1.708	2.680	58.7
15X-3, 74–76	130.10	1.754	2.702	56.5
15X-4, 74–76	131.60	1.706	2.672	58.6
16X-1, 68–70	138.18	1.631	2.686	63.5
16X-3, 74–76	141.24	1.688	2.648	59.1
16X-5, 74–76	144.24	1.741	2.715	57.6
17P-1, 34–36	147.44	1.859	2.704	50.3
17P-1, 56–58	147.66	1.820	2.758	54.1
17P-1, 83–85	147.93	1.813	2.746	54.2
18X-1, 74–76	149.84	1.807	2.728	54.0
18X-3, 74–76	152.72	1.768	2.740	56.6
18X-6, 74–76	155.89	1.694	2.687	59.7
19X-1, 85–87	157.85	1.732	2.677	57.1
19X-2, 74–76	159.24	1.779	2.698	54.9
19X-3, 74–76	160.74	1.792	2.685	53.8
19X-4, 74–76	162.24	1.794	2.700	54.1
20X-1, 74–76	167.24	1.816	2.666	51.8
20X-3, 58–60	170.08	1.816	2.659	51.5
20X-5, 63–65	173.13	1.828	2.673	51.3
21X-1, 76–78	176.86	1.837	2.703	51.6
21X-2, 14–16	177.74	1.826	2.665	51.1
21X-2, 39–41	177.99	1.749	2.418	48.0
21X-2, 74–76	178.34	1.825	2.659	51.0
21X-2, 88–90	178.48	1.721	2.409	49.7
21X-3, 12–14	179.14	1.754	2.440	48.5
21X-3, 48–50	179.50	1.804	2.660	52.3
21X-3, 87–89	179.89	1.917	2.636	44.6
21X-3, 125–127	180.27	1.804	2.645	51.9
21X-4, 16–18	180.66	1.753	2.468	49.5
21X-4, 42–44	180.92	1.732	2.409	48.8
21X-4, 62–64	181.12	1.813	2.636	51.1
21X-5, 10–12	181.62	1.836	2.635	49.6
21X-5, 46–48	181.98	1.820	2.626	50.3
22X-1, 76–78	186.16	1.901	2.700	47.7
22X-2, 45–47	187.35	1.882	2.768	50.8
22X-2, 78–80	187.68	1.843	2.670	50.2
22X-3, 72–74	189.12	1.866	2.659	48.5
22X-4, 62–64	190.52	1.811	2.750	54.4
22X-4, 80–82	190.70	1.836	2.679	50.9
22X-6, 85–87	193.75	1.852	2.709	50.8
23X-1, 74–76	195.44	1.792	2.669	53.3
23X-3, 74–76	198.44	1.854	2.731	51.4
23X-6, 74–76	202.94	1.856	2.716	50.8
24X-1, 72–74	205.02	1.816	2.778	54.8
24X-3, 74–76	207.94	1.789	2.687	54.0
24X-5, 74–76	210.94	1.769	2.633	53.7
25X-1, 74–76	214.74	1.892	2.780	50.6
25X-3, 99–101	217.98	1.849	2.789	53.3
25X-5, 74–76	220.73	1.839	2.729	52.2
26X-1, 27–29	223.97	1.852	2.736	51.6
26X-3, 82–84	227.40	1.806	2.702	53.4
26X-6, 54–56	231.12	1.293	1.456	37.7
27X-1, 68–70	233.98	1.843	2.743	52.3
27X-3, 76–78	237.06	1.844	2.707	51.3
27X-5, 64–66	239.94	1.913	2.755	48.6
28X-1, 102–104	244.02	1.369	1.570	36.8
28X-3, 55–57	246.48	1.818	2.709	52.9
28X-5, 72–74	249.65	1.803	2.668	52.6
29X-1, 72–74	253.32	1.842	2.735	52.2
29X-3, 84–86	256.44	1.816	2.626	50.6
29X-5, 76–78	259.36	1.808	2.713	53.6
30X-1, 74–76	262.94	1.857	2.697	50.2
30X-3, 74–76	265.94	1.830	2.695	51.8
30X-5, 74–76	268.91	1.836	2.725	52.2
30X-7, 33–35	271.45	1.862	2.716	50.5
31X-1, 74–76	272.64	1.902	2.802	50.6
31X-3, 69–71	275.49	1.852	2.704	50.7
31X-6, 76–78	279.77	1.853	2.699	50.5
32X-1, 82–84	282.32	1.857	2.695	50.2

Table T16 (continued).

Core, section, interval (cm)	Depth (mbsf)	Density (g/cm³) Bulk	Density (g/cm³) Grain	Porosity (%)
32X-3, 87–89	285.37	1.814	2.648	51.4
32X-5, 113–115	288.63	1.858	2.746	51.6
32X-7, 32–34	290.32	1.855	2.744	51.7
33P-1, 27–29	291.47	1.780	2.747	56.1
33P-1, 44–46	291.64	1.848	2.711	51.1
34X-1, 74–76	293.94	1.817	2.689	52.3
34X-3, 75–77	296.95	1.831	2.633	49.8
34X-5, 74–76	299.94	1.795	2.643	52.4
34X-7, 46–48	302.16	1.830	2.700	51.9
35X-1, 61–63	301.41	1.823	2.618	49.9
35X-3, 79–81	304.59	1.876	2.734	50.1
35X-5, 71–73	307.51	1.892	2.785	50.7
35X-7, 26–28	309.85	1.889	2.724	49.2
36X-1, 69–71	311.09	1.858	2.736	51.3
36X-3, 59–61	313.99	1.879	2.744	50.3
36X-5, 70–72	317.10	1.878	2.787	51.5
37X-1, 74–76	320.74	1.841	2.653	49.9
37X-1, 135–136	321.35	1.878	2.696	48.9
37X-1, 138–140	321.38	1.867	2.819	53.0
37X-4, 66–68	325.16	1.816	2.618	50.3
37X-6, 74–76	328.24	1.874	2.654	47.9
38X-1, 80–82	330.50	1.927	2.791	48.9
38X-3, 85–87	333.55	1.941	2.830	49.2
38X-6, 70–72	337.90	1.958	2.895	50.1
39X-1, 77–79	339.97	1.949	2.844	49.2
39X-3, 69–71	342.89	1.905	2.755	49.1
39X-5, 70–72	345.83	1.948	2.771	47.1
40X-1, 30–32	349.20	1.858	2.708	50.5
40X-1, 80–82	349.70	1.827	2.670	51.2
40X-3, 82–84	352.72	1.916	2.799	49.8
40X-5, 108–110	355.95	1.882	2.696	48.7
41X-1, 61–63	359.11	1.913	2.778	49.3
41X-3, 61–63	362.11	1.922	2.789	49.1
41X-4, 61–63	363.11	1.946	2.857	49.7
42X-1, 90–92	369.10	1.894	2.738	49.3
42X-3, 68–70	371.88	1.889	2.708	48.6
42X-5, 56–58	374.74	1.974	2.771	45.6
43X-1, 68–70	378.48	1.921	2.742	47.8
43X-3, 68–70	381.48	1.932	2.752	47.5
43X-5, 68–70	384.48	1.947	2.739	46.2
44X-1, 78–80	388.18	1.977	2.739	44.4
44X-3, 72–74	391.12	1.931	2.725	46.7
44X-5, 56–58	393.96	1.948	2.734	46.0
45X-1, 74–76	397.84	1.931	2.701	45.9
45X-3, 71–73	400.81	1.948	2.720	45.5
45X-5, 19–21	403.25	1.968	2.663	42.4
47X-1, 60–62	408.30	1.931	2.716	46.4
47X-3, 74–76	410.79	1.921	2.730	47.4
48X-1, 71–73	417.01	1.898	2.674	47.0
48X-3, 74–76	420.04	1.921	2.748	48.0
48X-5, 80–82	423.10	1.876	2.619	46.6
49X-1, 71–73	426.61	1.858	2.638	48.3
49X-3, 86–88	429.47	1.906	2.640	45.4
49X-5, 57–59	432.12	1.917	2.693	46.5
50X-1, 80–82	436.40	1.975	2.763	45.3
50X-3, 71–73	439.23	1.972	2.755	45.2
51X-1, 91–93	446.11	1.945	2.700	45.0
51X-3, 17–19	448.37	2.007	2.738	42.7
51X-3, 52–54	448.72	1.940	2.713	45.8
51X-5, 84–86	452.04	1.978	2.743	44.5
52X-1, 98–100	455.68	1.927	2.678	45.4
52X-3, 76–78	458.46	1.945	2.710	45.4
52X-5, 76–78	461.13	1.973	2.684	42.8
52X-7, 35–37	463.58	1.966	2.715	44.3
53X-1, 72–74	464.72	1.938	2.710	45.8
53X-3, 68–70	467.44	1.971	2.683	42.9
53X-5, 74–76	470.50	1.933	2.688	45.3
204-1245C-				
1H-1, 115–117	1.15	1.637	2.737	64.2
1H-2, 27–29	1.68	1.621	2.726	64.9
1H-2, 73–75	2.14	1.648	2.741	63.6
1H-2, 128–130	2.69	1.640	2.829	65.9
1H-3, 21–23	3.12	1.664	2.835	64.7
1H-3, 60–62	3.51	1.655	2.736	63.1
1H-3, 125–127	4.16	1.673	2.731	62.0
1H-4, 18–20	4.59	1.674	2.817	63.7
1H-4, 67–69	5.08	1.663	2.725	62.4
1H-6, 24–26	7.15	1.666	2.684	61.3
2H-1, 28–30	7.78	1.670	2.721	61.9
2H-1, 72–74	8.22	1.633	2.645	62.4
2H-1, 128–130	8.78	1.690	2.779	62.1
2H-2, 20–22	9.20	1.662	2.709	62.2
2H-2, 54–56	9.54	1.732	2.723	58.3
2H-2, 137–139	10.37	1.702	2.741	60.5
2H-3, 71–73	11.21	1.674	2.664	60.3
2H-4, 12–14	12.12	1.708	2.710	59.5
2H-6, 134–136	16.34	1.704	2.724	60.0
3P-1, 16–18	17.16	1.605	2.695	65.2
3P-1, 47–49	17.47	1.620	2.711	64.7
3P-1, 86–88	17.86	1.645	2.718	63.3
8P-1, 8–10	57.08	1.694	2.715	60.4
8P-1, 45–47	57.45	1.690	2.700	60.3
8P-1, 88–90	57.88	1.688	2.651	59.2
16P-1, 7–9	120.07	1.674	2.651	60.1
16P-1, 24–26	120.24	1.670	2.625	59.7
16P-1, 46–48	120.46	1.688	2.671	59.7
28H-3, 9–11	199.49	1.812	2.647	51.4
28H-3, 32–34	199.72	1.585	2.726	67.0
28H-3, 34–36	199.74	1.696	2.770	61.5
28H-3, 38–40	199.78	1.642	2.707	63.3
28H-3, 53–55	199.93	1.843	2.676	50.5
204-1245E-				
1R-1, 16–17	473.86	1.950	2.665	43.6
1R-1, 85–86	474.55	1.952	2.675	43.8
1R-2, 16–17	475.21	1.953	2.665	43.4
2R-1, 12–14	481.72	1.888	2.685	48.0
2R-1, 46–47	482.06	1.890	2.695	48.2
2R-2, 12–14	482.61	1.950	2.717	45.3
2R-2, 94–96	483.43	1.971	2.720	44.2
3R-1, 68–70	491.88	1.946	2.736	46.1
3R-2, 48–50	493.12	1.955	2.705	44.6
4R-1, 73–75	501.63	1.965	2.746	45.4
4R-2, 60–62	503.00	1.930	2.732	46.9
4R-2, 100–102	503.40	1.864	2.653	48.5
5R-1, 48–50	510.98	2.005	2.759	43.5
5R-2, 28–30	512.22	1.991	2.698	42.2
6R-1, 48–50	520.68	1.989	2.701	42.4
6R-1, 65–75	520.85	1.976	2.738	44.5
6R-2, 64–66	521.89	1.945	2.704	45.2
7R-1, 74–76	530.54	2.021	2.709	40.8
7R-2, 77–79	532.07	1.926	2.686	45.7
8R-1, 45–47	539.75	1.913	2.700	46.9

Table T17. Compressional wave velocity measurements, Holes 1245B, 1245C, and 1245E.

Core, section, interval (cm)	Depth (mbsf)	V_p (mls) PWS3	PWS2	PWS1
204-1245B-				
1H-1, 94.0	0.94	1561		
1H-2, 20.8	1.71	1557		
1H-3, 20.3	3.20	1550		
1H-4, 20.5	4.71	1541		
1H-5, 91.3	6.91	1551		
1H-6, 80.8	8.31	1586		
2H-1, 33.6	9.84	1550		
2H-1, 89.6	10.40	1551		
2H-2, 80.6	11.81	1560		
204-1245C-				
1H-1, 112.5	1.13	1550		
1H-1, 114.7	1.15		1534	
1H-1, 113.9	1.14			1521
1H-4, 15.3	4.56	1530		
1H-4, 16.1	4.57		1545	
1H-4, 15.8	4.57			1526
1H-4, 63.8	5.05	1535		
1H-4, 64.5	5.06		1539	
1H-4, 65.2	5.06			1526
1H-4, 128.4	5.69	1567		
1H-4, 127.9	5.69		1536	
1H-4, 121.0	5.62			1529
1H-5, 18.5	6.10	1533		
1H-5, 19.3	6.10		1547	
1H-5, 60.5	6.52	1542		
1H-5, 60.5	6.52		1542	
1H-5, 20.0	6.11			1530
1H-5, 60.2	6.51			1527
1H-6, 20.4	7.11	1561		
1H-6, 21.1	7.12		1565	
1H-6, 20.7	7.12			1542
2H-1, 26.9	7.77	1553		
2H-1, 29.5	7.80		1484	
2H-1, 70.3	8.20	1531		
2H-1, 71.4	8.21		1484	
2H-1, 127.0	8.77	1554		
2H-1, 129.2	8.79		1477	
2H-2, 17.4	9.17	1550		
2H-2, 18.2	9.18		1409	
2H-2, 55.0	9.55	1584		
2H-2, 54.6	9.55		1501	
2H-2, 135.6	10.36	1480		
2H-2, 102.0	10.02		1468	
204-1245E-				
1R-1, 16.0	473.86	1700 (x)		
1R-2, 15.0	475.20	2018 (z)		
1R-2, 15.0	475.20	1941 (y)		
1R-2, 15.0	475.20	2090 (x)		
2R-1, 46.0	482.06	1915 (x)		
2R-1, 46.0	482.06	1927 (y)		
2R-2, 12.0	482.61	1985 (x)		
4R-2, 101.0	503.41	2013 (z)		
4R-2, 101.0	503.41	2035 (x)		
6R-2, 65.0	521.90	2115 (z)		
7R-1, 75.0	530.55	2219 (z)		
7R-2, 78.0	532.08	1971 (z)		

Table T18. Thermal conductivity, Holes 1245B and 1245C.

Core, section, interval (cm)	Depth (mbsf)	Thermal conductivity (W/[m·K])	Individual measurements (W/[m·K])		
204-1245B-					
1H-3, 75	3.75	1.031	1.046	1.008	1.040
2H-3, 75	13.25	0.991	0.995	1.005	0.972
3H-3, 75	22.75	1.007	0.998	1.003	1.021
4H-2, 64	30.64	0.856	0.834	0.863	0.872
4H-3, 75	32.25	0.997	1.032	1.001	0.950
4H-5, 70	35.20	1.029	1.024	1.039	1.024
5H-3, 79	41.79	0.979	0.983	0.984	0.970
6H-3, 41	50.91	0.986	0.977	0.990	0.991
7H-2, 40	57.95	0.932	0.944	0.916	0.937
7H-3, 75	59.80	1.033	1.044	1.007	1.047
7H-5, 90	62.48	0.869	0.866	0.870	0.870
8H-4, 75	71.67	0.972	0.965	0.971	0.979
9H-3, 20	78.96	1.046	1.076	1.051	1.010
10H-1, 35	85.85	1.056	1.081	1.042	1.046
10H-3, 68	88.81	0.977	0.984	0.991	0.956
10H-5, 75	91.88	0.999	1.005	0.982	1.010
11H-3, 53	98.00	0.947	0.948	0.950	0.943
11H-4, 75	99.72	1.008	0.977	0.994	1.034
12H-3, 76	108.23	0.940	0.935	0.947	0.939
13H-1, 80	114.80	0.911	0.920	0.917	0.897
13H-3, 70	117.46	0.900	0.893	0.909	0.898
13H-5, 50	120.26	1.010	1.014	1.014	1.002
14H-1, 45	123.15	1.006	1.008	0.993	1.016
14H-2, 85	124.95	1.047	1.054	1.054	1.032
14H-4, 33	127.29	1.051	1.047	1.037	1.068
15X-1, 60	128.40	0.981	0.970	0.984	0.990
15X-3, 75	130.11	1.013	1.020	1.025	0.993
16X-1, 64	138.14	0.948	0.964	0.927	0.954
16X-3, 75	141.25	0.973	0.973	0.971	0.976
16X-5, 46	143.96	0.953	0.954	0.955	0.951
18X-3, 75	152.73	1.029	1.032	1.028	1.027
19X-3, 75	160.75	0.962	0.961	0.958	0.967
20X-3, 75	170.25	1.063	1.069	1.066	1.053
21X-3, 61	179.63	0.979	0.962	1.005	0.970
22X-3, 75	189.15	0.995	1.014	0.981	0.990
23X-3, 70	198.40	1.042	1.036	1.043	1.046
24X-3, 75	207.95	1.004	1.008	1.006	0.997
25X-3, 75	217.74	1.223	1.225	1.208	1.237
26X-3, 85	227.43	0.990	0.994	0.994	0.982
27X-3, 75	237.05	1.035	1.034	1.009	1.063
28X-3, 75	246.68	1.018	1.045	1.018	0.991
29X-3, 87	256.47	1.023	1.050	1.009	1.009
30X-3, 70	265.90	0.996	0.996	1.006	0.986
31X-3, 72	275.52	0.996	1.005	0.994	0.990
32X-3, 69	285.19	0.920	0.943	0.899	0.917
34X-3, 57	296.77	0.947	0.959	0.953	0.929
35X-3, 69	304.49	0.982	0.981	0.983	0.981
36X-3, 75	314.15	1.027	1.041	1.027	1.012
37X-3, 75	323.75	1.028	1.033	1.032	1.018
38X-3, 72	333.42	0.965	0.973	0.946	0.976
39X-3, 40	342.60	0.962	0.981	0.943	0.963
40X-1, 54	349.44	0.975	0.993	0.954	0.977
40X-3, 65	352.55	0.817	0.822	0.816	0.813
40X-5, 53	355.40	0.967	0.991	0.963	0.946
42X-3, 94	372.14	0.941	1.016	0.924	0.882
43X-3, 41	381.21	0.988	0.980	1.008	0.977
44X-3, 81	391.21	0.932	1.046	0.883	0.866
45X-3, 77	400.87	0.997	1.018	0.996	0.978
47X-3, 58	410.63	0.999	1.028	0.983	0.985
48X-3, 64	419.94	1.035	1.035	1.050	1.021
49X-3, 33	428.94	0.872	0.925	0.860	0.832
204-1245C-					
24H-2, 75	179.35	1.110	1.136	1.116	1.079
24H-4, 75	182.35	1.116	1.110	1.096	1.141
24H-6, 51	185.11	1.026	1.002	1.015	1.061
25H-1, 75	187.35	0.995	0.994	0.992	1.000
26H-1, 70	191.80	1.064	1.061	1.068	1.064
26H-3, 55	194.65	0.930	0.934	0.932	0.923

Table T19. Shear strength values, Holes 1245B and 1245C. (See table notes. Continued on next page.)

Core, section, interval (cm)	Depth (mbsf)	Torvane (kPa)	Torvane size	ASV (kPa)
204-1245C-				
1H-1, 127.5	1.28			14.0
1H-2, 49	1.90			24.5
1H-3, 73.1	3.64			48.0
1H-3, 96.1	3.87			76.0
1H-3, 129.6	4.21			37.0
1H-4, 22	4.63			46.0
1H-4, 71.7	5.13			50.5
1H-5, 27.4	6.18			45.0
1H-5, 75.3	6.66			81.0
1H-6, 8.5	7.00			66.0
2H-1, 82.5	8.33			46.0
2H-3, 60	11.10			70.0
4H-1, 124	20.40			38.5
4H-2, 49	20.99			66.5
204-1245B-				
1H-1, 82	0.82	8.4	L	
1H-3, 88	3.88	42.5	S	
1H-5, 88	6.88	52.5	S	
2H-1, 81	10.31	60.0	S	
2H-3, 81	13.31	90.0	S	
2H-5, 37	15.87	62.5	S	
3H-1, 86	19.86	37.5	S	
3H-3, 85	22.85	102.5	S	
3H-5, 85	25.85	80.0	S	
4H-2, 128	31.28	29.0	M	
5H-1, 104	39.04	50.0	M	
5H-2, 111	40.61	46.0	M	
5H-3, 21	41.21	32.0	M	
6H-2, 117	50.17	65.0	M	
6H-3, 118	51.68	66.0	M	
6H-5, 7	53.57	60.0	M	
7H-3, 44	59.49	60.0	M	
8H-2, 28	68.28	59.0	M	
8H-4, 56	71.48	70.0	M	
8H-7, 10	75.46	65.0	M	
9H-1, 21	76.21	60.0	M	
9H-1, 115	77.15	75.0	M	
9H-4, 47	80.69	64.0	M	
9H-6, 26	83.48	70.0	M	
10H-1, 30	85.80	130.0	S	
10H-4, 85	90.48	70.0	S	
10H-5, 130	92.42	95.0	S	
11H-5, 42	100.89	142.5	S	
12H-1, 140	105.90	137.5	S	
12H-4, 123	110.20	105.0	S	
204-1245C-				
1H-1, 122	1.22	20.0	M	
1H-2, 35	1.75	27.0	M	
1H-2, 81	2.22	28.0	M	
1H-2, 142	2.83	30.0	M	
1H-3, 97	3.88	45.0	M	
1H-3, 74	3.65	47.0	M	
1H-3, 83	3.74	44.0	M	
1H-4, 29	5.70	62.5	S	
1H-4, 78	5.19	70.0	S	
1H-4, 142	5.83	62.5	S	
1H-5, 35	6.26	75.0	S	
1H-5, 74	6.65	77.5	S	
2H-1, 44	7.94	60.0	M	
2H-1, 48	7.98	62.5	S	
2H-1, 124	8.74	82.5	S	
2H-2, 25	9.25	80.0	S	
2H-2, 62	9.62	115.0	S	
2H-2, 112	10.12	95.0	S	
2H-3, 20	10.70	75.0	S	
2H-3, 69	11.19	85.0	S	
2H-3, 125	11.75	75.0	S	
2H-4, 8	12.08	100.0	S	
2H-4, 46	12.46	112.5	S	
2H-4, 130	13.30	100.0	S	
2H-6, 14	15.14	105.0	S	
2H-6, 138	16.38	95.0	S	
4H-1, 56	19.56	87.5	S	
4H-1, 124	20.24	65.0	S	
4H-2, 50	21.00	87.5	S	
4H-3, 60	22.60	87.5	S	
4H-4, 87	24.37	105.0	S	
4H-5, 44	25.44	100.0	S	
4H-6, 70	27.25	105.0	S	
5H-1, 18	28.68	102.5	S	
5H-3, 71	32.21	102.5	S	
5H-5, 40	34.90	115.0	S	
6H-2, 54	39.23	92.5	S	
6H-4, 6	41.18	117.5	S	
7H-1, 28	47.78	107.5	S	
7H-3, 48	50.99	120.0	S	
7H-7, 88	56.26	112.5	S	
9H-1, 16	59.16	112.5	S	
9H-2, 82	61.32	80.0	S	
9H-2, 105	62.55	87.5	S	
9H-3, 134	63.34	75.0	S	
9H-4, 105	64.55	87.5	S	
9H-5, 44	65.44	85.0	S	
9H-6, 82	67.32	87.5	S	
10H-1, 8	68.58	105.0	S	
10H-3, 8	70.53	105.0	S	
10H-4, 21	72.18	117.5	S	
10H-4, 128	73.25	130.0	S	
10H-5, 20	73.59	122.5	S	
10H-6, 42	74.90	137.5	S	
10H-7, 46	76.44	142.5	S	
11H-1, 41	78.41	130.0	S	
11H-3, 100	80.80	130.0	S	
11H-4, 60	81.90	125.0	S	
11H-4, 98	82.28	100.0	S	
11H-5, 85	83.65	112.5	S	
11H-6, 100	85.30	75.0	S	
11H-6, 145	85.75	80.0	S	
11H-7, 5	85.85	75.0	S	
11H-7, 82	86.62	70.0	S	
12H-1, 13	87.63	107.5	S	
12H-3, 14	90.64	97.5	S	
13H-2, 94	99.44	75.0	S	
13H-3, 83	100.70	102.5	S	
13H-5, 35	101.98	105.0	S	
13H-6, 95	104.08	95.0	S	
14H-1, 54	107.04	77.5	S	
14H-1, 85	107.35	100.0	S	
14H-2, 119	109.19	115.0	S	
14H-3, 20	109.70	102.5	S	
14H-4, 87	111.87	100.0	S	
14H-6, 69	114.54	102.5	S	
15X-2, 29	116.93	40.0	S	
15X-3, 61	118.75	45.0	S	
15X-5, 61	121.43	40.0	S	
17X-1, 98	122.98	72.5	S	
17X-2, 51	124.01	75.0	S	
17X-3, 44	125.20	80.0	S	
17X-5, 39	127.94	95.0	S	
19X-1, 103	131.03	70.0	S	
19X-2, 81	132.31	65.0	S	
19X-4, 40	134.36	65.0	S	
19X-4, 99	134.95	75.0	S	
20X-1, 55	139.25	65.0	S	
20X-2, 65	140.85	90.0	S	
20X-3, 76	142.46	65.0	S	

Table T19 (continued).

Core, section, interval (cm)	Depth (mbsf)	Torvane (kPa)	Torvane size	ASV (kPa)
20X-6, 101	146.06	70.0	S	
21X-1, 124	149.64	80.0	S	
21X-3, 77	152.17	72.5	S	
22X-1, 129	159.19	112.5	S	
22X-2, 48	159.88	100.0	S	
22X-3, 62	161.52	117.5	S	
22X-4, 80	163.20	125.0	S	
22X-4, 126	163.66	105.0	S	
22X-6, 90	166.30	110.0	S	
22X-6, 134	166.74	137.5	S	
23X-1, 76	168.16	100.0	S	
23X-2, 108	169.98	57.5	S	
23X-3, 65	171.05	125.0	S	
23X-4, 104	172.94	85.0	S	
23X-6, 73	175.63	110.0	S	
23X-7, 45	176.35	120.0	S	

Note: L = large, M = medium, S = small. AVS = automated shear vane.

Table T20. Temperature measurements, Holes 1245B and 1245C.

Hole, core	Depth (mbsf)	Temperature (°C)	Thermal conductivity (W/[m·K])	Tool ID
204-				
1245C-1H	00.0	3.82	1.20	12
1245B-4H	38.0	5.98	1.03	12
1245B-7H	66.5	8.09	0.87	12
1245B-10H	95.0	8.95	1.00	12
1245B-13H	122.7	10.71	1.01	12
1245B-14H	127.8	11.00	1.03	12
1245C-24H	186.6	13.93	1.00	12
1245C-25H	191.1	14.52	1.00	12
1245C-26H	195.9	14.71	1.04	12
1245C-28H	200.7	14.94	1.00	12
1245B-20X–21X	176.6	—	—	2
1245B-27X–28X	243.0	—	—	2
1245B-39X–40X	348.9	—	—	2

Notes: APCT measurements were made at the core catcher of the core listed. For APCT measurements, thermal conductivity represents the average of the nine measurements taken in the adjacent core. Measurements for two core numbers are given (e.g. 204-1245B-20X–21X) were made with the DVTP between these two cores. At this site, none of the DVTP deployments yielded temperature time series indicative of a reliable measurement. ID = identification.

Table T21. Results from degassing experiments, Holes 1245B and 1245C.

Core	Depth (mbsf) Top	Depth (mbsf) Bottom	Run time (min)	Total volume of gas released (mL)	Volume of components released (mL) $O_2 + N_2$	Volume of components released (mL) C_1	Volume of components released (mL) CO_2	Volume of components released (mL) C_{2+}	Concentration of components released (%) $O_2 + N_2$	Concentration of components released (%) C_1	Concentration of components released (%) CO_2	Concentration of components released (%) C_{2+}	Core length (m)	Porosity (%)	C_1 concentration in situ (mM)
204-1245B-															
17P	147.1	148.1	1,668	1,700	177.4	1,512.6	5.7	4.22	10.4	89.0	0.3	0.248	1.00	57	74.3
33P	291.2	292.2	1,754	1,065	48.3	1,013.5	3.0	0.12	4.5	95.2	0.3	0.011	1.00	52	54.6
204-1245C-															
3P	17.0	18.0	334	315	92.4	221.8	0.8	0.01	29.3	70.4	0.3	0.003	0.90–1.00	61	10.2–11.3
8P	57.0	58.0	1,358	1,460	161.7	1,296.1	2.1	0.06	11.1	88.8	0.1	0.004	0.93–1.00	60	60.0–64.5
16P	120.0	121.0	4,685	19,025	489.4	18,489.3	40.3	6.08	2.6	97.2	0.2	0.032	0.80–1.00	58	893.3–1,116.6

Note: Core length is reported as measured after the core was degassed and split (i.e., curator length) and as cored in subsurface.

Table T22. HYACINTH pressure coring summary, Holes 1245B and 1245C.

Core	Deployment number	Date (Aug 2002)	Local time (hr)	Depth Water (mbsl)	Depth Core (mbsf)	BSR (mbsf)	Lithology	Core recovered (cm)	Pressure (bar)	Comments
204-1245B-										
46E	HRC 5	9	0020	876	407	134	Stiff indurated silty claystone	38	0	Tool problems, poor hole conditions.
204-1245C-										
18Y	FPC 7	10	0830	876	129	134	Lightly indurated silty clay	90	0	Cut good core, lower valve didn't close properly.
27Y	FPC 8	10	1935	876	195	134	Moderately indurated silty clay	15	0	Formation too stiff, liner imploded, seal dislodged, valve not closed.
29E	HRC 6	10	2220	876	201	134	Moderately indurated silty clay	20	0	Active heave compensator failed during coring, poor test.

Notes: HRC = HYACE rotary corer, FPC = Fugro Pressure corer. BSR = bottom-simulating reflector.

Table T23. Conventional wireline logging operations summary, Hole 1245E.

Date (Aug 2002)	Local time (hr)	Tool depth (mbsf)	Remarks
13	2300		Last core on deck
14	1500–1615		Wiper trip up to 345 mbsf; back down to 380 mbsf
14	1645–1715		Hole displaced with sepiolite mud
14	1715–1900		Set back top drive; bottom of pipe put at 88 mbsf
14	1900		Start logging rig-up
14	2030		Start going down with the triple combination (TAP/DIT/HLDT/APS/HNGS/QSST) tool string
14	2115	0	Stop 5 min at mudline for temperature calibration
14	2153	320	Tool at TD; start logging up at 900 ft/hr
14	2245	73	Tool back into pipe; speed up to 1500 ft/hr to log mudline
14	2255	0	End of pass 1
14	2315	319	Tool at TD for QSST checkshot survey
15	0035	319	Tool at TD; start logging-up pass 2 at 900 ft/hr
15	0110	104	End of pass 2; speed up tool to 6000 ft/hr
15	0112	73	Tool back in pipe
15	0140		Tool back on rig floor
15	0300		Finish rig-down
15	0305		Start logging rig-up
15	0410		Start going down with the FMS-sonic (FMS/DSI/SGT) tool string
15	0445	319	Tool at TD; start logging up at 900 ft/hr
15	0530	73	Tool back into pipe; end of pass 1
15	0550	316	Tool at TD; start logging-up pass 2 at 900 ft/hr
15	0640	73	End of pass 2; speed up tool to 6000 ft/hr
15	0715		Tool back on rig floor
15	0830		Finish rig-down

Notes: TD = total depth. See Table **T8,** p. 102, in the "Explanatory Notes" chapter for definitions of acronyms.